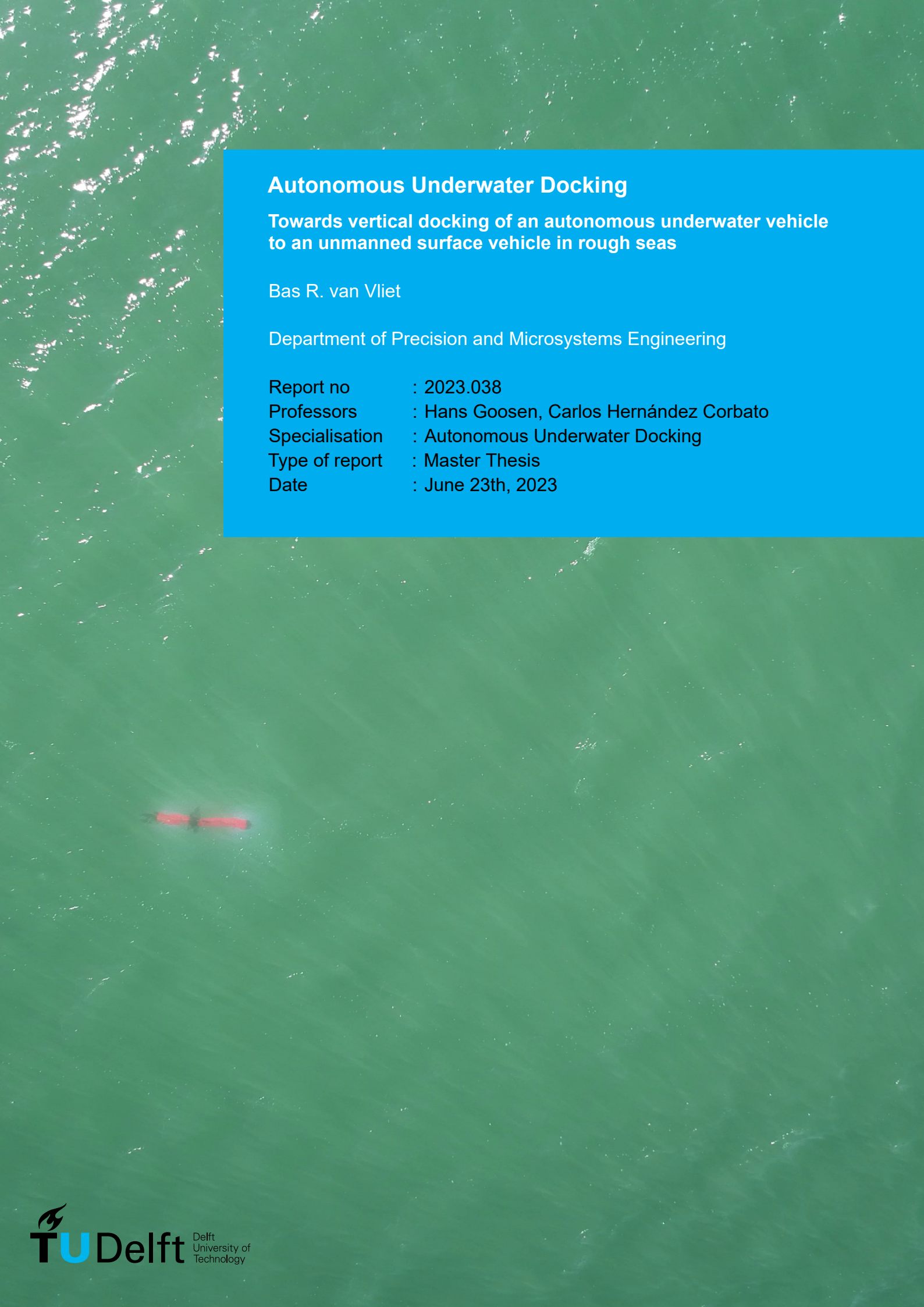

Autonomous Underwater Docking

Towards vertical docking of an autonomous underwater vehicle to an unmanned surface vehicle in rough seas

Bas R. van Vliet

Department of Precision and Microsystems Engineering

Report no : 2023.038
Professors : Hans Goosen, Carlos Hernández Corbato
Specialisation : Autonomous Underwater Docking
Type of report : Master Thesis
Date : June 23th, 2023

TU Delft Delft University of Technology

Autonomous Underwater Docking

Towards vertical docking of an autonomous underwater vehicle to an unmanned surface vehicle in rough seas

by

Bas R. van Vliet

Master Thesis

To obtain the degree of Master of Science in Mechanical Engineering for the track High-Tech Engineering at the Delft University of Technology,

Student Name	Student Number
Bas R. van Vliet	4594959

First Supervisor:	Hans Goosen
Second Supervisor:	Carlos Hernández Corbato
Project Duration:	February 2022 - June 2023
Faculty:	Faculty of 3ME, TU Delft

This thesis is confidential and cannot be made public until June 23th, 2025.

TU Delft

Abstract

The offshore industry is adopting Autonomous Underwater Vehicles (AUVs), to decrease the costs associated with surveying underwater sites. Despite requiring less human supervision, AUVs still depend on costly servicing from a vessel, before and after deployment. Combining an AUV with an Unmanned Surface Vessel (USV), a survey vessel that operates without humans on board, could drastically reduce operational costs. This thesis focuses on the crucial requirement of this combination: the autonomous docking of the AUV to the USV.

Current studies focused on the AUV-USV combination lack effective solutions for docking in rough ocean conditions, while this is key for its operational employability. These studies have explored horizontal docking approaches, while an unexplored alternative is a vertical docking approach from below the USV. This approach may experience reduced influence of waves, as the wave disturbance acting on the AUV and the USV are phase synchronized. The objective of this study is to evaluate the viability of vertically docking an AUV to a USV in rough seas, using the Lobster Scout AUV as a case study for an initial performance evaluation.

This study first identified and scoped the key elements for this initial performance evaluation, which included the waves, the USV, the Lobster Scout, the Docking Station (DS), and vertical docking Guidance Navigation and Control (GNC). Furthermore, the scope was limited to the critical docking stage, where the vehicles are within meters of each other. The study used simulation as the primary method to investigate the thesis objective and a 2-Dimensional (2D) model was developed to simulate the system dynamics, which was fitted and verified using a variety of methods, including analytical calculations, mesh convergence studies, experiments, and visual analysis.

To determine the viability of the vertical docking approach of the USV-AUV combination, a probability distribution-based method was developed. Viability was expressed in terms of the maximum operational sea state and the estimated operational up-time. Since docking success under the presence of waves is described probabilistically, the requirement was set that at least 991 out of a 1000 docks should be successful. Furthermore, Monte Carlo simulations were used to obtain the docking performance over a variety of sea states, navigational settings, and different guidance and control methods.

A target state vertical guidance method using way-points was designed with various Proportional-Integral-Derivative (PID) based controllers to guide the Lobster Scout to the DS. It was also determined whether kinematic prediction or polynomial prediction could improve docking performance and the impact of navigation on docking performance was investigated. It was found that the vertical docking approach shows promise for enabling a reliable AUV-USV combination for the Lobster Scout in medium to rough seas, with a significant wave height of 1.65 m and 3.6 m respectively, resulting in an estimated annual operational up-time of 59 % to 94 % in the North Sea. Furthermore, there is potential to achieve even higher sea states with improved GNC methods.

Overall, this study suggests that the vertical docking approach can lead to a viable AUV-USV combination with improved operational employability compared to current docking studies using horizontal approaches, although the author is of the opinion that both approaches require further investigation.

Preface

This report is the result of my research aimed at drastically reducing the cost of underwater data gathering. The large diversity of topics I had to familiarize myself with in this research has challenged me greatly while allowing me to apply and expand upon the skills and knowledge acquired during my studies. While conducting this research, I learned a great deal about underwater docking, programming, critical thinking, modeling, writing, and statistics.

I would like to express my sincere gratitude to my supervisors, Hans Goosen and Carlos Hernández Corbato, for their valuable guidance and feedback in the research process. Our collaborative brainstorming sessions were particularly enjoyable, enabling us to refine ideas and devise effective approaches for this work. Additionally, I would like to thank my colleagues at Lobster for their assistance with programming and experiments, as well as their constructive feedback on this report.

I hope you will find this report engaging and insightful.

Bas R. van Vliet
Delft, June 2023

Acronyms

2D	2-Dimensional
3D	3-Dimensional
ADCP	Acoustic Doppler Current Profiler
ANFIS	Adaptive Neuro-Fuzzy Interference System
AUV	Autonomous Underwater Vehicle
BEM	Boundary Element Method
CAD	Computer-Aided Design
CB	Center of Buoyancy
CG	Center of Gravity
CO	Coordinate Origin
CPV	Cascaded Pose and Velocity
CPVA	Cascaded Pose Velocity and Acceleration
DOF	Degrees of Freedom
DS	Docking Station
DVL	Doppler Velocity Log
EKF	Extended Kalman Filter
FoV	Field of View
GNC	Guidance Navigation and Control
GNSS	Global Navigation Satellite System
INS	Inertial Navigation System
JONSWAP	JOint North Sea WAve Project
KF	Kalman Filter
LBL	Long BaseLine
LED	Light Emitting Diode
LoS	Line of Sight
LQR	Linear–Quadratic Regulator
MPC	Model Predictive Control
NED	North-East-Down
NFZ	No-Fly Zone
PID	Proportional-Integral-Derivative
PNG	Proportional Navigational Guidance
PRM	Probabilistic Roadmap Method
RAO	Response Amplitude Operator
ROV	Remotely Operated underwater Vehicle
RRT	Random Rapid Tree
RSME	Root Mean Square Error
SBL	Short BaseLine
SISO	Single Input Single Output
SLAM	Simultaneous Localisation and Mapping
SQP	Sequential Quadratic Programming
SRG	Speed Regulated Guidance
USBL	Ultra-Short BaseLine
USV	Unmanned Surface Vehicle
UUV	Unmanned Underwater Vehicle

Contents

1 Introduction

1.1. Motivation

The offshore industry is undergoing significant changes with the transition towards a sustainable economy and renewable energy sources. One major trend is the rapid growth of the offshore wind energy market, while the oil and gas industry is simultaneously seeking cost reductions to maintain a competitive edge. Recent advances have been made in deep sea mining as trials started in 2022, which operations require continuous monitoring and surveying of vast areas [1]. To facilitate cost-effective operations, there is a significant developmental effort aimed at reducing the number of people and support vessels required by introducing robotic solutions for underwater surveying, inspection, maintenance, and repair tasks.

The Remotely Operated underwater Vehicle (ROV) (see Figure 1.1a) is one such solution, which is commonly used in the offshore industry as a partial replacement for human divers, as it enhances safety and reduces costs in many applications [12]. ROVs have a wide range of applications, from underwater surveys of cables and pipelines to structural inspections and repair tasks of underwater constructions. However, a fundamental challenge in underwater robotics is the limited penetration of radio signals (only a few centimeters), making high-bandwidth wireless communication over large distances impossible. ROVs solve this issue by utilizing a cable (tether) that allows for high bandwidth real-time communication and vehicle control [12]. Nonetheless, ROVs are human-operated from a ship, significantly increasing costs.

(a) An example of a ROV from [71].

(b) an example of a cruising Autonomous Underwater Vehicle (AUV) from [31].

(c) An example of an Unmanned Surface Vehicle (USV) from [26].

Figure 1.1: Commonly used offshore robotics

Autonomous Underwater Vehicles (AUVs) (see Figure 1.1b) are another solution that partially addresses the cost of operating ROVs. AUVs are capable of operating independently in underwater environments, which means that high-bandwidth communication is not necessary for vehicle control. Furthermore, these vehicles require little to no support from an operator during their deployment, thereby reducing the need for direct human involvement. AUV are commonly used for bathymetry mapping

and surveying of large areas. AUVs can be divided in cruising and hovering AUVs based on their control strategy. Cruising AUVs typically rely on a single thruster and control surfaces (fins) to maneuver, whereas hovering AUVs use multiple thrusters to maintain their position. As a result, cruising AUVs require a minimum forward velocity to be controllable, while hovering AUVs are controllable at zero velocity [15].

Although AUVs are promising in terms of reducing human labor, they face limitations due to their limited energy supply and low level of autonomy, which requires frequent reprogramming [15]. These factors limit their operational attractiveness as they can only perform relatively short missions before requiring human servicing from a vessel. In general, AUV operation includes the steps presented in Figure 1.2 and explained below [6]:

- **Mission programming** An operator programs a task to be done by the AUV. This often is some type of surveying task where the AUV is required to obtain data from a large area near the seabed.
- **Launching** One or multiple operators deploy the AUV from a vessel into the water. This operation often involves some kind of lifting equipment such as a crane.
- **Executing mission** The AUV executes its underwater mission and uses its sensors to collect data. No operators are required in this step, but simple instructions may be sent to the AUV acoustically by the operator.
- **Recovering** The AUV surfaces to the sea level and sends its location to the vessel crew via radio communication. The vessel is sailed next to the AUV and one or multiple operators recover the AUV from the water to the vessel. In case the AUV is more sophisticated, it can also position itself next to the vessel if a relative position is known, however, recovery is still done by the operators using lifting equipment.
- **Transferring data and charging** An operator charges the AUV and transfers the data from the AUV to a data storage device to be post-processed later.

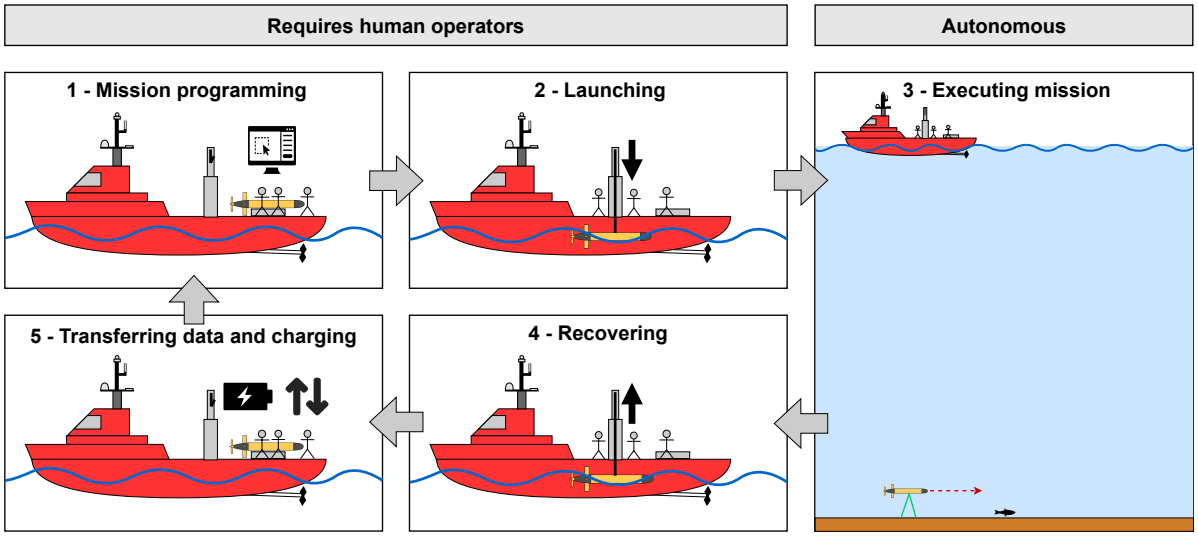

Figure 1.2: Typical operational procedure of an AUV.

Figure 1.2 shows that while AUVs execute their mission autonomously, the other steps in operating an AUV are not automated. This increases the operating costs of an AUV significantly. This raises the question of whether there is a way to automate these steps.

The concept of an underwater Docking Station (DS) has been proposed to enable longer deployment of AUVs. A DS is essentially an underwater garage that facilitates the recharging of batteries, data transfer, and mission reprogramming without requiring a vessel. In essence, it can automate steps 1, 2, 4, and 5 of Figure 1.2. Autonomous docking requires a reliable procedure that transitions the

AUV from free cruising to being locked and connected in the DS [15]. Generally, this involves relative localization (i.e., navigation), path planning (i.e., guidance), control, and capture of the AUV. Early concepts of docking systems envisioned AUVs being used for frequent and regular inspections of fixed underwater infrastructure, significantly reducing the operational costs associated with using a ship for vehicle deployment [75]. Consequently, most of the literature has focused on the case where the DS is fixed to the seafloor [75].

A fixed DS has a number of disadvantages, as it requires the construction of expensive underwater infrastructure, limits the AUV to a fixed operational area, and requires a dedicated rescue and repair mission with a vessel if the system is damaged. To address these issues, an AUV can be autonomously deployed from an Unmanned Surface Vehicle (USV), as illustrated in Figure 1.3. USVs (see Figure 1.1c) are remotely controlled and can be operated from land for various ocean surveying tasks. USVs have a range of sizes and can operate for days before refueling. However, USVs are constrained to surface operation and are susceptible to environmental disturbances, such as waves, winds, and currents, which pose significant challenges [15]. These challenges can be mitigated by deploying an AUV, which can perform inspections and high-resolution surveys close to the sea floor. However, autonomous docking of an AUV to an USV presents significant challenges due to the dynamic mismatch between the two vehicles in realistic offshore environmental conditions. As a result, successful docking solutions for this case are limited [75].

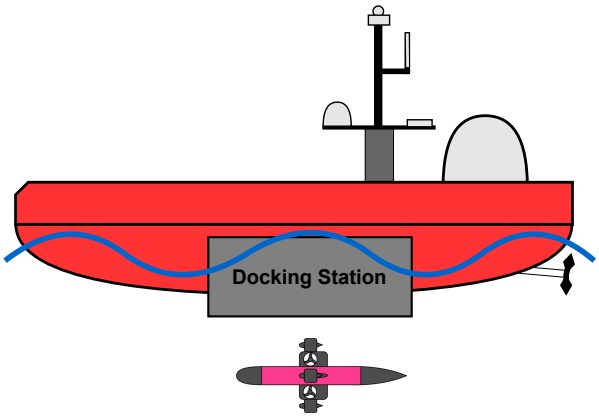

Figure 1.3: an USV-AUV combination with a DS.

While there has been extensive development of docking solutions for typical cruising AUVs, less attention has been given to docking solutions for hovering type AUVs [82]. However, due to the increased controllability of a hovering AUV during dynamic docking, exploring new solutions for hovering AUVs is of significant interest when docking to a floating DS such as an USV. This may provide a significant increase in viable operating conditions and improve the overall effectiveness of the AUV-USV combination, making it a promising area for research.

1.2. Knowledge gap

After reviewing a vast number of studies on docking, specifically for hovering AUVs and docking to vessels or floating elements, the results of which are presented in Appendix B, it has become apparent that only a few solutions for docking AUVs to a floating DS, such as an USV, have been explored. Two knowledge gaps have been identified in this area:

- **Approach direction** Firstly, studies that focus on docking to a floating DS have only considered horizontal approaches (see Figure 1.4a). An alternative solution is to approach the floating DS from below, as illustrated in Figure 1.4b, which is only possible with a hovering AUV, as cruising AUVs are generally only able to spiral up or down. To the best of the authors' knowledge, the vertical approach to a floating DS has not yet been addressed. [79, 22, 30, 64, 37, 55, 46, 75]
- **Environmental conditions** Secondly, most of these studies have only been conducted in mild environmental conditions. Operation of an AUV from a floating DS is fundamentally limited to

whether the AUV can be safely docked. In other words, one wants to maximize the range of environmental conditions in which docking is possible to increase operational employability. Horizontal approaches so far have been limited in their success regarding surface docking in rough seas. [79, 22, 30, 64, 37, 55, 46, 74, 83]

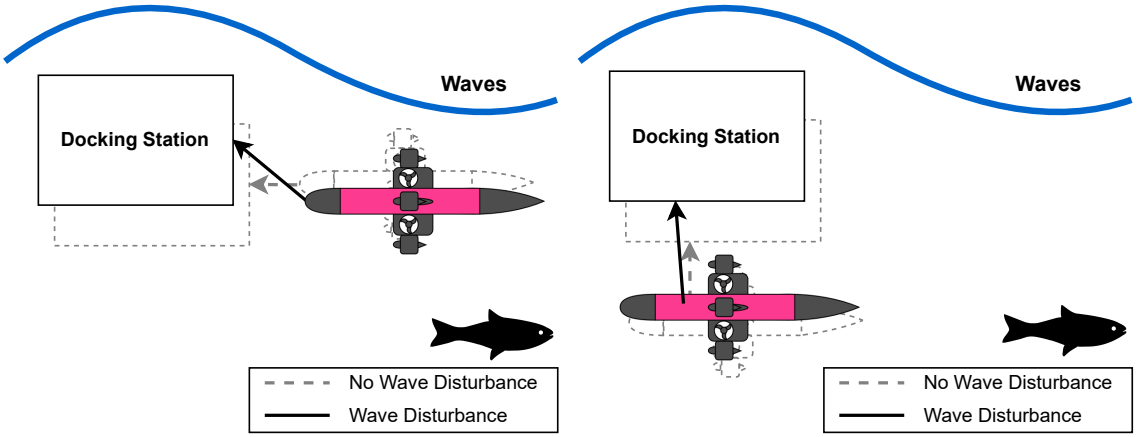

(a) Horizontal approach. The wave disturbance on the AUV and the DS are out of phase, resulting in a large relative disturbance.

(b) Vertical approach. The wave disturbance on the AUV and the DS are in phase, resulting in a small relative disturbance.

Figure 1.4: The intuition behind a horizontal docking approach and a vertical docking approach. The situation without waves is depicted by the dashed lines while the situation under the influence of waves is depicted by filled DS and AUV.

1.3. Gap relevance

This section explains the fundamental opportunity of vertical docking approaches to a floating DS in rough environmental conditions, and therefore why it is a relevant research area. To do so, wave motion is briefly discussed.

Wave motion Waves are one of the largest disturbances on the sea surface. The motions of water particles in waves are generally described as elliptical orbits with a specific phase and magnitude, as shown in Figure 1.5 [27]. As waves traverse over the sea surface, water particles differ in phase, depending on their horizontal coordinates. Furthermore, the deeper a water particle is, the smaller its magnitude of motion due to the wave [33]. The roughness of waves is generally indicated using the term sea state which indicates a certain wave height and the wave period combination.

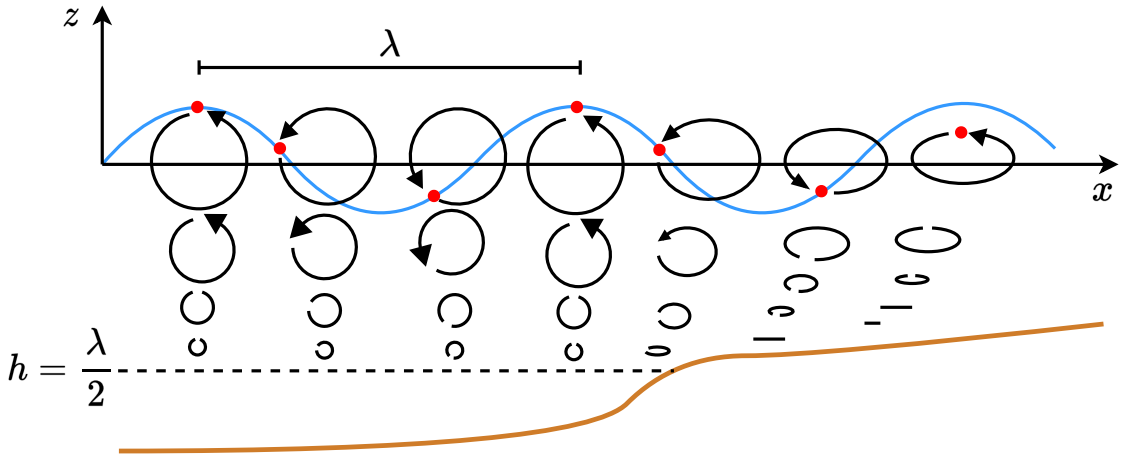

Figure 1.5: This figure shows the motion of fluid particles in a wave. In deep waters $h > \frac{\lambda}{2}$, the particles describe a circular motion. In shallow waters $h < \frac{\lambda}{2}$, fluid particles describe an elliptical motion. Furthermore, the red dots show that the particles are at different phases at different x coordinates. The size of the various ellipses shows that the magnitude of the particle motion decreases with depth

Wave phase synchronization of vertical approaches The disturbance of water particles in the presence of waves affects horizontal and vertical approaches differently. In horizontal approaches (see Figure 1.4a), the floating DS and the AUV experience a wave disturbance with the same magnitude, but with a shifting phase when the AUV approaches. On the other hand, in vertical approaches (see Figure 1.4b), the DS and the AUV experience a wave disturbance with the same phase, but with a shifting magnitude when the AUV approaches. This wave phase synchronization of the vertical approach, as opposed to wave magnitude synchronization, can potentially increase its operating conditions as the relative disturbance between the AUV and the DS can be smaller.

1.4. Stakeholders

Vertical docking to a floating DS has multiple stakeholders. The interest of these stakeholders is discussed below.

Science The novelty of this thesis lies in the unique vertical approach to a floating DS, which presents a critical gap in knowledge compared to the horizontal approach, and thus this approach is of scientific interest. The focus should be on designing a guidance system for this unique approach and determining its viability. Therefore, the goal of this thesis is to obtain an initial performance indication of the system in various ocean conditions through a proof of concept approach.

Industry Reducing the cost of operations is a significant concern for the industry. Combining an USV and an AUV is a potential solution, but current solutions have limited success in rough seas. A vertical docking approach with a floating surface element is a promising solution that could enable docking even in rough seas, thereby reducing operational costs. This thesis, therefore, considers the floating DS as an USV rather than a buoy or other floating structure.

Lobster Innovations BV The author is a co-founder of Lobster Innovations BV, a Dutch startup located in Delft that is developing a new type of hovering AUV called the Lobster Scout, which is shown in Figure 1.6 [6]. Lobster Innovations BV is interested in exploring docking solutions to reduce operational costs associated with deploying their AUV from a vessel. Before constructing a floating DS, it is crucial to have a thorough understanding of the design trade-offs and to make informed design decisions. Moreover, the unique design of the Lobster Scout may enable new docking solutions that provide advantages over existing ones.

Figure 1.6: The Lobster Scout, in development by Lobster Innovations BV

1.5. Research question

The goal of this thesis is to find out to what extent a vertical docking approach of the Lobster Scout to an USV is possible and how it performs in large waves. The hypothesis is that a vertical docking approach of the Scout leads to successful docking of the Scout to the USV at larger waves than current horizontal docking approaches have shown due to phase synchronization of the wave disturbance. The trade-offs between the complexity of the vertical guidance approach and its performance are also investigated. The main research question to be answered in this thesis is:

To what extent is a vertical docking approach of the Lobster Scout to an USV viable in rough seas?

To address the main research question, several sub-questions are formulated:

1. *What are the key elements to consider for an initial performance evaluation of the vertical docking approach to an USV?*
2. *How can the vertical docking system be modelled?*
3. *How to evaluate vertical docking performance?*
4. *What are effective vertical guidance and control methods for the Lobster Scout?*
5. *What is the influence of navigation on vertical docking performance?*

1.6. Approach

The study uses simulation as the primary method to investigate the vertical docking approach and the impact of various parameters on the docking performance. Simulation allows for efficient exploration of many different ocean conditions and vertical docking solutions at a low cost.

A simulation model was developed to simulate the system dynamics and a Monte Carlo simulation was used to obtain statistical data on the docking performance. The model was simulated over a large number of parameter configurations, including variations in sea state, guidance methods, and navigation parameters. Since the model contains random variables, statistical analysis was used to obtain their impact on vertical docking performance. The simulation model was developed primarily in Python such that the model could be easily integrated with the software developed by Lobster Innovations BV in the future.

The parameters and coefficients for the simulation model were obtained from multiple sources. Lobster Innovations BV has provided information on the design of the Lobster Scout. Furthermore, Ansys Aqua was used to obtain some of the hydrodynamic parameters of the Lobster Scout and was used to compute the motion responses of the USV. Various experiments with the Lobster Scout were performed to obtain key model coefficients.

To obtain confidence in the validity of the results, the main model assumptions have been either verified or justified. The results from Ansys Aqua have been verified with analytical calculations and mesh convergence studies. Confidence in the Lobster Scout model has been obtained with the support of experiments with the actual Lobster Scout. Furthermore, an extensive visualizer and animation toolbox was developed to verify the model.

However, there are limitations to the simulation approach, such as model assumptions, parameter inaccuracies, and modelling simplifications that affect the results. Critical assumptions in this thesis include the availability of navigation measurements and the assumption that entering the DS capture aperture results in a captured and locked AUV. Model limitations include the accuracy of the wave model at larger waves, the rough shape approximation of the USV, and the exclusion of asymmetries and thruster dynamics in the Lobster Scout model.

The expected outcomes of the study include identifying effective vertical docking guidance methods and obtaining an initial performance indication of the vertical docking approach to an USV for the Lobster Scout. Furthermore, insight into critical factors affecting vertical docking performance is expected,

and obtaining concept designs and design requirements of a vertical DS.

Overall, the simulation approach allows for fast generation of valuable insights and recommendations into the viability and characteristics of the vertical docking approach to an USV.

1.7. Scope

The vertical docking system is modelled in a 2-Dimensional (2D) setting, as the primary focus is on establishing a proof of concept and conducting an initial performance evaluation. The x-z plane is suitable for approximating the primary motions of water in waves [33]. Moreover, a 2D model has fewer parameters than a 3-Dimensional (3D) model, making it easier to identify the effect of each parameter on the model's behavior. In addition, a 2D setting offers benefits such as easier visualization, lower computational effort, and less model construction time. However, using a 2D model does lead to certain limitations. For instance, in a 2D setting, three out of six Degrees of Freedom (DOF) are always aligned, making it significantly easier to achieve a successful dock. Moreover, certain wave phenomena, such as directional spreading, are only present in a 3D setting and are thus not taken into account [33]. Finally, out-of-plane disturbance forces are not considered. Despite these limitations, using a 2D model provides a preliminary indication of the performance of the vertical approach. In future research, the 2D model can be converted to a 3D model to explore the influence of these limitations, as the model architecture and data structures are fundamentally similar.

1.8. Structure

The structure of this thesis is illustrated in Figure 1.7 and given below:

- **Chapter 2 Overview of vertical docking to an USV** - provides an overview of the existing underwater docking solutions, including their typical components and docking procedures and identifies and describes the key elements relevant for vertical docking to USV.
- **Chapter 3 Wave model** - describes the water motion caused by the waves. A regular wave model and an irregular North Sea wave model are described, after which the main assumptions are verified.
- **Chapter 4 AUV model** - describes the dynamic model of an AUV and verifies it, taking into account the inertial forces, the hydrostatic and hydrodynamic forces the control forces and the wave forces. Furthermore, the AUV model is verified and adapted for the Lobster Scout.
- **Chapter 5 USV model** - describes the motion response of the USV and the attached DS to the waves.
- **Chapter 6 Vertical docking performance** - Discusses the docking evaluation criteria to determine the performance of a vertical docking method.
- **Chapter 7 Vertical docking guidance and control** - describes and evaluates the performance of various vertical docking guidance and control methods for the Lobster Scout. The simulation results between the different guidance and control methods are compared over increasing sea states.
- **Chapter 8 Vertical docking navigation** - investigates the influence of vertical docking navigation on docking performance. The simulation results between various navigation settings are compared over the docking performance.
- **Chapter 9 Conclusion** - summarizes the conclusions from the various sub-questions to answer the main research question of this thesis and provides recommendations for future work.

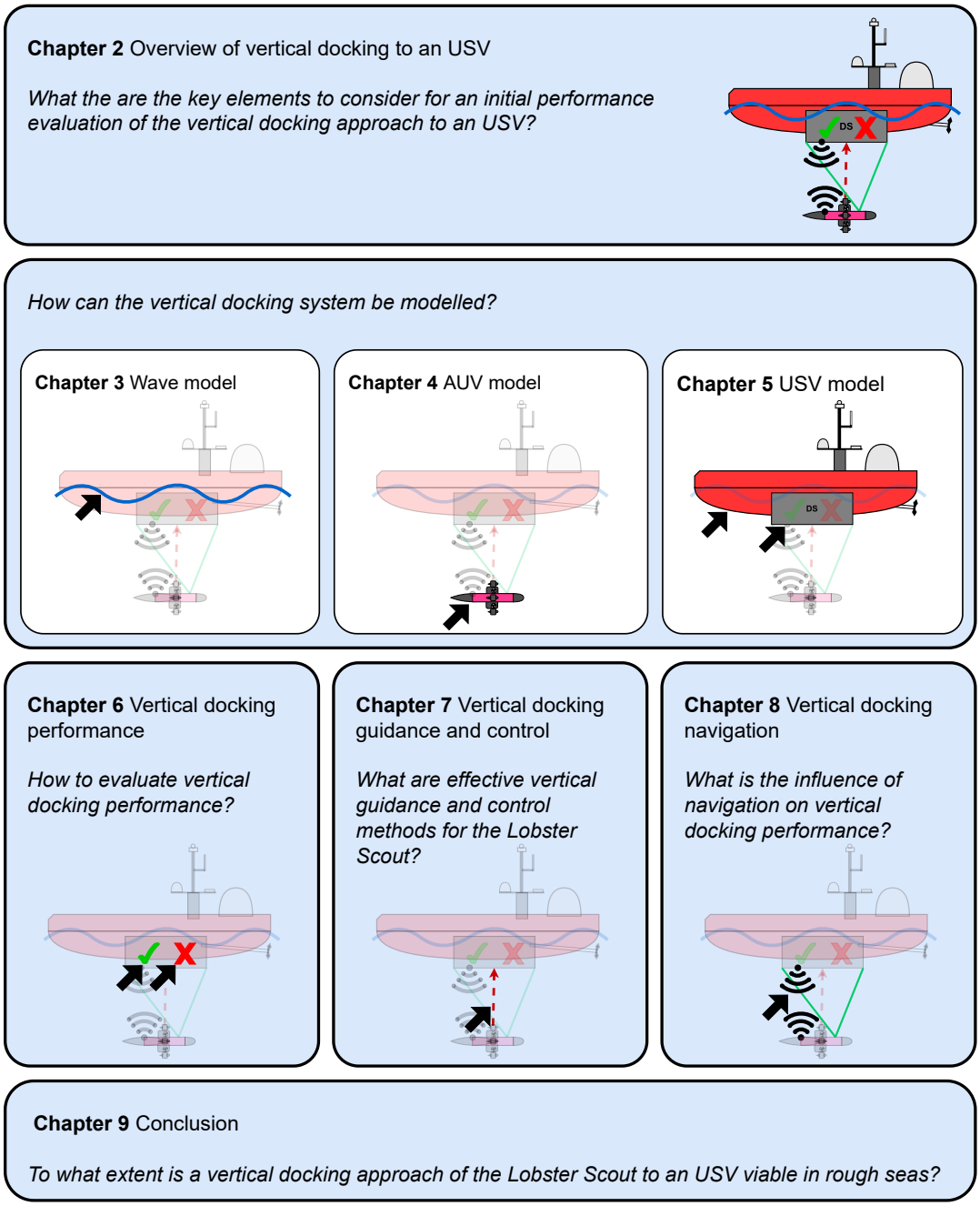

Figure 1.7: Thesis structure.

2

Overview of vertical docking to an USV

Vertical docking to an USV might result in an AUV-USV combination that can operate at higher sea states and ultimately result in more cost-effective underwater operations. However, to conduct an initial performance evaluation of vertical docking and to determine to what extent a vertical docking approach is viable in rough seas, not all components and procedure steps have to be considered. The objective of this chapter is to identify and define the key elements of the vertical docking problem to an USV to be able to conduct an initial performance evaluation.

The main research question to be answered in this chapter is:

What are the key elements to consider for an initial performance evaluation of the vertical docking approach to an USV?

Section 2.1 provides a short overview of key preliminaries required for this chapter. Existing literature is described in Section 2.2 to provide an overview of underwater docking. In Section 2.3, the elements of vertical docking to an USV are identified and analyzed, and the research is further scoped.

The insights gained in this chapter are used in later chapters where the vertical docking system is modelled and are helpful for future research focused on the overall design of vertical docking systems for USVs.

2.1. Preliminaries

It may require some effort to get familiar with some of the relevant concepts, notations, and definitions used for describing marine vehicles in this chapter and throughout the thesis. Understanding the definition of DOF and reference frames is crucial for comprehending this thesis, and both are explained in this section. A broader overview of these preliminaries is provided in Appendix A.

DOF Free rigid bodies have six DOF. These consist of three translations along the axis, namely surge, sway, and heave, and three rotations around the axis, namely roll, pitch, and yaw. This is shown for a floating surface element such as a ship in Figure 2.1a and for an AUV in Figure 2.1b.

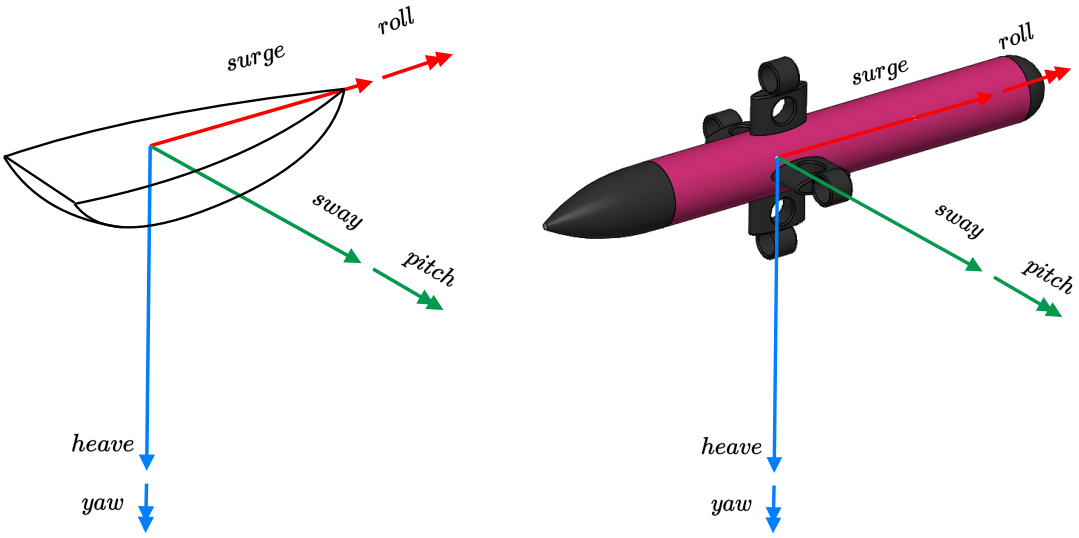

(a) DOF for a floating surface element.

(b) DOF for an AUV.

Figure 2.1: DOF for offshore robotics.

DOF for a 2D setting The goal of the docking operation is to position the AUV in the DS. This requires aligning all six DOF of the AUV with a certain final docking state in the DS. However, given that the scope is limited to a 2D setting for an initial performance evaluation of the vertical docking approach, only three out of six DOF are considered, while the other three DOF are always aligned. It was chosen to consider the surge, heave, and pitch DOF. This choice is explained below.

For an initial performance evaluation, it makes sense to only consider the DOF most impacted by the waves. Therefore, the heave DOF is a straightforward choice and the yaw DOF is automatically neglected due to the 2D setting. This leaves two main docking scenarios in a 2D setting, the parallel scenario and the perpendicular scenario, which are shown in Figure 2.2. These scenarios differ in terms of the alignment of the vehicles to the wave progagation direction.

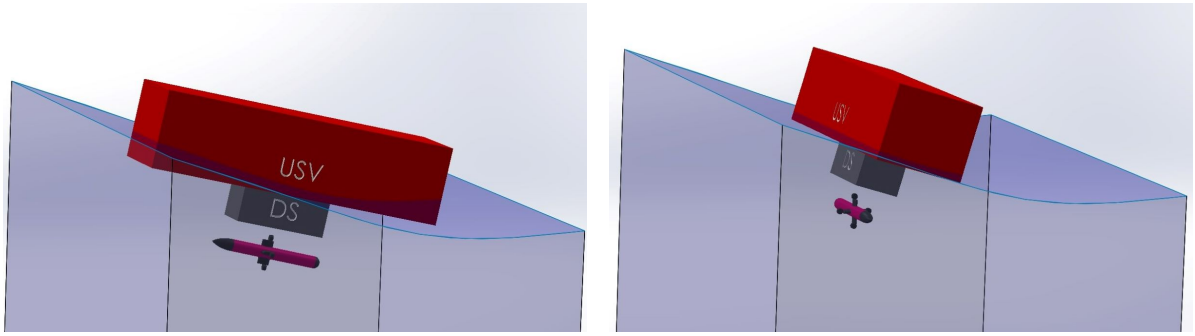

(a) Parallel scenario. The surge axis of the USV and AUV are aligned with the wave propagation direction. The surge, heave and pitch DOF are considered in the 2D setting.

(b) Perpendicular scenario. The sway axis of the USV and AUV are aligned with the wave propagation direction. The sway, heave and roll DOF are considered in the 2D setting.

Figure 2.2: Two main scenarios to consider while docking.

For the USV, the sway and roll DOF will likely be most sensitive to the waves due to its large sideways area (poor streamline) and its relatively small roll stability compared to its pitch stability [33]. Therefore, excitation of the roll and sway DOF due to the wave disturbance should be avoided. Furthermore, the

Scout has less control authority along its sway axis than along its surge axis.

In the parallel scenario (Figure 2.2a), the surge-axis of the USV and the AUV are aligned with the wave propagation direction using their thrusters, which minimizes the impact of the wave disturbance on the sway and roll DOF. In the perpendicular scenario (Figure 2.2a), the sway, heave and roll DOF are primarily impacted by the waves and this scenario should be avoided.

In conclusion, this study focuses on the parallel scenario in the 2D setting, in which the surge, heave, and pitch DOF are primarily excited.

Reference frames The use of reference frames is crucial for navigation purposes. The reference frames used in this thesis are graphically shown in Figure 2.3 for the 2D setting.

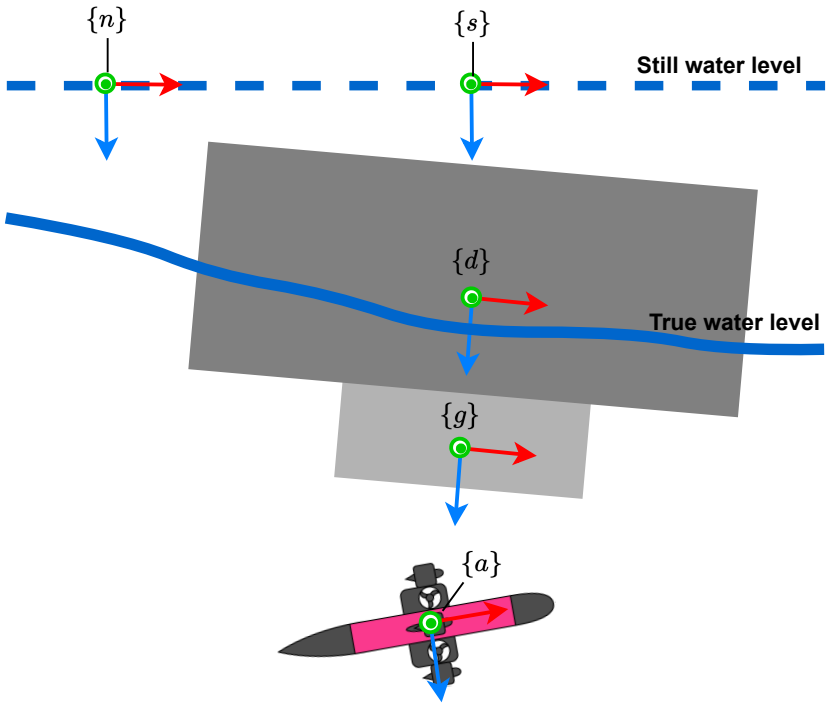

Figure 2.3: The relevant reference frames in the 2D setting. The red, green and blue arrows indicate the $\hat{i}, \hat{j}, \hat{k}$-axes respectively.

The reference frames are explained below:

- **The North-East-Down (NED) frame** is used when the vehicle operates within a limited geographic area and then serves as the global reference frame. It assumes a flat Earth approximation and is denoted by $\{n\}$ [24]. The x-axis ($\hat{i}_n$) points towards the true North, the y-axis ($\hat{j}_n$) points towards the East and the z-axis ($\hat{k}_n$) points down towards the Earth's center. The NED frame is locally tangent to the surface of the Earth and longitude and latitude angles fix the origin o_n of the frame relative to the center of the Earth.
- **The AUV body frame** is denoted with $\{a\}$. This frame is fixed to the AUV and moves along with its motion. The x-axis ($\hat{i}_a$) points towards the front of the AUV, the y-axis ($\hat{j}_a$) points to starboard and the z-axis ($\hat{k}_a$) points down such that a right-handed coordinate frame is formed. The origin of the $\{a\}$ frame is indicated with o_a.
- **The USV body frame** is denoted with $\{d\}$. This frame is fixed to the USV and moves along with its motion. The x-axis ($\hat{i}_d$) points towards the front of the USV, the y-axis ($\hat{j}_d$) points to starboard and the z-axis ($\hat{k}_d$) points down such that a right-handed coordinate frame is formed. The origin of the $\{d\}$ frame is indicated with o_d.

- **The USV sea keeping frame** is denoted with $\{s\}$. This frame is located at the equilibrium position of the USV with a fixed orientation but moves along with the USV in the inertial $\hat{i}_n$-$\hat{j}_n$ plane. Thus, without wave excitation, the sea-keeping frame would coincide with the USV body frame.
- **The DS goal frame** is denoted with $\{g\}$ and defines the docking state. This frame is located at some fixed point underneath the USV with a certain fixed orientation relative to the $\{d\}$ frame. The $\{g\}$ frame is a translated and possibly rotated version of the $\{d\}$ frame, and its origin is denoted by o_g.

2.2. Overview of underwater docking

This section discusses the components of a DS, the docking procedure and the different DS types.

2.2.1. DS components

An underwater DS is an automated garage for underwater vehicles that can carry out tasks such as charging, data transfer, and re-programming missions without requiring a vessel or humans. While various types of DS exist, there is a certain commonality in the components used [15]. Using the example of a seafloor fixed funnel-shaped DS (see Figure [48]), an overview of these components is presented in Figure 2.4b. These components are briefly described below:

- **Homing sensors** determine the relative pose (position and orientation) between the AUV and the DS. The term 'homing' represents the phase where the AUV is approaching the DS but is still more than a number of vehicle lengths away from the DS entrance.
- **Docking sensors** determine the relative pose between the AUV and the DS. These sensors may have better performance allowing for better pose estimates. The term 'docking' represents the phase where the AUV is approaching the DS and is within a couple of vehicle lengths from the DS entrance.
- **Capturing mechanism** overcomes final spatial and temporal errors once the AUV enters the DS and guides the vehicle to a final constraint configuration.
- **Locking mechanism** secures the AUV in the DS when it has reached its final position.
- **Connecting mechanism** establishes data and power connections when the AUV is locked.

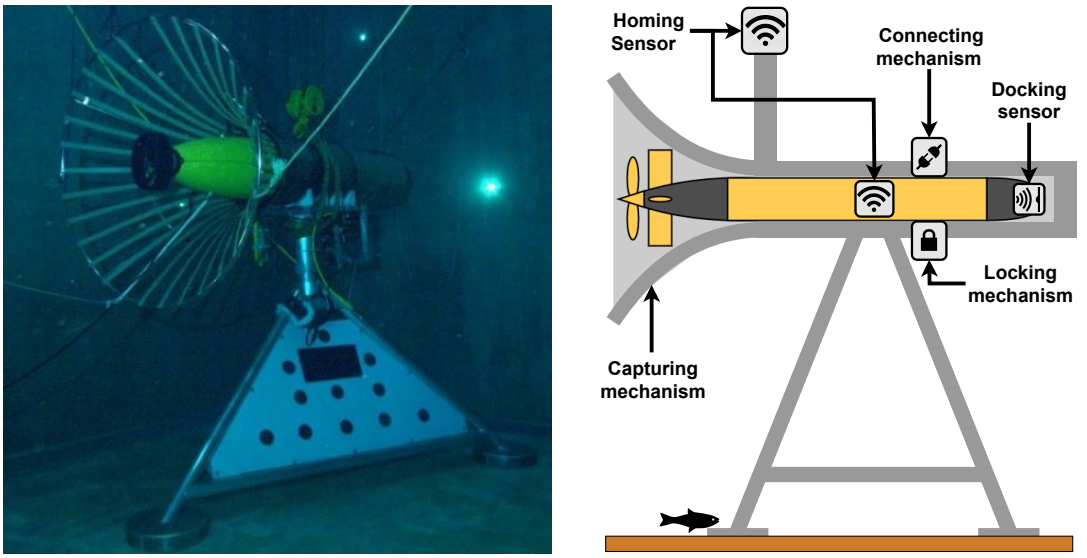

(a) An example of a fixed funnnel-shaped DS [48].

(b) Typical components of a DS, using a fixed funnel-type DS as example.

Figure 2.4: DS components.

2.2.2. Docking procedure

The docking procedure is usually initiated when the vehicle is at the end of its mission or when its battery is empty. In most cases, the vehicle starts the docking procedure when far away from the DS and therefore unable to directly communicate with the DS. According to [15], the docking procedure then generally follows a set of steps, which are shown in Figure 2.5 and described below:

1. **En route** The vehicle navigates closer to the DS using the on-board sensors, without direct communication to the DS.
2. **Approach setup** The vehicle is close enough to the DS and can directly communicate to the DS. Using homing sensors, the vehicle determines its relative position and orientation to the DS.
3. **Approach (homing)** The vehicle can now compute an initial trajectory and follow it to the dock.
4. **Terminal homing (docking)** In this phase the vehicle has positioned itself to within a couple of meters of the DS entrance and more docking sensors may become available. The vehicle then moves towards the DS in a final approach.
5. **Capture** The vehicle has made it to within the capture aperture of the DS. The vehicle now moves forwards until it can engage with the locking (latching) mechanism. The locking (latching) mechanism is activated and the vehicle is secured in the DS.
6. **Missed approach** There is a chance that the vehicle fails to enter the capture mechanism. When this happens, the docking system should be able to detect the failure and attempt a successive approach.
7. **Connection** In this phase, the vehicle is secured in the dock. Power and data connections are now made.
8. **Servicing** The vehicle is serviced. This includes tasks like recharging or refueling, downloading data, uploading a new mission, or updating the vehicle software.
9. **Undocking** The vehicle is ready for a new mission and the vehicle should break any both electrical and mechanical connections, leave the DS, and start a new mission. Generally, the undocking procedure is simpler than the docking procedure, as the procedure does not require very high accuracy. Simple backwards trust often is enough to clear the DS and start the new mission.

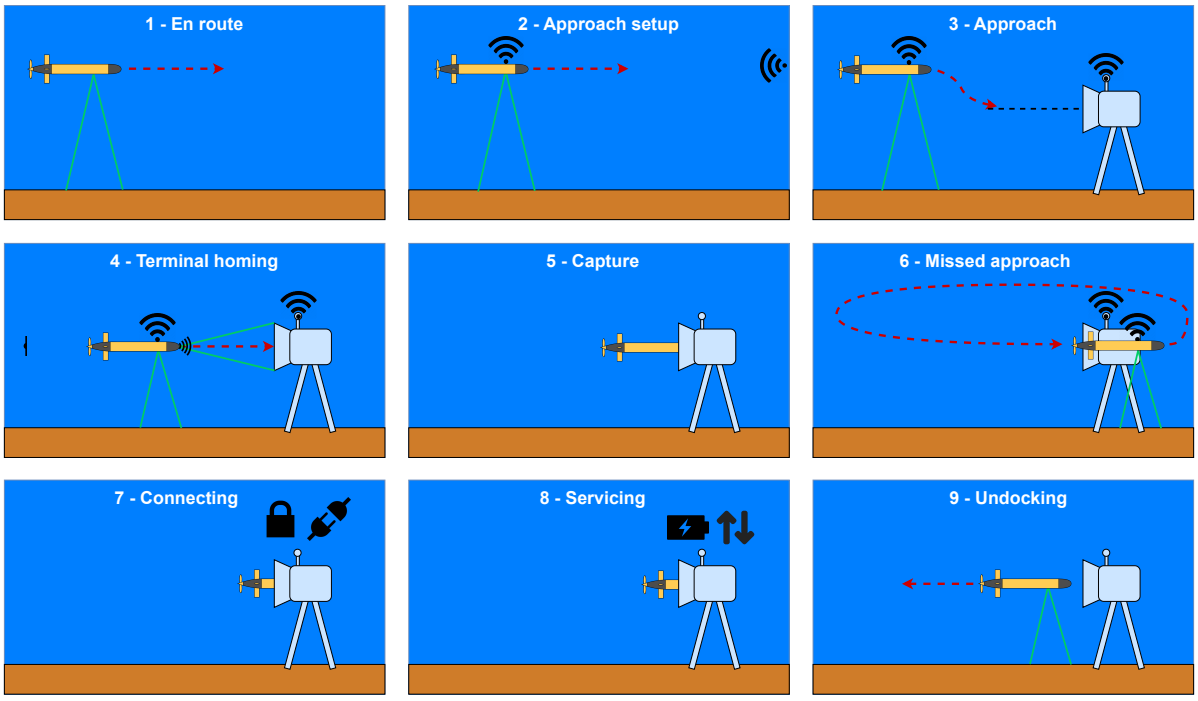

Figure 2.5: Typical docking procedure of an AUV to a fixed funnel-shaped DS.

2.2.3. DS types

The capture mechanisms is a key characteristic of DS and often defines the requirements for the docking guidance and navigation. It can therefore be used to classify different DS types.

Unidirectional DS

As the name implies, unidirectional DS can only be approached from only a single direction. The most notable feature of this DS is the entrance cone which guides the AUV to enter the DS. Executions of the unidirectional DS can generally be divided into two classes:

- **Horizontal funnel-shaped DS** such as shown in Figure 2.6a is a common execution of the unidirectional DS and is typically used for cruising AUVs. An example is given in [48, 30]
- **Cage-type DS** is another type of unidirectional DS that is common to be used for hybrid ROVs as shown in Figure 2.6b. Due to their box-like structure, the DS will look more like a cage instead of a cone. This means that a strict roll constraint is added during entry, thus requiring better alignment before entrance than with a funnel-shaped DS.

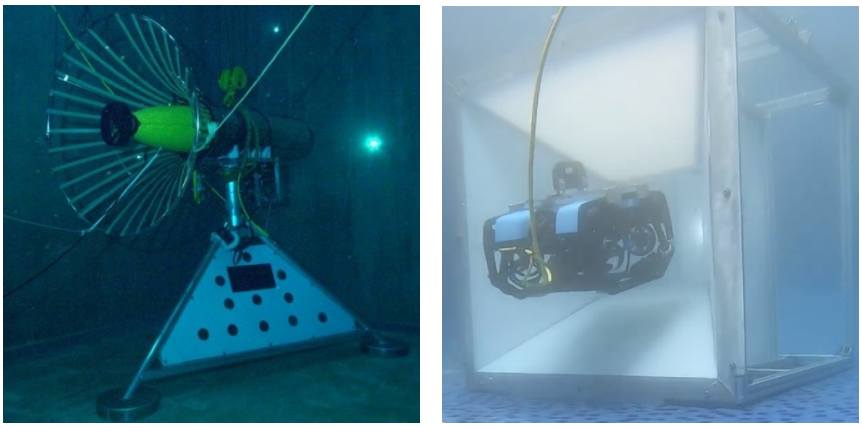

(a) An example of a funnnel-shaped DS [48]. **(b)** An example of a cage-type DS [79].

Figure 2.6: Examples of unidirectional DS.

Omnidirectional DS

An omnidirectional DS comes with the great advantage of being able to be horizontally approached from any direction. Therefore, in the horizontal plane, the orientation of the DS is not required to be controlled and the orientation of the DS does also not need to be communicated with the AUV. This simplifies both the guidance and the navigational requirements of such a system. Furthermore, this allows the vehicle to always align its minimum drag orientation with the current direction, thus minimizing the impact of the current disturbance, given that the current is measurable. Omnidirectional DS can generally be divided into two classes:

- **Pole-shaped DS** A typical omnidirectional concept consist of a vertical pole or cable and a fork-shaped structure and latching mechanism mounted on the vehicle as shown in Figure 2.7a [15]. Examples of pole shaped DS are given in [64, 49]
- **Cradle-type DS** A cradle-type DS or platform-type DS consists of a simple open structure that allows for servicing of the vehicle, which makes it very simple to design and build. This type of DS is approachable from any direction in the horizontal plane until the vehicle is located above the cradle, after which the vehicle aligns its orientation and moves vertically into the DS. An example is shown in Figure 2.7b. Examples are given [14, 82].

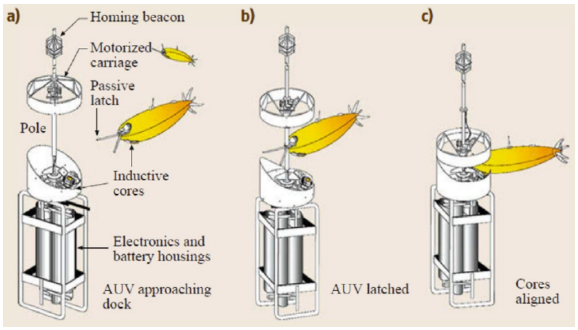

(a) An example of a pole-shaped DS [49].

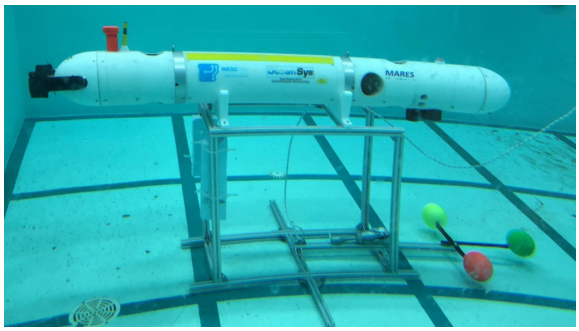

(b) An example of a cradle-type DS [14].

Figure 2.7: Examples of omnidirectional DS.

2.2.4. Docking guidance navigation and control

The Guidance Navigation and Control (GNC) architecture is a common framework used in literature to organize and structure the various systems required for motion control of a vehicle. This architecture has also been applied in the field of offshore robotics [24] and autonomous underwater docking [85]. Figure 2.8a depicts the GNC architecture in the context of docking for AUVs. The three components of the GNC architecture, namely guidance, navigation, and control, are described below:

- **Guidance** involves generating set-points and interpolating between them to create a feasible path based on input from the navigation system.
- **Navigation** refers to estimating the environment and the state of the vehicle and the DS using sensors to create situational awareness.
- **Control** involves producing control forces to steer the AUV along the trajectory towards the DS and to reject disturbances caused by the environment, such as waves.

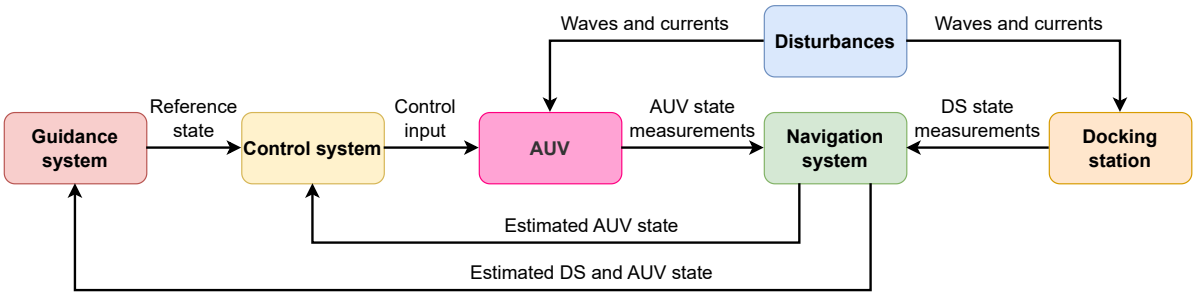

(a) The GNC architecture conceptualized by the author, based on [24].

Figure 2.8: The GNC architecture in the context of underwater docking

Docking guidance method classification

Numerous docking guidance methods exist, which are discussed in Appendix D. These guidance methods are divided in three categories in this thesis, namely local guidance methods, global guidance methods, and predictive guidance methods:

- **Local guidance methods** Local guidance methods may only work for part of the docking procedure but are very simple. These guidance methods are most often a variation on pointing the vehicle to the DS. These types of algorithms are used mostly in the docking stage where the vehicle makes a final approach to the DS. Since oceans are relatively sparse in obstacles, these types of algorithms can still work well over longer distances.
- **Global guidance methods** The type of guidance algorithms can be used for both the homing and docking stage. These types of algorithms require more computational effort but can provide more complex motions and may be able to deal with various constraints such as obstacles.

- **Predictive guidance methods** The methods are relevant when the DS is moving. These methods try to predict the future state of the DS based on the current state and previous states of the DS and then plan a path to this future state.

Navigation sensors
An AUV has on-board sensors to determine its location with respect to the earth navigation frame and given it has some idea of where the DS is as well, it can cruise towards the neighborhood of the DS. However, this information is likely not sufficient, and accurate relative state information is required to dock [15]. This section discusses the typical underwater vehicle navigation and docking sensors that can provide this information.

Onboard sensors An AUV has onboard sensors to determine its location with respect to the earth navigation frame. The simplest form of onboard navigation is an Inertial Navigation System (INS), which estimates the vehicle's position and orientation using accelerometers and gyroscopes. However, these sensors have limited accuracy and can cause significant drift in position due to the double integration of small errors over time. Additional sensors such as a Doppler Velocity Log (DVL), magnetometer, pressure sensor, and Global Navigation Satellite System (GNSS) can improve accuracy significantly [15]. The quality of the state estimate is ultimately limited by the accuracy of the sensors, which may not be sufficient for docking purposes [15].

Docking sensors Docking sensors are used to directly measure the relative pose of the vehicle to the DS, resulting in a bounded uncertainty of the position estimate that is small enough for docking. Dedicated docking sensors are often essential for docking and particularly for docking to an USV as onboard sensors cannot measure the changing position of the DS over time.[51]

Docking sensors can be categorized in three groups: acoustic, optical, and electromagnetic sensors [15]. Acoustic sensors, such as Ultra-Short BaseLine (USBL), Short BaseLine (SBL), and Long BaseLine (LBL), have a long acquisition range but require careful calibration and are sensitive to acoustic noise and reflections. Optical sensors can provide higher accuracy and higher update rates than acoustic sensors and are often used in combination with recognizable markers on the DS. However, optical sensors have a lower range and are sensitive to environmental conditions, such as underwater visibility, and can suffer from optical interference and occlusions of the markers. Electromagnetic sensors can provide both angular and positional information of the AUV relative to the DS. Additionally, these systems are less sensitive to common sources of underwater phenomena like turbidity, bubbles, fouling, floating organic material, and boundary effects at the sea surface and at the sea floor. [21]. However, these systems can be less effective near large ferromagnetic objects like vessel hulls.

AUV control
Perhaps the most common type of control for AUVs is Proportional-Integral-Derivative (PID) control. An advantage of PID control is that it does not require a model of the AUV, and that it is relatively simple. In this type of control, a particular error, the error integral and the error derivative between an AUV state and a desired state are each multiplied with their respective gain in order to obtain a certain control output that steers the AUV to the reference path. If an AUV model is available, many more advanced model-based control algorithms can be used such as state feedback control, Linear–Quadratic Regulator (LQR) control, and output feedback control [5].

2.3. Analysis of vertical docking to an USV

This section provides an overview of the key elements involved in vertical docking to an USV. As with general underwater docking, discussed in Section 2.2, this docking process involves an AUV (i.e. the Lobster Scout), a DS, and docking guidance navigation and control. However, in the case of vertical docking to an USV, there are additional factors to consider, such as the environmental conditions and the characteristics of the USV itself. An overview of these elements is given in Figure 2.9.

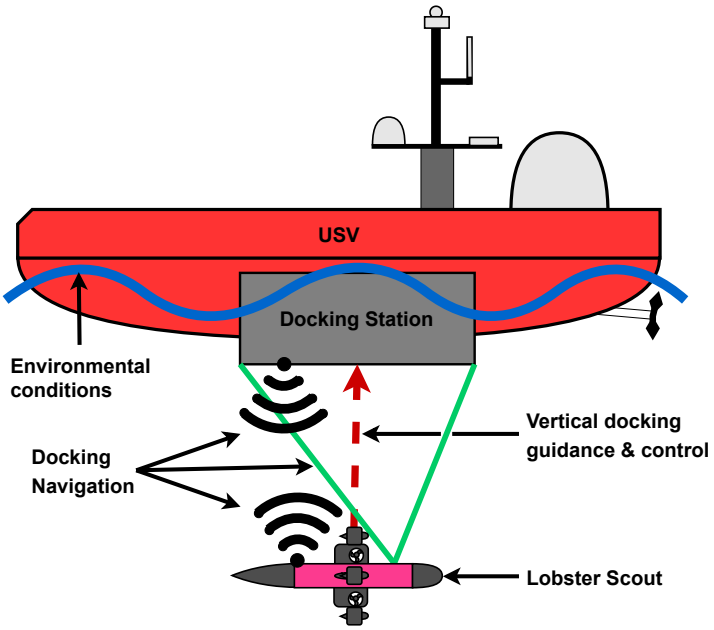

Figure 2.9: Elements of the vertical docking problem

2.3.1. Analysis of vertical docking procedure

The docking procedure explained in Section 2.2.2 is suitable for vertical docking with an USV. Although all the steps are necessary for docking, the focus of this thesis is on the critical steps that affect vertical guidance methods and the unique aspects of vertical docking. Therefore, the En Route, Approach Setup, and Servicing steps are excluded since they are not specific to vertical docking with an USV. Although Missed Approach and Undocking differ from other docking systems, they are not discussed in this thesis. Undocking is relatively straightforward, as explained in Section 2.2.2, so this is not considered a bottleneck for vertical docking. Furthermore, dealing well with missed approaches can increase the success rate of vertical docking, but is not deemed critical for the initial evaluation of the vertical docking procedure. The remaining steps are the Approach, Terminal Homing, Capture, and Connecting, which are illustrated in Figure 2.10.

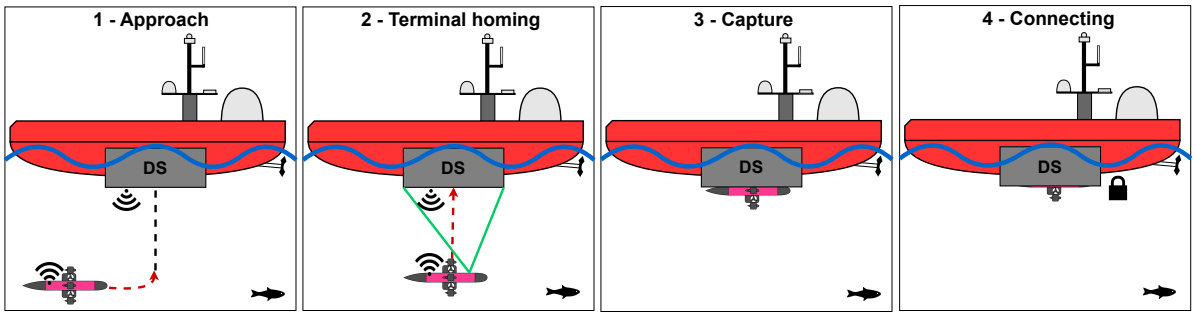

Figure 2.10: The steps of the vertical docking procedure to an USV that are considered in this thesis.

2.3.2. The environmental conditions

This section discusses the relevance of wind, waves and currents and defines the environmental conditions during the vertical dock.

No current disturbance Ocean currents can be treated as universal flow, where the current is coming from a single direction with constant velocity [33]. Currents can exert significant loads on offshore vehicles or structures and for sailing ships, it is generally assumed that a ship is moving with the current [33]. Assuming the USV is not anchored (see Section 2.3.3) during the docking procedure and the AUV

is close to the water surface, it is assumed that both the USV and AUV move along with the currents and the differential impact of current is negligible. For a first study into vertical docking, currents are therefore not taken into account.

No wind disturbance Wind loads can act on the USV as it partially is above the water surface. However, wind loads are assumed to be small with respect to the loads of currents and waves. According to [33]: ”Wind loads on offshore structures often play a relatively minor role in comparison to the hydrodynamic loads”. To conclude, wind is not taken into account for an initial performance indication of vertical docking to an USV.

Yes wave disturbance The central idea of this thesis is that employing vertical docking to an USV may enable the operational use of the USV-AUV combination in rougher seas with larger waves, thus wave loads are considered. The viability of the vertical approach is evaluated in the North Sea environment, which is conveniently located near Lobster Innovations BV and could provide a testing ground for the USV-AUV combination if ever realized by Lobster Innovations BV. Additionally, the North Sea region has significant economic activity, making it a highly probable deployment area of the USV-AUV combination. Furthermore, extensive information is available on the North Sea, which will facilitate the research process.

2.3.3. The USV: DUS V5750

This section discusses various aspects of the USV considered in this thesis, including anchoring, controllability, shape and specifications.

No anchoring In order to evaluate the effectiveness of the vertical docking approach to an USV, it is assumed that the USV is floating freely and not anchored. This means that the forces and dynamics resulting from an attached chain are not taken into consideration. Although anchoring may be necessary for an USV that needs to remain in a specific location for an extended period, it would significantly complicate the docking procedure. An anchor chain would need to be avoided by the Scout, and an anchor would prevent the USV from drifting with the currents, which means the Scout needs to be able to handle both currents and waves. To anchor the USV in this scenario, one possible procedure could be to anchor the USV while the AUV is still a far distance away and then raise the anchor as soon as the AUV approaches.

No dynamic positioning In order to evaluate the effectiveness of the vertical docking approach to an USV, it is assumed that the USV does not use its thrusters to assist the Scout in the vertical docking approach. Moreover, dynamic positioning systems of vessels are generally unsuitable to reject primary wave disturbances [33].

Box shaped To conduct an initial evaluation of vertical docking, a simple box-shaped USV was chosen as a first approximation. While a more accurate representation of an USV was considered, it would have made the modelling efforts more complex without prior knowledge of the effectiveness of vertical docking. Moreover, the presence of the DS in reality also affects the motion of the USV. Therefore, even with an accurate vessel model, obtaining accurate motions without experiments would have been challenging as it is influenced by the exact design of the DS. Hence, the influence of the DS on the dynamics of the USV was ignored as well.

Specifications The specifications of the box used in this study are roughly based on the DUS V5750 USV from Demcon [72]. This thesis uses this USV for a case study of the vertical docking approach.

2.3.4. The AUV: Lobster Scout

For the AUV, the Lobster Scout is considered. The Lobster Scout built by Lobster Robotics is a fully hovering AUV with 8 thrusters resulting in control of all six DOF. Since the Lobster Scout is still in development and modular, its configuration changes with time. In this thesis, the January 2023 version of the Scout is considered. The Scout contains a number of onboard sensors, namely an accelerometer, gyroscope, magnetometer, DVL GNSS, and pressure sensor. The Scout has a mass of approximately

60 kg, and is 1.9 m in length. Its maximum velocity is approximately 2 $\frac{\text{m}}{\text{s}}$ forwards and 0.4 $\frac{\text{m}}{\text{s}}$ sideways.

It is assumed that docking sensors are easily added to the Scout without changing its dynamics. This assumption is justifiable as in the past, the Scout has remained approximately the same size while increasing functionality due to improving the integrated design.

2.3.5. The vertical DS

This sub-section defines the vertical DS. The controllability of the DS is first discussed. Then various vertical capturing mechanisms are explored based on different vertical docking approaches. Finally, the cradle-type DS is selected as it best suits the Lobster Scout.

No DS controllability

Many vertical DS concepts are possible that also include active control of the DS, however, this thesis focuses on the guidance for the Scout, which is a fully hovering capable AUV. This makes it interesting to see how well the system performs if the DS does not have any control authority. This excludes the use of manipulators or thrusters mounted on the DS aimed to ease the guidance for the AUV. Another advantage is that the DS is simpler and likely more affordable. This leaves 'passive' DS types.

Vertical docking approaches

This thesis classifies vertical docking approaches into two main categories:

- **Vertical oriented vertical docking** Vertical docking where the Scout is also oriented vertically during the final approach (see Figure 2.11a). The x-axis $\hat{i}_g$ of the goal frame $\{g\}$ points up.
- **Horizontal oriented vertical docking** Vertical docking where the Lobster Scout is oriented horizontally during the final approach (see Figure 2.11b). The x-axis $\hat{i}_g$ is parallel to the $\hat{i}_d$ axis.

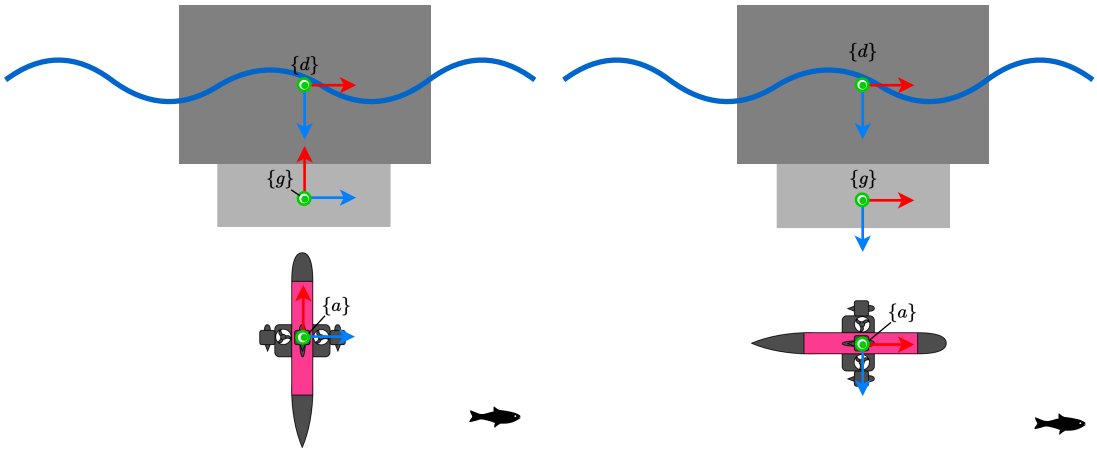

(a) Vertical docking with the hovering AUV orientated vertical. **(b)** Vertical dock with the hovering AUV orientated horizontal.

Figure 2.11: Two final docking approaches to vertically dock to a floating DS.

Vertical capturing mechanism types

The two vertical approaches lead to three different capturing mechanisms concepts:

- **Funnel-shaped DS** as shown in Figure 2.12a. A typical funnel-shaped dock is oriented vertically, such that the Lobster Scout enters from below.
- **Pole-shaped DS** as shown in Figure 2.12b. A horizontal pole serves as the docking structure. The Lobster Scout is equipped with a latching fork, such that this pole can be caught. Note that this concept allows the Scout to approach from all angles in the vertical $y^g_{ng} - z^g_{ng}$ plane.
- **Cradle type DS** as shown in Figure 2.12c. In this concept, a typical cradle-type DS is turned upside down. The Scout can approach this while oriented horizontally.

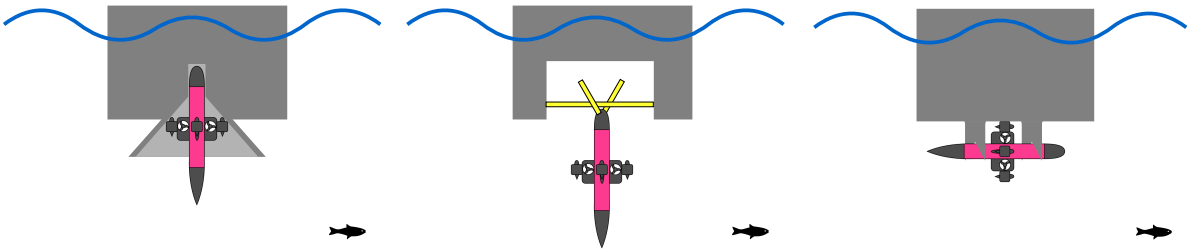

(a) Vertical docking with a funnel-shaped DS. **(b)** Vertical docking with a pole-shaped DS. **(c)** Vertical docking with a cradle-type DS.

Figure 2.12: Vertical docking concepts.

Vertical capturing mechanism selection

Because this thesis is only a limited-time project, it is chosen to only explore the cradle-type DS while leaving the other concepts for future research. This section explains the reasoning for this choice. Table 2.1 describes the evaluation criteria and Table 2.2 evaluates the three capturing mechanisms. Three important considerations are highlighted:

- The evaluation is done for the Lobster Scout, thus other AUVs may be evaluated differently.
- The suitability of the docking mechanism for servicing of the AUV is included as criteria. Docking applications that do not require servicing could score differently.
- While this thesis does not model currents, they are included as selection criteria.

Table 2.1: Evaluation criteria for the different vertical capturing mechanisms.

ID	Criteria
C1	Ability to deal with horizontal disturbances.
C2	Ability to deal with vertical disturbances.
C3	Availability of sensors.
C4	Reliability of capture and latching.
C5	Ease of connecting and servicing.

Table 2.2: Evaluation of the three vertical capturing mechanisms. A score is given from ++, +, o, -, - -.

ID	Funnel-shaped DS		Pole-shaped DS		Cradle-type DS	
C1	- -	Very susceptible to currents and horizontal wave disturbances	o	Susceptible but AUV can compensate by arriving at an angle.	+	Best suited to deal with currents and horizontal disturbances.
C2	+	Barely susceptible	+	Barely susceptible	o	Susceptible, however, wave disturbance is phase synchronized.
C3	-	Scout loses DVL bottom-lock. Minima; frontal surface for forwards-facing docking sensors.	- -	Scout loses DVL bottom-lock. Minimal frontal surface for docking sensors due to fork.	+ +	Scout keeps DVL bottom-lock. Large side area to add docking sensors.
C4	+ +	Very forgiving in alignment errors due to large capture aperture. Fully constrained when latched.	-	Forgiving in alignment errors, however, very loosely constrained when latched. The relative pitch and roll angles are critical.	-	Forgiving in alignment errors along the y-axis due to forks. The relative x-position and pitch angle are critical.
C5	+ +	Straightforward as AUV is fully constrained.	- -	Challenging as AUV is loosely constrained. Requires a second latching maneuver.	+	Straightforward as AUV is well secured.

Conclusion Based on the evaluation presented in Table 2.2, the cradle-type DS holds the most promise for the Lobster Scout's. While this design is more susceptible to vertical disturbances (C2) and requires more critical alignment for reliable latching (C4), it outperforms other concepts in dealing with horizontal disturbances (C1) and offers better sensor availability (C3). Figure 2.13 illustrates the Scout in the docked position in the cradle. Note that with this implementation, the fins of the Lobster Scout can guide it in the surge direction, while the forks guide it in the sway direction.

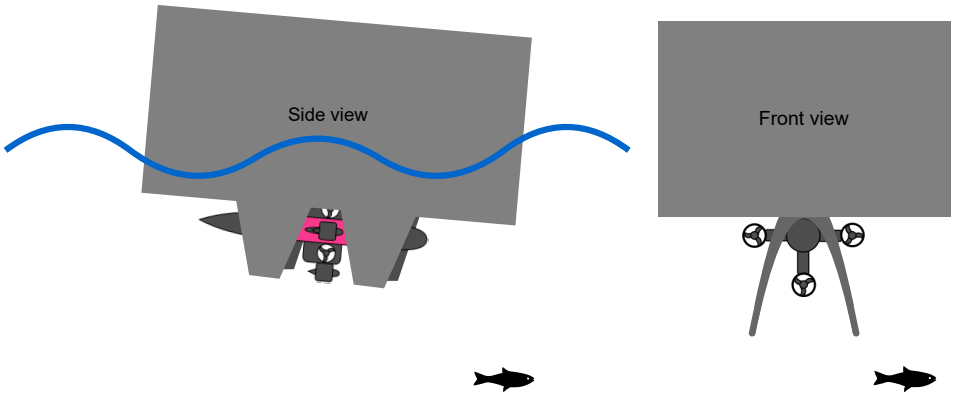

(a) Side view **(b)** Front view

Figure 2.13: The Scout docked in the cradle

2.3.6. Vertical docking GNC

The final meters of the vertical docking procedure are the main focus of this thesis, which includes the Approach, Terminal Homing, Capture and Connecting as procedure steps as discussed in Section 2.3.1. During this final stage, it is assumed that the navigation system can make measurements of both the AUV, the USV, and the DS.

Furthermore, this study does not address obstacle detection or avoidance for the USV, No-Fly Zone (NFZ), or path obstructions. Avoiding collisions with the USV and certain NFZ near its thrusters is crucial. However, since the USV is fixed with respect to the DS and its relative location is known, these zones can be avoided simply by guiding to the DS. Additionally, the sea is relatively obstacle-free, so no path obstructions are expected.

2.4. Conclusion

This chapter started with the question: *What are the key elements to consider for an initial performance evaluation of the vertical docking approach to an USV?* It was found that for an initial evaluation, the surge, heave, and pitch DOF should be considered along with the key elements which include the environmental conditions, the USV, the Lobster Scout, the DS and vertical docking guidance navigation and control. The key decisions made in this chapter are listed below:

- This study evaluates the viability of a vertical docking approach for an AUV-USV combination in the North Sea environment.
- The study is focused on the final meters of the docking procedure.
- Only waves are considered due to their differential impact on the USV and the Lobster Scout.
- The USV is defined as a free-floating box without anchoring or dynamic positioning and its specifications are roughly based on the DUS V5750 USV by Demcon [72].
- The Lobster Scout is used for the AUV, which is a fully hovering AUV with a mass of approximately 60 kg and a length of 1.9 m.
- The DS mounted on the USV was analyzed and an upside-down cradle DS design was found to best suit the Lobster Scout.

- Navigation measurements for the Scout, the USV and the DS are assumed to be available in the final meters of the docking procedure.
- Obstacle detection and avoidance are not considered for designing the GNC methods.

This study presents a number of avenues for future research. For instance, the simulation could be expanded to a 3D setting, taking into account all DOF and 3D wave properties. In addition, an accurate shape for the USV should be considered. Finally, the design of the cradle type DS, including the capture mechanism, the homing and docking sensors, the locking and connecting mechanisms, and the integration with the USV is interesting to investigate.

Overall, this chapter has presented the key elements for assessing the viability of a vertical docking approach for an AUV-USV combination to operate in rougher sea conditions. The succeeding chapters go into detail on the design and modelling of each of these key elements.

3

Wave model

To evaluate the performance of the vertical docking approach in rough seas, this thesis utilizes a simulation approach that requires modelling the system dynamics. This led to the research question:

How can the vertical docking system be modelled?

The system dynamic model requires a wave model, as well as the dynamic models of the AUV, the USV, and the attached DS, which are discussed in later chapters. The objective of this chapter is to develop a model of waves in the North Sea, which an expected operating area of the AUV-USV combination.

The wave model of irregular North Sea waves presented in this chapter is based on linear velocity potential theory. The purpose of the wave model is to replicate the water movement around the USV and the AUV. The model inputs are the key parameters that define a regular or irregular wave and the model outputs are the water particle kinematics. An overview of the wave model is presented in Figure 3.1.

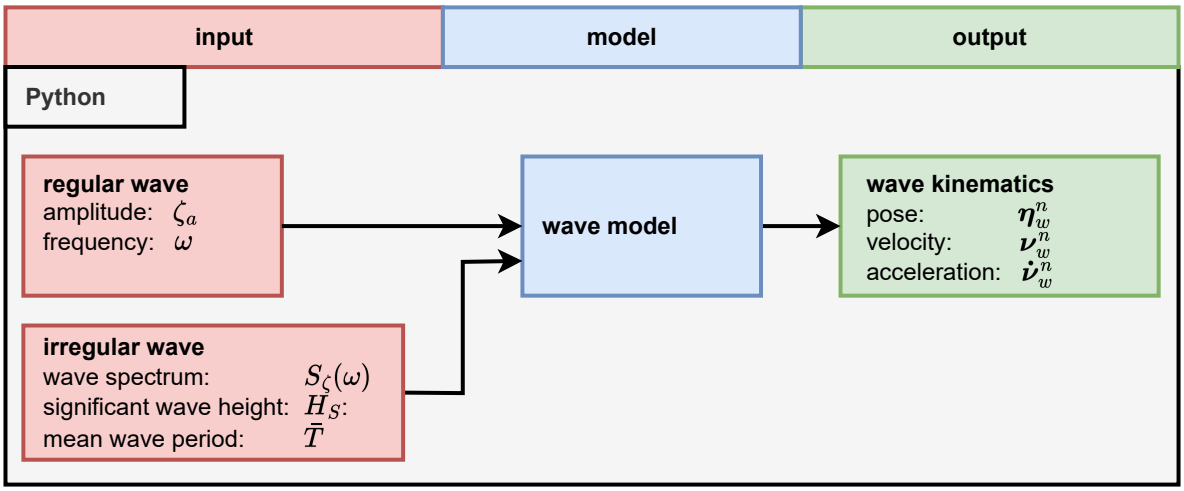

Figure 3.1: An input-output diagram of the wave model.

This chapter begins by addressing wave preliminaries in Section 3.1 which defines relevant variables and discusses key concepts for wave modelling. In Section 3.2, different wave models with increasing complexity are compared to select a suitable wave model. Section 3.3 describes a regular wave model based on linear velocity potential theory which is then used to model irregular North Sea waves in Sec-

tion 3.4. The main assumptions of the wave model are verified in Section 3.5 and finally, a conclusion is presented in Section 3.6 which relates the obtained wave model to the research question.

3.1. Wave preliminaries

This section aims to define essential variables, discuss types of wind-generated waves, and highlight the differences between deep and shallow water waves.

3.1.1. Relevant variables

Some of the relevant variables that are used to discuss waves are presented below:

- **Wave height** The wave height H is the difference between the trough (lowest point of a wave) and crest (highest point of a wave) of a wave. Hence, the wave height H is twice the amplitude ζ_a of the wave.
- **Wavelength** The wavelength λ is the distance between two successive crests of a wave.
- **Wave period** The wave period T is the time it takes for two identical wave points to pass the same spacial position.
- **Water depth** The water depth h is the distance between the sea surface and the sea floor.
- **Wave steepness** The wave steepness S is the ratio between wave height and wave length $S = \frac{H}{\lambda}$.

3.1.2. Wind generated waves

While various wave types exist such as waves generated by moving ships, winds, tides, and tsunamis, this thesis is limited to wind generated waves. Wind generated waves can generally be divided into two types with distinct characteristics:

- **Sea waves** are formed due to local wind fields and have highly irregular patterns. These waves have unpredictable alternations between large and small wave heights and have steep crests, resulting in a distinct wave profile.
- **Swell waves** are formed due to a wind field far away and travel to the place of observation. These waves are not dependent on local winds. Since waves unravel over a distance as waves with longer wavelengths travel faster, they become more regular (see Section 3.3.4). Swell waves are generally more predictable, have longer wavelengths, and have a more constant wave height.

3.1.3. Deep and shallow waves

Wave propagation in shallow waters differs significantly from wave propagation in deeper waters, thus some attention on this topic is required. In order to do this a distinction is made in waves on the basis of the wavelength and water depth.

- **Deep water waves or short waves** - Water waves are considered deep water waves if the $\frac{\lambda}{h} < 2$. In this case, the influence of the sea floor on the wave is very small and is ignored.
- **Shallow water waves or long waves** - The body of water is very shallow. That is, $\frac{\lambda}{h} > 20$. In this case, the seafloor has a significant effect on the waves.

3.2. Wave model selection

This sub-section explains why linear wave potential theory was used to model waves in this thesis. A number of wave models exist:

- **Linear wave potential theory** Linear wave potential theory has a significant advantage in that it can approximate the irregularity of actual wind-generated waves by utilizing the superposition principle. This means that multiple harmonic components are combined to produce an irregular sea model from for example the North Sea. However, this first-order linear model is only accurate when the wave steepness $S < \frac{1}{20}$. Although this model is significantly simplified with respect to reality, it is still widely applicable in practical scenarios [27].

- **Higher-order non-linear models** such as the Cynoidal theory and Stokes' second, third, and fifth-order theories more accurately represent reality at steeper wave profiles. These models can also capture the Stokes drift, which describes the slow movement of wave particles in the wave propagation direction. However, these wave models have a limitation in that the superposition principle cannot be applied, making them less suitable for describing irregular waves.
- **Profile extension methods** can be used to adapt the linear wave theory to describe steeper wave profiles. More on this can be found in [33].

It is chosen to use linear wave potential theory, mainly due to the advantages of the superposition principle. However, linear wave theory does have some limitations listed below:

- **High waves steepness** The wave profile is not accurate for steep wave profiles. This is relevant in for example the splash zone, in very shallow waters, or for very large waves as the wave steepness condition is not met.
- **Stokes drift** 'Stokes drift' is not captured by this first-order model.

The following sections will explain linear wave theory. First regular waves are discussed, after which irregular waves are discussed. The following sections are mainly based on [27, 33].

3.3. Regular wave model

This section explains the kinematic motion of water in a regular wave using linear potential flow theory.

3.3.1. Regular wave simplifications

Real waves are very irregular and have a peaky higher crest and a longer shallower trough as shown in Figure 3.2a. For the regular wave model, two main simplifications are made:

- **Constant wave period** It is assumed that waves are regular or harmonic, meaning that the wave has a constant period.
- **Sine wave approximation** It is assumed that waves can be modelled as a sine wave (see Figure 3.2b), thereby neglecting non-linear terms.

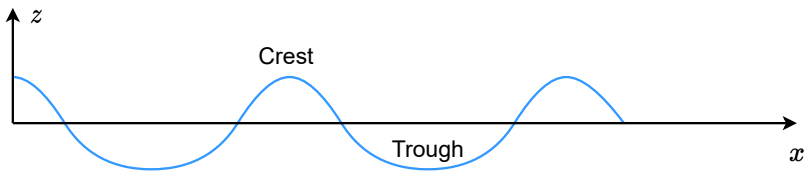

(a) Regular true wave.

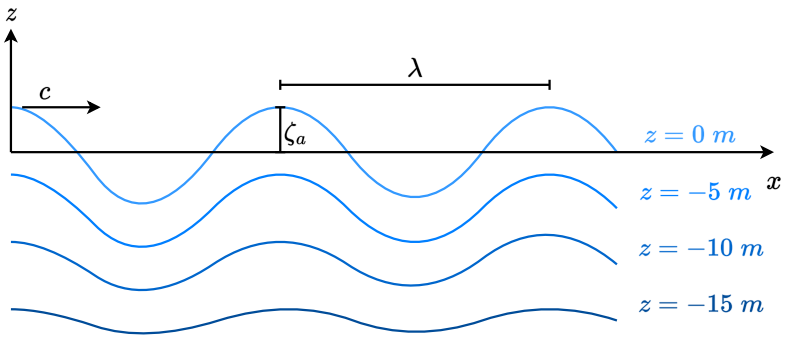

(b) Regular wave approximation using a sine wave. Wave amplitude decreases with depth. c is the wave phase velocity, λ is the wave length and ζ_a is the wave amplitude.

Figure 3.2: A regular true wave and a sine wave approximation.

3.3.2. Progressive wave

The amplitude of a wave at a specific time and place at the sea surface is described by Equation 3.1:

$$\zeta(x^n, t) = \zeta_a cos(k(x^n - ct)). \tag{3.1}$$

Here, $\zeta(x^n, t)$ is the wave amplitude at a specific time and place. k is the wave number given by $k = \frac{2\pi}{\lambda}$, c is the wave phase velocity given by $c = \frac{\lambda}{T}$.

3.3.3. Wave velocity potential

A wave velocity potential function is used to describe a wave. [33] states: 'A velocity potential of a flow is simply a mathematical expression, which has the property that the velocity component in a point in the fluid in any chosen direction is simply the derivative of this potential function in that point to that chosen direction.' The derivation of function will not be discussed and can be found in [33], however, the most important boundary conditions and assumptions are mentioned and their implications are shown. The following simplifications are made with respect to the fluid properties:

- Non-viscous.
- Homogeneous.
- Incompressible.
- Rotation free.
- Linear approximation ($S < \frac{1}{20}$).
- The water depth is constant.

Four boundary conditions have to be considered:

- **Continuity condition** The water volume that enters the systems minus the water volume that leaves the system is zero.
- **Seabed boundary condition** The vertical velocity of the water at the sea floor is zero.
- **Kinematic boundary condition** The vertical velocity of a water particle at the surface is equal to the vertical velocity of the wave surface.
- **Dynamic boundary condition** The air pressure at the sea surface is constant and equal to atmospheric pressure.

With these boundary conditions and simplifications in mind, the following wave potential function can be derived:

$$\phi(x^n, z^n, t) = \frac{\zeta_a g}{\omega} \frac{cosh(k(h - z^n)}{cosh(kh)} sin(kx^n - \omega t), \tag{3.2}$$

where $\omega = kc = \frac{2\pi}{T}$ in to describe the angular frequency of the wave, and g is the gravity constant.

3.3.4. Dispersion relationship

The dispersion relationship, which is shown in Equation 3.3 follows from the kinematic boundary condition. This equation couples ω and k or similarly T and λ as with the following relationship:

$$\omega^2 = kg\ tanh(kh). \tag{3.3}$$

Since $c = \frac{\omega}{k} = \frac{\lambda}{T}$ a relationship follows that couples the phase velocity of a wave with the wave number and thus wavelength. This relationship shows that smaller waves propagate with lower velocities than larger waves and waves thus disperse. The equation is shown below:

$$c = \sqrt{\frac{g}{k} tanh(kh)}. \tag{3.4}$$

Furthermore, a clear relationship is found between the wavelength and the wave period. This means that once either the wavelength or the wave period is known, the other can be calculated. This relationship is shown in Equation 3.5:

$$T = \frac{\sqrt{2\pi\lambda}}{\sqrt{g\ tanh(\frac{2\pi}{\lambda h})}}. \tag{3.5}$$

The function $tanh(kh) = 1$ for $kh \to \infty$ and $tanh(kh) = kh$ for $kh \to 0$. Because of this, deep water waves behave differently than shallow water waves. This greatly simplifies the equation which makes them easily usable. Table 3.1 shows these differences mathematically.

Table 3.1: Key differences between shallow waters $\frac{\lambda}{h} > 20$ and deep waters $\frac{\lambda}{h} < 2$.

	Shallow waters	**Deep waters**
Velocity potential function	$\phi = \frac{\zeta_a g}{\omega}\frac{cosh(k(h-z^n)}{cosh(kh)}sin(kx^n - wt)$	$\phi \approx \frac{\zeta_a g}{\omega}e^{-kz^n}sin(kx^n - wt)$
Wave velocity	$c \approx \sqrt{gh}$	$c \approx \sqrt{\frac{g}{k}} \approx 1.25\sqrt{\lambda}$
Wave period	$T \approx \frac{\lambda}{gh}$	$T \approx \sqrt{\frac{2\pi\lambda}{g}} \approx 0.8\sqrt{\lambda}$
Wave angular velocity	$\omega \approx k\sqrt{gh}$	$\omega \approx \sqrt{kg}$

3.3.5. Fluid particle kinematics

Taking the derivative of the velocity potential function to model results in the velocity of a fluid particle in a wave. This is given in Equation 3.6:

$$\begin{aligned} u_w^n(x^n, z^n, t) &= \frac{d\phi}{dx^n} = \frac{dx^n}{dt} = \zeta_a\omega\frac{cosh(k(h-z^n))}{sinh(kh)}cos(kx^n - wt), \\ w_w^n(x^n, z^n, t) &= \frac{d\phi}{dz^n} = \frac{dz^n}{dt} = -\zeta_a\omega\frac{sinh(k(h-z^n))}{sinh(kh)}sin(kx^n - wt). \end{aligned} \tag{3.6}$$

The resting (average) position of a water particle in a wave is given by $(x_1^n,\ z_1^n)$. Because the small wave steepness assumption is made, the difference between the velocity at the actual position of the water particle and the mean position of the water particle ($x^n - x_1^n$ and $z^n - z_1^n$ respectively) is small. Substituting for $(x_1^n,\ z_1^n)$ and integrating the velocity function over time, results in the position of a particle as shown in Equation 3.7:

$$\begin{aligned} x_w^n(x_1^n, z_1^n, t) &= -\zeta_a\frac{cosh(k(h-z_1^n))}{sinh(kh)}sin(kx_1^n - wt) + C_1, \\ z_w^n(x_1^n, z_1^n, t) &= -\zeta_a\frac{sinh(k(h-z_1^n))}{sinh(kh)}cos(kx_1^n - wt) + C_2. \end{aligned} \tag{3.7}$$

Here $(C_1,\ C_2)$ is the center of an oscillating motion of the particle. It is assumed that the particle remains close to the resting position $(x_1^n,\ z_1^n)$ so the constants C_1 and C_2 are substituted, that is $C_1 \approx x_1^n$ and $C_2 \approx z_1^n$. The trajectory of a particle is obtained by squaring both position equations of the water particles, and then adding and redistributing the result:

$$\frac{(x_w^n - x_1^n)^2}{(-\zeta_a\frac{cosh(k(h-z_1^n))}{sinh(kh)})^2} + \frac{(z_w^n - z_1)^2}{-(\zeta_a\frac{sinh(k(h-z_1^n))}{sinh(kh)})^2} = sin^2(kx_1^n - wt) + cos^2(kx_1^n - wt) = 1 \tag{3.8}$$

This shows that fluid particles will move in elliptical orbits as shown in Figure 3.3.

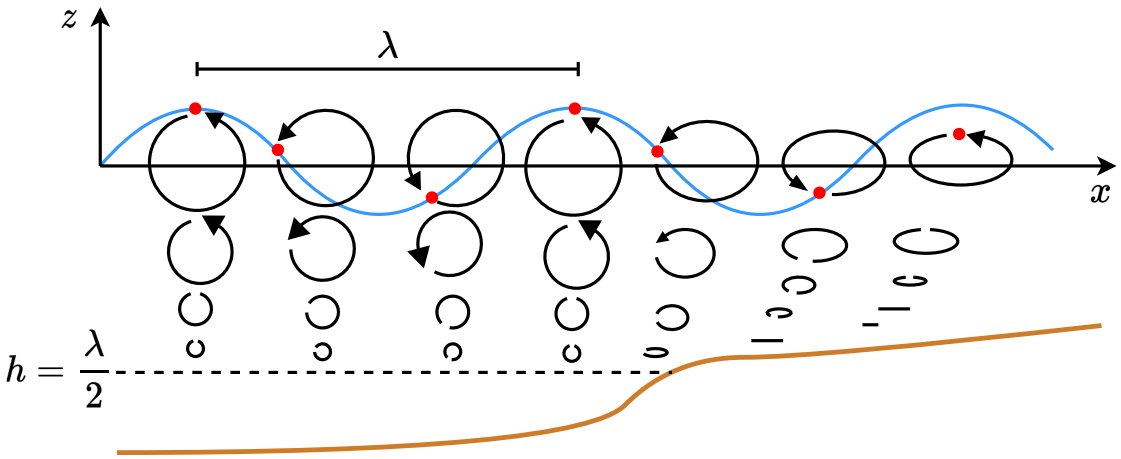

Figure 3.3: This figure shows the motion of fluid particles in a wave. In deep waters $h > \frac{\lambda}{2}$, the particles describe a circular motion. In shallow waters $h < \frac{\lambda}{2}$, fluid particles describe an elliptical motion. Furthermore, the red dots show that the particles are at different phases at different locations.

Finally, the acceleration of the water particle can also be calculated by taking the time derivative of the particle velocity. This results in:

$$\begin{aligned} \dot{u}_w^n &= \frac{du_w^n}{dt} = \zeta_a \omega^2 \frac{cosh(k(h-z^n))}{sinh(kh)} sin(kx^n - wt), \\ \dot{w}_w^n &= \frac{dw_w^n}{dt} = \zeta_a \omega^2 \frac{sinh(k(h-z^n))}{sinh(kh)} cos(kx^n - wt). \end{aligned} \tag{3.9}$$

Deep water approximation For the sake of simplicity, this thesis assumes that $\frac{\lambda}{h} < 2$, enabling the use of the deep water approximation. However, the deep water assumption should be checked for application in the North Sea. In this case, regular waves are described with the following velocity potential function:

$$\phi_w(x^n, z^n, t) = \frac{\zeta_a g}{\omega} e^{-kz^n} sin(kx^n - wt). \tag{3.10}$$

Given this potential function, the vectorial equation of the velocity of a wave particle is given by:

$$\boldsymbol{\nu}_w^n(x^n, z^n, t) = \begin{bmatrix} \frac{\partial \phi_w}{\partial x^n} \\ \frac{\partial \phi_w}{\partial z^n} \\ 0 \end{bmatrix} = \begin{bmatrix} \zeta_a \omega e^{-kz^n} cos(kx^n - wt) \\ -\zeta_a \omega e^{-kz^n} sin(kx^n - wt) \\ 0 \end{bmatrix}. \tag{3.11}$$

The wave particle position is given by:

$$\boldsymbol{\eta}_w^n(x_1^n, z_1^n, t) = \begin{bmatrix} x_1^n - \zeta_a e^{-kz_1^n} sin(kx_1^n - wt) \\ z_1^n - \zeta_a e^{-kz_1^n} cos(kx_1^n - wt) \\ 0 \end{bmatrix} = \boldsymbol{\eta}_{w,1}^n - \begin{bmatrix} \zeta_a e^{-kz_1^n} sin(kx_1^n - wt) \\ \zeta_a e^{-kz_1^n} cos(kx_1^n - wt) \\ 0 \end{bmatrix}, \tag{3.12}$$

where (x_1^n, z_1^n) is the mean position of the wave particle. Finally, the accelerations of a wave particle are given by:

$$\dot{\boldsymbol{\nu}}_w^n(x^n, z^n t) = \begin{bmatrix} \zeta_a \omega^2 e^{-kz^n} sin(kx^n - wt) \\ \zeta_a \omega^2 e^{-kz^n} cos(kx^n - wt) \\ 0 \end{bmatrix}. \tag{3.13}$$

In deep waters, the particle orbit reduces to a circular path as shown in Figure 3.3. The orbital velocity of a fluid particle in deep water is then given by Equation 3.14:

$$V_0 = \sqrt{(u_w^n)^2 + (w_w^n)^2} = \zeta_a \omega e^{-kz^n}. \tag{3.14}$$

3.3.6. Wave energy

The total waver energy per unit of horizontal sea surface area is the sum of the kinetic and potential energy of a wave $E = K + P$ and is given by Equation 3.15:

$$E = \frac{1}{2}\rho g \zeta_a^2 \tag{3.15}$$

This relationship shows that the energy of a wave is proportional to the square of the wave amplitude.

Conclusion regular waves

In summary, this section has identified the key parameters to describe a wave. By knowing just the wave height H, the wave period T, and the water depth h a regular wave is fully defined, which is an important result for simulating a docking procedure under the influence of wave disturbances. This provides significant insight into the wave disturbance surrounding the AUV and the USV. For example, in a deep water wave (that is $h > 0.5\lambda$) a wave height of $H = 1.1$ m, a wavelength or $\lambda = 33$ m at the surface $z = 0$ m will result in a fluid particle velocity $V_0 = 0.75$ $\frac{\text{m}}{\text{s}}$

3.4. Irregular wave model

In reality, sea waves are not simply harmonic the sea surface seems to be constantly changing. This section handles some of the important concepts regarding sea waves in order to construct an irregular wave. Sea waves constantly change in wavelength, wave height, and wave period. To construct an approximation of the North Sea, it is required to address the wave spectrum, linear superposition, and sea state.

Three terms that are useful to know for the discussion on irregular waves are described below. Recording the wave motion during a certain time span and location results in:

- **The mean wave period** denoted with $\bar{T}$ is the average wave period
- **Mean wave height** denoted with $\bar{H}$ is the average wave height.
- **The significant wave height** denoted with $H_{\frac{1}{3}}$ is the average wave height of the highest $\frac{1}{3}$ of the waves recorded.

3.4.1. Wave superposition

In order to construct irregular waves, a superposition is made of regular waves. Since linear regular wave theory is used, the superimposed regular waves still fulfill the boundary conditions. Simply summing the amplitude functions of different waves is used to construct an irregular wave as shown in Equation 3.16:

$$\zeta(t, x^n) = \sum_{m=1}^{N} \zeta_{a,m} cos(k_m x^n - \omega_m t + \epsilon_m) \tag{3.16}$$

Here $\zeta_{a,m}$ and ω_m are the amplitude and the wave angular frequency of a single regular wave respectively, and ϵ_m is a random phase between 0 and 2π. Similarly to Equation 3.16, the velocity potential functions are summed to construct a deep water irregular velocity potential as:

$$\phi_{irr}(x^n, z^n, t) = \sum_{m=1}^{N} \phi_m(x^n, z^n, t), \tag{3.17}$$
$$\phi_m(x^n, z^n, t) = \frac{\zeta_{a,m} g}{\omega_m} e^{-k_m z^n} sin(k_m x^n - \omega_m t + \epsilon_m),$$

where N is the number of superimposed waves.

Irregular fluid particle kinematics Given this irregular potential, the particle velocity is then given by:

$$\boldsymbol{\nu}^n_{w,irr}(x^n, z^n, t) = \begin{bmatrix} \frac{d\phi_{irr}}{dx^n} \\ \frac{d\phi_{irr}}{dz^n} \end{bmatrix} = \sum_{m=1}^{N} \boldsymbol{\nu}^n_{w,m}(x^n, z^n, t). \tag{3.18}$$

The position of a water particle over time is obtained by integrating the irregular velocity function with respect to time. Note that this is not the same as individually integrating each regular velocity function and then summing them, as this will result in an incorrect addition of each constant $\boldsymbol{\eta}^n_{w,1}$. Instead $\boldsymbol{\eta}^n_{w,1}$ should be added only once, as shown below:

$$\boldsymbol{\eta}^n_{w,irr}(x^n_1, z^n_1, t) = \boldsymbol{\eta}^n_{w,1} + \sum_{m=1}^{N} (\boldsymbol{\eta}^n_{w,m}(x^n_1, z^n_1, t) - \boldsymbol{\eta}^n_{w,1}). \tag{3.19}$$

Finally, the irregular accelerations of a water particle are obtained as follows:

$$\dot{\boldsymbol{\nu}}^n_{w,irr}(x^n, z^n, t) = \sum_{m=1}^{N} \dot{\boldsymbol{\nu}}^n_{w,m}(x^n, z^n, t). \tag{3.20}$$

3.4.2. Wave energy spectrum

The wave energy spectrum is a distribution of wave energy over a range of frequencies. The wave energy spectrum is used to find a range of wave amplitudes and period combinations that together construct an irregular wave potential. The wave energy spectrum is defined by some wave period (either the mean period $\bar{T}$ or the mean zero-crossing period T_2 or the peak period T_p) and the significant wave height $H_{\frac{1}{3}}$. The mean wave energy spectrum for wind generated waves in the North Sea is given by the JOint North Sea WAve Project (JONSWAP) spectrum [28].

JONSWAP The JONSWAP spectrum is designed for the North Sea, which has a rough surface and is a common operating area for many ships. The JONSWAP spectrum is significantly narrower than other spectra, where most of the wave energy is located in a narrow frequency band. The JONSWAP spectrum is given in Equation 3.21 and shown Figure 3.4:

$$\begin{aligned} S(\omega) &= 320 \frac{H^2_{1/3}}{T^4_p \omega^5} e^{-\frac{1950}{T^4_p \omega^4}} 3.3^A, \\ A &= e^{-(\frac{\frac{\omega}{\omega_p}-1}{\sigma\sqrt{2}})^2}, \\ \sigma &= 0.07 \; \forall \; \omega < \frac{5.240}{\bar{T}}, \\ \sigma &= 0.09 \; \forall \; \omega > \frac{5.240}{\bar{T}}, \\ \omega_p &= \frac{2\pi}{T_p}, \\ T_p &= 1.199\bar{T}. \end{aligned} \tag{3.21}$$

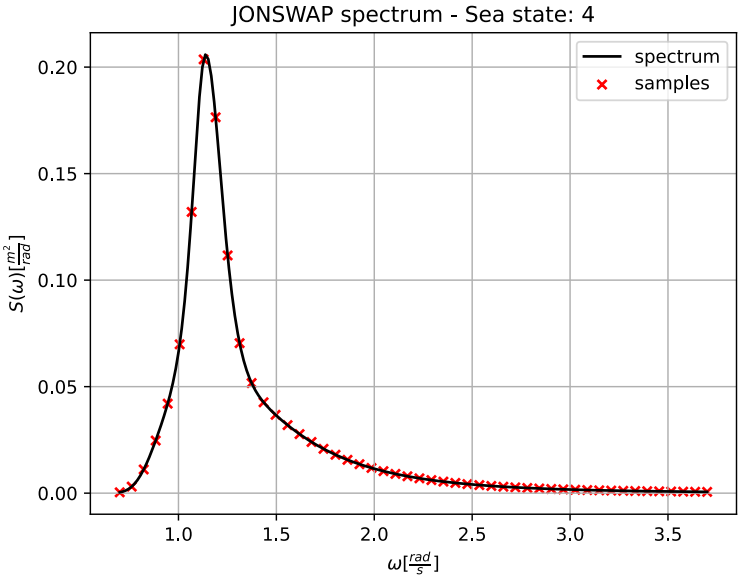

Figure 3.4: Sampling the JONSWAP wave spectrum.

The amplitude samples to construct an irregular wave are then given by:

$$\zeta_{a,m} = \sqrt{2S(\omega_m)\Delta\omega}. \tag{3.22}$$

The number of samples N should be chosen to construct the irregular wave from regular wave components. While a higher number of samples better captures the wave energy spectrum, it will also result in longer simulation times. To capture a wave spectrum, this thesis uses $N = 50$, which is considered the minimum requirement according to [33].

3.4.3. Sea state definition

Sea state is a measure to classify the surface roughness of a sea and is defined by a significant wave height and a wave period. A wave scatter diagram can be used to obtain the probability of occurrence of a specific wave period and significant wave height combination. However, it is impractical to simulate all possible sea state combinations due to time constraints. Instead, this thesis uses a simplified description of sea states based on the scale of Beaufort to provide an initial performance indication of the vertical docking approach. The scale of Beaufort is a well-known one that was originally used to classify winds by observing their effects on waves and other ocean conditions [33]. It ranges from 1 to 12 and is associated with specific significant wave heights and wave periods, as shown in Table 3.2 for the JONSWAP spectrum.

Table 3.2: Sea state definitions for the JONSWAP spectrum on the scale of Beaufort from [33]. Description from [50].

Sea state	Description	Wind speed [kn]	$H_{\frac{1}{3}}$ [m]	$\bar{T}$ [s]
1	Calm	<1.0	0.0	-
1	Light air	2.0	0.50	3.50
2	Light breeze	5.0	0.65	3.80
3	Gentle breeze	8.0	0.80	4.20
4	Moderate breeze	13.5	1.10	4.60
5	Fresh breeze	19.0	1.65	5.10
6	Strong breeze	24.5	2.50	5.70
7	Near gale	30.5	3.60	6.70
8	Gale	37.0	4.85	7.90
9	Strong gale	44.0	6.10	8.80
10	Storm	51.5	7.45	9.50
11	Violent storm	59.5	8.70	10.00
12	Hurricane	>64.0	10.25	10.50

Conclusion irregular waves

This section has presented the irregular wave model that is used to simulate North Sea wave conditions that surround the AUV-USV combination during operation. An irregular wave is composed of superimposed regular wave components and the irregular wave pattern of the North Sea is replicated using the JONSWAP wave energy spectrum. The roughness of the sea is described by the sea state, which consists of the significant wave height and the mean wave period. The scale of Beaufort is used to provide a simplified description of a range of increasing sea states, which is used in later chapters to evaluate the performance of the vertical docking approach using different guidance methods.

3.5. Verification

This section aims to verify the main assumptions that must be met for the linear potential wave theory for deep water to be applicable. These include the wave steepness assumption and the deep water assumption. Additionally, the wave model is verified visually by animating its motion, providing an intuitive understanding of the wave motion.

3.5.1. Wave steepness assumption

The critical parameter for this model to be valid is the wave steepness $\frac{H}{\lambda}$ which should be smaller than $\frac{1}{20}$ [33]. Using the significant wave height $H_{\frac{1}{3}}$ instead of the mean wave height $\bar{H}$, this assumption is verified for different sea states as shown in Table 3.3

Table 3.3: The wave steepness at different sea states.

Sea state	1	2	3	4	5	6	7	8	9	10	11	12
Wave steepness	$\frac{1}{38.3}$	$\frac{1}{34.7}$	$\frac{1}{34.4}$	$\frac{1}{30.0}$	$\frac{1}{24.6}$	$\frac{1}{20.3}$	$\frac{1}{19.5}$	$\frac{1}{20.1}$	$\frac{1}{19.8}$	$\frac{1}{18.9}$	$\frac{1}{17.9}$	$\frac{1}{16.8}$
satisfied	✓	✓	✓	✓	✓	✓	X	✓	X	X	X	X

This result shows that the wave steepness assumption is satisfied for sea states 1-6 and 8 but not for the other sea states, indicating that non-linear effects play a non-negligible role in the motion of larger waves. Despite this, the model is still considered for this study because it is valid for lower sea states, and the steepness assumption for higher sea states is only slightly violated. However, this limitation is important to keep in mind when interpreting the result of this study at higher sea states.

3.5.2. Deep water assumption

The assumption that the North Sea can be approximated as deep water is verified by evaluating the $\frac{h}{\lambda} < 0.5$ assumption. The average water depth of the North sea is 95 m while the average water in the Dutch North Sea is 46 m [81, 61]. Verifying the deep water assumption for the sea states defined in

Table 3.2 results in Table 3.4.

Table 3.4: The minimum water depth required for the deep water assumption to be valid for each of the sea states.

Sea state	1	2	3	4	5	6	7	8	9	10	11	12
Wavelength [m]	19.1	22.5	27.5	33.0	40.6	50.7	70.1	97.4	121	141	156	172
Min depth [m]	9.6	11.3	13.8	16.5	20.3	25.4	35.0	48.7	60.5	70.5	79.1	86.1

This result shows that the deep water assumption is valid for all waters deeper than 86.1 m which is shallower than the average depth of the North Sea, while the sea state $1-7$ are also within the average depth of the Dutch North Sea. The deep water assumption is therefore reasonable for an initial evaluation of the vertical docking procedure in the North Sea.

3.5.3. Visual analysis

To ensure the correct implementation of the simulation model and to catch implementation errors, an animation and visualization toolbox was developed. Figure 3.5a displays the wave motion for the regular wave model and Figure 3.5b for the irregular wave model. The corresponding animation for each model can be viewed by scanning or clicking their respective QR code.

Animation

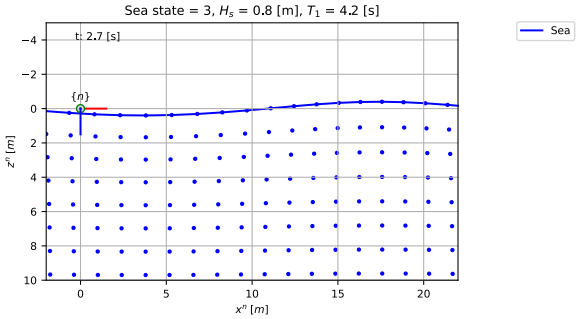

(a) water motion with regular wave model.

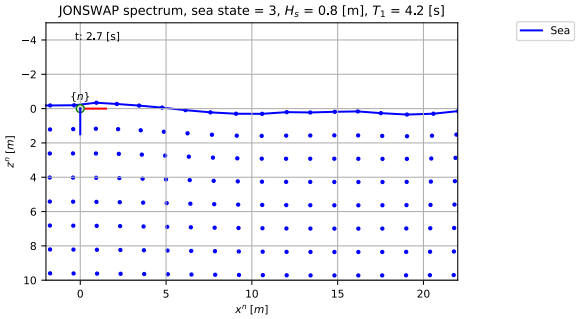

(b) water motion with irregular wave model.

Animation

Figure 3.5: Wave model visualization.

Some basic tests were performed to ensure that a certain wave period and wave height combination resulted in the correct regular wave profile. The results of these tests are shown in Table 3.5 confirming that the wave periods and heights are correctly visualized.

Table 3.5: Visual analysis of regular waves

Wave height [m]	**Wave period** [s]	**Correct wave profile?**
0.0	1.0	✓
2.0	5.0	✓
5.0	10.0	✓

For irregular waves, it was observed that for lower sea states up to sea state 9, the wave profile looked realistic, however, the steepness of the waves at higher sea states seemed too steep and unrealistic. These observations are in agreement with the violation of the wave steepness assumption at higher sea states.

3.6. Conclusion

This chapter aimed to develop a model of waves in the North Sea to evaluate the vertical docking approach of an AUV to an USV in rough seas. To reach this objective, linear velocity potential theory was utilized which is applicable if the wave steepness remains smaller than $\frac{1}{20}$.

In summary, this chapter started by describing regular waves and concluded that the key parameters to define a regular wave in deep water were the wave height H and the wave period T. This result was then used to obtain an irregular wave model using superposition of regular waves, that can simulate North Sea conditions. The irregular wave pattern of the North Sea is replicated using the JONSWAP wave energy spectrum, where the roughness of the sea is described by the sea state, consisting of the significant wave height and the mean wave period. The scale of Beaufort was used to provide a simplified description of a range of increasing sea states.

The main limitation of the presented wave model is its applicability at higher sea states, where the wave steepness assumption was not satisfied. Future research could address this shortcoming with higher-order wave models that remain valid at larger wave steepnesses.

In the end an expression for the pose, velocity, and acceleration vector of a water particle in a North Sea wave was obtained:

$$\begin{aligned} \boldsymbol{\eta}_w^n &= [x_w^n, z_w^n, 0]^T, \\ \boldsymbol{\nu}_w^n &= [u_w^n, w_w^n, 0]^T, \\ \dot{\boldsymbol{\nu}}_w^n &= [\dot{u}_w^n, \dot{w}_w^n, 0]^T. \end{aligned} \tag{3.23}$$

This expression concludes the objective of this chapter. The results obtained in this chapter provide insight into the environmental conditions surrounding the AUV-USV combination. In addition, the results are used in later chapters to evaluate the performance of different vertical guidance methods at different sea states. The next chapter describes the Lobster Scout model utilizing the wave kinematics to obtain the wave disturbance forces acting on the Scout.

4

AUV model

When this research was started, a dynamic model of the Lobster Scout AUV was not yet developed. Therefore, the objective of this chapter is to develop a model that accurately describes the dynamic behavior of the Lobster Scout. As the Scout is operating in the wave-affected zone during the vertical docking approach, this model must consider the dynamic wave disturbance forces acting on the Scout. This chapter contributes to answering the research question:

How can the vertical docking system be modelled?

To this end, this chapter presents the general three DOF AUV model, accounting for the surge, heave, and pitch DOF. This model is based on the six DOF model developed by Fossen [24], which is widely used in the literature on AUV control, including various studies on underwater docking [78, 77, 74, 83, 88]. An overview of the model is provided in Figure 4.1. The model takes wave kinematics and control forces as inputs and generates the motion response of the Lobster Scout as output.

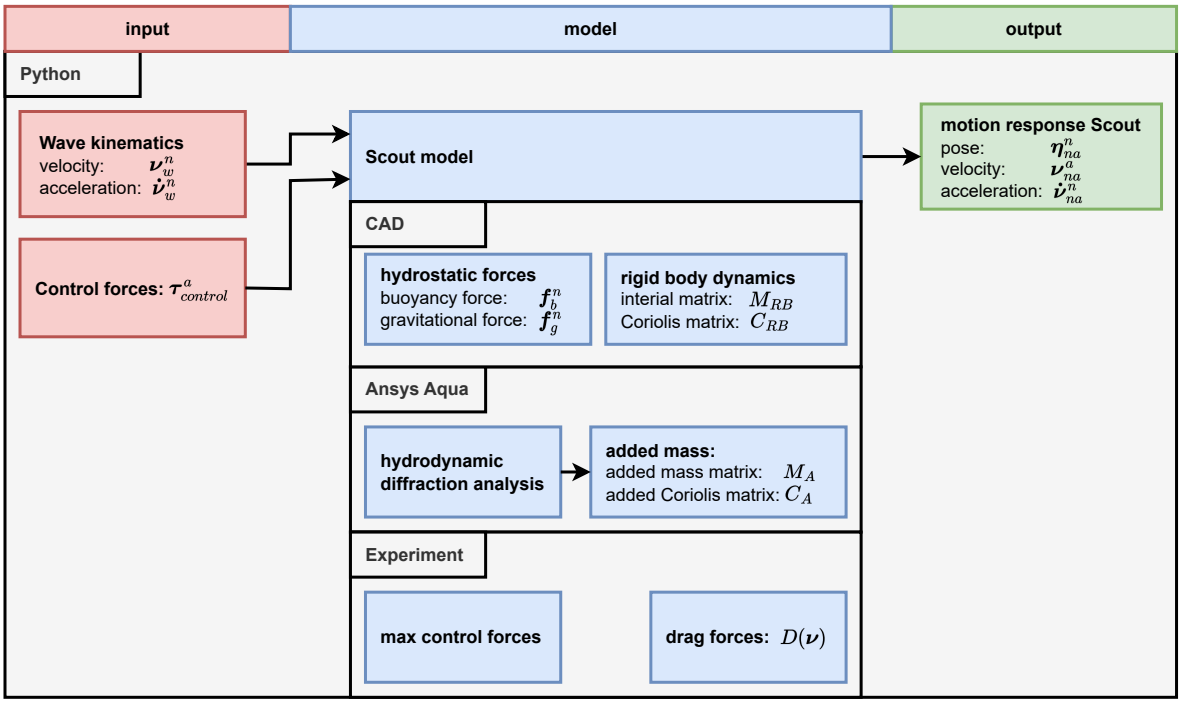

Figure 4.1: an input-output diagram of the Lobster Scout model

The general vertical plane kinematic and kinetic equations for an underwater vehicle in the presence of waves that this chapter builds up to are shown below:

$$\dot{\boldsymbol{\eta}} = J(\boldsymbol{\eta})(\boldsymbol{\nu}_w^a + \boldsymbol{\nu}_r^a), \tag{4.1}$$
$$M_{RB}\dot{\boldsymbol{\nu}} + C_{RB}(\boldsymbol{\nu})\dot{\boldsymbol{\nu}} + M_A\dot{\boldsymbol{\nu}}_{\boldsymbol{r}} + C_A(\boldsymbol{\nu}_r)\boldsymbol{\nu}_r + D(\boldsymbol{\nu}_{\boldsymbol{r}})\boldsymbol{\nu}_r + \boldsymbol{g}(\boldsymbol{\eta}) = \boldsymbol{\tau}_{control},$$

The model parameters for the Lobster Scout have also been determined using several sources, calculations, and experiments.

In Section 4.1, the main vector definitions used throughout this chapter are given. The kinematics and kinetics of a general AUV model are provided in Section 4.2 and Section 4.3 respectively. The general AUV model is then adapted for the Lobster Scout in Section 4.4, after which various verification tests are done. Finally, a conclusion is given in Section 4.5

4.1. Vector definitions

The vectors and variables used for the vertical plane AUV model are defined in Table 4.1.

Table 4.1: Definition on vectors based as described in [24]. Note that the rotation vectors are scalars in a 2D vertical plane model.

Description	Variable	Definition
NED position AUV	$\boldsymbol{p}_{na}^n$	$[x_{na}^n \; z_{na}^n]^T \in \mathbb{R}^2$
Attitude AUV	Θ_{na}^n	$\theta_{na}^n \in \mathbb{S}$
Body-fixed linear velocity	$\boldsymbol{v}_{na}^a$	$[u_{na}^a \; w_{na}^a]^T \in \mathbb{R}^2$
Body-fixed angular velocity	ω_{na}^a	$q_{na}^a \in \mathbb{R}$
Body-fixed force	$\boldsymbol{f}_a^a$	$[X_a^a \; Z_a^a]^T \in \mathbb{R}^2$
Body-fixed moment	m_a^a	$M_a^a \in \mathbb{R}$

To keep the notation short in this section, some notation is changed as follows:

- $\boldsymbol{\eta} = \boldsymbol{\eta}_{na}^n$
- $\boldsymbol{\nu} = \boldsymbol{\nu}_{na}^a$
- $\boldsymbol{\tau} = \boldsymbol{\tau}_a^a$

4.2. Kinematics

This section discusses the 3 DOF kinematic motion model that couples the linear and angular velocities in $\{a\}$ to the linear and angular velocities in $\{n\}$ frame. A kinematic model captures the motion of a vehicle without considering the forces at play. The linear velocities in $\{a\}$ are related to the linear velocities in $\{n\}$ by:

$$\begin{aligned} \dot{\boldsymbol{p}}_{na}^n &= \boldsymbol{v}_{na}^n, \\ &= R_a^n(\Theta_{na}^n)\boldsymbol{v}_{na}^a, \end{aligned} \tag{4.2}$$

here the rotation matrix R_a^n transforms the linear velocities in the $\{a\}$ frame to the linear velocities in the $\{n\}$ frame which is given by:

$$R_a^n(\Theta_{na}^n) = \begin{bmatrix} cos(\theta) & sin(\theta) \\ -sin(\theta) & cos(\theta) \end{bmatrix}. \tag{4.3}$$

The angular velocities in the $\{a\}$ frame are related to the angular velocities in the $\{n\}$ by:

$$\dot{\Theta}_{na} = \omega^n_{na} = \omega^a_{na}. \tag{4.4}$$

The aforementioned equations are represented in a combined kinematic equation as shown below:

$$\begin{bmatrix} \dot{\boldsymbol{p}}^n_{na} \\ \dot{\Theta}^n_{na} \end{bmatrix} = \begin{bmatrix} R^n_a(\Theta^n_{na}) & 0_{2\times 1} \\ 0_{1\times 2} & 1 \end{bmatrix} \begin{bmatrix} \boldsymbol{v}^a_{na} \\ \omega^a_{na} \end{bmatrix}, \tag{4.5}$$
$$\dot{\boldsymbol{\eta}} = J(\boldsymbol{\eta})\boldsymbol{\nu}.$$

This expression relates all the velocities in the $\{a\}$ frame to the velocities in the $\{n\}$ frame, which concludes this section.

4.3. Kinetics

This section discusses the nonlinear dynamic equation that relates the forces in the $\{a\}$ frame to the accelerations in the $\{a\}$ frame, based on [25]. The goal here is to provide a quick overview of the modelling steps to obtain a basic 3 DOF model of an AUV. The reader is referred to [24] for a more detailed explanation of all the modelling steps, derivations, and options. An overview of the kinetic equation that is discussed in this section is shown below:

$$M\dot{\boldsymbol{\nu}} + C(\boldsymbol{\nu})\boldsymbol{\nu} + D(\boldsymbol{\nu})\boldsymbol{\nu} + \boldsymbol{g}(\boldsymbol{\eta}) = \boldsymbol{\tau}_{control}, \tag{4.6}$$

where Table 4.2 describes the various terms in the kinetic equation.

Table 4.2: Explanation of terms in the kinetic equation.

Variable	Description
$M = M_{RB} + M_A$	Generalized inertia matrix.
$C(\boldsymbol{\nu}) = C_{RB}(\boldsymbol{\nu}) + C_A(\boldsymbol{\nu})$	Generalized Coriolis-centripetal matrix.
$D(\boldsymbol{\nu}) = D + \boldsymbol{d}(\boldsymbol{\nu})$	Generalized damping matrix.
$g(\boldsymbol{\eta})$	Generalized restoring force vector.
$\boldsymbol{\tau}_{control}$	Generalized control input vector.

4.3.1. Simplifications

The model explained in this section is based on a couple of simplifications that are discussed below.

Choice of Coordinate Origin (CO) location The origin o_a of the $\{a\}$ frame CO coincides with the Center of Gravity (CG), that is the distance vector $\boldsymbol{r}^a_{ag} = \boldsymbol{0}$. This simplifies the model as no translation step is required to alter the equations of motion. However, in some scenarios, the CG may change location, for example when the payload of the vehicle is changed. In that case, it may be better to choose a fixed CO.

Choice of frame axis orientation The axes of the $\{a\}$ frame are co-linear with the principle axis of inertia of the vehicle. This simplifies the model, as the moment of inertia matrix is now diagonal. However, the axis of the $\{a\}$ frame may not align with the longitudinal, lateral, and normal symmetry axes of the vehicle.

Vehicle symmetry assumption The vehicle is assumed to be symmetric in the $\hat{i}_a\hat{k}_a$-plane, the $\hat{i}_a\hat{j}_a$-plane and the $\hat{j}_a\hat{k}_a$-plane, simplifying the model as several off-diagonal matrix coefficients in the model equal zero. However, it is important to note that while the Lobster Scout is reasonably symmetric along these planes, it is not perfectly symmetrical. For instance, the Scout has a streamlined shape in the forward cruising direction, and only one recovery fin on the top side of the hull, while the internal

components are not uniformly distributed. While this assumption will lead to some modelling errors, it provides a good starting point for an initial evaluation of vertical docking. Future research could focus on developing a more accurate model of the Lobster Scout.

4.3.2. Rigid body dynamics

The rigid body dynamics around the CG are expressed with the following vectorial equation:

$$M_{RB}\dot{\boldsymbol{\nu}} + C_{RB}(\boldsymbol{\nu})\boldsymbol{\nu} = \boldsymbol{\tau}_{RB}. \tag{4.7}$$

In this equation, M_{RB} is the diagonal rigid body inertia matrix given by:

$$M_{RB} = \begin{bmatrix} m & 0 & 0 \\ 0 & m & 0 \\ 0 & 0 & I^a_{g,y} \end{bmatrix} \tag{4.8}$$

where m is the mass of the vehicle and $I^a_{g,y}$ is the moment of inertia around the CG in $\{a\}$.

C_{RB} is the Coriolis-Centripetal matrix. The Coriolis-Centripetal force is a fictitious force that acts on the vehicle as a result of the rotation of the $\{a\}$ frame with respect to the fixed $\{n\}$ frame when the vehicle is in motion. A linear velocity-independent parametrization is a good choice for constructing this matrix as it has a nice property which is that the off-diagonal matrix blocks are zero [24]. The following matrix is obtained:

$$C_{RB}(\boldsymbol{\nu}) = \begin{bmatrix} 0 & mq & 0 \\ -mq & 0 & 0 \\ 0 & 0 & 0 \end{bmatrix} \tag{4.9}$$

External forces and moments The generalized external forces and moments are all captured by the $\boldsymbol{\tau}_{RB}$ term in Equation 4.7. This includes hydrodynamic forces hydrostatic forces, control forces, and disturbance forces. The external forces and moments are decomposed as follows:

$$\boldsymbol{\tau}_{RB} = \boldsymbol{\tau}_{static} + \boldsymbol{\tau}_{dynamic} + \boldsymbol{\tau}_{control} + \boldsymbol{\tau}_{disturbance}. \tag{4.10}$$

4.3.3. Hydrostatic forces

The hydrostatic forces include the buoyancy force B and the gravitational force W, which are:

$$W = mg,\ B = \rho g V, \tag{4.11}$$

here, m is the mass of the vehicle, g is the gravitational constant, ρ is the density of the water and V is submerged volume. In the $\{n\}$ frame, these forces will result in the following vectors:

$$\boldsymbol{f}^n_g = \begin{bmatrix} 0 \\ W \end{bmatrix},\ \boldsymbol{f}^n_b = -\begin{bmatrix} 0 \\ B \end{bmatrix}. \tag{4.12}$$

The resulting restoring force vector $\boldsymbol{g}(\boldsymbol{\eta})$ in $\{a\}$ then is given by:

$$\begin{aligned} \boldsymbol{g}(\boldsymbol{\eta}) &= -\begin{bmatrix} R^a_n(\Theta^n_{na})(\boldsymbol{f}^n_g + \boldsymbol{f}^n_b) \\ \boldsymbol{r}^a_{ag} \times R^a_n(\Theta^n_{na})\boldsymbol{f}^n_g + \boldsymbol{r}^a_{ab} \times R^a_n(\Theta^n_{na})\boldsymbol{f}^n_b \end{bmatrix}, \\ R^a_n(\theta) &= \begin{bmatrix} cos(\theta) & -sin(\theta) \\ sin(\theta) & cos(\theta) \end{bmatrix}, \\ \boldsymbol{r}^a_{ab} &= [x_b, z_b]^T, \\ \boldsymbol{r}^a_{ag} &= [x_g, z_g]^T = [0, 0]^T, \end{aligned} \tag{4.13}$$

where $\boldsymbol{r}_{ab}^{a}$ is the distance between the Center of Buoyancy (CB) and the CO and $\boldsymbol{r}_{ab}^{a}$ is distance between the CG and the CO respectively.

4.3.4. Hydrodynamic forces

The generalized hydrodynamic forces are the result of the water surrounding the vehicle being brought into motion by the motion of the vehicle. The forces that result from this can be categorized into two groups, added mass and damping forces. The coefficients of these terms term can be calculated using system identification or can be approximated with for example [36] or hydrodynamic programs.

Added mass

The added mass is a force that acts as if the vehicle has a larger mass. The vehicle does not actually have a larger mass, but the increased pressure in the fluid as a result of the acceleration of the vehicle has the same effect as if the vehicle had a larger mass. The added mass is modelled using the hydrodynamic inertia matrix M_A and the hydrodynamic Coriolis-centripetal matrix.$C_A(\boldsymbol{\nu})$. For an underwater vehicle, the motion at high speed is highly non-linear and coupled. However, in the situation of docking, the vehicle will likely be moving at lower speeds. Since the Scout model is assumed to be symmetry in all three planes, the off-diagonal elements of the hydrodynamic inertia matrix are assumed to be zero resulting in the following matrices [24]:

$$M_A = -\begin{bmatrix} X_{\dot{u}} & 0 & 0 \\ 0 & Z_{\dot{w}} & 0 \\ 0 & 0 & M_{\dot{q}} \end{bmatrix}, \tag{4.14}$$

$$C_A(\boldsymbol{\nu}) = \begin{bmatrix} 0 & 0 & -Z_{\dot{w}}w \\ 0 & 0 & X_{\dot{u}}u \\ Z_{\dot{w}}w & -X_{\dot{u}}u & 0 \end{bmatrix},$$

The terms in the added mass matrices should be read as for example: the hydrodynamic force X along the x-axis, as a result of an acceleration $\dot{u}$ in the x direction is written as $X_{\dot{u}}\dot{u}$.

In practice, the off-diagonal terms of M_A are often significantly smaller than the diagonal terms. Therefore, this approximation often works quite well. Furthermore, the off-diagonal terms are challenging and time-consuming to obtain [24]. Hence, the errors resulting from this approximation are accepted in this thesis.

Finally, the combined effect of terms $C_{A,13}$ and $C_{A,23}$ is called the Munk moment, which can cause destabilizing effects at higher velocities [24].

Damping

Hydrodynamic damping forces arise from the relative velocity between the vehicle and the water. They may be caused by potential damping, skin friction, wave drift damping, vortex shedding, and lifting forces [24]. Typically, these various sources of damping are combined in a linear and a quadratic damping term. Since the scout is assumed to be symmetric in all three planes, the linear damping term can be expressed as:

$$D = -diag(X_u, Z_w, M_q). \tag{4.15}$$

This term is generally sufficient when the robot is moving at lower velocities. However, at higher velocities, the non-linear damping term $\boldsymbol{d}(\boldsymbol{\nu})$ dominates. The non-linear damping term cannot be ignored when considering waves because, even if the absolute velocity of the robot is zero, the relative velocity with respect to the moving water can be large. The total damping force is then given by:

$$D(\boldsymbol{\nu}) = D + \boldsymbol{d}(\boldsymbol{\nu}). \tag{4.16}$$

To determine the non-linear drag vector, a drag-lift model can be used as described in [24]. The drag force is always parallel to the relative velocity direction, while the lift force is perpendicular to it. The lift and drag forces are given by:

$$f_D = \frac{1}{2}\rho A_{ref} C_D(\alpha) V_r^2, \tag{4.17}$$
$$f_L = \frac{1}{2}\rho A_{ref} C_L(\alpha) V_r^2,$$

where ρ is the density of the water, A_{ref} is the reference surface area, C_D and C_L are the drag and lift coefficients, respectively, α is the angle of attack of the AUV with respect to the relative water flow, and V_r is the magnitude of the relative flow velocity. The angle of attack and the relative velocity are visualized in Figure 4.2a. The angle of attack is given by:

$$\alpha = tan^{-1}(\frac{w_r^a}{u_r^a}), \tag{4.18}$$
$$u_r^a = u_{na}^a - u_w^a,$$
$$w_r^a = w_{na}^a - w_w^a,$$

where u_w^a and w_w^a are the water velocities along the surge and heave DOF, expressed in $\{a\}$ at the location of the AUV. Furthermore, the magnitude of the relative velocity is given by:

$$V_r = \sqrt{u_r^2 + w_r^2}. \tag{4.19}$$

The drag and lift forces acting on a robot do not necessarily attach at the CG and can therefore create a stabilizing or destabilizing moment on the AUV. However, for the sake of simplicity, this thesis assumes that the drag and lift forces attach at the CG. This assumption is reasonable given that the Lobster Scout lacks stabilizing fins at the stern side of the robot and is reasonably symmetric, such that any drag moment will likely be loosely coupled to the relative linear velocity of the robot. Additionally during the docking procedure, the robot will likely only have a high pitch rate at a small linear velocity, reducing the influence of modelling errors. The quadratic pitch moment can then be expressed as:

$$m_{a,q} = M_{q^2} |q_a^a| q_a^a, \tag{4.20}$$

where M_{q^2} is the quadratic pitch drag coefficient.

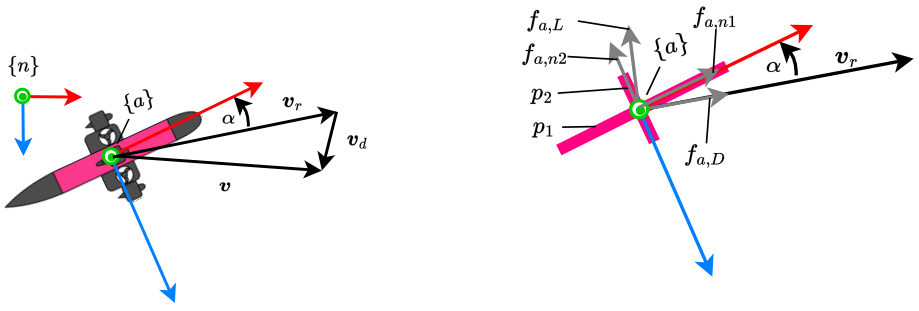

(a) Angle of attack and relative velocity

(b) Double flat plate drag approximation. p_1 and p_2 indicate the two plates.

Figure 4.2: Non-linear drag visualization

During the docking procedure, the Lobster Scout will operate under the influence of waves, where water particles approach a circular orbit. Therefore, the angle of attack is in the range of $0° - 360°$.

However, the drag and lift coefficients of the Scout at every angle of attack are currently unknown, and obtaining them is beyond the scope of this thesis. Consequently, a simplified approach for approximating non-linear lift and drag forces was necessary. This was achieved by utilizing a double flat plate approximation, as illustrated in Figure 4.2b.

The flat plate approximation assumes that drag can be modelled as a collection of particles that do not interact with each other. Instead, they transfer their momentum to the surface of the plate in the normal direction before sliding off along the plate surface without any friction [39]. The normal force $f_{a,n1}$ for plate p_1 in Figure 4.2b is given by:

$$f_{a,n1} = \rho A_1 sin^2(\alpha) V_r^2, \tag{4.21}$$

The normal force for plate p_2 is obtained in a similar manner by using $\alpha + \frac{\pi}{2}$ for the angle of attack and A_2 for the plate area. These normal forces can be utilized to determine the drag and lift forces, which can then be used to calculate the drag forces in the $\{a\}$ frame. However, since the normal forces are already aligned in the $\{a\}$ frame, they are directly used as the drag forces expressed in the a frame.

To obtain a more realistic drag force, an experiment with the Lobster Scout is performed to estimate the pure surge, heave, and pitch drag further described in Section 4.4.5. In the experiment, it was assumed that the requested control force equals the drag force at constant velocity and that the water velocity is negligible. Using the symmetry assumption of the Lobster Scout, pure surge drag is assumed when $\alpha = 0^\circ,\ 180^\circ$, pure heave drag when $\alpha = 90^\circ,\ -90^\circ$, and pure pitch drag when the forward velocity is zero and the Scout rotates in place. A quadratic fit of this data results in the following expression:

$$\begin{aligned} f_{a,n1} &= \rho A_1 sin^2(\frac{\pi}{2}) V_r^2 = Z_{w^2} V_r^2, \\ f_{a,n2} &= \rho A_2 cos^2(0) V_r^2 = X_{u^2} V_r^2 \\ m_{a,q} &= M_{q^2} |q_a^a| q_a^a, \end{aligned} \tag{4.22}$$

where $X_{u^2},\ Z_{w^2},\ M_{q^2}$ are the quadratic drag coefficients obtained in the experiment for surge heave and pitch respectively. The non-linear damping force is then given by:

$$\boldsymbol{d}(\boldsymbol{\nu}) = \begin{bmatrix} Z_{w^2} sign(u_r^a) sin^2(\alpha) V_r^2 \\ X_{u^2} sign(w_r^a) cos^2(\alpha) V_r^2 \\ M_{q^2} |q_{na}^a| q_{na}^a, \end{bmatrix} \tag{4.23}$$

where the $sign(.)$ makes sure the drag force is in the correct direction. All hydrodynamic forces are now obtained. To conclude, the total hydrodynamic force is given by:

$$\boldsymbol{\tau}_{dynamic} = -M_A \dot{\boldsymbol{\nu}} - C_A(\boldsymbol{\nu})\boldsymbol{\nu} - D(\boldsymbol{\nu})\boldsymbol{\nu}. \tag{4.24}$$

4.3.5. Control forces

The control force, denoted as $\boldsymbol{\tau}_{control}$, refers to the forces generated by the thrusters or control surfaces of the AUV that guide it towards a desired state, based on the current estimated state of the vehicle. Chapter 7 discusses the methods used to determine these control forces.

The desired control force is determined along the DOF in the a frame. In this thesis, it is assumed that these control forces are perfectly actuated by the AUV. Although this assumption may overestimate the control performance, it is reasonable as the Scout has full hovering capability and can produce any force within its control limits. In practical applications, a thrust allocation matrix is utilized to translate the desired forces into the thruster forces or control surface forces [24]. Modelling errors in the thrust allocation matrix can result in differences between the desired and the produced control forces.

Furthermore, in reality, the thrust force is a function of the velocity of the AUV. However, for practical considerations, this thesis assumes that the control force is not a function of the vehicle's velocity. Unfortunately, no information is available from the thruster manufacturer regarding the thrust force at different velocities. Additionally, the only known source that attempted to characterize these thruster forces at various velocities is [54], but their exact results remain unclear. Furthermore, since the side thrusters of the Lobster Scout are modified versions of this thruster, additional characterization would be necessary. While the thrust forces of the side thruster have been determined within the time frame of this thesis at zero velocity, it was not possible to determine these forces at various velocities due to the requirement for specialized facilities, such as a towing tank.

4.3.6. Environmental disturbance forces

To discuss environmental disturbance forces, it is helpful to summarize the kinematic and kinetic equations discussed thus far. The equations are presented below:

$$\begin{aligned} \dot{\boldsymbol{\eta}} &= J(\boldsymbol{\eta})\boldsymbol{\nu}, \\ M\dot{\boldsymbol{\nu}} + C(\boldsymbol{\nu})\boldsymbol{\nu} + D(\boldsymbol{\nu})\boldsymbol{\nu} + \boldsymbol{g}(\boldsymbol{\eta}) &= \boldsymbol{\tau}_{control}, \end{aligned} \tag{4.25}$$

When accounting for environmental disturbances forces $\boldsymbol{\tau}_{disturbance}$ caused by water motion from waves, only a minor modification is needed from these equations. Instead of using the absolute velocity vector $\boldsymbol{\nu}$, the water velocity vector $\boldsymbol{\nu}_w$ and the relative velocity vector $\boldsymbol{\nu}_r$ is used. The relationship between these three vectors is shown below:

$$\begin{aligned} \boldsymbol{\nu}_r^a &= \boldsymbol{\nu} - \boldsymbol{\nu}_w^a, \\ &= \boldsymbol{\nu} - R_n^a(\boldsymbol{\Theta}_{na}^n)\boldsymbol{\nu}_w^n. \end{aligned} \tag{4.26}$$

Note that the 2D rotation matrix notation here is abused for the purpose of shorter notation, that is:

$$R_a^n(\Theta_{na,k}) = \begin{bmatrix} cos(\theta_{na,k}) & sin(\theta_{na,k}) & 0 \\ -sin(\theta_{na,k}) & cos(\theta_{na,k}) & 0 \\ 0 & 0 & 1 \end{bmatrix} \tag{4.27}$$

Additionally, the relative acceleration vector $\dot{\boldsymbol{\nu}}_r$ is obtained by taking the time derivative of this equation:

$$\dot{\boldsymbol{\nu}}_r = \dot{\boldsymbol{\nu}} - \dot{\boldsymbol{\nu}}_{\boldsymbol{w}} = \dot{\boldsymbol{\nu}} - (\dot{R}_n^a(\boldsymbol{\Theta}_{na})\boldsymbol{\nu}_w^n + R_n^a(\boldsymbol{\Theta}_{na})\dot{\boldsymbol{\nu}}_d^n), \tag{4.28}$$

where the derivative of a rotation matrix is obtained

$$\dot{R}_n^a(\boldsymbol{\Theta}_{na}) = \omega_{na}^n R_n^a(\boldsymbol{\Theta}_{na}) \tag{4.29}$$

Note that the wave model from Chapter 3 provides the vectors $\boldsymbol{\nu}_w^n$ and $\dot{\boldsymbol{\nu}}_w^n$ at the a frame position.
The kinematic and kinetic equations can now be rewritten using the relative velocity and relative acceleration in addition as follows:

$$\begin{aligned} \dot{\boldsymbol{\eta}} &= J(\boldsymbol{\eta})(\boldsymbol{\nu}_w^a + \boldsymbol{\nu}_r^a), \\ M_{RB}\dot{\boldsymbol{\nu}} + C_{RB}(\boldsymbol{\nu})\dot{\boldsymbol{\nu}} + M_A\dot{\boldsymbol{\nu}}_{\boldsymbol{r}} + C_A(\boldsymbol{\nu}_r)\boldsymbol{\nu}_r + D(\boldsymbol{\nu}_{\boldsymbol{r}})\boldsymbol{\nu}_r + \boldsymbol{g}(\boldsymbol{\eta}) &= \boldsymbol{\tau}_{control}, \end{aligned} \tag{4.30}$$

4.3.7. State space representation

The model is simulated using an ordinary differential solver, which requires that the model is represented as a non-linear state space model. This state space model is given by Equation 4.31:

$$\begin{bmatrix} \dot{\boldsymbol{\eta}} \\ \dot{\boldsymbol{\nu}} \end{bmatrix} = \begin{bmatrix} J(\boldsymbol{\eta})\boldsymbol{\nu} \\ (M_{RB} + M_A)^{-1}(\boldsymbol{\tau}_{control} + M_A\dot{\boldsymbol{\nu}}_d - C_{RB}(\boldsymbol{\nu})\boldsymbol{\nu} - C_A(\boldsymbol{\nu}_r)\boldsymbol{\nu}_r - D(\boldsymbol{\nu}_r)\boldsymbol{\nu}_r - \boldsymbol{g}(\boldsymbol{\eta})) \end{bmatrix} \tag{4.31}$$
$$\dot{\boldsymbol{x}} = f(\boldsymbol{x}, \boldsymbol{u}).$$

4.4. Model fitting and verification

To verify the AUV model and the methods for obtaining model parameters for the Scout, mesh convergence studies, analytical calculations, and visual analysis were performed. The AUV model was fitted using the parameters of the Lobster Scout, which are estimated from various information sources, calculations, and experiments.

4.4.1. Lobster Scout specifications

Table 4.3 provides an overview of the relevant parameters to build a model for the Lobster Scout, as well as the source of each parameter.

Table 4.3: General Lobster Scout specifications, from [6].

Description	Symbol	Value	Source
Mass in water	m	61.5 kg	Computer-Aided Design (CAD) realistic model
Length	L	1.9 m	Computer-Aided Design (CAD)
Diameter	d	0.2 m	Computer-Aided Design (CAD)
Inertia around y-axis	I_y	14.22 kgm^2	Computer-Aided Design (CAD) realistic model
Volume	V	0.061 m^3	Computer-Aided Design (CAD) realistic model
Distance CG to CO	r^a_{ag}	$[0,\ 0]$ m	By definition
Distance CB to CO	r^a_{ab}	$[0,\ -0.01]$ m	Computer-Aided Design (CAD)

4.4.2. Rigid body dynamics

The Computer-Aided Design (CAD) model of the Lobster Scout can provide a reasonable estimate of the rigid body dynamics parameters. However, the CAD model does not account for water inside the robot's wet modules, namely the nosecone and tail cone. The wet modules contain water that enters the wet modules through holes in the hull. It is assumed that this water inside the robot behaves as a rigid body as the holes are very small. To account for this water, a simplified CAD model of the Lobster Scout has been constructed, shown in Figure 4.3b.

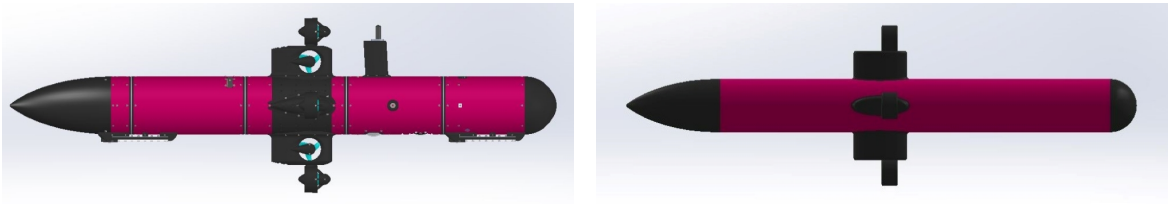

(a) Real Lobster Scout CAD model.

(b) Approximation of the Lobster Scout.

Figure 4.3: The Scout CAD model and the simplified CAD model.

This simplified model is used to obtain an estimate of the mass in water. A slight positive buoyancy and uniform density is assumed:

$$m = c\rho_{water}V, \tag{4.32}$$

where m is the estimated mass of the Scout, $0.98 < c < 1.00$ is a factor that accounts for slight positive buoyancy, $\rho_{water} = 1025$ kg is the assumed density of salt water and V is the volume of the Scout realistic model. Similarly, the inertia around the y-axis is obtained using this method. Using the values from Table 4.3, the following matrices are obtained for the rigid body dynamics:

$$M_{RB} = \begin{bmatrix} 61.5 & 0 & 0 \\ 0 & 61.5 & 0 \\ 0 & 0 & 14.22 \end{bmatrix}, \tag{4.33}$$

$$C_{RB}(\boldsymbol{\nu}) = \begin{bmatrix} 0 & 61.5q & 0 \\ -61.5q & 0 & 0 \\ 0 & 0 & 0 \end{bmatrix}. \tag{4.34}$$

4.4.3. Hydrostatic forces

The CAD model is used to obtain the center of volume relative to the center of mass. Assuming full submersion of the Scout during docking, the center of volume is equivalent to the center of buoyancy. The buoyancy force is around $1 - 2$ % higher than the force of gravity, ensuring that the robot always floats to the water surface if loss of control occurs. The estimated distances from the CG to CO and from the CB to CO are given in Table 4.3. The hydrostatic forces in the $\{n\}$ frame are given by:

$$\boldsymbol{f}_g^n = \begin{bmatrix} 0 \\ 603.3 \end{bmatrix}, \ \boldsymbol{f}_b^n = -\begin{bmatrix} 0 \\ 613.3 \end{bmatrix}. \tag{4.35}$$

4.4.4. Added mass

This sub-section discusses the estimation of the added mass parameters for the Scout and the verification of the methods for obtaining these parameters.

Verification added mass

Ansys Aqua was used to obtain the added mass coefficients of the Lobster Scout. Ansys Aqua uses a Boundary Element Method (BEM) to calculate the Froude-Krylov forces, diffraction forces, and radiation forces, including the added mass of an object. In order to verify the results obtained from Ansys Aqua, an analytical model was used and compared to the results obtained by Ansys Aqua. The following procedure was taken to verify the results from Ansys Aqua:

- **Analytical ellipsoid approximation** Approximate the Lobster Scout as a prolate ellipsoid (see Figure 4.4), for which an analytical solution of the added mass coefficients exist. The shape of the Lobster Scout differs from an ellipsoid, mainly due to its fins at the middle of the body, therefore this result is only used for verification purposes and not for parameter estimation.
- **Ansys Aqua ellipsoid approximation** Obtain the added mass coefficients of the same prolate ellipsoid using Ansys aqua to confirm that the results from Ansys Aqua agree with the analytical solution. Furthermore, a mesh convergence study was done to conclude that the result does not change significantly with various mesh sizes. This now gives reasonable confidence in the validity of the results.

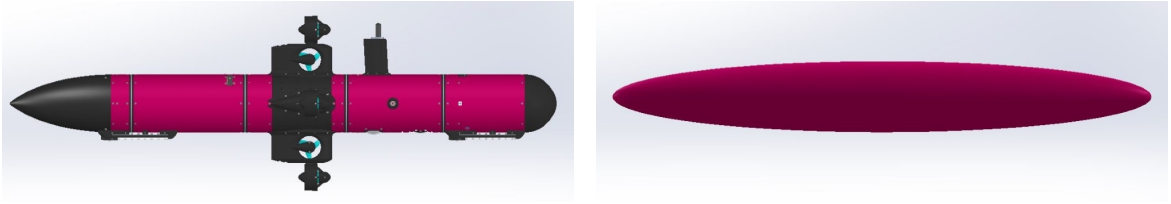

(a) Real Lobster Scout CAD model.

(b) Prolate ellipsoid approximation Lobster Scout.

Figure 4.4: The Scout CAD model vs the ellipsoid approximation.

Analytical added mass calculation for ellipsoid approximation The hydrodynamic added mass coefficients of a prolate spheroid are obtained using the method described in [24]. The Scout can be approximated using an ellipsoid given its volume is equivalent:

$$\frac{4}{3}\pi a b^2 = V_{auv}, \tag{4.36}$$

where the coefficients a and b are the semi-major and semi-minor axis of the prolate spheroid respectively and V_{auv} is the volume of the Scout. The coefficients a and b are then obtained as follows:

$$\begin{aligned} a &= L_{auv}, \\ b &= \sqrt{\frac{V_{auv}}{\pi a}}, \end{aligned} \tag{4.37}$$

where L_{auv} is the length of the Lobster Scout. The inertia of this ellipsoid around its center of mass is calculated with:

$$I_{y,speroid} = \frac{1}{5}m(a^2 + b^2) \tag{4.38}$$

where m is the mass of the ellipsoid given by $m = \rho_{water}V$ assuming neutral buoyancy. Using ellipsoid, the added mass coefficients for M_A and C_A are calculated as follows:

$$\begin{aligned} M_A &= -\begin{bmatrix} X_{\dot{u}} & 0 & 0 \\ 0 & Z_{\dot{w}} & 0 \\ 0 & 0 & M\dot{q} \end{bmatrix} = \begin{bmatrix} k_1 m & 0 & 0 \\ 0 & k_2 m & 0 \\ 0 & 0 & k' I_y \end{bmatrix}, \\ C_A(\boldsymbol{\nu}_r) &= \begin{bmatrix} 0 & 0 & -Z_{\dot{w}} w_r \\ 0 & 0 & X_{\dot{u}} u_r \\ Z_{\dot{w}} w_r & -X_{\dot{u}} u_r & 0 \end{bmatrix} = \begin{bmatrix} 0 & 0 & k_2 m w_r \\ 0 & 0 & -k_1 m u_r \\ -k_2 m w_r & k_1 m u_r & 0 \end{bmatrix}. \end{aligned} \tag{4.39}$$

Here, the terms k_1, k_2 and k' are called Lambs k-factor [36]. These terms are given by:

$$\begin{aligned} k_1 &= \frac{\alpha_0}{2 - \alpha_0}, \\ k_2 &= \frac{\beta_0}{2 - \beta_0}, \\ k' &= e^4 \frac{\beta_0 - \alpha_0}{(2 - e^2)(2e^2 - (2 - e^2)(\beta_0 - \alpha_0))}, \end{aligned} \tag{4.40}$$

where:

$$\begin{aligned} e &= 1 - (\frac{b}{a})^2, \\ \alpha_0 &= \frac{2(1 - e^2)}{e^3}(0.5 ln(\frac{1 + e}{1 - e}) - e), \\ \beta_0 &= \frac{1}{e^2} - \frac{1 - e^2}{2e^3} ln(\frac{1 + e}{1 - e}). \end{aligned} \tag{4.41}$$

Ansys Aqua added mass calculation for ellipsoid approximation This thesis will not go into detail on the theory behind Ansys Aqua, but the general modelling steps are provided in Appendix C. However, when modelling an AUV, it is acceptable to assume frequency-independent hydrodynamic coefficients outside the wave-affected zone [24]. While the docking procedure is taking place in the wave-affected zone, it is still assumed that the hydrodynamic coefficients are frequency independent. This assumption is justifiable as the added mass coefficients are almost constant with frequency as shown in Figure 4.5. Therefore, the added mass coefficients derived in Ansys Aqua are evaluated at the longest period and then compared against the analytical solution.

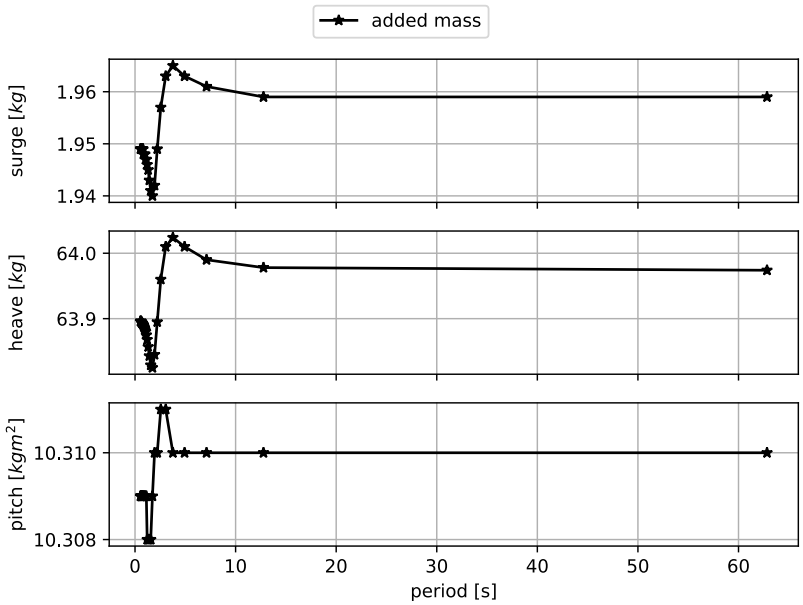

Figure 4.5: The added mass coefficient of the 4cm meshed ellipsoid approximation over a period range. Only a small frequency dependency is observed over the period range.

Mesh size typically affects the accuracy of a numerical solver's solution. Hence, a mesh convergence study was done. Figure 4.6 compares the analytically obtained mass of the prolate ellipsoid with the mass obtained using Ansys Aqua, while Figure 4.7 compares the analytically determined added mass coefficients with those computed using Ansys Aqua.

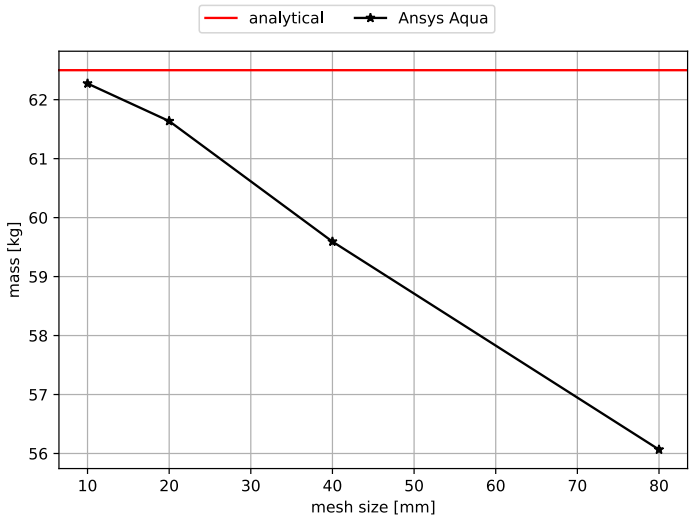

Figure 4.6: Comparison of the ellipsoid mass calculated analytically and calculated using Ansys Aqua for varying mesh sizes.

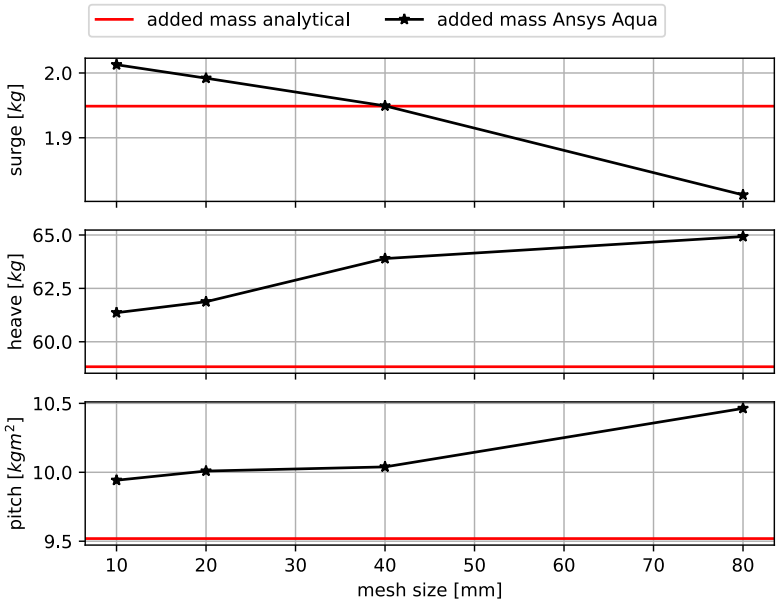

Figure 4.7: Comparison of the ellipsoid added amss calculated analytically and calculated using Ansys Aqua for varying mesh sizes.

Added mass verification conclusions The following conclusions are drawn from the results:

- The added mass coefficients are close to frequency independent.
- The analytical solution and the numerical solution match within 5% for the 10mm and 20mm mesh sizes. This gives confidence that the result is valid.
- The mesh size does influence the result somewhat, but the results are reasonably consistent.
- The analytical mass and the mass calculated by Ansys Aqua for the ellipsoid match closed with the smallest mesh size.

This has the following implications for estimating the added mass parameters for the Scout model:

- The added mass coefficients are assumed constant and not dependent on frequency.
- A mesh size of 20mm is chosen to obtain the added mass coefficients for the Lobster Scout as it strikes a good balance between computation time and accuracy.

Added mass parameter estimation
Given that the added mass coefficients of obtained via Ansys Aqua for an ellipsoid match those of the analytical solution of an ellipsoid, Ansys Aqua was trusted to obtain reasonable estimates of the added mass coefficients for the Lobster Scout. To obtain the most accurate results, the Lobster Scout should be closely matched, however, too many small features result in lengthy computation and inaccuracies as the mesh can not accurately capture small features. To balance, computation time, mesh size, and accuracy, a realistic approximation of the Lobster Scout with a reduction of features is made for the added mass estimation and is shown in Figure 4.3. The obtained added mass coefficients are given in the equations below:

$$M_A = \begin{bmatrix} 5.8 & 0 & 0 \\ 0 & 65.1 & 0 \\ 0 & 0 & 11.9 \end{bmatrix}, \tag{4.42}$$

$$C_A(\boldsymbol{\nu}_r) = \begin{bmatrix} 0 & 0 & 65.1w_r \\ 0 & 0 & -5.8u_r \\ -65.1w_r & 5.8u_r & 0 \end{bmatrix},$$

4.4.5. Damping

This section discusses the validity of the damping matrix of the Lobster Scout.

Damping verification

In order to access whether the quadratic form explained in Section 4.3.4 of the damping matrix is a good approximation, an experiment has been conducted with the Lobster Scout to determine the drag coefficients in the surge heave and pitch direction.

The damping experiment The goal of the experiment is to estimate the drag force at a given robot velocity for the surge, heave, and pitch DOF. The following assumptions are made in order to estimate the viscous drag force at a certain velocity for the Lobster Scout:

- The water velocity is zero. As such there are no currents present during the experiment. Figure 4.8 shows the test environment.
- The control force is not a function of robot velocity. This assumption is certainly false, as the control force of a T200 thruster drops with velocity [54]. However, the thrust force at different velocities of the thrusters is not provided by the manufacturer and the author has found no good source for this information as explained in section 4.3.5
- Furthermore, it is assumed that the drag coefficient for both sway and heave, as well as for yaw and pitch, are equivalent based on the symmetry of the Lobster Scout, as detailed in Section 4.3.1. This assumption allows the experiment to be conducted in the horizontal plane, reducing the risk of collision with the bottom of the shallow lake.
- During the experiment, a line was attached to the Scout for risk mitigation purposes. The drag force resulting from this line is included in the estimation.

Figure 4.8: The environment for the viscous damping experiment.

Based on these assumptions, multiple data points of the robot velocity in a specific DOF at a given control force are logged, which are then used to calculate the corresponding damping coefficients.

Fitting the control force-velocity data points The control force-velocity data is fitted using a least squares method to fit a function through the data points. It is assumed that the velocity at zero control force is zero, so any function goes through the origin. The following functions are fitted:

- **Linear fit** $y = ax$,
- **Quadratic fit** $y = bx^2$,
- **Linear Quadratic fit** $y = cx + dx^2$,

where for each DOF, y is the control force, x is the velocity, and a, b, c, d are the damping coefficients.

Results The results of the experiment are shown in Figure 4.9.

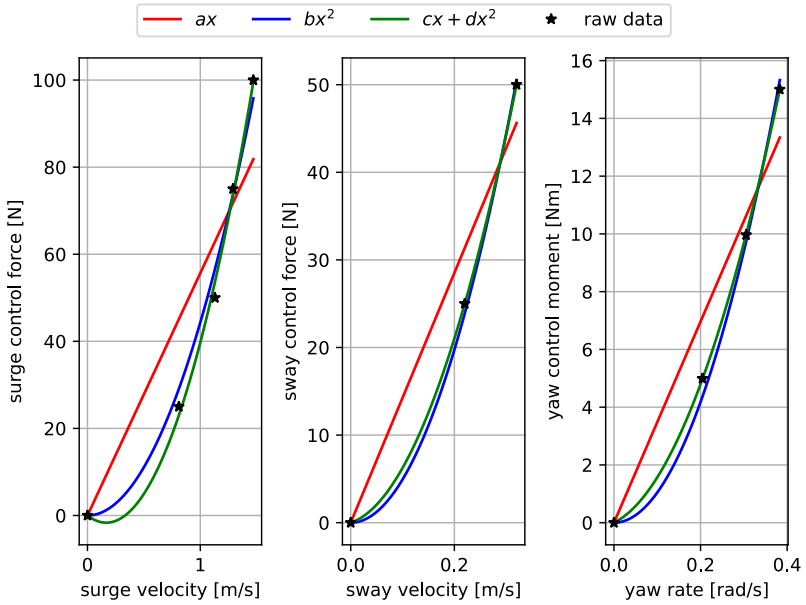

Figure 4.9: Obtained velocity of the Scout plotted against the required control force in the surge, sway, and yaw directions in the damping experiment. Furthermore, a linear fit and a quadratic fit are included.

Figure 4.9 clearly shows that a purely quadratic drag assumption results in a good fit with the data. Therefore a quadratic damping model is used for the Lobster Scout.

Damping fitting
Assuming purely quadratic damping, thus using the quadratic fit $y = bx^2$, the following nonlinear damping vector is obtained:

$$\boldsymbol{d}(\boldsymbol{\nu}) = \begin{bmatrix} Z_{w^2} sign(u_r^a) sin^2(\alpha) V_r^2 \\ X_{u^2} sign(w_r^a) cos^2(\alpha) V_r^2 \\ M_{q^2} |q_{na}^a| q_{na}^a, \end{bmatrix} = \begin{bmatrix} 42.1 sign(u_r^a) sin^2(\alpha) V_r^2 \\ 502.4 sign(w_r^a) cos^2(\alpha) V_r^2 \\ 109.5 |q_{na}^a| q_{na}^a, \end{bmatrix} \tag{4.43}$$

4.4.6. Control forces

The maximum thruster forces of the forward-facing thrusters and the side thrusters of the Lobster Scout are determined using a thrust measurement setup shown in Figure 4.10. The thrust measurement setup comprises an extrusion profile frame and a motor driver housed in a waterproof casing. The motor driver powers the thruster, which is connected to a rotating arm. This arm transfers the force exerted by the thruster to a load cell, enabling the measurement of thrust at a specific motor current. Table 4.4 presents the total maximum control forces in surge and heave direction and the maximum pitch moment.

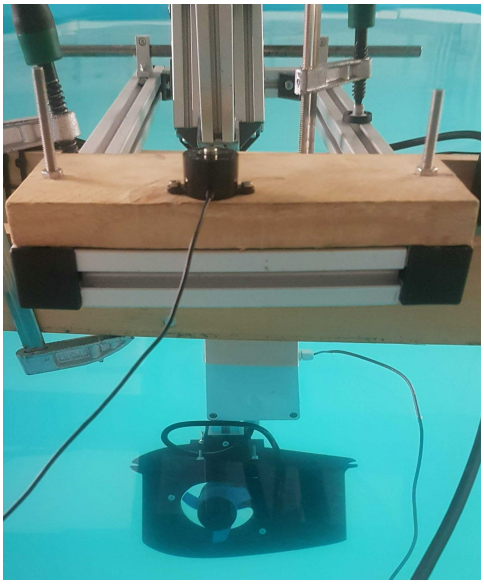

Figure 4.10: The thrust measurement setup.

Table 4.4: The maximum forwards and backwards thrust of the Scout in each DOF.

DOF	Maximum forwards thrust [N]	Maximum backwards thrust [N]
Surge	192	−152
Heave	68	−68
Pitch	20	−20

4.4.7. Visual analysis

To ensure correct implementation of AUV model and to catch and correct obvious modelling errors, the visualization toolbox was used to animate the behavior of the Lobster Scout in waves.

Figures 4.11a and 4.11b display the Scout's response to regular and irregular waves, respectively. The corresponding animation can be seen by scanning or clicking the QR codes. It is important to note that the Scout model was initiated with a certain forward velocity, but that the response is purely passive, meaning that no control forces were applied. Since the Scout is slightly positively buoyant, it was expected that the Scout eventually loses its forward momentum and slowly floats to the water surface. The observations confirm that this is indeed the case.

Animation

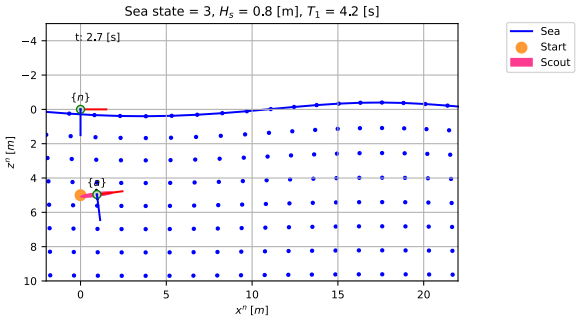

(a) AUV response with regular wave disturbance.

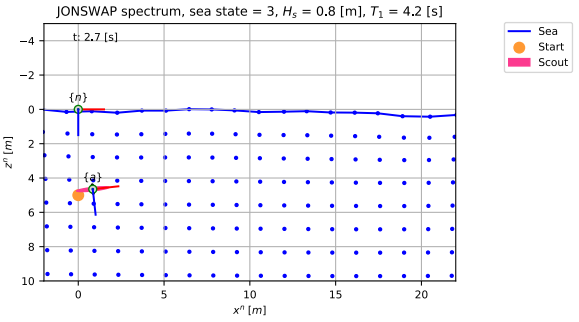

(b) AUV response with irregular wave disturbance.

Animation

Figure 4.11: AUV response to waves with initial surge velocity of 0.5 m.

The response of the Scout was observed for many initial states to catch any implementation errors. This process was repeated several times after which it passed all initial states presented in Table 4.5.

Table 4.5: Evaluation of the Scout response to various initial states.

x^n_{na} [m]	z^n_{na} [m]	θ^a_{na} [rad]	u^a_{na} $[\frac{\text{m}}{\text{s}}]$	w^a_{na} $[\frac{\text{m}}{\text{s}}]$	q^a_{na} $[\frac{\text{rad}}{\text{s}}]$	**matches expected behavior?**
0.0	5.0	0.0	0.0	0.0	0.0	✓
1.0	4.0	1.0	0.0	0.0	0.0	✓
1.0	4.0	0.5π	0.0	0.0	0.0	✓
0.0	5.0	0.0	1.0	0.0	0.0	✓
0.0	5.0	0.0	0.0	1.0	0.0	✓
0.0	5.0	0.0	0.0	0.0	1.0	✓

All in all, the behavior of the Lobster Scout model seems to match the behavior of the Lobster Scout during field tests closely.

4.5. Conclusion

This chapter contributes to the answer to the research question *How can the vertical docking system be modelled?* The objective of this chapter was to obtain a model for the Lobster Scout that accurately describes its dynamics in the wave-affected zone.

First, the general vertical plane kinematic and kinetic equations for an underwater vehicle in the presence of waves were obtained. The resulting equations are repeated below:

$$\dot{\boldsymbol{\eta}} = J(\boldsymbol{\eta})(\boldsymbol{\nu}^a_w + \boldsymbol{\nu}^a_r), \tag{4.44}$$
$$M_{RB}\dot{\boldsymbol{\nu}} + C_{RB}(\boldsymbol{\nu})\dot{\boldsymbol{\nu}} + M_A\dot{\boldsymbol{\nu}}_{\boldsymbol{r}} + C_A(\boldsymbol{\nu}_r)\boldsymbol{\nu}_r + D(\boldsymbol{\nu}_{\boldsymbol{r}})\boldsymbol{\nu}_r + \boldsymbol{g}(\boldsymbol{\eta}) = \boldsymbol{\tau}_{control},$$

The model parameters for the Lobster Scout have been determined using a number of sources, calculations, and experiments. The rigid body matrices and the restoring force vector were obtained from the CAD design of the Scout. Ansys Aqua was used to obtain the added mass coefficients and a drag experiment has been performed to obtain quadratic damping coefficients. Finally, the maximum control forces have been determined using a thrust measurement experiment. This verification and fitting process was extensive, resulting in confidence in the model.

Overall, the Lobster Scout model presented in this chapter provides a realistic description of the vehicle's dynamics in the wave-affected zone. The next chapter will describe the USV model and the motion of the attached DS.

Future research can focus on including the Lobster Scout's asymmetries which cause coupling between motions, and increasing the modelling accuracy of the control forces at non-zero relative velocities, leading to more realistic responses and more precise drag coefficients.

5

USV model

In Chapter 2 it was decided to base the USV on the DUS V5750 USV developed by Demcon [72] and approximate it as a simple box. The objective of this chapter is to model the motion of this USV and the DS located on the bottom of the USV in North Sea waves. This objective contributes to answering the research question:

How can the vertical docking system be modelled?

This chapter concludes the answer to this research question in combination with the two preceding chapters that described the wave model and the AUV model.

Figure 5.1 provides an overview of the USV model. The model generates the motion response of the USV to a wave, which is used for verification and navigation purposes. Secondly, the model generates the corresponding motion response of the DS mounted on the bottom of the USV, which serves as the docking goal state. The required inputs of the model are the key parameters that define a regular or irregular wave and the Response Amplitude Operators (RAOs) obtained in Ansys Aqua.

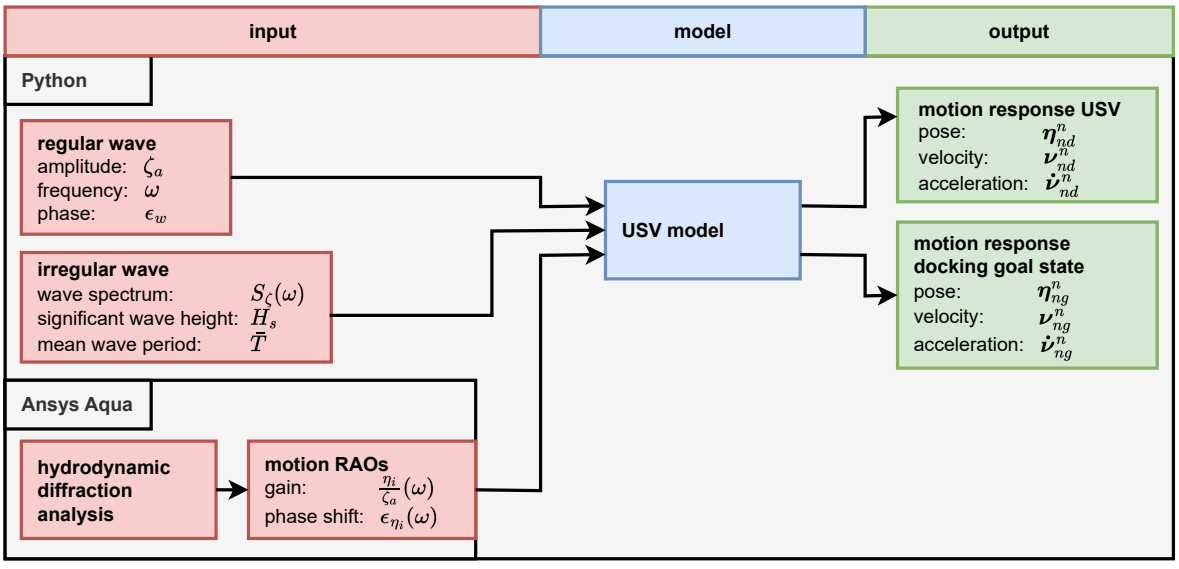

Figure 5.1: an input-output diagram of the USV model

Note that the inputs of the wave model are used as input for the USV model, rather than the outputs of the wave model such as is the case with the AUV model. This is because the motion of the USV model

relies solely on kinematic equations, rather than kinetic equations. By using motion RAOs to obtain a phase-shifted and scaled version of the wave elevation level at the location of the USV, as explained in Section 5.3, the kinematics of the USV can be described.

This chapter is organized as follows: In Section 5.1 various vessel models are explored resulting in the selection of the linear mass-spring-damper model. Section 5.2 described this model including the main assumptions for linearity, the definition of necessary vectors, and the kinematics and kinetics that describe the USV motion. The chapter then proceeds to discuss the vessel motions based on RAOs which were obtained from Ansys Aqua in Section 5.3. The motion of the goal state is derived from the motion of the USV in Section 5.4. The USV model is verified in Section 5.5. To close this chapter, a conclusion is given in Section 5.6.

5.1. USV model selection

This section explains why the linear mass-spring-damper vessel model is identified to be most suitable for an initial performance indication of the vertical docking approach to an USV in rough seas. Various vessel models are evaluated based on the following requirements:

- **R1:** The USV model must be compatible with the irregular wave model in order to simulate North Sea waves.
- **R2:** The USV model must not require extensive computation as this would make it impractical to evaluate the vertical docking approach.
- **R3:** The model must be implementable in Python to allow for integration with the other models of the system.

The literature presents a number of vessel modelling options:

- **Maneuvering theory-based models** are used for ship motion in calm water when ships are moving with a constant forward speed, and are primarily used for surface maneuvering rather than ship motion due to waves [24]. This model is not suitable with requirement R1.
- **Linear mass-spring-damper models** only consider the first harmonics of each motion direction of a floating structure and can result in a realistic model for small wave steepnesses [33]. This type of model behaves linearly towards individual wave components, meaning that for a certain wave frequency and wave amplitude, the USV will move in a proportional manner to this wave with a certain scaled amplitude and phase shift, but with the same frequency. An irregular wave response can be easily obtained by the superposition of all responses to regular wave components. This model fulfills all requirements.
- **Second-order models**: While first-order forces are typically more significant for the primary motion of ships, a second-order model also considers the second-order forces and moments, which become significant for waves with large wave steepness, such as in shallow waters where nonlinear effects cannot be ignored [89]. Second-order wave forces can cause drift and generate harmonics at lower and higher multiples of the base wave frequency, which can resonate with the vessel if not properly taken into account, resulting in large motions. This type of model is significantly more complex due to non-linearity, and thus this model does not fulfill requirement R3. [33]

The author has selected the linear mass-spring-damper model primarily to its compatibility with the linear wave model. In both models, the superposition principle is employed to generate the motion response of irregular waves. Although the linear model may be less suitable in shallow waters where wave steepness can surpass the limits accurately predicted by linear theory, it is a suitable starting point for evaluating the potential of vertical docking. Additionally, steady second-order drift forces are expected to have a minor impact on docking, similar to currents, as both the AUV and the USV will drift in similar amounts, and thus, this phenomenon is not important to model. The linear mass-spring-damper model described in the following sections is largely based on [33].

5.2. Linear mass-spring-damper vessel model

This section provides an explanation of the linear mass-spring-damper vessel model. Firstly, the main assumptions and vector definitions are presented. Secondly, the kinematic equations and kinetic equations are discussed. It was discovered that obtaining the kinetic equations without utilizing software programs like Ansys Aqua is challenging. Consequently, this approach to acquiring vessel motions was discontinued and another approach using motion RAOs was taken, explained in Section 5.3.

5.2.1. Model assumptions

The following assumptions are required for linear approximations:

1. **A1** The body fixed frame $\{d\}$ will only rotate small angles from the $\{s\}$ frame. Therefore $cos(\theta) \approx 1$ and $sin(\theta) \approx \theta$. The author found no standard for the maximum allowed angle in the literature, therefore a maximum of 2% deviation for the sine and cosine value is assumed, which results in a maximum angle of $\approx 11.5°$.
2. **A2** In steady state, the gravitational forces and the buoyancy forces together equal zero, that is $mg + V\rho g = 0$. Thus, only variations from the steady-state scenario are considered. This assumption is in general true for any floating structure.
3. **A3** Second-order wave forces are small and are neglected, which is reasonable as long as the wave steepness is small. The wave steepness assumption is verified in Section 3.5.1.
4. **A4** The wave forces acting on the AUV and the USV are decoupled.

5.2.2. Vector definitions

Table 5.1 defines the relevant vectors for the USV model with respect to the $\{s\}$ frame.

Table 5.1: The vector definition for the USV model Note that the rotation vectors actually are scalars.

Description	Variable	Definition
Sea keeping position	$\boldsymbol{p}^s_{sd}$	$[x^s_{sd}\ z^s_{sd}]^T \in \mathbb{R}^2$
Sea keeping attitude	Θ^s_{sd}	$\theta^s_{sd} \in \mathbb{S}$
Body-fixed linear velocity	$\boldsymbol{v}^s_{sd}$	$[u^s_{sd}\ w^s_{sd}]^T \in \mathbb{R}^2$
Body-fixed angular velocity	ω^s_{sd}	$q^s_{sd} \in \mathbb{R}$
Body-fixed force	$\boldsymbol{f}^s_d$	$[X^s_d\ Z^s_d]^T \in \mathbb{R}^2$
Body-fixed moment	m^s_d	$M^s_d \in \mathbb{R}$

Sea keeping frame $\{s\}$ In this thesis, the $\{s\}$ is static at the still water line and thus simply a translation of the $\{n\}$ frame:

$$\begin{aligned} \boldsymbol{p}^n_{ns} &= [x^n_{ns}\ 0]^T, \\ \Theta^s_{sd} &= 0. \end{aligned} \tag{5.1}$$

In order to express the $\{d\}$ frame in the $\{n\}$ frame, the following transformation are used:

$$\begin{aligned} \boldsymbol{p}^n_{nd} &= \boldsymbol{p}^n_{ns} + \boldsymbol{p}^n_{sd}, \\ \Theta^n_{nd} &= \Theta^s_{sd}, \\ \boldsymbol{v}^n_{nd} &= \boldsymbol{v}^s_{sd}, \\ \omega^n_{nd} &= \omega^s_{sd}, \\ \boldsymbol{f}^n_d &= \boldsymbol{f}^s_d, \\ m^n_d &= m^s_d. \end{aligned} \tag{5.2}$$

5.2.3. Kinematics

This section presents the kinematics of the USV. With a linear mass-spring-damper model, the vessels motion response to a regular wave is described with a harmonic function of the same wave frequency for all DOF. To keep this section concise, the heave DOF is used as an example, but note that the model is equivalent for surge and pitch DOF. Recall that the equation for the wave elevation at a specific position for regular waves is given by:

$$\zeta = \zeta_a cos(\omega t), \tag{5.3}$$

where the wave elevation ζ is dependent on the wave amplitude ζ_a and the wave frequency ω. The heave response in the $\{s\}$ frame for a wave moving in the positive x^n direction is then given by:

$$\begin{aligned} z^s_{sd} &= -z_a cos(\omega t - \epsilon_{z,\zeta}), \\ \dot{z}^s_{sd} &= \frac{\partial z^s_{sd}}{\partial t} = -\omega z_a sin(\omega t - \epsilon_{z,\zeta}), \\ \ddot{z}^s_{sd} &= \frac{\partial \dot{z}^s_{sd}}{\partial t} = \omega^2 z_a cos(\omega t - \epsilon_{z,\zeta}), \end{aligned} \tag{5.4}$$

where z^s_{sd} is the heave displacement of the CG relative to the still water surface, z_a is the displacement amplitude of the heave motion and $\epsilon_{z,\zeta}$ is a phase shift between the elevation of the wave and the heave displacement. Both the displacement amplitude and the phase shift are dependent on the wave frequency. A positive phase shift value indicates that the vessel lags behind the wave. The surge and pitch responses are obtained analogously to the heave response where the position equations are given by:

$$\begin{aligned} x^s_{sd} &= -x_a cos(\omega t - \epsilon_{x,\zeta}), \\ \theta^s_{sd} &= -\theta_a cos(\omega t - \epsilon_{\theta,\zeta}), \end{aligned} \tag{5.5}$$

5.2.4. Kinetics

This section presents the kinetic equations that describe the linear dynamics of the USV. To start, Newton's second law is applied, by equating the product of the generalized inertia matrix M and the USV acceleration $\ddot{\boldsymbol{\eta}}^s_{sd}$ around the CG with the generalized external forces and moments vector $\boldsymbol{\tau}^s_d$:

$$M\ddot{\boldsymbol{\eta}}^s_{sd} = \boldsymbol{\tau}^s_d, \tag{5.6}$$

where $\boldsymbol{\tau}^s_d$ consists of the generalized external forces $\boldsymbol{f}^s_d$ and moments m^s_d:

$$\boldsymbol{\tau}^s_d = \begin{bmatrix} \boldsymbol{f}^s_d \\ m^s_d \end{bmatrix} \tag{5.7}$$

note that m^s_d is a scalar as only the pitch moment is considered. The generalized external forces and moments can be obtained by integrating the pressure that results from the first-order wave velocity potential on the submerged part of the hull's surface:

$$\begin{aligned} \boldsymbol{f}^s_d &= -\int\int_S p \cdot \boldsymbol{n} \cdot dS, \\ m^s_d &= -\int\int_S p \cdot (\boldsymbol{r} \times \boldsymbol{n}) \cdot dS, \end{aligned} \tag{5.8}$$

where S is the hull's surface, p is the pressure, $\boldsymbol{n}$ is the normal vector of surface element dS and $\boldsymbol{r}$ is the position vector of surface element dS. Since the system is linear, the external forces acting on the body can be superimposed as:

$$\boldsymbol{\tau}_d^s = \boldsymbol{\tau}_h^s + \boldsymbol{\tau}_w^s, \tag{5.9}$$

where $\boldsymbol{\tau}_h^s$ are the hydromechanic forces and $\boldsymbol{\tau}_w^s$ the wave exciting forces and moments:

- **Hydromechanic forces** are the forces and moments resulting from the oscillating body moving through the water.
- **Wave exciting forces and moments** are the forces resulting from the waves acting on the body.

The pressure is given by:

$$\begin{aligned} p &= -\rho\frac{\partial\Phi}{\partial t} - \rho g z \\ &= -\rho(\frac{\partial\Phi_r}{\partial t} + \frac{\partial\Phi_w}{\partial t} + \frac{\partial\Phi_d}{\partial t}) - \rho g z, \end{aligned} \tag{5.10}$$

where $\frac{\partial\Phi_r}{\partial t}$ is the radiative potential and $\rho g z$ is the hydrostatic pressure resulting in the hydromechanic forces and $\frac{\partial_w\Phi}{\partial t}$ and $\frac{\partial\Phi_d}{\partial t}$ are the undisturbed wave potential and the diffracted wave potential respectively, resulting in the wave exciting forces and moments.

Hydromechanic forces
The hydromechanic forces consist of the hydrostatic restoring forces and the radiative forces:

- **Hydrostatic restoring force** $\boldsymbol{\tau}_s^s$ are the forces that result from the buoyancy and gravitational forces that change with a change in the water plane area and are in phase with the position or rotation of the body.
- **Radiative force** $\boldsymbol{\tau}_r^s$ are the forces that result from the radiative waves generated by an oscillating structure and are in phase with the velocity and acceleration of the body.

Ignoring the wave exciting forces and moments for the moment, the kinetic equation looks like:

$$M\ddot{\boldsymbol{\eta}}_{sd}^s = \boldsymbol{\tau}_s^s + \boldsymbol{\tau}_r^s \tag{5.11}$$

Taking the heave motion as an example, the hydromechanic forces are written as follows:

$$m\ddot{z}_{sd}^s = -a_z\ddot{z}_{sd}^s - b_z\dot{z}_{sd}^s - c_z z_{sd}^s \tag{5.12}$$

or rewritten as:

$$(m_z + a_z)\ddot{z}_{sd}^s + b_z\dot{z}_{sd}^s + c_z z_{sd}^s = 0 \tag{5.13}$$

Where m_z is the mass coefficient, a_z is the added mass coefficient, b_z the potential damping coefficient c_z is the restoring coefficient. In matrix form, considering surge heave and pitch the kinetic equation looks like:

$$(M + A)\ddot{\boldsymbol{\eta}}_{sd}^s + B\dot{\boldsymbol{\eta}}_{sd}^s + C\boldsymbol{\eta}_{sd}^s = 0 \tag{5.14}$$

Where A is the added mass matrix, B is the potential damping matrix and C is the restoring matrix. Note that only linear potential damping is assumed, while the forces resulting from non-linear viscous damping are assumed to be zero, as they are deemed small compared to potential damping. However, note that for some motions such as roll motion, viscous effects can not be ignored [33].

The restoring coefficient can be obtained using static floating stability equations and the frequency-dependent added mass coefficient and potential damping coefficient can be obtained in a forced oscillation test [33]. Another option is to use some potential theory based software program such as Ansys Aqua to obtain the required coefficients. The first option is not practically feasible in the time frame of this Thesis. But Ansys Aqua is used to obtain an initial estimate of these coefficients.

Wave exciting forces and moments
The wave exciting forces and moments consist of the following forces:

- **Froude Krylov force** $\boldsymbol{\tau}_{fk}^{s}$ is the force acting on the body as if the body was transparent. In other words, the force on the body due to the undisturbed wave velocity potential $\frac{\partial \Phi_w}{\partial t}$.
- **Diffracting force** $\boldsymbol{\tau}_{d}^{s}$ is the force resulting from the diffracted velocity potential $\frac{\partial \Phi_d}{\partial t}$ due to the presence of the body in the waves.

Froude Krylov force The undisturbed wave potential for deep water was given in Chapter 3 and is repeated below:

$$\Phi_w = \frac{\zeta_a g}{\omega} e^{-kz^n} sin(kx^n - wt) \tag{5.15}$$

For simple geometric structures consisting of box-shaped sections, the Froude-Krylov forces resulting from this undisturbed wave potential can still be analytically calculated even by hand, using Equation 5.10 and Equation 5.8.

Diffracting force The disturbed wave potential can be obtained using various 2D potential theory methods such as the Theory of Ursell, Conformal Mapping, the theory of Tasai, or Frank's pulsating source theory [33], which remain outside the scope of this thesis. Furthermore, 3D theories can be used such as diffracting theory.

The resulting kinetic equation looks like:

$$(M + A)\ddot{\boldsymbol{\eta}}_{sd}^{s} + B\dot{\boldsymbol{\eta}}_{sd}^{s} + C\boldsymbol{\eta}_{sd}^{s} = \boldsymbol{\tau}_{fk}^{s} + \boldsymbol{\tau}_{d}^{s}, \tag{5.16}$$

where the left side of the equation is resulting from the inertial forces and the hydro-mechanical forces and moments while the right side is the result of the wave exciting forces and moments.

Conclusion In summary, the kinetic equations of the linear mass-spring-damper vessel model are now obtained, which can be used to compute the motion response of the USV in waves. The vessel's motion response to a regular wave for each DOF is described by a harmonic function that oscillates with the wave frequency. The forces acting on the USV include the hydrostatic restoring force, the radiative force, the Froude Krylov force, and the diffracting force. However, it was found that obtaining the radiative force and the diffracting force is challenging without the use of experiments or software programs like Ansys Aqua. Since experiments are not practically feasible, Ansys Aqua is used.

Ansys aqua can also be used to compute the motion RAOs, which can be used to compute the motion response of the USV without requiring the kinetic equations. This approach is less complex and is therefore chosen in this thesis. The approach is discussed in the next section.

5.3. USV motions using RAOs

This section describes the motion for the USV in regular and irregular waves using motion RAOs.

5.3.1. Motion RAOs

It is possible to obtain a linear transfer function that maps the wave elevation level to the motion response amplitude. The transfer function consists of a frequency-dependent gain and a phase shift and is referred to as a RAO. Taking the heave motion as an example, the gain is denoted with $\frac{z_a}{\zeta_a}(\omega)$ and the phase shift is denoted with $\epsilon_{z,\zeta}(\omega)$. The transfer functions of DOF can be found by solving the kinetic equation for each state:

$$(-\omega^2(M_{ij} + A_{ij}(\omega)) + i\omega B_{ij}(\omega) + C_{ij}) \cdot \eta^s_{sd,j}(\omega) = \tau^s_{w,i}(\omega), \quad for\ i = 1, ..., 3\ ,\ j = 1, ..., 3 \tag{5.17}$$

Ansys Aqua This thesis utilizes Ansys Aqua to compute the motion RAOs. Ansys Aqua uses a BEM to calculate the RAOs using Green's theorem [3]. In a BEM, the surface of a structure is discretized into a set of elements, and the governing equations are solved for each element to obtain an overall solution [3]. Appendix C provides instructions on setting up an Ansys model and obtaining the RAOs.

5.3.2. Motion in regular waves

Given an RAO, the response of the USV to a certain wave can be easily computed. Taking heave again as example, rewriting Equation 5.18 using the RAO, results in:

$$\begin{aligned} z^s_d &= -\zeta_a \frac{z_a}{\zeta_a}(\omega) cos(\omega t - \epsilon_{z,\zeta}(\omega)), \\ \dot{z}^s_d &= -\omega\zeta_a \frac{z_a}{\zeta_a}(\omega) sin(\omega t - \epsilon_{z,\zeta}(\omega)), \\ \ddot{z}^s_d &= \omega^2\zeta_a \frac{z_a}{\zeta_a}(\omega) cos(\omega t - \epsilon_{z,\zeta}(\omega)), \end{aligned} \tag{5.18}$$

5.3.3. Motion in irregular waves

Similarly to irregular waves that are generated using a wave spectrum $S_\zeta(\omega)$, a motion response spectrum can be obtained. The heave response spectrum is given by:

$$S_z(\omega) = |\frac{z_a}{\zeta_a}(\omega)|^2 S_\zeta(\omega) \tag{5.19}$$

where the heave amplitude samples to construct the response to an irregular wave are then given by:

$$z_{a,m} = \sqrt{2S_z(\omega_m)\Delta\omega}. \tag{5.20}$$

In order to construct the USV motion response to irregular waves, a superposition is made of its responses to a spectrum of regular waves, similar to the construction of an irregular wave spectrum described in Section 3.4.1. The following equation shows the irregular USV heave response:

$$z^s_{sd} = \sum_{m=1}^{N} -z_{a,m} cos(\omega_m t - \epsilon_{z,\zeta}(\omega_m) + \epsilon_m), \tag{5.21}$$

Conclusion The first output of the USV model was the motion response of the USV in both regular and irregular waves. This has been obtained using RAOs obtained in Ansys Aqua, which translate the motion of the waves to the motion of the vessel.

5.4. Docking goal state

The AUV does not dock at the $\{d\}$ frame, but at $\{g\}$ frame as shown in Figure 2.3. This section describes how to determine the state of the $\{g\}$ frame with respect to the $\{d\}$ frame. The following assumptions are made:

- The $\{g\}$ frame translated with a vector $\boldsymbol{r}^d_{gd} = [x^d_{gd}, z^d_{gd}]^T$.
- The $\{g\}$ frame rotated with an angle $\Theta^d_{dg} = \theta^d_{dg}$ relative to the $\{d\}$ frame. Note that this angle is zero for the horizontal oriented vertical approach.
- The $\{g\}$ frame is fixed in place with respect to the $\{d\}$ frame. As such the derivatives of the translation vector and rotation angle are zero

Given these assumptions the goal position and orientation in the $\{n\}$ frame is given by:

$$\boldsymbol{\eta}^n_{ng} = \begin{bmatrix} \boldsymbol{p}^n_{ng} \\ \Theta_{ng} \end{bmatrix} = \begin{bmatrix} \boldsymbol{p}^n_{nd} + R^n_d \boldsymbol{r}^d_{gd} \\ \Theta_{nd} + \Theta_{dg} \end{bmatrix}. \tag{5.22}$$

The goal linear and angular velocity are obtained by taking the derivative of the goal position and orientation:

$$\boldsymbol{\nu}^n_{ng} = \begin{bmatrix} \dot{\boldsymbol{p}}^n_{ng} \\ \dot{\Theta}_{ng} \end{bmatrix} = \begin{bmatrix} \dot{\boldsymbol{p}}^n_{nd} + \dot{R}^n_d \boldsymbol{r}^d_{gd} + R^n_d \dot{\boldsymbol{r}}^d_{gd} \\ \dot{\Theta}_{nd} + \dot{\Theta}_{dg} \end{bmatrix} = \begin{bmatrix} \dot{\boldsymbol{p}}^n_{nd} + \dot{R}^n_d \boldsymbol{r}^d_{gd} \\ \dot{\Theta}_{nd} \end{bmatrix}, \tag{5.23}$$
$$\dot{R}^n_d = \omega^n_{nd} \begin{bmatrix} -sin(\theta_{nd}) & cos(\theta_{nd}) \\ -cos(\theta_{nd}) & -sin(\theta_{nd}) \end{bmatrix}.$$

Finally, the goal linear and angular acceleration are obtained by taking the second derivative of the goal position and orientation:

$$\dot{\boldsymbol{\nu}}^n_{ng} = \begin{bmatrix} \ddot{\boldsymbol{p}}^n_{ng} \\ \ddot{\Theta}_{ng} \end{bmatrix} = \begin{bmatrix} \ddot{\boldsymbol{p}}^n_{nd} + \ddot{R}^n_d \boldsymbol{r}^d_{gd} + 2\dot{R}^n_d \dot{\boldsymbol{r}}^d_{gd} + R^n_d \ddot{\boldsymbol{r}}^d_{gd} \\ \ddot{\Theta}_{nd} + \ddot{\Theta}_{dg} \end{bmatrix} = \begin{bmatrix} \dot{\boldsymbol{p}}^n_{nd} + \ddot{R}^n_d \boldsymbol{r}^d_{gd} \\ \ddot{\Theta}_{nd} \end{bmatrix}, \tag{5.24}$$

here $\ddot{R}^n_d$ is given by:

$$\ddot{R}^n_d = \dot{\omega}^n_{nd} \begin{bmatrix} -sin(\theta_{nd}) & cos(\theta_{nd}) \\ -cos(\theta_{nd}) & -sin(\theta_{nd}) \end{bmatrix} + (\omega^n_{nd})^2 \begin{bmatrix} -cos(\theta_{nd}) & -sin(\theta_{nd}) \\ sin(\theta_{nd}) & -cos(\theta_{nd}) \end{bmatrix}. \tag{5.25}$$

Conclusion The second output of the USV is the motion of the DS. This output has been obtained by the transformation functions that map the position, velocity, and acceleration of the USV to those of the DS defined at the docking goal state. With this, the USV model can now simulate both the USV motion as well as the DS motion.

5.5. Model fitting and verification

Verification of the box-shaped USV model involves a series of checks and controlled simulations. First, a mesh convergence study is conducted to verify the solution produced by Ansys Aqua. Second, the remaining unverified assumptions outlined in Section 5.2.1 are addressed. Finally, a visual analysis of the USV motions is done to verify the model is correctly implemented.

5.5.1. Model specifications

The specifications of the box were derived from the DUS V5750 USV developed by Demcon [72], although it should be noted that the DUS v5750 has a different shape compared to the box-shaped USV model. Therefore, it was aimed to balanance maintaining a similar mass and keeping the overall dimensions comparable. The specifications of the box-shaped USV are provided in Table 5.2.

Table 5.2: General USV specifications

Description	Symbol	Value
USV length	L_{usv}	5m
USV width	W_{usv}	1.5m
USV height	H_{usv}	1.3m
USV draft	d_{draft}	0.3m
USV Distance CG to CO	r^d_{dg}	$[0,\ 0]$m
USV Distance CB to CO	r^d_{db}	$[0,\ 0.15]$m
USV mass	m_{usv}	2306kg
USV inertia around y-axis	$I_{y,usv}$	5412kg m^2

5.5.2. Ansys Aqua mesh convergence study

A mesh convergence study was conducted to assess the stability and accuracy of the RAOs obtained from Ansys Aqua. The goal was to determine if the RAOs converge to a consistent plot and remain relatively unchanged as the element size of the mesh is varied. This analysis helps identify any potential inaccuracies in the solution and ensures that the obtained RAOs are reliable.

To compute the RAOs, a wave period range must be selected for evaluation. In the case of the sea states defined in Section 3.4.3, the wave period ranges from 3.5 to 10.5 s. For regular waves, the USV will have a motion response with the same periods. However, for irregular waves, some wave energy will also be present at smaller periods. Therefore, it is important to calculate the RAOs for these periods as well. As the wave energy shifts to higher frequencies for smaller waves in the JONSWAP spectrum [33], sea state 1, has the most energy at small wave periods. By integrating the wave energy density spectrum it was apparent that only 0.26 % of the total wave energy is present in the period range of $0-1$ s. For the largest wave of sea state 12, almost no energy is present after 30s. Therefore, it is chosen to evaluate the RAOs for a period range of $1-30$ s. The obtained RAOs of the box-shaped USV for different mesh sizes are presented in Figure 5.2.

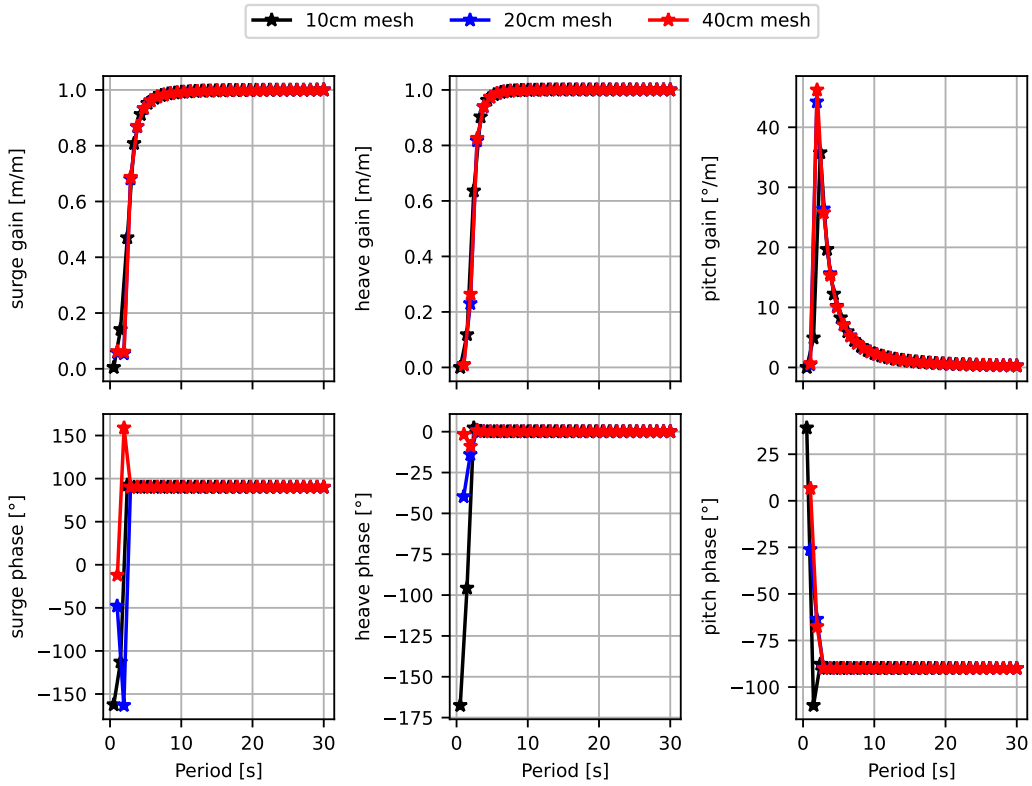

Figure 5.2: The RAO of the boxed-shaped USV for evaluated for different mesh sizes.

Figure 5.2 shows that the RAO solution for the different mesh sizes is quite similar, indicating good convergence for these values. However, some variations are observed in the phase plots at small periods. This may be caused by under-sampling at these periods as the data points for the different mesh sizes are not taken at the exact same intervals. Additionally, it is possible that the solution is not converged at these smaller periods.

Despite the observed variations in the phase plot at small periods, the low RAO gain at these frequencies suggests that the motion response of the USV at these periods is small and is dominated by other irregular wave components. Additionally, considering that 90 % of the wave energy in sea state 1 exists above a period of 2.5 seconds, the motion response of the USV at these small periods is assumed to be negligible.

Moreover, the solution seems to be converged for most of the desired period range, therefore, the obtained RAOs are accepted. As a result, the RAO obtained using a 10 cm mesh is exported to Python and utilized in the simulation.

5.5.3. USV small rotation assumption

The assumption that the body fixed frame $\{d\}$ will only rotate small angles from the $\{s\}$ frame (Assumption 1) is verified by checking the maximum pitch angle of the USV at each sea state, as shown in Table 5.3. Table 5.3 shows the maximum obtained angle of the USV for each of the sea states. All maximum pitch angles are within the small angle assumption limit of $11.5°$.

Table 5.3: The maximum angle of the USV at the different sea states for regular waves.

Sea state	1	2	3	4	5	6	7	8	9	10	11	12
Maximum Angle $[°]$	4.7	5.3	5.3	6.1	7.4	9.0	9.4	9.0	9.2	9.6	10.0	10.8

5.5.4. Scout-USV multibody interaction verification

To verify Assumption 4 that the wave forces acting on the AUV and the USV are decoupled, a multibody hydrodynamic diffraction study was conducted in Ansys Aqua. Two multibody scenarios were constructed, in which the Scout was located closely underneath the USV at two different depths of 1 m and 2 m, as shown in Figure 5.3. In order to access if wave forces acting on the two vehicles are independent of each other, the following tests were done to observe the differences in RAOs:

- The Scout is tested individually at depths of 1 m and 2 m without the USV.
- The USV is tested without the presence of the Scout.
- The USV and the Scout are tested together, with the Scout located at a depth of 1 m and 2 m.

Figure 5.4 displays the Lobster Scout's RAOs at different depths, both with and without the USV. Figure 5.5 depicts the RAOs of the USV both with and without the Scout at various depths.

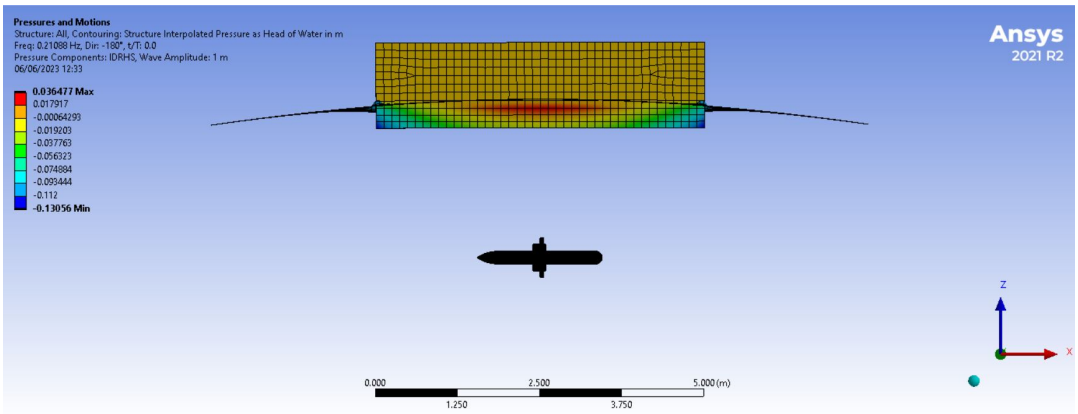

Figure 5.3: The multibody scenario, the Scout is positioned underneath the USV at a depth of 1 m and 2 m.

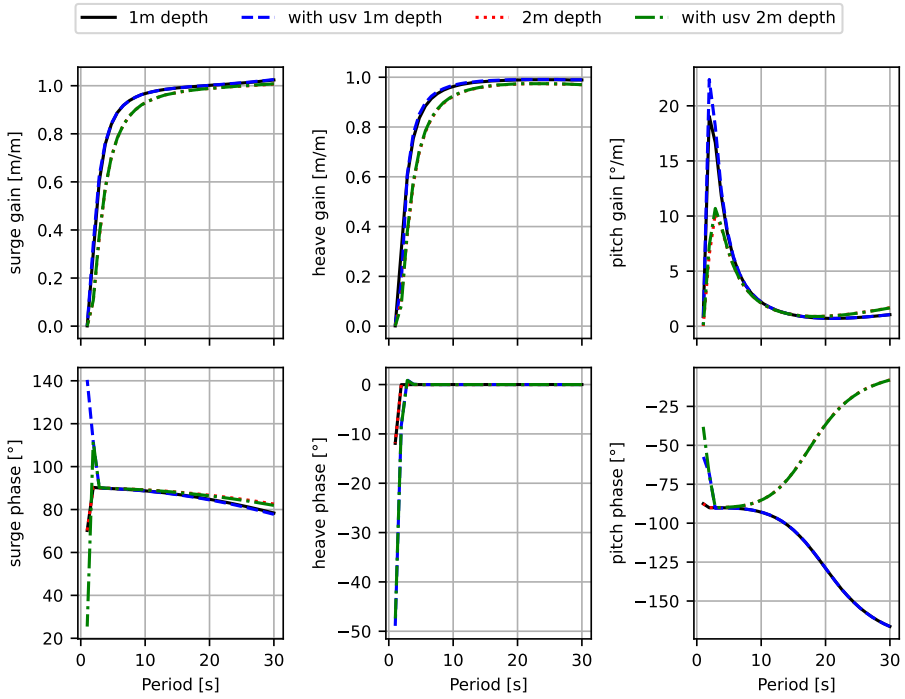

Figure 5.4: The RAO of Lobster Scout at different depths with and without the presence of the USV above the Scout. The blue and black lines overlap as well as red and green lines.

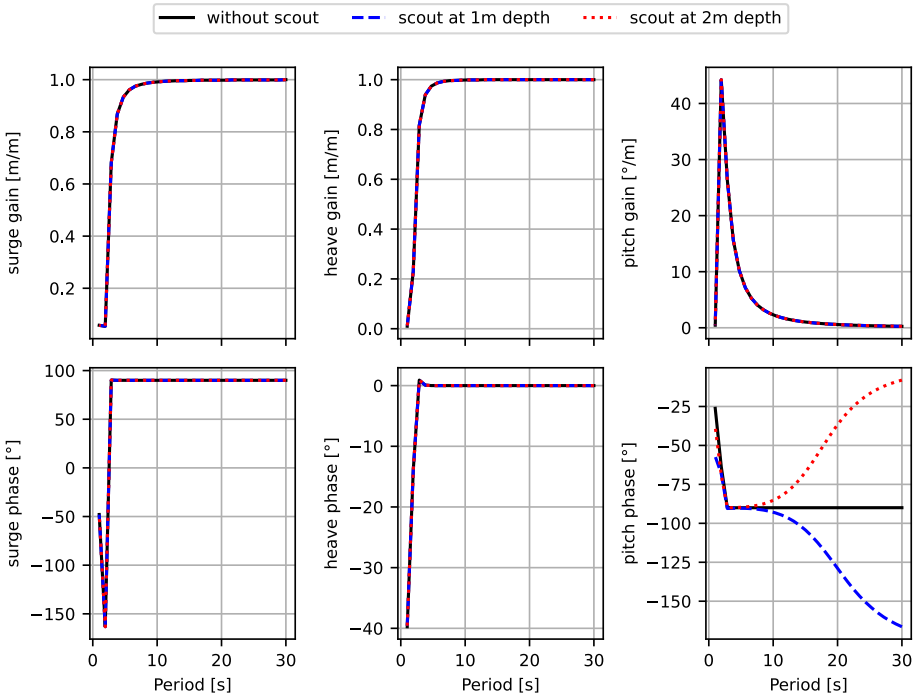

Figure 5.5: The RAO of the boxed-shaped USV with and without the presents of the Scout underneath the USV at different depths.

From Figure 5.4 it is clear that the RAOs for the Scout do not change significantly due to the presence of the USV. Furthermore, the surge and heave RAOs and the pitch gain for the USV also show no significant change. However, it can be seen that the pitch phase of the USV is significantly impacted

by the presence of the Scout. This was not investigated further, therefore, it remains unclear whether this results from inaccuracies of the solution or that this results from the coupling of wave forces.

5.5.5. Visual analysis

In order to evaluate whether the USV model is correctly implemented in Python, the motion obtained in the simulation was visually compared to the pressures and motion result of Ansys Aqua (further explained in Appendix C). The USV has been initialized at $x^n_{na} = 0.0$ m, 3.0 m, 6.0 m, 10.0 m. The other states are then automatically calculated. Figure 5.6 shows an example of the motion of the USV in the Python animator versus the pressures and motions result of Ansys Aqua for the same period amplitude combination. By initializing the USV at different surface coordinates ($z^n_{nd} = 0$ m), it was confirmed that the USV:

- The overall motion of the USV is correct.
- The USV moves with approximately the correct amplitude.
- The USV takes into account the phase of the wave.
- The DS moves correctly underneath the USV.

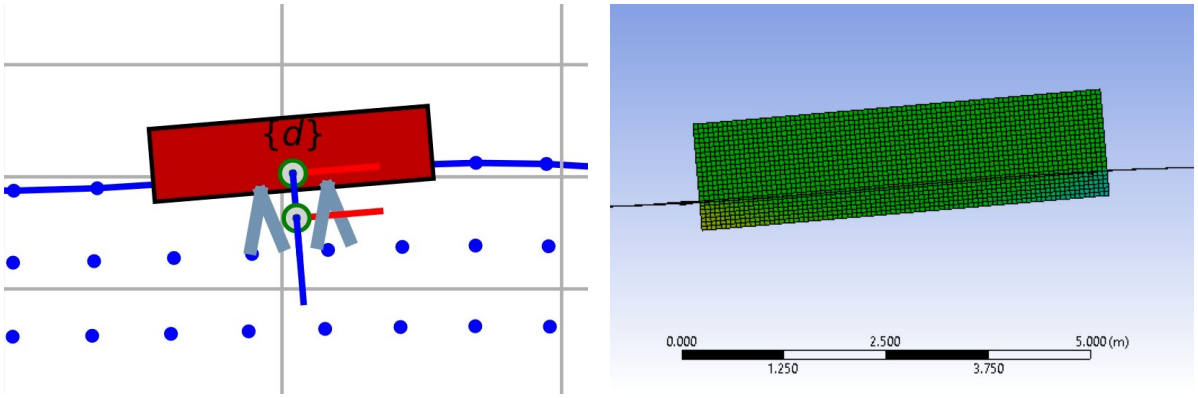

(a) Python animator. The red box represents the USV, the gray forks represent the cradle forks, the $\{d\}$ frame and the $\{g\}$ frame are shown underneath each other

(b) Ansys pressures and motions result

Figure 5.6: USV motions for $T = 3.37$ s, $\zeta_a = 0.25$ m at approximately the same phase angle.

Figures 5.7 display the USV response to regular and irregular waves, respectively. The clickable QR codes next to each sub-figure link to an animation showing the Scout's response.

Animation

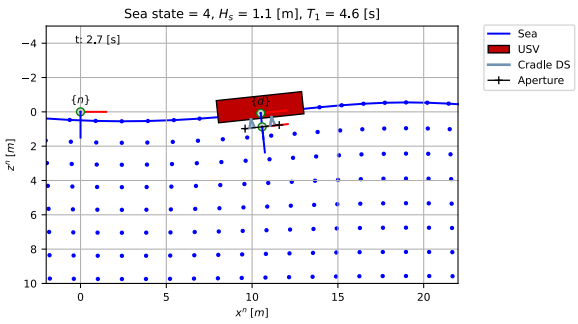

(a) USV response to a regular wave disturbance.

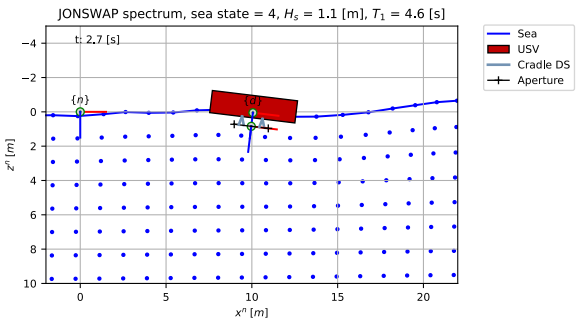

(b) USV response to an irregular wave disturbance.

Animation

Figure 5.7: Motion response of USV model.

5.6. Conclusion

The objective of this chapter was to develop a model capable of simulating the motions of the USV and the DS in North Sea waves. The main contributions of this chapter are:

- It was found that the USV can be modelled using a linear mass-spring-damper model. An overview of the kinematic and kinetic equation governing the motion of the USV was given.
- It was found that obtaining radiative and diffracting forces is challenging, which led to the use of Ansys Aqua to compute the motion RAOs. These motion RAOs were used to simulate the motion response of the USV to regular and irregular North Sea waves.
- The pose velocity and acceleration of the docking goal state located at $\{g\}$ with respect to the USV body-fixed frame $\{d\}$ was obtained using various transformations.
- Finally the model was verified. A mesh convergence study was done for Ansys Aqua, to verify that the numerical solution is accurate. The critical small rotation assumption required for linearity was verified and it was verified that interaction due to wave diffraction between the scout and the USV was minimal. Finally, it was visually confirmed that the motion response of the USV was correct for both regular and irregular waves.

One of the main limitations of the USV model of the DUS V5750 USV developed by Demcon [72] is approximating it as a simple box, resulting in inaccurate motions. Furthermore, there remains some uncertainty that the wave forces acting on the USV and the Scout are indeed mostly decoupled, which is required for the validity of the model. Future research can address these limitations.

This chapter also completes the answer to the research question *How can the vertical docking system be modelled?*. The ocean conditions were limited to waves and modelled using linear velocity potential wave theory. The Lobster Scout was modelled using a sea-keeping AUV model. The USV was modelled as a free-floating box which dimensions were roughly based on the DUS V5750 USV [72] using a linear mass-spring-damper model. Finally, the USV motions could be transformed to obtain the motions of the DS.

6

Docking performance

To determine to what extent a vertical docking approach of the Lobster Scout to a USV is viable in rough seas, it is crucial to determine the definition of a docking attempt and how to evaluate docking performance. This evaluation method is important in later chapters for determining the effectiveness of vertical guidance methods and investigating the influence of navigation parameters on docking performance. Therefore, the objective of this chapter is to define a performance evaluation method of the vertical docking approach. The main research question to be answered in this chapter is:

How to evaluate vertical docking performance?

Figure 6.1 provides an overview of the performance evaluation method. The AUV state and the DS state are required inputs to evaluate the vertical docking performance. A probability distribution method is used to evaluate docking performance. The evaluation outputs are an indication of the maximum operational sea state and the annual operational up-time of the AUV-USV combination given for a given DS design, GNC method, and required success probability.

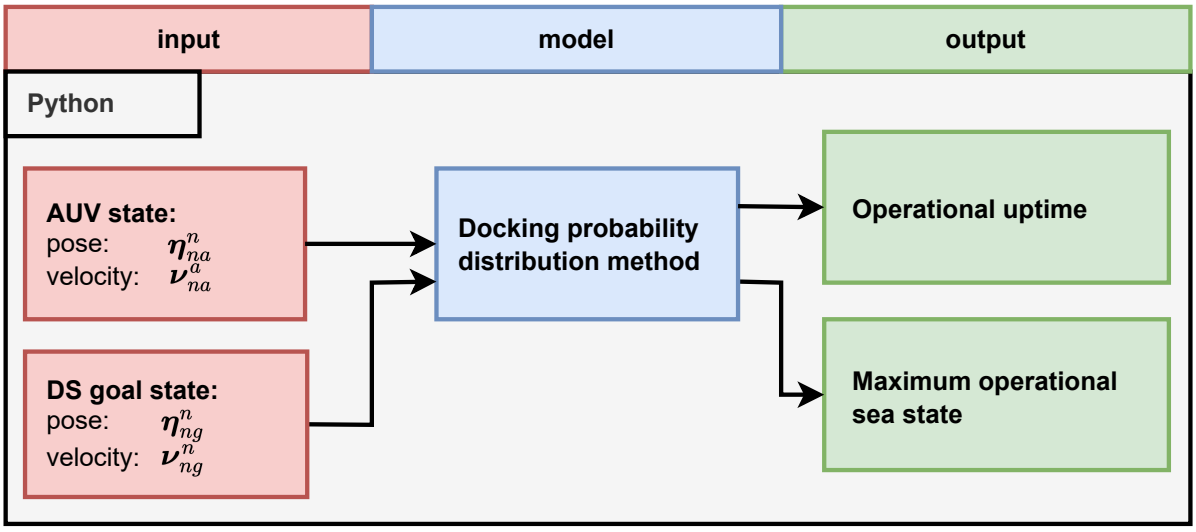

Figure 6.1: An input-output diagram of the docking performance evaluation method.

This chapter is structured as follows: Section 6.1 describes a successful docking attempt in reality. Based on this description, Section 6.2 discusses several docking performance evaluation methods, and the probability distribution based evaluation method is selected for this thesis. Section 6.3 elaborates on this method and finally, a conclusion is drawn in Section 6.4.

6.1. A successful docking attempt in reality

In reality, a successful dock can be defined as the engagement of the latching mechanism to lock the AUV in the DS without causing damage to either in the docking process. However, the latch mechanism can only engage if the relative error between the latch mechanisms on the AUV and the DS falls within a predefined maximum error margin. Furthermore, since the latching action is not instantaneous, the AUV needs to maintain this error margin for a certain amount of time to allow the latch to properly lock. Finally, to avoid any damage to the system, the AUV must not crash into the DS or the USV during the docking process.

The cradle capture mechanism as discussed in Section 2.3.5, can facilitate the alignment of the AUV with the latch, thereby reducing the required accuracy of the AUV controller for successful docking. Damping material can be attached to this cradle to dissipate the impact energy during entry. The cradle forks then guide the AUV to the latch, thereby gradually decreasing the relative surge and heave errors between the latch mechanisms. Finally, a small relative pitch angle between the AUV and the DS is diminished as the AUV makes contact with the bottom of the cradle after which the AUV is locked.

6.2. Evaluation methods for docking success probability

The objective of any docking system is to obtain the largest docking success probability. This section evaluates three methods for defining a docking attempt and for evaluating the dock success probability. Ultimately, the probability distribution-based method was selected.

6.2.1. Docking success probability

The performance of the vertical docking approach is measured by the sea state it can successfully dock in, which is an important indicator of the AUV-USV combination's operational employability. However, docking success is assumed to be probabilistic, as both the irregular wave model (Chapter 3) and the navigation model (Chapter 8) contain random variables. A sufficiently large sample size is necessary to confidently estimate the probability of successful docking for any vertical GNC method. Consequently, a significant number of simulations are required to obtain the docking success probability across a wide range of methods and scenarios.

6.2.2. Binary success conditions method

One approach to defining a docking attempt is to establish a set of binary docking conditions. An estimate of the success probability can be obtained by the ratio between successful docks and failed docks over a certain simulation sample size.

Single condition method A single condition for defining a successful docking attempt is when the AUV enters the capture aperture. The capture aperture is modelled with tolerance margins around the docking goal state, and reaching the goal state within these margins is necessary for a successful dock. Several studies on docking have used this as the only condition for success [79, 20, 73].

Set of conditions method A set of binary success conditions can be used to more accurately model a successful dock in reality. An example of such a set is given below and illustrated in Figure 6.2, where the moment of latching is considered the moment of success:

- **Docking error condition** The latch mechanism is capable of locking the AUV only within a specific tolerance space, which can be modelled using a similar tolerance condition as before.
- **Impact condition** The system is damaged if the impact force is too large [15]. A successful dock requires that the impact force of the dock should not exceed the maximum allowed impact force.
- **Latch time condition** The locking mechanism does not close instantaneously. A successful dock requires that the AUV should remain within the error margins for a minimum time duration.

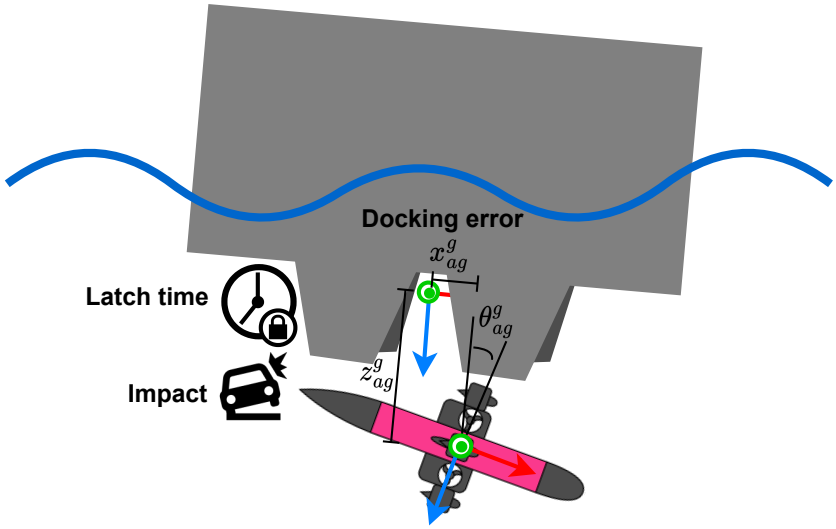

Figure 6.2: The docking conditions visualized

Evaluation The two binary condition methods described above can be used to closely approximate a real successful docking attempt. However, a major limitation of defining a docking attempt based on binary conditions is that it leads to an unmanageably large number of simulations. The success probability of a vertical docking method is highly dependent on the strictness of the binary conditions, which is directly related to the exact design of the cradle DS. Therefore, using this method to determine to what extent vertical docking is viable in rough seas would require to evaluate a range of DS designs. Running simulations for this additional dimension across a broad range of methods and scenarios makes this an unsuitable approach for vertical docking evaluation.

To demonstrate the unmanageable number of simulations required, consider a sample size of 60, necessary to obtain a reliable success probability estimate for a single scenario. For a single DS design, the number of scenarios can be estimated as 12 sea states, multiplied by 100 GNC methods with varying parameters, resulting in a total of $60 * 12 * 100 = 72000$ simulations. Each simulation requires approximately 10 seconds to run on the author's laptop, therefore, to evaluate each DS design, it would take a total of roughly 200 hours of simulation time. This indicates it becomes impractical to evaluate multiple DS designs. To address this, future research could utilize more powerful cloud computing or cluster computing resources available at the Delft University of Technology, as well as further run-time optimization of the program.

An additional problem with the second method, which takes the moment of latching as the moment of success, is that the impact dynamics that result from the cradle's ability to align the AUV with the latch should be taken into account, which are challenging to model [86].

6.2.3. Entry quality score method

In [16], a different method for evaluating docking is presented, which compares various docking guidance methods in ocean currents. Unlike binary success conditions, this method uses a continuous docking quality score to evaluate performance. The quality score is calculated using a weighted sum of the AUV's momentum loss during entry, resulting from collisions with the DS, and the deviation of the entry pose from the ideal pose. The docking success probability can be determined by setting a threshold for the entry quality score.

Evaluation The main advantage of this method is that it enables a straightforward comparison of the performance of different docking GNC methods using a single quality score. However, a limitation of this approach is that it still necessitates modelling the impact dynamics, which can vary depending on the cradle design. Similar to the binary condition method, this equates to approximately 200 hours of simulation time per DS design. Furthermore, although the simplicity of using a single score is conve-

nient for comparison purposes, it may result in a loss of nuance regarding the actual success probability, given that the weights used to calculate the quality score are chosen arbitrarily.

6.2.4. Probability distributions method

In this method, illustrated in Figure 6.3, the definition of a docking attempt is defined as the moment when the AUV enters the capture mechanism at the capture aperture ($z^g_{ag} = 0$). It is assumed that given favorable entry conditions, the capture mechanism can align the AUV with the latch, thereby eliminating the need to model the latch or impact dynamics of the dock. The impact is evaluated based on the relative kinetic energy of the DS and the AUV while crossing the capture aperture, instead of the momentum loss or impact force.

In order to directly relate the performance of a vertical docking approach to the success probability, the docking surge error x^g_{ag}, pitch error θ^g_{ag}, and relative kinetic energy K_{dock} are recorded over multiple docking attempts and fitted with a suitable probability distribution. The probability of a successful dock for any DS cradle design can now be efficiently evaluated by calculating the ratio between the area under the distribution curve that falls within the cradle capture limits and the total area of the distribution.

To the best of the author's knowledge, this method has not yet been utilized in the field of docking.

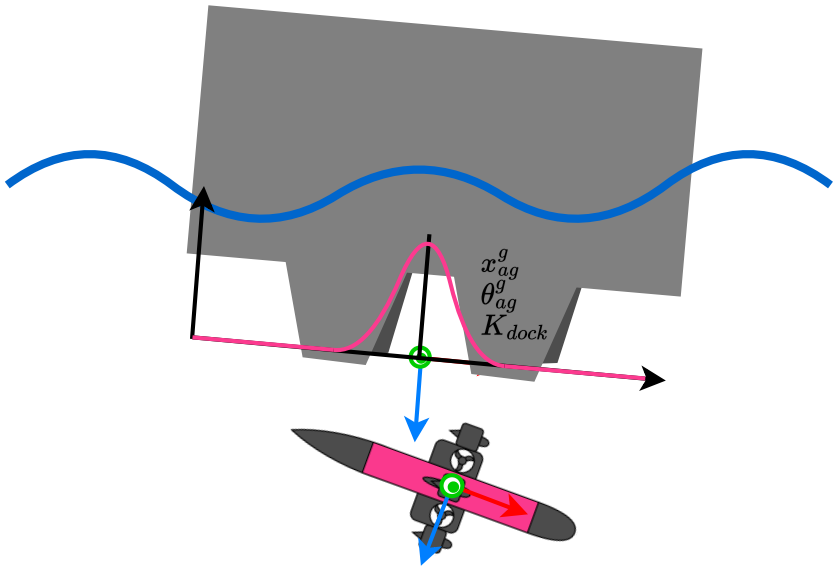

Figure 6.3: The docking performance visualized

Evaluation This method has several advantages. The key advantage is that the success probability of any cradle design can be determined by obtaining the docking probability distribution for each GNC method. This reduces the number of simulations needed to compare different DS designs significantly, as it will only take approximately 200 hours of simulation to evaluate the success probability for all DS designs.

A limitation of this method is that it relies on the assumption that the capture mechanism can align the AUV with the latch under favorable entry conditions, which will not always be true in practice [37].

Conclusion It is required to evaluate a range of DS designs to determine to what extent vertical docking is viable in rough seas, as the DS design significantly impacts the docking success probability. The probability distributions method was chosen mainly because it requires only an estimated 200 hours of simulation time to evaluate all DS designs over a range of scenarios, in contrast to 200 hours per DS design for the binary conditions method and the entry quality score method.

6.3. Probability distribution based performance evaluation

This section provides further explanation of the probability distribution-based evaluation method.

6.3.1. Docking attempt registration

A docking attempt should be registered when the heave error z^g_{ag} between $\{a\}$ and $\{g\}$ is zero and should then record the surge error, pitch error, and kinetic impact energy. The error vector $\boldsymbol{\eta}^g_{ag}$ between the AUV state and the goal state in the $\{g\}$ frame is given by:

$$\boldsymbol{\eta}^g_{ag} = R^g_n(\theta^n_{ng})(\boldsymbol{\eta}^n_{na} - \boldsymbol{\eta}^n_{ng}). \tag{6.1}$$

The kinetic impact energy is defined as the kinetic energy between the goal state and the state of the AUV when $z^g_{ag} = 0$. The kinetic impact energy is given by:

$$K_{dock} = 0.5(\boldsymbol{\nu}^a_{na} - \boldsymbol{\nu}^a_{ng})^T M_{RB}(\boldsymbol{\nu}^a_{na} - \boldsymbol{\nu}^a_{ag}), \tag{6.2}$$

where $\boldsymbol{\nu}^a_{na}$ and $\boldsymbol{\nu}^a_{ng}$ are the velocities of the AUV and the docking goal respectively expressed in $\{a\}$, and M_{RB} is the generalized inertia matrix of the AUV described in Chapter 4. Note that the added mass of the AUV is not considered in this definition of kinetic impact energy.

Through visual observation and by recording and evaluating z^g_{ag} for 200 simulations, it is confirmed that the docking attempts are correctly registered when the Scout crosses the line located at the capture aperture of the dock. Figure 6.4 displays a snapshot of this moment and the corresponding animation can be seen by scanning or clicking the QR code.

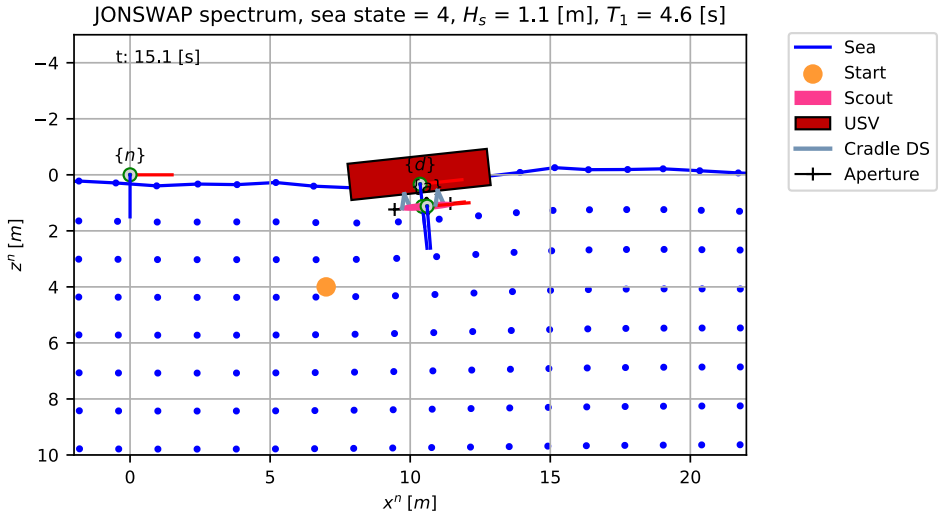

Animation

Figure 6.4: A snapshot of the AUV at the moment of entering the capture aperture.

6.3.2. Shapes of the docking probability distributions

In order to determine the shape of the probability distribution for surge error, pitch error, and kinetic impact energy, a large sample of 200 simulations was collected over a range of sea states. These simulations utilized irregular waves and position control (Section 7.2.1). Figure 6.5 presents this data in histograms and presents the fitted probability distributions to this data.

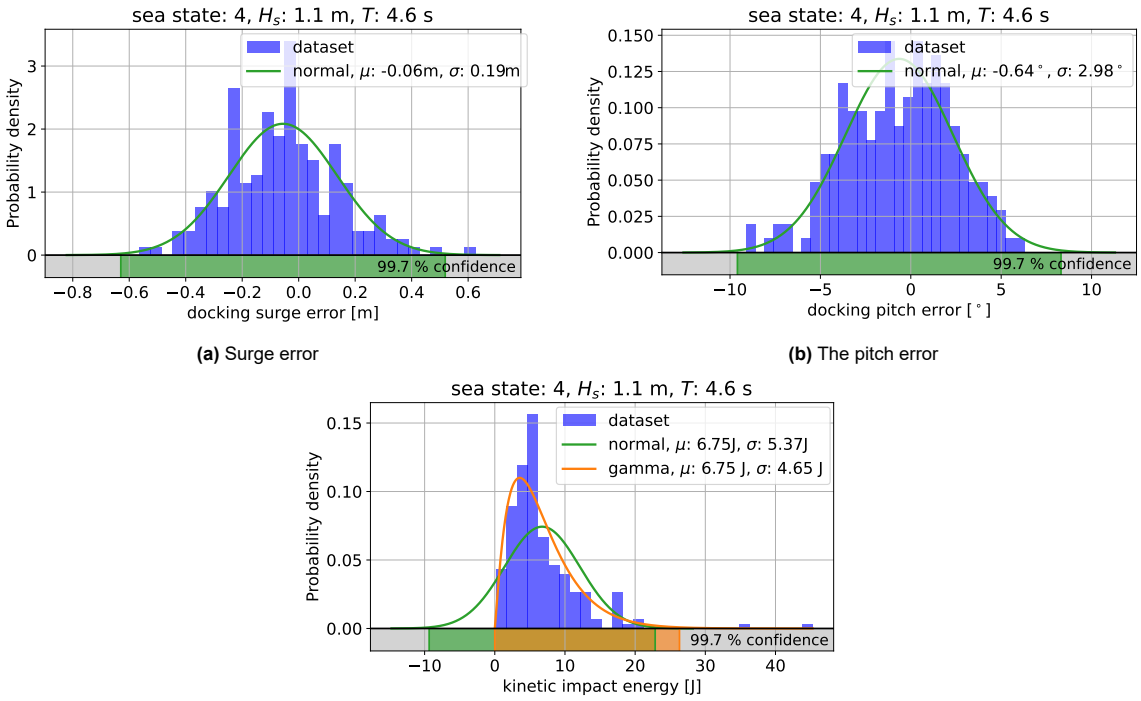

(a) Surge error

(b) The pitch error

(c) Kinetic impact energy, represented by a gamma distribution.

Figure 6.5: The docking probability distributions for 200 docks at sea state 4. The data is represented in a histogram consisting of 30 bins. The 95 % confidence interval is displayed below the zero probability density line.

Figure 6.5a and Figure 6.5b show that the surge error and pitch error dataset are well fitted with a normal distribution $N(\mu, \sigma)$, where μ is the mean and σ is the standard deviation. The dataset of the kinetic impact energy shown in Figure 6.5c is better captured by a gamma distribution $G(\alpha, \beta)$, where α is the shape parameter and β is the scale parameter. This is because the kinetic impact energy can only be larger than zero and is a function of the squared relative velocity between the AUV and the goal state. For the gamma distribution, the mean and the standard deviation are calculated as:

$$\mu = \alpha\beta, \quad \sigma = \sqrt{\alpha\beta^2}. \tag{6.3}$$

In conclusion, the normal distribution is a good fit for the data sets on the docking surge error and the docking pitch error, while the gamma distribution provides a good fit with the kinetic impact energy.

6.3.3. DS design based on confidence interval

In the previous section, the shapes of the docking probability distributions were determined, which can be used to obtain the requirements of a cradle DS design for a given guidance method, based on the desired sea state with a desired confidence interval. In this study, a 99.7% confidence level was deemed acceptable, which indicates that 997 out of 1000 docking attempts will succeed. This choice is supported by a brief economic analysis.

Let's consider a hypothetical scenario where the AUV-USV combination is heavily utilized, requiring 3 docks per day, and the AUV has a return of investment time of 20 days. All three docking criteria, the docking surge error, the docking pitch error, and the kinetic impact energy need to be met for a successful dock. When failures for each criterion are assumed completely independent from the other criterion, with a 99.7% confidence interval for each of the docking criteria, at most 9 failures per 1000 docks will occur. Under this scenario, a failed dock occurs on average once every 37 days of operation. In a conservative scenario, where it is assumed that a failed dock also results in the loss of the AUV, so options such as aborting and reattempting a docking procedure are not considered, a 1.85x return of investment is expected on the AUV. While an environmental impact assessment in addition to a thorough economic analysis is required, this supports the choice for a 99.7% confidence interval.

The cradle DS requirements for a given guidance method can be designed based on a desired confidence interval. Let's say an DS designer is given the task to build a DS according to a 99.7 % confidence interval up to sea state 4 using pose target state control (Section 7.2.1). The confidence intervals for this scenario are shown in Figure 6.5 and set the following requirements to the DS design:

- The capture aperture of the DS along the surge direction needs to be larger than $[-0.63,\ 0.52]$ m. Taking the largest magnitude, the capture aperture must be 1.26 m.
- The capture aperture needs to align pitch errors between $[-9.6,\ 8.3]^\circ$ Taking the largest magnitude, the capture aperture must align docking pitch errors of around $\pm 10^\circ$.
- The kinetic impact energy that must be safely dissipated without damage by the DS is 26.3 J.

6.3.4. Vertical docking viability

This section describes how to relate the obtained probability distributions to the viability of the vertical docking approach for a given GNC method.

Maximum operational sea state Given a particular DS design, GNC method, and a minimum required success probability, the maximum operational sea state is determined. For the cradle-type DS shown in Figure 2.13, a surge aperture of 1 m, a pitch aperture of $\pm 15^\circ$ and the ability to dissipate up to $30\ J$ ($|\boldsymbol{v}_{ag}^{a}| \approx 0.7\ \frac{\text{m}}{\text{s}}$) of kinetic energy without damaging the DS or the AUV seems realistic. In this study, this DS design is used to compare the maximum operational sea state for each of the GNC methods in Chapters 7 and 8. The maximum operational sea state for this DS is obtained by ensuring that all 99.7 % confidence intervals lie within these constraints. This means that when the AUV-USV combination is operational at this sea state, less than 9 docks per 1000 attempts will fail.

Operational up-time Statistical sea state data is used to relate the maximum operational sea state to the actual operational uptime of the AUV-USV combination in the North Sea. Figure 6.6 presents the number of occurrences of significant wave heights observed throughout 2017 in the Alpha Ventus Offshore Wind Farm located in the North Sea. The uptime percentile for the defined sea states in Table 3.2 is indicated in the legend [8]. While the significant wave height statistics vary across different geographical areas in the North Sea, this figure is used to obtain an estimate of the operational uptime of the USV-AUV combination, given an achieved maximum operational sea state. For instance, for a maximum operational sea state of 6, the AUV-USV combination can operate 82.7 % annually

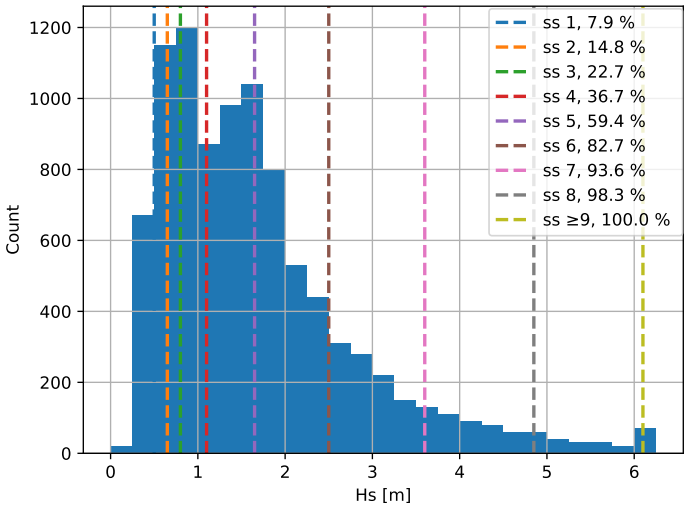

(a) Significant wave height occurrence in Alpha Ventus Offshore Wind Farm in the year 2017 [8]. The uptime percentile is also shown for the sea states from Table 3.2.

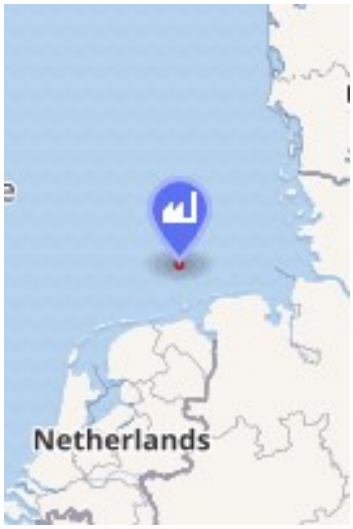

(b) Location of Alpha Ventus Offshore Wind Farm, Image from [80].

Figure 6.6: The operational uptime related to the significant wave height occurrence in the North Sea.

Effectiveness benchmark Ideally, the ability to dock the AUV after returning from a mission does not limit the operational employability of the USV. Therefore, the operating limit of the USV serves as a good comparison benchmark for the effectiveness of the vertical guidance methods.

As detailed in Section 2.3.3, the USV in this thesis was roughly modelled based on the specifications of Demcon's DUS V5750 USV [72]. This particular USV was developed specifically for operating at challenging offshore environments and is capable of surveying up to a significant wave height of 4.5 m. Sea state 8 with a significant wave height of 4.85 m just exceeds the operating limit of this USV and thus serves as a good comparison benchmark for the effectiveness of the vertical guidance methods. The motion of the USV and the irregular waves can be seen by clicking or scanning the QR code.

Animation

6.3.5. Sample size

A sample size should be determined such that the docking probability distributions of the sample accurately reflect the docking probability distribution of the population. Determining the sample size is a trade-off between simulation time and the statistical power of the study.

To determine the sample size, a large number of simulations have been run over a range of sea states using pose control (Section 7.2.1). It was assumed that 200 simulations per sea state would be a sufficiently large sample size to accurately represent the population. Three smaller samples were then obtained from this larger sample, first, by randomly selecting a subset of data points, second, by selecting based on a regular interval, and third, by taking the first X number of data points. The effect size, which is a metric to indicate statistical power, was then determined using Cohen's d test for each of the three samples [13]. Cohen's d test is given by:

$$d = \frac{\mu_1 - \mu_2}{s}, \tag{6.4}$$
$$s = \sqrt{\frac{(n_1 - 1)\sigma_1^2 + (n_2 - 1)\sigma_2^2}{n_1 + n_2 - 2}},$$

where μ_1, σ_1 and n_1 are the mean, the standard deviation, and the sample size of the large sample respectively, while μ_2, σ_2 and n_2 are the corresponding quantities for the three small samples. Furthermore, s is the pooled standard deviation.

A d value smaller than $d < 0.2$ is considered a small effect size which means that the normal distributions mostly overlap, which indicates significant statistical power. Increasing the sample size of the small samples tends to decrease the d value. In this study, the sample size was increased until all samples had a d value of less than 0.2 across the entire range of sea states. Figure 6.7 shows the values of the Cohen's d test for a sample size of 60. All d values across all distributions, except one, were less than 0.2, indicating that the sample size was sufficient. The one exception had a d value that was only slightly larger than 0.2 and was therefore deemed acceptable.

While this statistical power analysis is by no means extensive, it provides some support for the sample size. Time considerations are also a factor as the current simulation time will already reach approximately 200 hours as briefly explained in Section 6.2.4. The goal of this study is to obtain an initial performance indication of the vertical docking approach and is of a more exploratory nature. Therefore the focus of this study lies on identifying large effects while identifying small effects is of less importance. This sample size of 60 is therefore deemed sufficient.

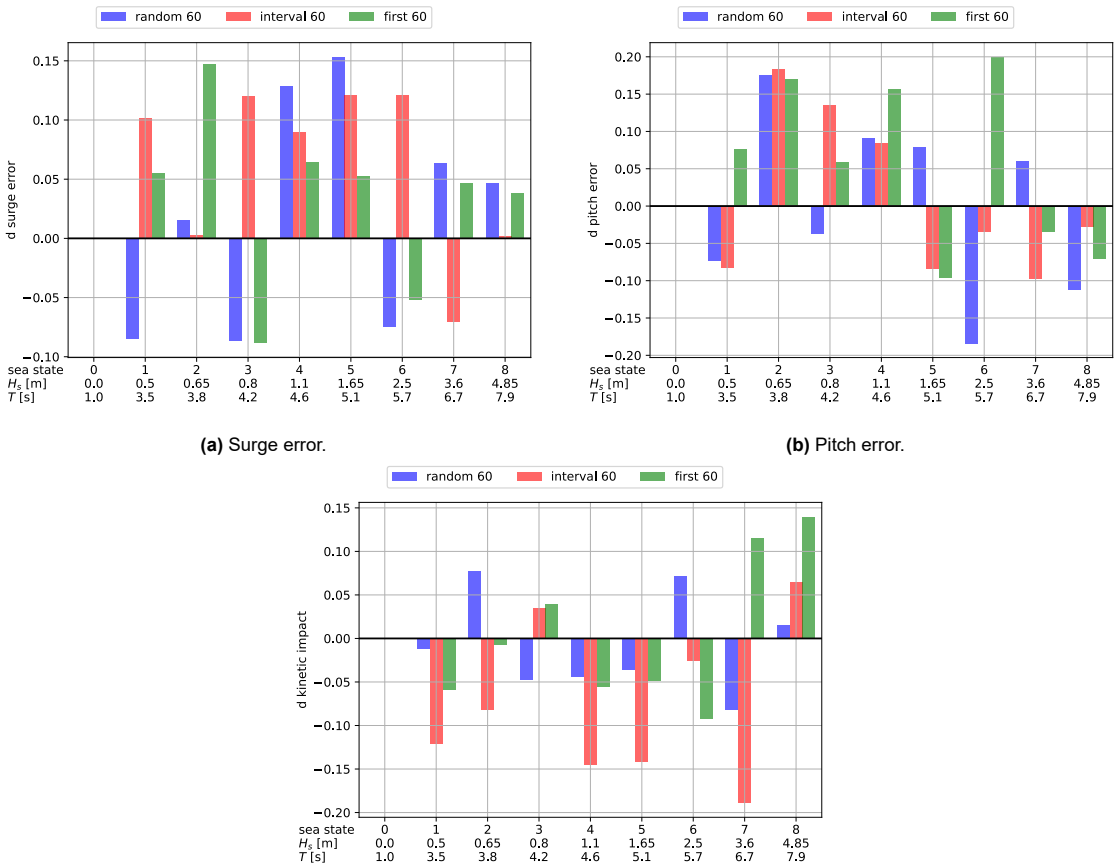

(a) Surge error.

(b) Pitch error.

(c) Kinetic impact energy.

Figure 6.7: Results from the Cohen's d test for the three samples.

6.4. Conclusion

This chapter started with the research question '*How to evaluate vertical docking performance?*' A novel probability distribution method was developed to estimate the success probability of a vertical docking approach. This method defines a docking attempt as the moment when the AUV enters the capture mechanism. For a particular GNC method, the docking probability distributions of the key docking entry metrics are obtained. In a 2D setting, these metrics include the docking surge error, docking pitch error, and the kinetic impact energy.

Using these distributions, the viability of vertical docking is quantified in terms of maximum operational sea state and operational uptime. The maximum operational sea state is determined for a given DS design, GNC method, and required success probability. The operational up-time of the AUV-USV combination in the North Sea can then be estimated using sea state statistics. Finally, based on the operating limit of Demcon's DUS V5750 USV [72], sea state 8 was identified to serve as a good benchmark for comparing the effectiveness of vertical GNC methods.

A limitation of this method is that it assumes that the capture mechanism can always align the AUV with the latch under favorable entry conditions, which may not always be the case. Moreover, the chosen sample size limits the statistical power. Future research should address these limitations.

This chapter contributed to the literature by introducing the docking probability distribution method to determine docking success probability. To the best of the author's knowledge, this method is not yet been utilized in the field of docking. This method also contributes to the next chapter, in which effective vertical guidance and control methods are identified.

7

Vertical docking guidance and control

Current horizontal docking approaches to an USV have only seen limited success at rough seas, resulting in operational employability of the USV-AUV combination. The vertical docking approach to an USV can possibly increase the sea state at which AUVs can dock to a USVs by leveraging wave phase synchronization. The objective of this chapter is to determine effective vertical guidance methods and control methods to dock the Lobster Scout to an USV at large sea states. The research question to be answered in this chapter is:

What are effective vertical guidance and control methods for the Lobster Scout?

Figure 7.1 provides an overview of the guidance and control methods. In general, a guidance algorithm takes as input the estimated states of the USV, the AUV, and the DS and using a controller, outputs the control forces and moments $\tau^a_{control}$ that steer the AUV along the path to the DS.

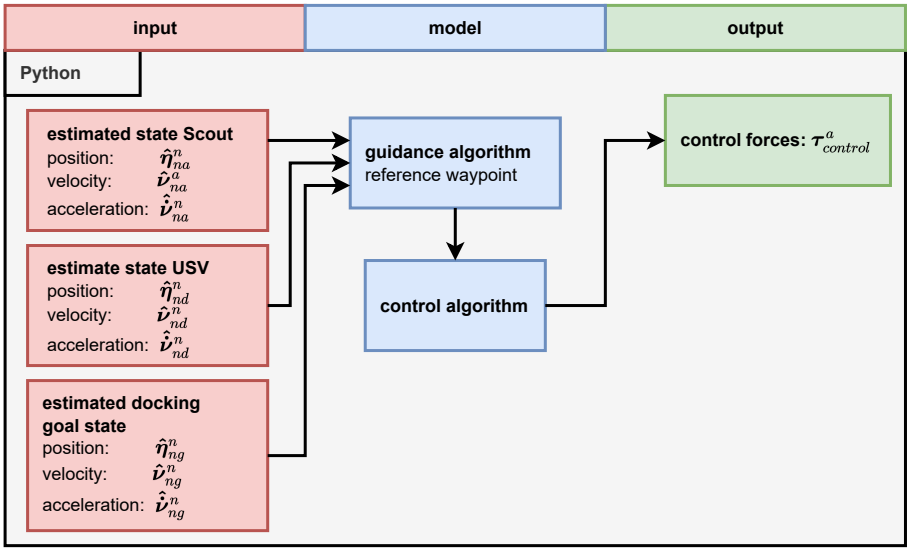

Figure 7.1: an input-output diagram of the guidance module

One of the main assumptions in this chapter is that the state estimates of the AUV, USV, and DS equal their true states. In other words, perfect navigation with perfect state measurements is assumed. This chapter serves as a baseline for the next Chapter 8, where the effect of noisy measurements is investigated.

Approach To obtain effective vertical guidance methods, the following approach was used:

1. **Select guidance methods** A number of docking guidance methods are evaluated for applicability to vertical docking. Target state guidance, polynomial prediction, and kinematic prediction methods were selected.
2. **Develop vertical guidance methods** The selected guidance methods are adapted and tuned for vertical docking and their implementation was verified.
3. **Obtain docking distributions** The docking probability distributions were obtained for each of the selected guidance methods over a range of sea states.
4. **Compare guidance methods** Based on the obtained probability distributions, the 99.7 % confidence interval was used to compare the performance of different guidance methods.
5. **Determine guidance method effectiveness** The maximum operational sea state and operational uptime for all vertical guidance methods, given the DS described in Section 6.3.4, was obtained and compared to the effectiveness benchmark of sea state 8.

Only the irregular North Sea wave model was considered as the regular waves model does not represent realistic wave motion. The sea state definitions used in this thesis were outlined in Table 3.2, which are reiterated in Table 7.1. This table also includes the operational uptime percentage as outlined in Figure 6.6a.

Table 7.1: Sea states definitions used in this thesis

Sea state	**0**	**1**	**2**	**3**	**4**	**5**	**6**	**7**	**8**	**9**	**10**	**11**	**12**
$H_{\frac{1}{3}}$ [m]	0.0	0.5	0.65	0.8	1.1	1.65	2.5	3.6	4.85	6.1	7.45	8.7	10.25
$\bar{T}$ [s]	1.0	3.5	3.8	4.2	4.6	5.1	5.7	6.7	7.9	8.8	9.5	10.0	10.5
Uptime [%]	≈ 0	7.9	14.8	22.7	36.7	59.4	82.7	93.6	98.3	≈ 100			

In Section 7.1 docking guidance methods described in the docking literature are evaluated and promising methods are selected for the vertical docking approach. The selected guidance methods are described in detail in Section 7.2 and then tuned and verified in Section 7.3. The vertical guidance methods are evaluated at increasing sea states in Section 7.4 and these results are discussed in Section 7.5. Finally, a conclusion to the research question of this chapter is given in Section 7.6.

7.1. Selection of guidance methods for vertical docking

Numerous guidance methods have been developed for both general AUV guidance and specifically for AUV docking guidance, as detailed in Appendix D. However, due to project time constraints, it is not feasible to examine all of them for vertical guidance and an informed decision must be made to determine which guidance methods to investigate for the vertical docking approach. The evaluation led to the selection of the target state guidance method, the polynomial prediction method, and the kinematic prediction method.

Scenario-based selection A set of criteria has been established for this scenario to evaluate the guidance methods which are described in Table 7.2. These criteria are used to evaluate the guidance methods in Table 7.3. Although the implementation of different guidance methods can affect their performance significantly, those which are clearly worse are eliminated.

Table 7.2: Evaluation criteria for vertical docking guidance methods

ID	Criteria	Justification
C1	Good ability to deal with horizontal disturbances	Dealing with currents and waves.
C2	Good ability to deal with vertical disturbances	Dealing with waves.
C3	Less navigation information required	A more complex and expensive navigation system is required to obtain more state information.
C4	Good ability to dock with an under-powered AUV	At large sea states, the AUV will likely be underpowered. Smart guidance methods can compensate for this lack of power.
C5	Less computational time	Surface docking is a dynamic scenario, the guidance path will have to be updated many times. As such, less costly guidance methods are preferred.
C6	Good final alignment	The AUV has to match the docking state exactly at the final moment. While the cradle can help with final alignment, the guidance method should minimize docking errors.

Table 7.3: Evaluation of the guidance methods. A score is given from +, o, -

	C1	C2	C3	C4	C5	C6	Total
Local methods							
Line of Sight (LoS) [37, 22, 87, 46, 64, 57]	-	o	+	-	+	-	-
Proportional Navigational Guidance (PNG) [53, 37, 84]	-	o	+	-	+	-	-
Pure pursuit [84, 16, 58, 20]	-	o	+	-	+	-	-
Cross-track [49, 35, 55, 38]	-	o	+	-	+	-	-
Touchdown alignment [60, 16]	-	o	+	-	+	o	o
Crab angle [84, 58, 16, 20]	o	o	-	o	+	-	-
Side-slip [59, 16]	o	o	-	o	+	o	o
Sliding path [62, 16]	o	o	-	o	+	o	o
Target state [6, 83, 88]	+	+	o	-	+	+	3+
Fuzzy controller based [73]	-	o	+	-	+	-	-
Artificial potential fields [63]	o	o	o	-	-	+	-
Lyapunov-controller [9]	+	+	o	-	+	+	3+
Global methods							
Graph search [11]	o	o	o	-	-	+	-
Probabilistic sampling-based [68]	o	o	o	-	-	+	-
Predictive methods							
Adaptive Neuro-Fuzzy Interference System (ANFIS) [75]	+	+	o	+	-	+	3+
Model Predictive Control (MPC) [79, 67]	+	+	o	+	-	+	3+
Grey model prediction [83]	+	+	o	o	o	+	3+
Kinematic prediction	+	+	o	o	o	+	3+
Polynomial prediction	+	+	o	o	o	+	3+

Evaluation local methods the Line of Sight (LoS), Proportional Navigational Guidance (PNG), pure pursuit, cross-track guidance methods and touchdown alignment methods, along with the crab angle, touchdown-alignment, side-slip, and sliding path methods are primarily intended for cruising AUVs and not well suited for a hovering AUV such as the Lobster Scout. This is because these methods would only use the side thrusters of the Lobster Scout in a vertical approach orientated horizontally. While the crab angle, touchdown-alignment, side-slip, and sliding path do compensate for currents, they would require direct information about the water velocity and are still not effective at handling highly dynamic disturbances.

The application of artificial potential fields is generally less suitable for highly dynamic systems that involve moving obstacles [63], which makes them less well-suited for this scenario. The fuzzy controller-based approach, as described in [73], would not be effective because it would only utilize the side thrusters of the Lobster Scout. Although it was not investigated in this thesis, the fuzzy controller itself may be used in combination with a different guidance method.

Target state guidance received a high score as it is expected to deal well with both horizontal and vertical disturbances in a highly dynamic environment, by making use of all thrusters, and is expected to result in accurate final alignment with the DS. This makes it a promising method to explore further. Additionally, Lyapunov-based guidance, as utilized in [10], has potential for success, but its implementation is similar to target state guidance and therefore received a comparable score.

Evaluation global methods Global methods received an average score due to their inability to predict or compensate for currents or waves and high computational demands. In a highly dynamic environment where the path must be updated frequently, they are less suitable because they require a significant amount of computational time and do not scale well with the number of considered system states. Global methods are more generally applicable for planning, and can plan around obstacles. This can be used to avoid a NFZ of the USV, for example near the thrusters, however, this is mostly irrelevant as discussed in Section 2.3.6.

Evaluation predictive methods The previously evaluated guidance methods steer the Lobster Scout towards the current estimated state of the DS, but in a highly dynamic environment, these methods can fall behind as the DS moves while the Lobster Scout is approaching it. Predictive guidance methods offer a solution to this by predicting the future motion of both the Lobster Scout and the docking station, allowing the Lobster Scout to anticipate and adjust its approach accordingly (as illustrated in Figure 7.2). Overall, these methods have the potential to produce good results and are worth further exploration.

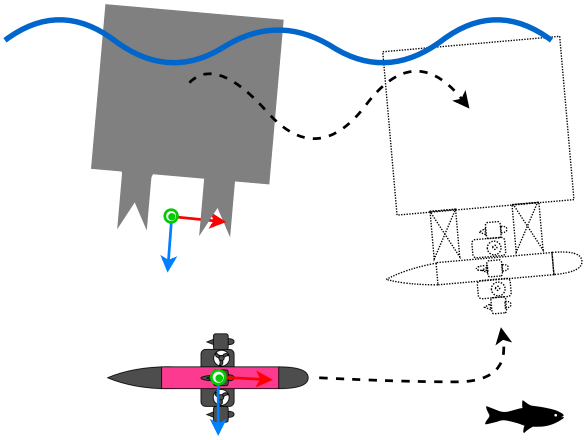

Figure 7.2: Predictive guidance visualized

Final selection The evaluation based on the established criteria has narrowed down the set of guidance methods to target state guidance and a number of predictive guidance methods. However, due to the large number of options, further selection was necessary. Using the criteria of simplicity to allow for quick implementation and fast initial results, the author has selected:

- Target state guidance method
- Kinematic prediction guidance
- Polynomial prediction guidance

To the best of the author's knowledge, the polynomial prediction method and the kinematic prediction method have not yet been used in the docking literature, making them interesting to investigate.

The remaining guidance methods are considered for future research. Model Predictive Control (MPC) would be interesting since it is widely used and effective in various vehicle control schemes. While the author has attempted to implement an MPC using MPC Python packages (e.g. do-mpc [41] and pyMPC [23]), this was not successful as they require significant reformulating of the optimization problem such that these packages were implementable. Particularly the fact that the future states of the goal state were unknown resulted in issues. Due to time constraints, this was not feasible within the project. Furthermore, the Adaptive Neuro-Fuzzy Interference System (ANFIS) method required significant effort to understand fully before implementation, which was also not feasible within the project time frame.

7.2. Detailed description of selected vertical guidance methods

In this section, the selected guidance methods are described in detail and adapted for vertical docking.

7.2.1. Cascaded vertical target state guidance

A significant advantage of a fully hovering type AUV like the Lobster Scout is that all its states are controlled. Therefore, a promising guidance strategy is to match the dynamics of the DS, as depicted in Figure 7.3. This matching is achieved in a cascaded manner, with each step increasing the level of matching:

- **Match position and orientation:** This method only requires the AUV to know the relative pose.
- **Match linear and angular velocity:** In addition to the relative pose, this method also requires the relative velocities to be known.
- **Match linear and angular acceleration:** The next step is to anticipate the relative acceleration as well.

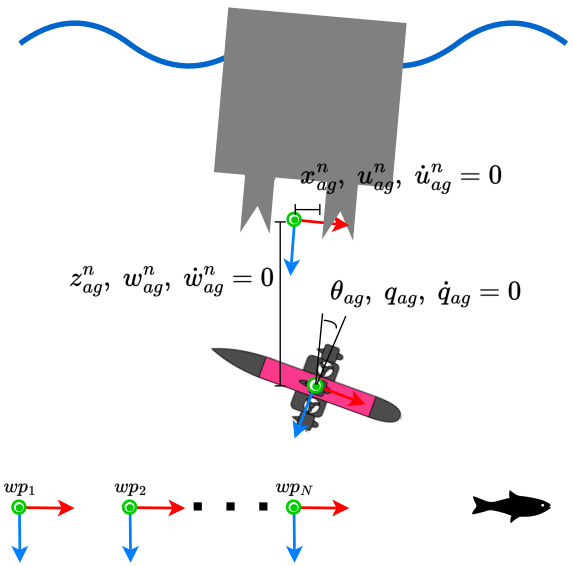

Figure 7.3: Target state guidance visualized

The following sub-sections illustrate this guidance method using the docking goal state g as the target state. However, the same approach is adaptable to any desired target state. Moreover, this method is combined with waypoint guidance to plan complex paths, which is described in Section 7.2.1.

Hydrostatic force feed-forward compensation

Since the model of the AUV is known, it is possible to compensate for the hydrostatic forces acting on the AUV. This is shown in Figure 7.4. Using the estimated attitude $\hat{\theta}_{na}$, the compensating hydrostatic force is calculated as:

$$\boldsymbol{\tau}_{hydrocomp} = -\boldsymbol{g}(\hat{\boldsymbol{\eta}}^n_{na}) = \begin{bmatrix} R^a_n(\hat{\theta}_{na})(\boldsymbol{f}^n_g + \boldsymbol{f}^n_b) \\ \boldsymbol{r}^a_{ag} \times R^a_n(\hat{\theta}_{na})\boldsymbol{f}^n_g + \boldsymbol{r}^a_{ab} \times R^a_n(\hat{\theta}_{na})\boldsymbol{f}^n_b \end{bmatrix}. \tag{7.1}$$

Note the pitch angle is the only used estimate in this implementation, while perfect knowledge of the buoyancy force magnitude, gravitational force magnitude, the CB and CG is assumed. This assumption is accepted for the purpose of evaluating this method, but may lead to higher accuracy than in reality where all quantities and vectors are estimated.

Pose control

A control scheme to match the pose of the goal frame $\{g\}$ is shown in Figure 7.4. A simple PID controller is chosen to follow the reference pose for the purpose of simplicity.

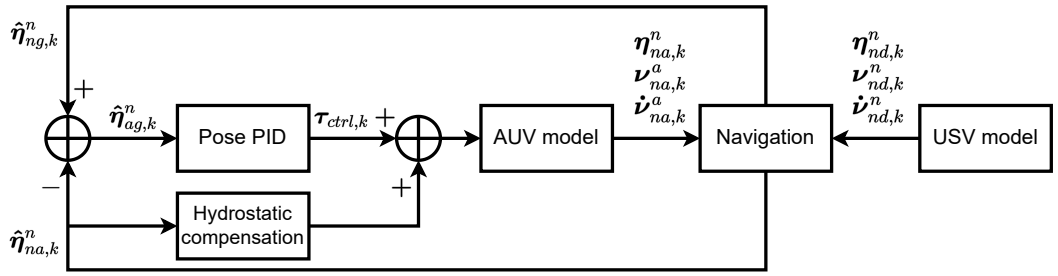

Figure 7.4: Pose target control scheme

If the estimated goal pose at time k is given by $\hat{\boldsymbol{\eta}}^n_{ng,k}$ and the estimated AUV pose is given by $\hat{\boldsymbol{\eta}}^n_{na,k}$ then the error between them is given by:

$$\hat{\boldsymbol{\eta}}^n_{ag,k} = \hat{\boldsymbol{\eta}}^n_{na,k} - \hat{\boldsymbol{\eta}}^n_{ng,k}. \tag{7.2}$$

Since the control force should be given in the $\{a\}$ frame, this vector is rotated as:

$$\hat{\boldsymbol{\eta}}^a_{ag,k} = \tilde{R}^a_n(\hat{\Theta}^n_{na,k})\hat{\boldsymbol{\eta}}^n_{ag,k} \tag{7.3}$$

Note that the notation of the rotation matrix is abused, as $\tilde{R}^n_a(\hat{\Theta}^n_{na,k})$ is of the form:

$$\tilde{R}^a_n(\hat{\Theta}^n_{na,k}) = \begin{bmatrix} cos(\theta^n_{na,k}) & -sin(\theta^n_{na,k}) & 0 \\ sin(\theta^n_{na,k}) & cos(\theta^n_{na,k}) & 0 \\ 0 & 0 & 1 \end{bmatrix} \tag{7.4}$$

Then the derivative of the error is given by:

$$\dot{\hat{\boldsymbol{\eta}}}^a_{ag,k} = \frac{\hat{\boldsymbol{\eta}}^a_{ag,k} - \hat{\boldsymbol{\eta}}^a_{ag,k-1}}{dt}, \tag{7.5}$$

where $dt = t_k - t_{k-1}$. Finally, the integral of the error equals:

$$\int \hat{\boldsymbol{\eta}}^a_{ag,k} dt = \sum_{i=1}^{k} \hat{\boldsymbol{\eta}}^a_{ag,k} dt. \tag{7.6}$$

The control force in the $\{a\}$ frame is then given by the following equation:

$$\boldsymbol{\tau}^a_{control,k} = \boldsymbol{P}\hat{\boldsymbol{\eta}}^a_{ag,k} + \boldsymbol{I}\int \hat{\boldsymbol{\eta}}^a_{ag,k} dt + \boldsymbol{D}\dot{\hat{\boldsymbol{\eta}}}^a_{ag,k}, \tag{7.7}$$

where the $\boldsymbol{P}$, $\boldsymbol{I}$ and $\boldsymbol{D}$ are the vectors that contain the PID parameters.

Finally, integral windup should be prevented and the output limits respected. Integral windup is prevented by limiting the integral term to half the output limits. The output limits in this case are given by the maximum force and moment that the Lobster Scout can produce as discussed in Section 4.4.6.

Cascaded pose and velocity control
An advantage of the pose target controller is that only pose information of the DS is required. This lowers the complexity of the navigation system. However, the pose target controller has a number of disadvantages:

- The velocity of the $\{g\}$ frame is not matched, which may result in a large kinetic impact with the DS.
- Less control is obtained over the velocity of the AUV. The control force resulting from the P term of the pose PID is proportionate to the pose error. At large pose errors, the AUV will have a large control force, resulting in unwanted high velocities and possible overshoots.

If accurate velocity information of both the AUV and the DS is available, these disadvantages can be mitigated as the velocity can be directly controlled. This is done using Cascaded Pose and Velocity (CPV) control as shown in Figure 7.5.

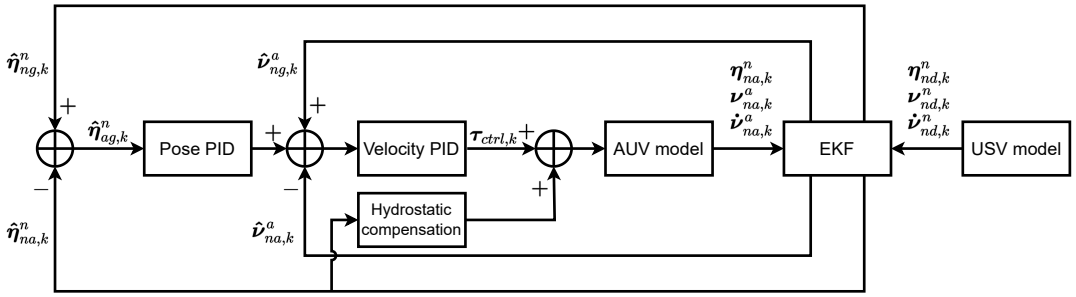

Figure 7.5: CPV target control scheme

The pose PID outputs a desired velocity towards target. This desired velocity is limited by the output limits, thus obtaining finer control over the velocity. The velocity error between the AUV and the target state is added to this signal. The velocity of the target is then matched using a second PID stage that converts the combined velocity target to a control force.

Cascaded pose, velocity, and acceleration control
The CPV controller only anticipates the velocity error, which may be too slow and can still result in a large kinetic impact with the DS. When the target experiences a large acceleration due to a disturbance, the AUV only starts producing a significant control force as the velocity error becomes significant. The controller can anticipate quicker if it also aims to match the acceleration of the target. This control scheme is shown in Figure 7.6.

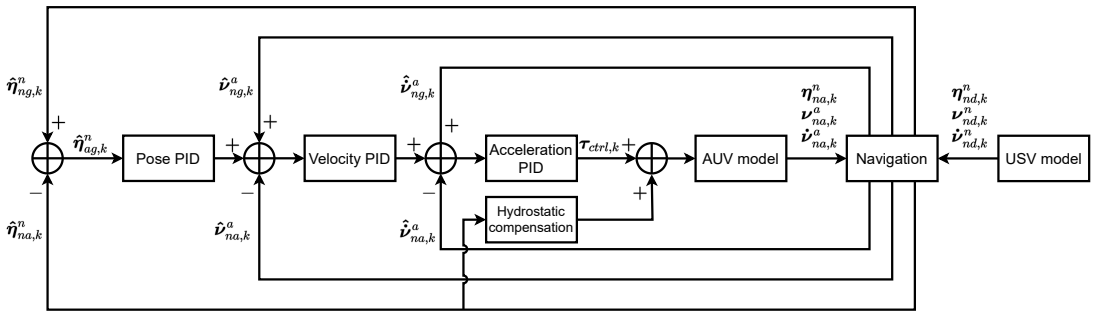

Figure 7.6: Cascaded Pose Velocity and Acceleration (CPVA) target control scheme

The Cascaded Pose Velocity and Acceleration (CPVA) target control scheme works as follows. The pose PID outputs a desired velocity towards a target. This desired velocity is limited by the output limits, thus obtaining finer control over the velocity. The velocity error between the AUV and the target state is added to this signal. The velocity of the target can then be matched using a second PID stage that converts the combined velocity target to a desired acceleration. If required, the acceleration towards the target is also limited using the output limits. Finally, the acceleration error between the AUV and the target state is added to this signal. The acceleration of the target can then be matched using a third PID stage that converts the combined acceleration error to a control force.

waypoint management
The above discussion has limited itself to docking goal state as the target state. In order for the AUV to follow a path, the method is well suited to be combined with waypoints guidance. The states of these waypoints are planned using a number of assumptions:

waypoints path

- The AUV can use its INS to obtain its pose, velocity, and acceleration without relying on docking sensors. Therefore, waypoints can be set relative to the $\{n\}$ frame.
- A state estimate of the $\{d\}$ and $\{g\}$ frame are available at every time step. As such it is possible to simply plan waypoints relative to these states.

Given these assumptions, a path is planned from the AUVs initial state to the goal state. This path should result in the AUV to vertically dock. This path may improve the docking performance by planning the waypoints strategically, gradually matching more of the docking goal states as the AUV near the goal state. Figure 7.7 shows a guidance path with 4 intermediary waypoints.

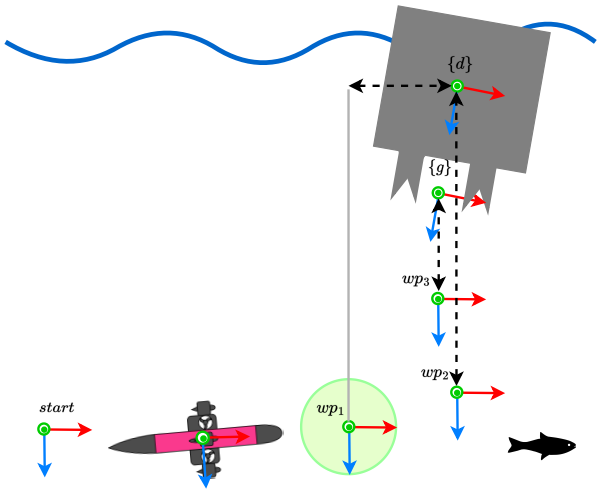

Figure 7.7: Waypoints method for vertical docking guidance.

Waypoint switching For the intermediary waypoints, the target waypoint is shifted to the next waypoint using a simple acceptance region condition around target waypoint. This condition is given by:

$$|\hat{\boldsymbol{p}}^n_{wp,i} - \hat{\boldsymbol{p}}^n_{na}| < r_{accept}. \tag{7.8}$$

where r_{accept} is the acceptance radius.

Wave cancellation waiting strategy In Chapter 3, it was explained that irregular waves are modelled by superimposing regular wave components. It can be assumed that, at some point in the future, these wave components will cancel each other out and the water motion becomes much calmer than usual for that sea state. This assumption is used to improve the docking performance in irregular waves by

having the Scout wait at the last waypoint before attempting to dock until the water motion becomes relatively still.

While wave motion cannot be directly measured, the relative velocity between the AUV and the USV can be measured and is used to start or abort a dock if it exceeds a certain maximum threshold. This is implemented as follows:

1. The Scout moves along the waypoint path until the target waypoint is the last waypoint before the dock.
2. The Scout stays at this waypoint until the relative velocity between the Scout and the USV is below the threshold. The target waypoint is then switched to the goal state.
3. If the relative velocity exceeds the threshold while the Scout is moving to the goal state, the target waypoint is reset to the last waypoint before the goal state.

From observing the described algorithm, it is clear that there is a trade-off between the maximum threshold and the average time it takes to dock over multiple docking attempts. In addition, higher sea states will increase the probability of exceeding the maximum threshold, further increasing the average time it takes to dock. Therefore multiple thresholds are explored in Section 7.4.5.

7.2.2. Future state prediction methods

This section describes the kinematic prediction method and the polynomial prediction method.

Kinematic prediction guidance

The Extended Kalman Filter (EKF) used in the navigation model in Section 8 employs a time update that provides a one-time step prediction to obtain a priori state estimate using a kinematic process model and an acceleration input. The kinematic prediction guidance method utilizes this kinematic process model and by running it sequentially, using each priori state estimate to predict the next, in order to predict a number of time steps into the future. This method is used to predict the future state of the AUV, and the USV. The future states of the waypoints and goal state are then predicted based on the predicted states of the USV, and then any target state controller can be used to steer towards the predicted waypoints. This method is illustrated in Figure 7.8.

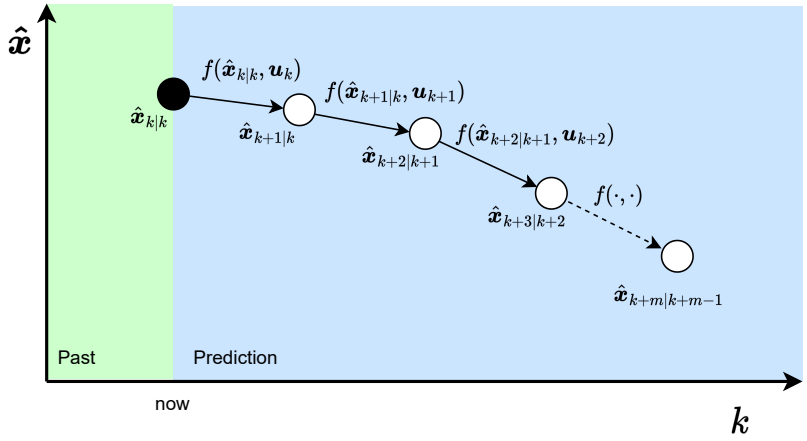

Figure 7.8: The kinematic prediction method visualized.

For the kinematic prediction method to work, it is required to assume future input accelerations to the process model:

1. Future acceleration inputs are assumed to be zero.
2. Future acceleration inputs are assumed to remain equal to the last estimated acceleration.
3. Predict the future acceleration input based on the past accelerations using for example the polynomial prediction method explained in Section 7.2.2

The kinematic prediction algorithm is then shown below, where it is assumed that future acceleration inputs remain zero.

$$\begin{aligned}
\hat{\boldsymbol{x}}_{k+1|k} &= f(\hat{\boldsymbol{x}}_{k|k}, \boldsymbol{u}_k, \boldsymbol{0}), \quad \boldsymbol{u}_k = \boldsymbol{0}, \\
\hat{\boldsymbol{x}}_{k+2|k+1} &= f(\hat{\boldsymbol{x}}_{k+1|k}, \boldsymbol{u}_{k+1}, \boldsymbol{0}), \quad \boldsymbol{u}_{k+1} = \boldsymbol{0}, \\
\hat{\boldsymbol{x}}_{k+3|k+2} &= f(\hat{\boldsymbol{x}}_{k+2|k+1}, \boldsymbol{u}_{k+2}, \boldsymbol{0}), \quad \boldsymbol{u}_{k+2} = \boldsymbol{0}, \\
&\dots \\
\hat{\boldsymbol{x}}_{k+m|k+m-1} &= f(\hat{\boldsymbol{x}}_{k+m-1|k+m-2}, \boldsymbol{u}_{k+m-1}, \boldsymbol{0}), \quad \boldsymbol{u}_{k+m-1} = \boldsymbol{0},
\end{aligned} \tag{7.9}$$

where the m is the number of prediction steps, given by the prediction time $t_{predict}$ divided control loop period T.

Four factors can be varied using this method, namely the prediction time $t_{predict}$, for which vehicles to predict, the future acceleration input assumption, and with which controller to combine it. However, due to time constraints, it was chosen to only combine it with the pose controller. Furthermore, only the option where future acceleration inputs are assumed to be zero is explored.

Polynomial prediction guidance
In the polynomial prediction guidance method, a set of p past state estimates is temporarily stored. After each new state estimate, the earliest past state estimate in the temporary storage is replaced by this new estimate. A polynomial of the nth order is then fitted through these past states to predict the future state of the system at a certain prediction time in the future. Similar to kinematic prediction, the target state guidance method is employed to steer the Scout towards the predicted waypoints. The polynomial prediction method is presented in Figure 7.9.

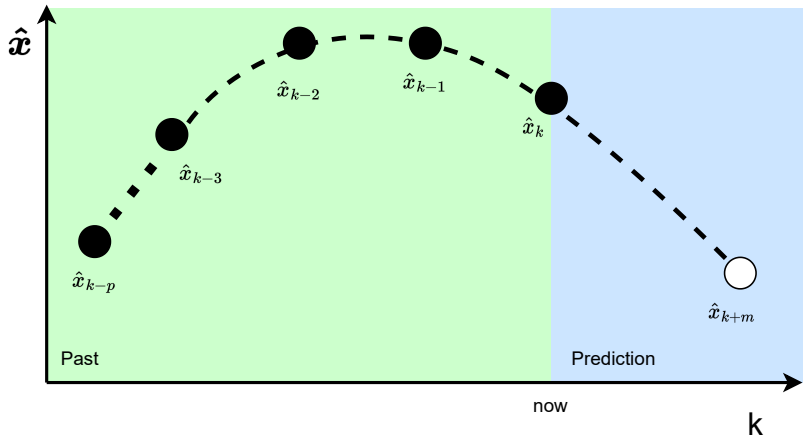

Figure 7.9: The polynomial prediction method visualized.

Five factors can be varied using this method, namely the polynomial order n, the past time horizon t_{past}, the future time horizon $t_{predict}$, for which vehicles to predict and with which controller to combine it with. However, due to time constraints, it was chosen to only combine it with the pose controller.

7.3. Tuning and verification

The performance and effectiveness of the vertical guidance methods is greatly influenced by their tuning. This section focuses on the tuning of PID controllers, the kinematic prediction method and the polynomial prediction method. Additionally, to ensure that the control forces are within the output limits and the guidance methods behave as expected, a visual analysis of each method has been conducted.

GNC loop frequency It is assumed that the GNC loop operates at a frequency of 100 Hz, which is equal to the frequency of the GNC loop of the Lobster Scout [6]. Therefore, it is assumed that all GNC calculations are performed within 0.01 s. The influence of the GNC loop frequency is not investigated in this study.

7.3.1. Target state guidance PID tuning

First the control parameters are justified after which the docking performance is shown. Finally, the different target guidance methods are directly compared.

Tuning evaluation scenario

To tune, evaluate and compare the target state guidance methods, a tuning scenario is been designed. In this scenario, the Root Mean Square Error (RSME) vector between a single target waypoint and the Scout's true state is computed over a period of 30 seconds. The RSME vector serves as the performance metric, where the best possible guidance method approximates the zero vector. The RSME vector is given by:

$$\boldsymbol{rmse} = [rmse_x,\ rmse_z,\ rmse_\theta,\ rmse_u,\ rmse_w,\ rmse_q]^T \tag{7.10}$$

The target waypoint used in this tuning scenario is the docking goal state shifted 1 m downward. The Scout was initially placed in close proximity to this waypoint but not equal to it, as to severely penalize controllers that are very slow or have no control (e.g. pure derivative control). The entire system is subject to wave disturbances. An animation of this tuning scenario can be viewed by scanning or clicking the provided QR code.

Animation

Tuning requires many iterations, which makes it greatly beneficial to reduce the number of simulations required to evaluate the RSME vector for a certain controller. As such, the tuning scenario used regular waves and perfect navigation to eliminate all random variables, allowing each controller to be simulated only once to obtain its RSME vector.

Pose control

Several methods were explored to obtain the pose control PID parameters for the Lobster Scout. The objective was to tune the PID controllers aggressively, allowing for a high bandwidth frequency to achieve good reference tracking performance and disturbance rejection.

The first method attempted was the Ziegler-Nichols rules, however, these rules resulted in significant oscillation and were not explored further [5]. The second approach involved loop shaping to design continuous-time PID controllers [5], which should then be converted to a discrete-time difference equation that is implementable in Python. In this approach, the Scout was approximated as a pure mass, which is a valid approximation at low velocities, due to the low drag at low velocities and because it is almost neutrally buoyant. Unfortunately, the author was not able to successfully convert the continuous time PID controllers to a discrete difference equation, so this method was also abandoned.

The third method involved manual tuning of the PID parameters using general rules of thumb, presented in [5]. The resulting manually tuned PID controller parameters are given in Table 7.4.

Table 7.4: Position PID parameters

State	P	I	D	Output limits
x^n	200	3	159	$[-152,\ 192]$ N
z^n	150	15	15	$[-68,\ 68]$ N
θ	100	10	2	$[-20,\ 20]$ Nm

Although the manual controller was functional, it had a slow response, the Scout motion showed significant oscillations and the desired control force outputs hardly surpassed the controller output limits, indicating the performance could still be improved. This led to the fourth and final method, in which the PID values were obtained and optimized using a brute force approach.

Brute force approach To identify a PID controller using a brute force approach, a large set of PID controllers was evaluated on the tuning evaluation scenario presented in Section 7.3.1. The optimal PID controller was obtained with significantly fewer simulations by evaluating the surge, heave, and pitch controllers simultaneously, which are mostly independent due to the Scout's symmetry. Additionally, the number of simulations was limited by only considering sea state 4.

Taking the surge controller as an example, the optimization objective is to minimize the sum of the surge RSME and the velocity RSME over a time period of 30 seconds. The best heave and pitch controllers are obtained in a similar fashion, where all objectives are shown below.

$$\begin{aligned} &\min_{P_x, I_x, D_x} rmse_x + rmse_u, \\ &\min_{P_z, I_z, D_z} rmse_z + rmse_w, \\ &\min_{P_\theta, I_\theta, D_\theta} rmse_\theta + rmse_\theta \end{aligned} \tag{7.11}$$

An initial set of 1000 different PID controllers was generated over a logarithmic range and evaluated, covering all combinations of 10 P values, 10 I values, and 10 D values, as presented in Figure 7.10. The initial search resulted in highly responsive controllers, as presented in Figure 7.15b. Although a second focused search could be done to further refine the controller with a more narrow range of PID values centered around the best PID controller from the initial search. This will likely only result in minor improvement, which was observed in earlier brute force searches. Therefore, the controller obtained from the first search was selected. Its parameters are found in Table 7.5.

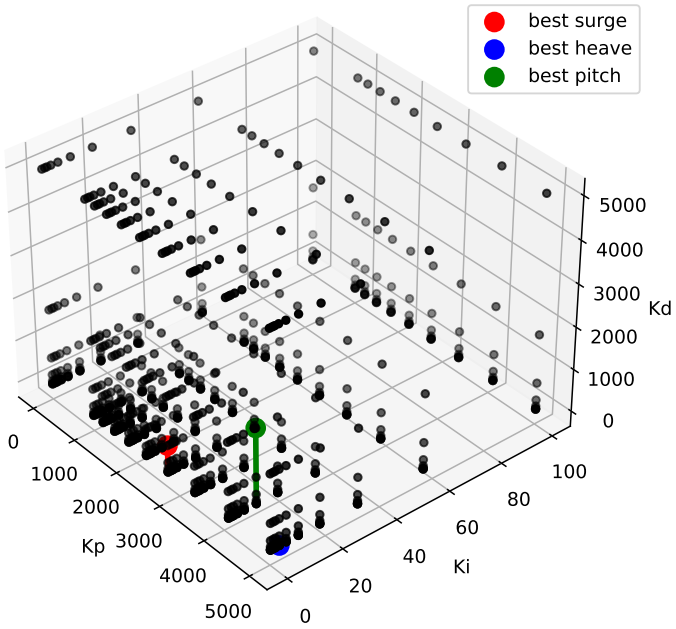

Figure 7.10: The first search with an initial set of 1000 different PID controllers was generated over a logarithmic range. The best performing PID controllers are highlighted.

Table 7.5: Brute force pose PID parameters

State	P	I	D	Output limits
x^n	2738.42	0	630.96	$[-152,\ 192]$ N
z^n	5011.87	3.16	0	$[-68,\ 68]$ N
θ	4097.32	10	1778.28	$[-20,\ 20]$ Nm

This brute force approach provides no guarantee that the found PID controller is truly optimal and it remains uncertain whether the optimum depends on sea state as only a single sea state was used. Nonetheless, the performance of the brute force controller was greatly improved compared to the manual pose controller, which is compared in Section 7.3.4.

CPV control
To tune the CPV control parameters, manual tuning is required as a brute force approach is not feasible. This is because this control strategy has six instead of three parameters. If a brute force approach was to be used to evaluate all combinations of 10 values for each control parameter, it would require testing of one million PID controllers.

Fortunately, the Lobster Scout uses a CPV PID control strategy, which can also be applied to the Scout model described in Chapter 4, given that this model is accurate. The results demonstrated that the CPV parameters used for the actual Lobster Scout worked surprisingly well for the Scout model. This outcome provides confidence that the Scout model is reasonably accurate.

Given that the reference signal for docking to an USV is constantly changing, it is desirable to decrease the rise time and settling time in exchange for larger control forces. Therefore, the PID parameters were slightly adjusted to improve the responsiveness. The corresponding PID parameters used for this control strategy are provided in Table 7.6.

Table 7.6: CPV PID parameters

State	P	I	D	Output limits
x^n	1	0	0.05	$[-0.5,\ 0.5]$ $\frac{\text{m}}{\text{s}}$
z^n	1.5	0	0.075	$[-0.5,\ 0.5]$ $\frac{\text{m}}{\text{s}}$
θ	1	0	0.1	$[-0.5,\ 0.5]$ $\frac{\text{m}}{\text{s}}$
u^a	200	10	5	$[-152,\ 192]$ N
w^a	200	15	15	$[-68,\ 68]$ N
q	60	2.5	2	$[-20,\ 20]$ Nm

It is very likely that a significantly more responsive controller can be obtained with more aggressive tuning. However, given the difficulties of manual tuning of this many parameter and time constraints, this was not explored.

CPVA control
The CPVA PID parameters were manually tuned, as with 9 parameters per DOF, the brute force approach would require testing of a billion PID controllers. The used PID constants are provided in Table 7.7. Similar to the CPV controller, the obtained performance can probably be improved but this was not explored in this thesis due to time constraints.

Table 7.7: CPVA PID parameters

State	P	I	D	Output limits
x^n	1	0	0.05	$[-0.5,\ 0.5]$ $\frac{\text{m}}{\text{s}}$
z^n	1.5	0	0.075	$[-0.5,\ 0.5]$ $\frac{\text{m}}{\text{s}}$
θ	1	0	0.1	$[-0.5,\ 0.5]$ $\frac{\text{rad}}{\text{s}}$
u^a	6	0.1	0.05	$[-2.3,\ 2.9]$ $\frac{\text{m}}{\text{s}^2}$
w^a	6	0.1	0.075	$[-0.55,\ 0.55]$ $\frac{\text{m}}{\text{s}^2}$
q	6	0.1	0.1	$[-0.77,\ 0.77]$ $\frac{\text{rad}}{\text{s}^2}$
$\dot{u}^a$	60	0	0	$[-152,\ 192]$ N
$\dot{w}^a$	80	0	0	$[-68,\ 68]$ N
$\dot{q}$	20	0	0	$[-20,\ 20]$ Nm

7.3.2. Kinematic prediction tuning

The brute force approach was applicable for tuning the kinematic prediction method in order to obtain the best prediction time $t_{predict}$ and for which vehicles to predict. The brute force approach was slightly adjusted, as the sum of the complete RSME vector was used. A linear range of 40 prediction times between 0 and 2 seconds was explored as well as the options for predicting only for the AUV, only for the USV, or both. The optimization objective is now given by:

$$\min_{t_{predict},\, vehicle} rmse_x + rmse_z + rmse_\theta + rmse_u + rmse_w + rmse_q. \tag{7.12}$$

Figure 7.11 presents the results from this brute force approach. Prediction for both the AUV and the USV is the clear winner and performs better than the pure brute force pose controller with no kinematic prediction. However, it seems that the best prediction time is highly dependend on the sea state, as the difference for $t_{predict}$ at sea state 4 and sea state 8 is large. Based on these results, prediction for both the AUV and the USV, seems optimal, but various prediction times will need to be explored.

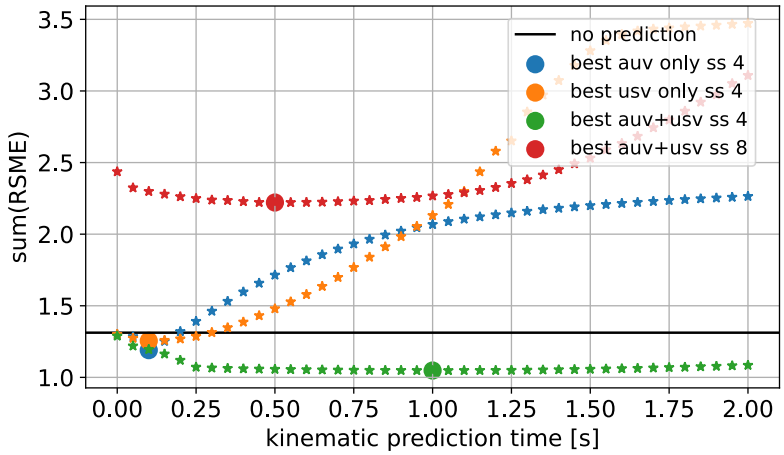

Figure 7.11: Results from the brute force method to obtain the best parameters for the kinematic prediction method.

The kinematic predictions for the AUV and the USV are visualized in Figure 7.12 for irregular waves at sea state 4, using $t_{predict} = 1.0$ s.

Observations For both the AUV as well as the USV, the kinematic predictions for the velocities are equal to the true state, as expected when future accelerations are assumed to be zero. Additionally, the kinematic predictions for surge, heave, and pitch are reasonably accurate, as they are similar to the true state, but shifted earlier in time. However, the predictions tend to overestimate the future poses of vehicles due to the zero acceleration input and the oscillatory nature of wave disturbance. Assuming sinusoidal future accelerations might result in better predictions.

The predictions for the AUV exhibit some oscillatory behavior, which is attributed to interactions between the aggressive brute-force PID controller and the magnifying effect of the kinematic predictive method. This creates a cycle, where a large initial error leads to a high desired control force. Since the thruster dynamics are not modelled, the desired control force directly acts on the Scout, resulting in a high acceleration that increases its velocity. Using 100 prediction steps for a prediction time of 1 second, the increased velocity is used to estimate the future pose of the AUV, which is then used to control it. However, since the future poses tend to be overestimated due to the assumption that future accelerations are zero, the error now swings in the opposite direction, leading to a large control force in the opposite direction, thus continuing the cycle. This is also supported by Figure 7.12b for the USV, which does not show this behavior and is also not controlled.

The oscillatory behavior could be decreased or removed by decreasing the prediction time, modelling

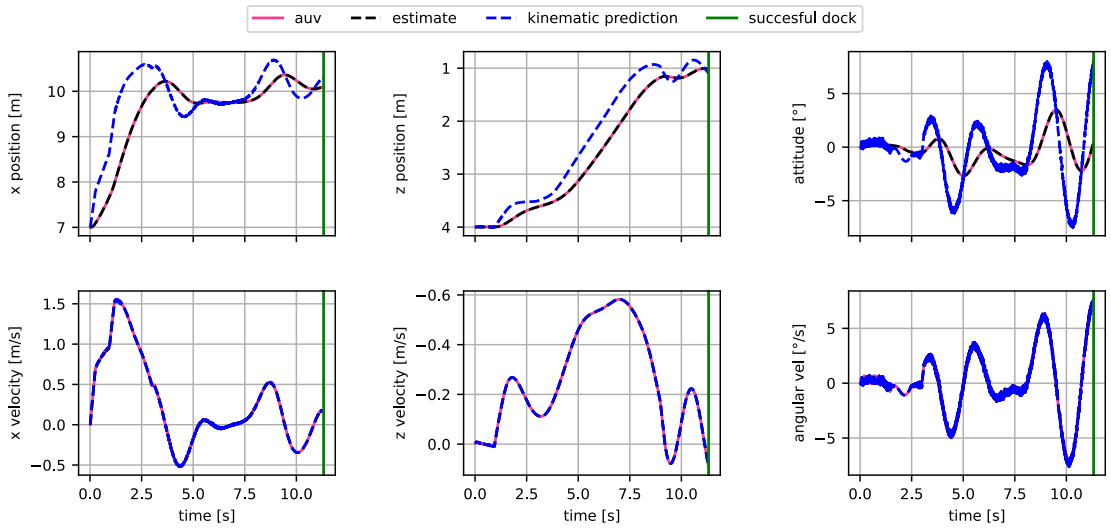

(a) Predicted state of the AUV.

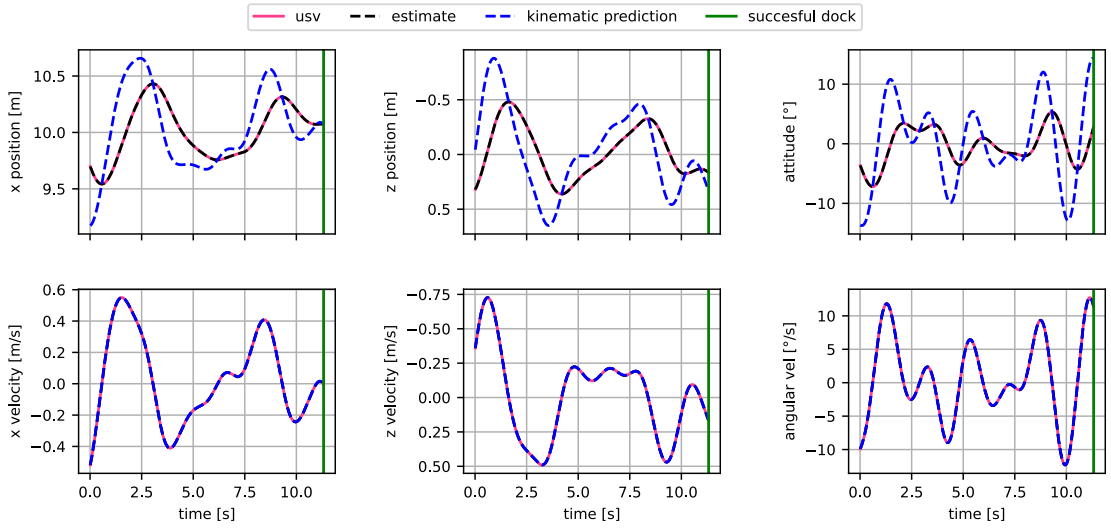

(b) Predicted state of the USV.

Figure 7.12: State prediction using the kinematic prediction method with $t_{predict} = 0.5$ s for irregular waves. The graphs show the true state, the estimated state, and the predicted state.

thruster dynamics, or low-pass filtering desired control inputs. Unfortunately, due to time constraints, this was not possible. Nonetheless, this should not impact the results significantly, as this oscillatory behavior occurs at a much higher frequency than the dynamics of the Scout, essentially low-pass filtering the control signal.

7.3.3. Polynomial prediction

The brute force approach was used to obtain the best parameters for the polynomial prediction method, using the following objective:

$$\min_{n,\, t_{past},\, t_{predict},\, vehicle} rmse_x + rmse_z + rmse_\theta + rmse_u + rmse_w + rmse_q. \tag{7.13}$$

To obtain the best parameters for the polynomial prediction method, first and second-order polynomials for predicting the future state of either the AUV, the USV, or both were evaluated. Several searches were conducted to identify a linear range of 10 values to evaluate for t_{past} and $t_{predict}$. Fitting a first-order polynomial requires a minimum of two measurements, while at least three are needed for a

second-order polynomial. To optimize for both simultaneously, a minimum of three measurements was used. This resulted in t_{past} values ranging from -0.03 s to -0.12 s and $t_{predict}$ values ranging from 0.1 s to 1.0 s. The results are presented in Figure 7.13, and Table 7.8 presents the optimal values obtained for both first and second-order polynomials.

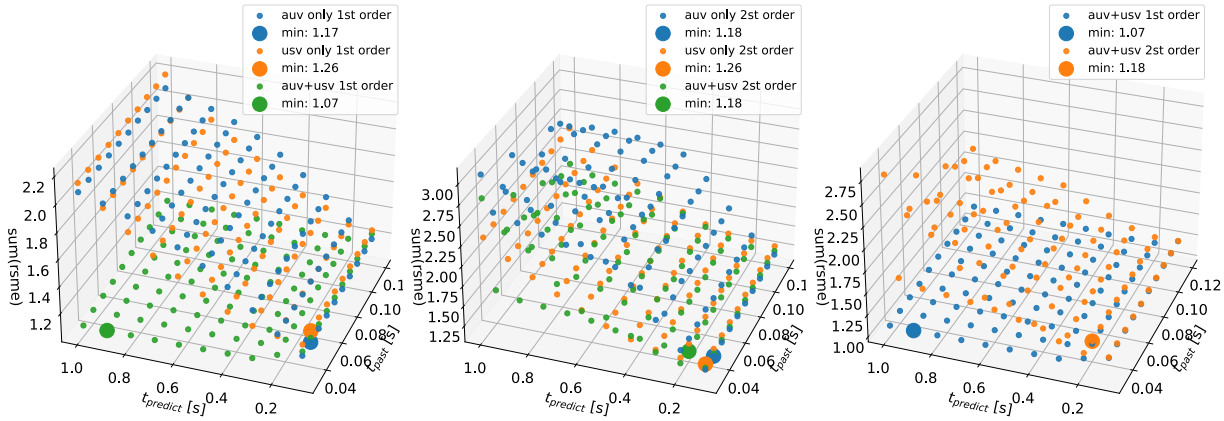

(a) First-order, predicting for the AUV only, the USV only or both.

(b) Second-order polynomial, predicting for the AUV only, the USV only or both.

(c) First order vs second order for while predicting for the AUV and the USV.

Figure 7.13: Evaluated values to obtain best parameters for the polynomial prediction method.

Table 7.8: The best parameters for the polynomial prediction method.

Vehicle	n	t_{past} [s]	$t_{predict}$ [s]	**Sum**
AUV	1	0.04	0.10	1.17
	2	0.04	0.10	1.18
USV	1	0.04	0.10	1.26
	2	0.03	0.10	1.26
AUV and USV	1	0.03	0.90	1.07
	2	0.04	0.20	1.18

The best performance was obtained when the future states of both the AUV and the USV were predicted while using a first-order polynomial with $t_{past} = -0.03$ s and $t_{predict} = 0.9$ s. Interestingly, the prediction time here is significantly larger than for the other options. Using these parameters, the polynomial predictions for the AUV and the USV are visualized in Figure 7.12 for irregular waves at sea state 4.

Observations In Figure 7.14b, the predictions for the USV accurately capture the motion amplitude of future states, although with a slight overestimation. However, for the AUV, oscillatory behavior is observed not only for the predicted future poses but also for the future velocities, as both are modelled using a polynomial. This behavior is similar to what is observed in the kinematic prediction method and is caused by the interactions between the aggressive brute-force PID controller and the magnifying effect of the polynomial prediction method.

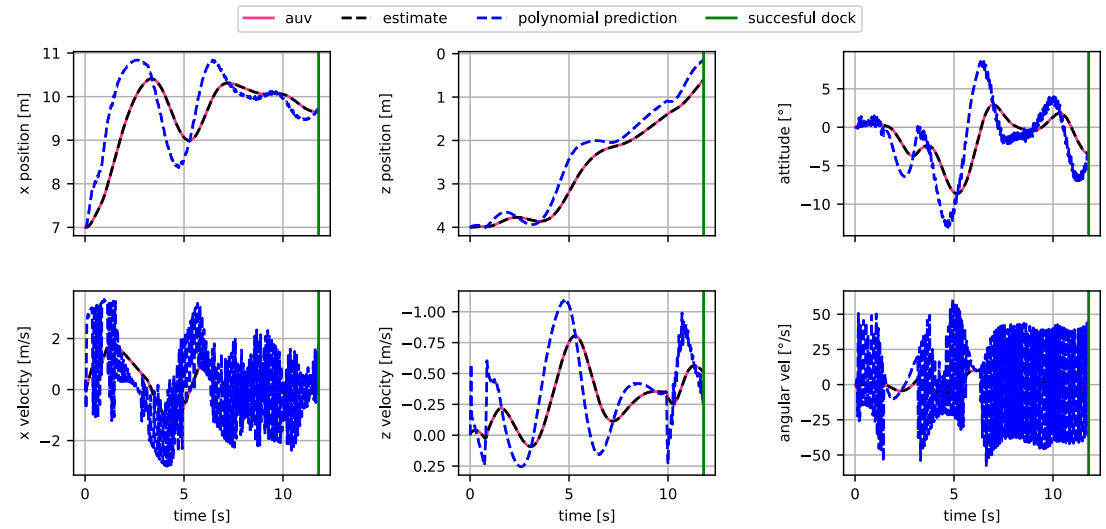

(a) Predicted state of the AUV.

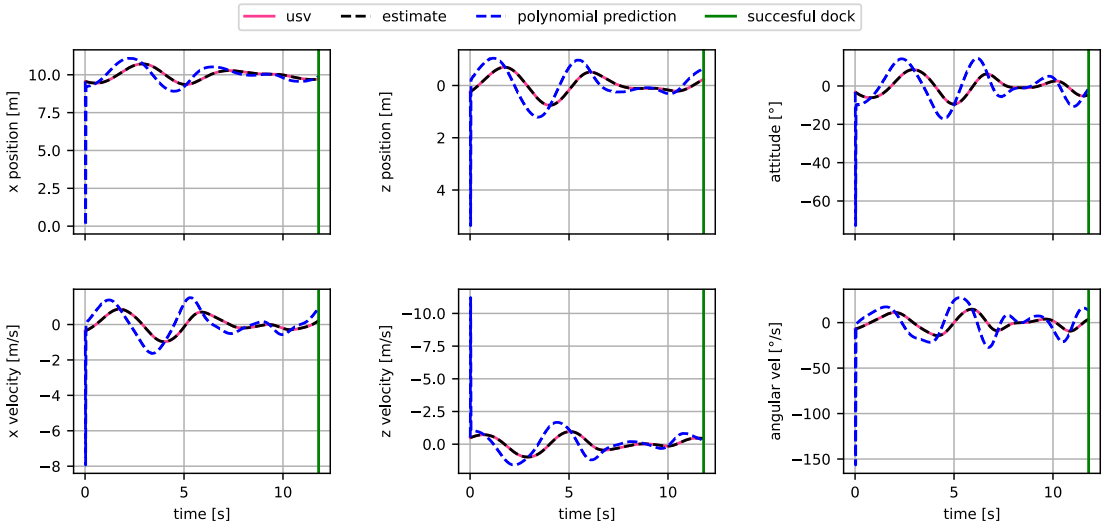

(b) Predicted state of the USV.

Figure 7.14: State prediction using first order polynomial prediction method with $t_{past} = -0.03$ s and $t_{predict} = 0.9$ s for both the AUV and the USV at sea state 4 for irregular waves.

7.3.4. Guidance comparison on tuning scenario

All the guidance methods have been tested on the tuning evaluation scenario. The resulting RSME vectors are provided in Table 7.9. Furthermore, Figure 7.15 presents the control forces, while the associated QR codes show the animation during this scenario.

Table 7.9: RSME of various controllers on test scenario, using the correct implementation of the output limits

Controller	$rmse_x$	$rmse_z$	$rmse_\theta$	$rmse_u$	$rmse_w$	$rmse_q$	Sum
Manual pose	0.43	0.45	0.10	0.50	0.40	0.17	2.05
Brute force pose	0.23	0.40	0.04	0.26	0.32	0.06	1.31
CPV	0.29	0.38	0.06	0.28	0.28	0.07	1.37
CPVA	0.25	0.36	0.04	0.21	0.22	0.04	1.12
Kinematic pred. with brute force pose	0.26	0.35	0.04	0.19	0.16	0.05	1.05
Polynomial pred. with brute force pose	0.27	0.35	0.04	0.20	0.17	0.05	1.07

Animation

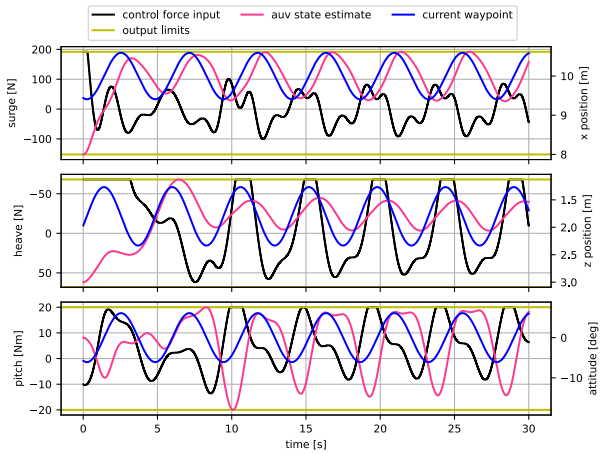

(a) Control forces of manual pose controller.

Animation

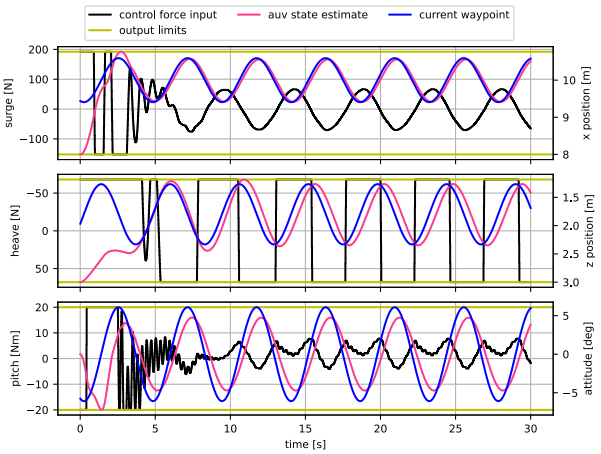

(b) Control forces of brute force pose controller.

Animation

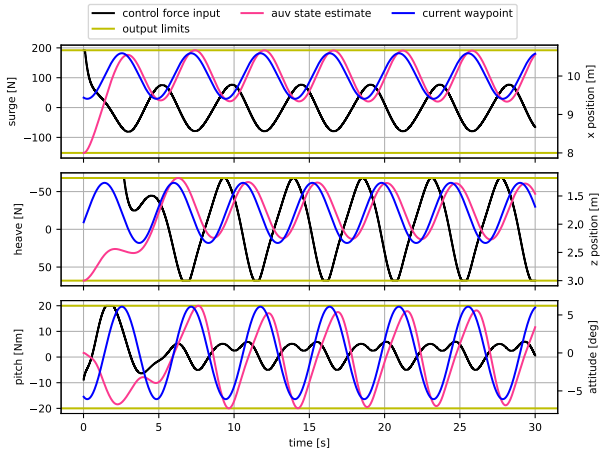

(c) Control forces of CPV controller.

Animation

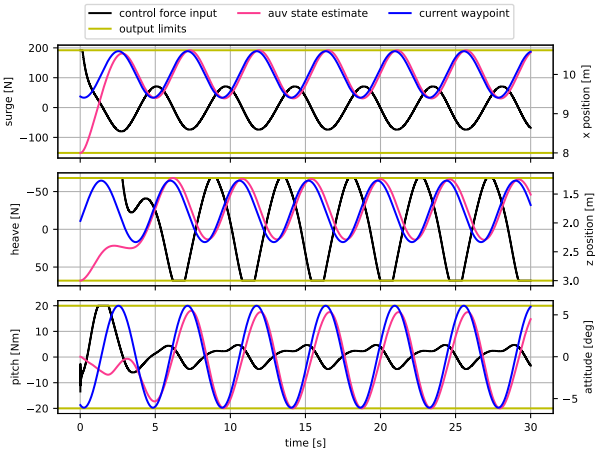

(d) Control forces of CPVA controller.

Animation

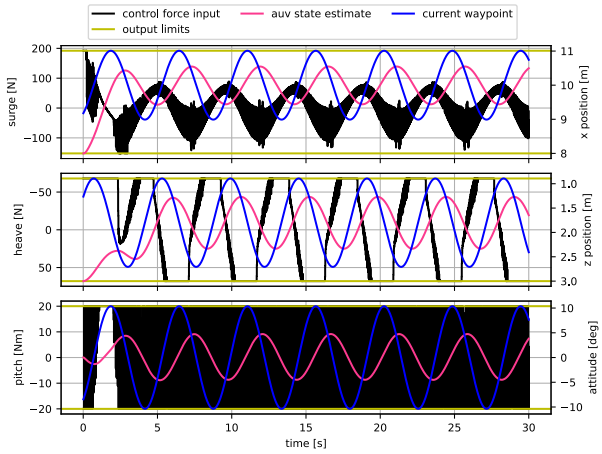

(e) Control forces of kinematic prediction method using the brute force pose controller.

Animation

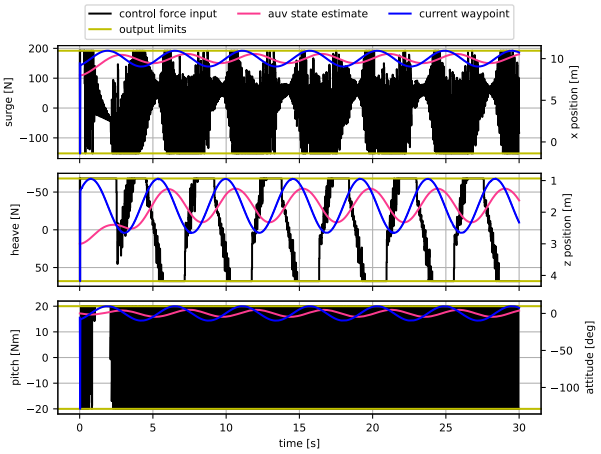

(f) Control forces of polynomial prediction method using the brute force pose controller .

Figure 7.15: Comparison of the control forces of the various guidance methods on the tuning evaluation scenario.

Observations The control forces for all methods were within the output limits. However, the brute force controller presented in Figure 7.15b shows some oscillatory behavior due to it highly aggressive tuning. Furthermore, both the prediction method presented in Figure 7.15e and Figure 7.15f show increased oscillations resulting from the interaction between the brute force controller and the prediction method. This conclusion is further supported by the observation that combining the prediction

methods with the slower manual pose controller, instead of the brute force controller, eliminates the high-frequency oscillations in the control input signal. Due to time constraints, eliminating the oscillatory behavior was not feasible. However, as the slow Scout dynamics effectively mitigate the effect of the high-frequency oscillations and only the low-frequency components of the control forces will significantly impact the Scout, the impact of this behavior on the validity of the results should be minimal.

As shown in Table 7.9, combining either of the prediction methods with the brute force pose controller leads to significantly improved performance compared to using the brute force controller alone and has the best performance overall. Excluding the prediction methods, the manually tuned CPVA controller outperforms all other tested controllers, indicating that controlling for acceleration does positively impact the performance. The CPV controller performed worse than the brute force pose controller, but it is expected that better performance can be obtained trough additional tuning efforts in future research.

7.3.5. Waypoint parameters

Table 7.10 shows the waypoint used for vertical docking. Each subsequent waypoint increasingly matches the docking goal state. In order to ensure the Scout passed the docking attempt registration line, the last goal waypoint was placed 5 cm behind this line. The acceptance radius r_{accept} to switch to the next waypoint is set to $r_{accept} = 0.3$ m. Due to time constraints, variations in these waypoints were not explored in this thesis, but could lead to improved vertical docking performance.

Table 7.10: Waypoints

Waypoint	**Variable**	$[x^n,\ z^n,\ \theta,\ u^n,\ w^n,\ q,\ \dot{u}^n,\ \dot{w}^n,\ \dot{q}]^T$
Initial state AUV	$\boldsymbol{x}_{start,k}$	$[7,\ 4,\ 0,\ 0,\ 0,\ 0,\ 0,\ 0,\ 0]^T$
Waypoint 1	$\boldsymbol{x}_{wp_1,k}$	$[\hat{x}^n_{nd} - 1,\ 4,\ 0,\ 0,\ 0,\ 0,\ 0,\ 0,\ 0]^T$
Waypoint 2	$\boldsymbol{x}_{wp_2,k}$	$[\hat{x}^n_{nd},\ \hat{z}^n_{nd} + 2,\ 0,\ 0,\ 0,\ 0,\ 0,\ 0,\ 0]^T$
Waypoint 3	$\boldsymbol{x}_{wp_3,k}$	$[\hat{x}^n_{ng},\ \hat{z}^n_{ng} + 1,\ 0,\ \hat{u}^n_{ng},\ \hat{w}^n_{ng},\ 0,\ 0,\ 0,\ 0]^T$
Goal waypoint	$\boldsymbol{x}_{ng,k}$	$[\hat{x}^n_{ng},\ \hat{z}^n_{ng},\ \hat{\theta}_{ng},\ \hat{u}^n_{ng},\ \hat{w}^n_{ng},\ \hat{q}_{ng},\ \hat{\dot{u}}^n_{ng},\ \hat{\dot{w}}^n_{ng},\ \hat{\dot{q}}_{ng}]^T$

7.3.6. Visual analysis

Using the animation tool to visualize the simulation, it was confirmed that all guidance methods correctly guide the Scout to the DS. A snapshot of the animation for each guidance method is presented in Figure 7.16 and the animations can be seen by clicking or scanning the associated QR codes. Note that the wave cancellation waiting strategy is also shown in Figure 7.16g.

A systematic test was performed to confirm that the AUV would be correctly controlled to a large set of waypoints, as presented in Table 7.11. It was confirmed that the AUV would either reach or pursue these test waypoints, providing strong evidence that the methods have been properly implemented.

Animation

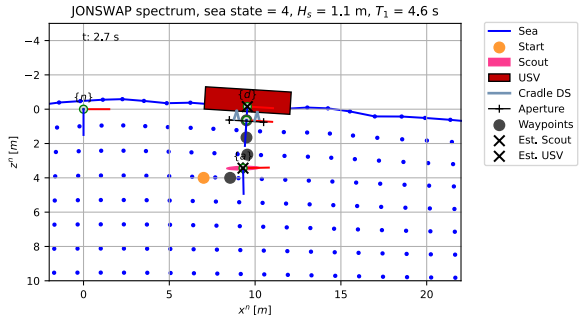

(a) Target state guidance with manual pose controller

Animation

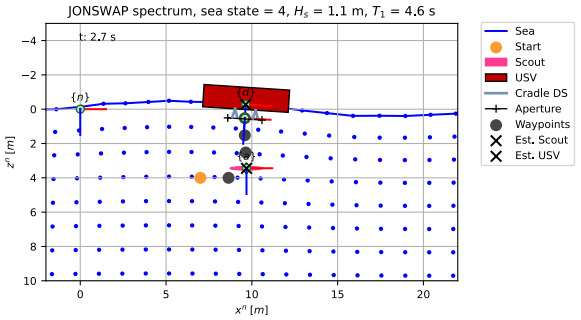

(b) Target state guidance with brute force pose controller.

Animation

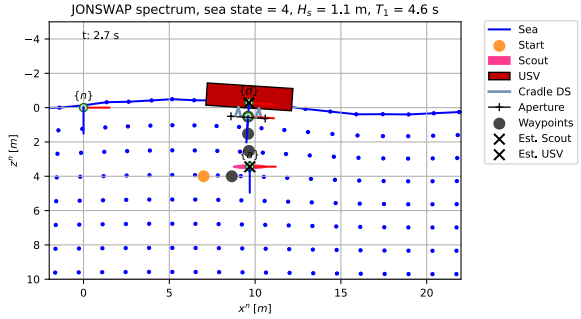

(c) Target state guidance with CPV controller.

Animation

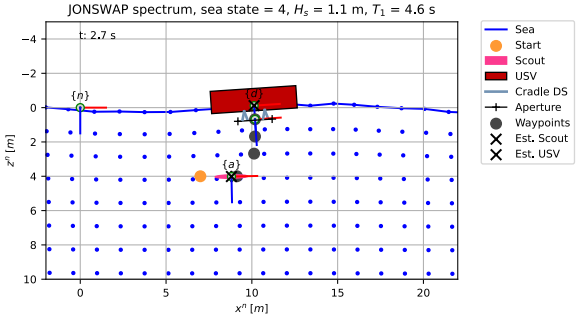

(d) Target state guidance with CPVA controller.

Animation

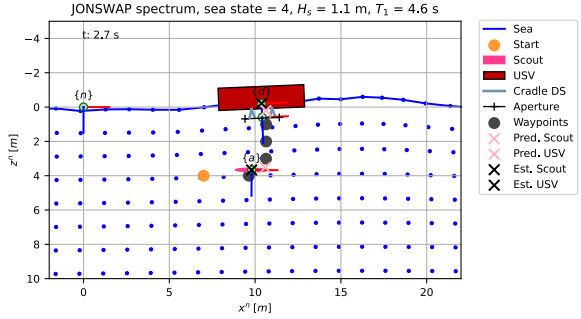

(e) Kinematic prediction combined with target guidance with the brute force pose controller.

Animation

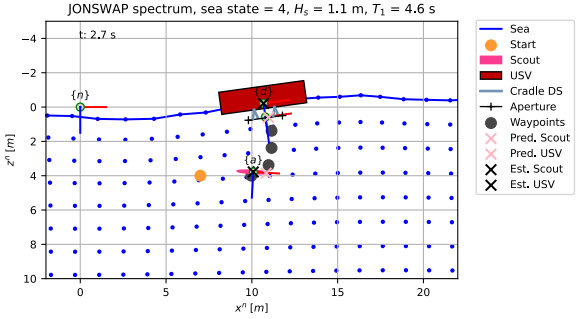

(f) Polynomial prediction combined with target guidance with the brute force pose controller.

Animation

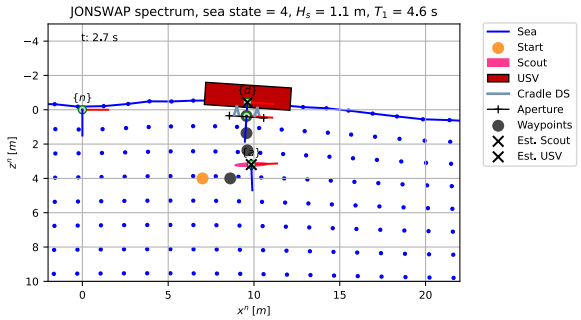

(g) Wave cancellation waiting strategy with target guidance with the brute force pose controller.

Figure 7.16: All guidance methods visualized.

Table 7.11: Evaluation of various waypoints. These tests were done using all target state controller variants. All waypoints were correctly reached or pursued by the Scout model.

x_{na}^n	z_{na}^n	θ_{na}^n	u_{na}^n	w_{na}^n	q_{na}^n	$\dot{u}_{na}^n$	$\dot{w}_{na}^n$	$\dot{q}_{na}^n$
Position tests								
2.0	5.0	0.0	0.0	0.0	0.0	0.0	0.0	0.0
-2.0	5.0	0.0	0.0	0.0	0.0	0.0	0.0	0.0
10.0	5.0	0.0	0.0	0.0	0.0	0.0	0.0	0.0
2.0	8.0	0.0	0.0	0.0	0.0	0.0	0.0	0.0
2.0	1.0	0.0	0.0	0.0	0.0	0.0	0.0	0.0
-2.0	8.0	0.0	0.0	0.0	0.0	0.0	0.0	0.0
10.0	8.0	0.0	0.0	0.0	0.0	0.0	0.0	0.0
Orientation tests								
-1.0	5.0	1.0	0.0	0.0	0.0	0.0	0.0	0.0
2.0	5.0	0.5π	0.0	0.0	0.0	0.0	0.0	0.0
2.0	5.0	1.0π	0.0	0.0	0.0	0.0	0.0	0.0
2.0	5.0	1.5π	0.0	0.0	0.0	0.0	0.0	0.0
2.0	5.0	2.0π	0.0	0.0	0.0	0.0	0.0	0.0
2.0	5.0	2.5π	0.0	0.0	0.0	0.0	0.0	0.0
2.0	5.0	3.0π	0.0	0.0	0.0	0.0	0.0	0.0
2.0	5.0	3.5π	0.0	0.0	0.0	0.0	0.0	0.0
2.0	5.0	4.0π	0.0	0.0	0.0	0.0	0.0	0.0
Velocity tests								
$2.0 + u_{na}^n t$	5.0	0.0	1.0	0.0	0.0	0.0	0.0	0.0
2.0	$5.0 + w_{na}^n t$	0.0	0.0	0.3	0.0	0.0	0.0	0.0
2.0	5.0	$q_{na}^n t$	0.0	0.0	0.5	0.0	0.0	0.0
Acceleration tests								
$2.0 + u_{na}^n t$	5.0	0.0	$\dot{u}_{na}^n t$	0.0	0.0	0.1	0.0	0.0
2.0	$5.0 + w_{na}^n t$	0.0	0.0	$\dot{w}_{na}^n t$	0.0	0.0	0.1	0.0
2.0	5.0	$q_{na}^n t$	0.0	0.0	$\dot{q}_{na}^n t$	0.0	0.0	0.1

7.4. Results

This section presents the results of the different guidance methods over increasing sea states based on the docking distributions. The simulations were performed for irregular North Sea waves at the different sea states described in Table 7.1. The performance of the guidance methods was evaluated based on the 99.7 % confidence interval obtained from 60 simulations. If the docking attempt did not occur within 120 seconds, the simulation was terminated for that particular sea state and higher ones in order to keep the simulation time manageable. As a result, some guidance methods have results at higher sea states than others.

7.4.1. Manual pose controller

For the manual pose control target guidance method, the obtained distributions are shown in Figure 7.17. The docking distribution is shown above the zero probability density line, while the 99.7 % confidence interval is shown in the shaded grey section below this line. In addition, these figures also display the capture limits of the DS described in Section 6.3.4, which is used to compare the effectiveness of the controllers.

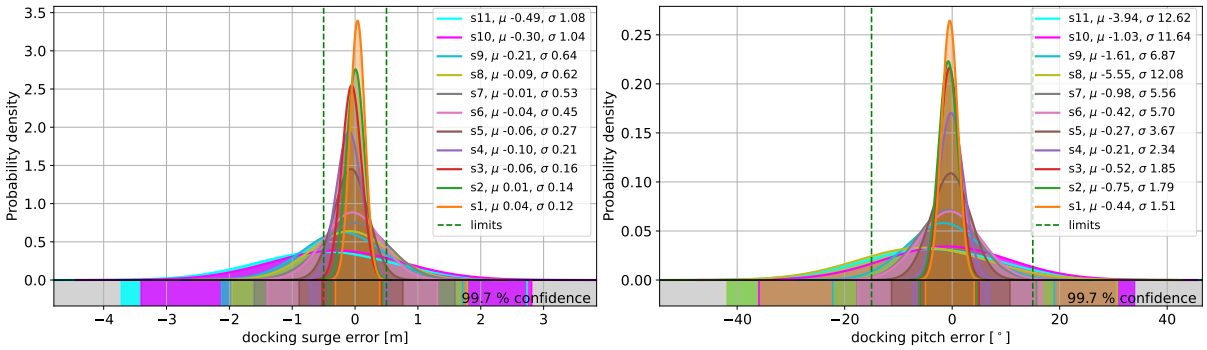

(a) Surge error. The mean surge error shifts to the left of the docking goal state with higher sea states, and the standard deviation increases.

(b) Pitch error. The mean pitch error shifts to the left of the docking goal state at higher sea states, and the standard deviation increases.

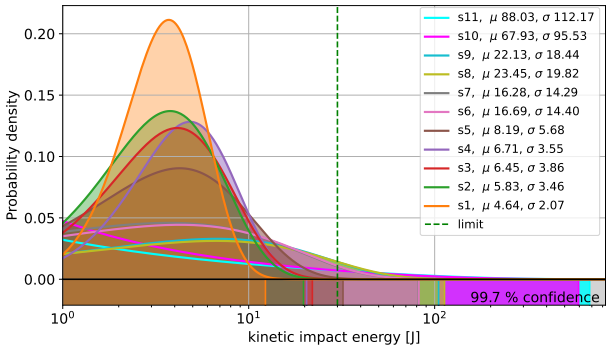

(c) Kinetic impact energy for each sea state fitted with a gamma distribution. The kinetic impact energy increases with the sea state.

Figure 7.17: Docking distribution for pose control with perfect navigation at different sea states. The 99.7% confidence interval is shown below the zero probability density line. Only sea state 1-11 are shown as the simulation was terminated at sea state 12 due to exceeding the maximum simulation time of 120 seconds.

As expected, the 99.7% confidence interval broadens for higher sea states. However, a shift of the mean is also apparent for the surge error distribution (Figure 7.17a) and the pitch error distribution (Figure 7.17b). This is likely caused by the asymmetry of the maximum thruster forces in the surge direction, as indicated in Table 4.4, but the particular tuning of this controller may increase this shift.

7.4.2. Target state guidance

The performance of the manual pose controller is compared to the performance obtained by the brute force controller, the CPV controller, and the CPVA controller. While Figure 7.17 provides a visual representation of the docking performance, a more compact representation is achieved by plotting only the 99.7 % confidence interval, as shown in Figure 7.18. For each sea state, the confidence intervals are plotted with the largest confidence interval behind and the smallest in front, which is used to identify the best-performing method. Furthermore, the capture limits are indicated with the vertical dashed green line. Table 7.12 presents the maximum operational sea state for each target state controller for this DS.

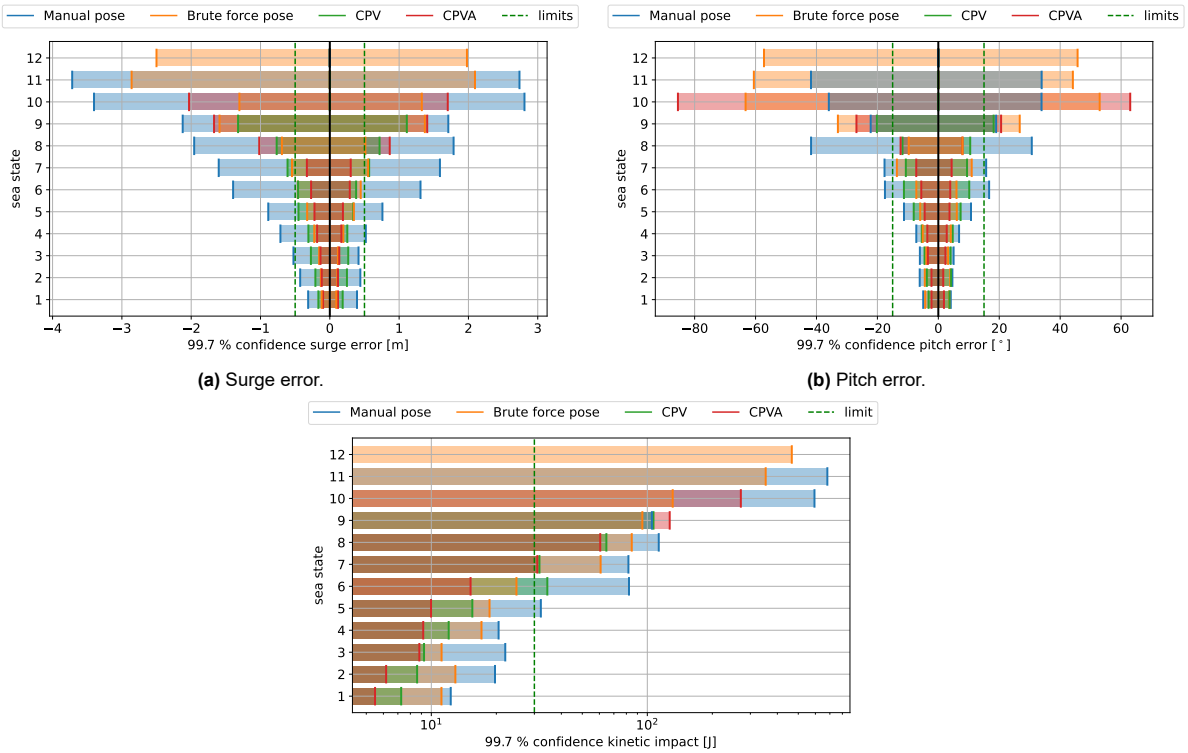

(a) Surge error.

(b) Pitch error.

(c) Kinetic impact energy. Since the kinetic impact energy is described with a gamma distribution, an one sided 99.7 % confidence interval used.

Figure 7.18: The 99.7 % confidence interval for different target state controllers at various sea states.

Table 7.12: Maximum operational sea state for different controllers

Controller	Surge	Pitch	Kinetic energy	Total	Uptime [%]
Manual pose	2	5	4	2	14.8
Brute force pose	6	8	6	6	82.7
CPV	6	8	5	5	59.4
CPVA	7	8	6	6	82.7

The performance of the controllers was evaluated within a simulation time frame of 120 seconds. Only the brute force controller was able to be simulated for all sea states within the given simulation time frame. As expected, the manual controller performed poorly, having a maximum operational sea state of 2. The CPV controller performed quite well despite being manually tuned, but it could benefit from additional tuning efforts. The CPVA controller came close to sea state 7, only being limited by the 99.7 % confidence interval for the kinetic impact energy of $[0,\ 30.96]$ J, which is very close to the 30 J threshold. Additional tuning efforts could help the CPVA controller achieve sea state 7. However, none of the controllers met the effectiveness benchmark of sea state 8.

7.4.3. Kinematic prediction

Figure 7.19 presents the 99.7 % confidence intervals of the kinematic prediction method using the brute force controller for various prediction times $t_{predict}$. In addition, Table 7.13 presents the maximum operational sea states based on the capture limits of the DS described in Section 6.3.4.

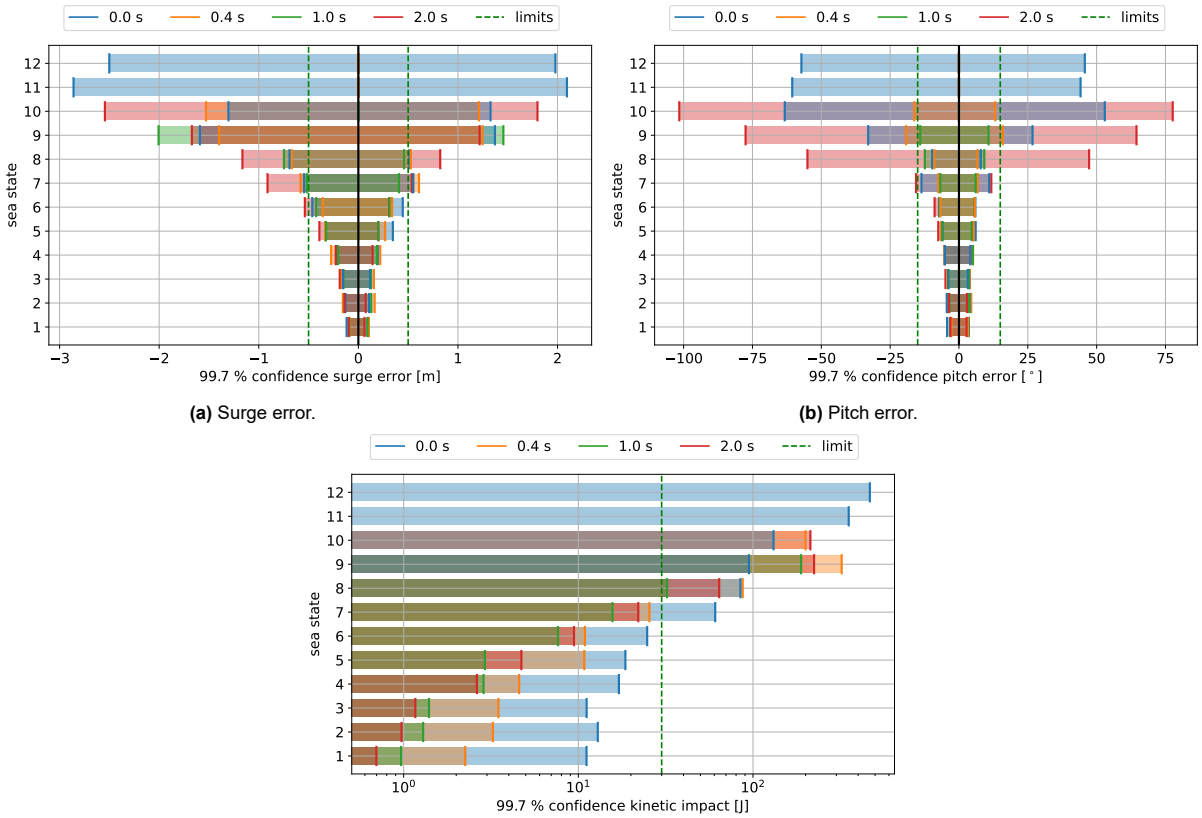

(a) Surge error.

(b) Pitch error.

(c) Kinetic impact energy.

Figure 7.19: The 99.7 % confidence interval over sea state for the kinematic prediction method for various prediction times. Predicting for both the AUV and the USV.

Table 7.13: Maximum operational sea state for kinematic prediction method using the brute force pose controller.

$t_{predict}$ $[\frac{m}{s}]$	Surge	Pitch	Kinetic energy	Total	Uptime [%]
0.0	6	8	6	6	82.7
0.4	6	8	7	6	82.7
1.0	6	9	7	6	82.7
2.0	5	6	7	5	59.4

Overall, the prediction times of 0.4 and 1.0 seconds show improved performance compared to no prediction while the 2.0-second prediction time seems to have decreased performance except for the kinetic energy. The data presented in the figures show that the confidence intervals for the kinetic impact energy, particularly at lower sea states, are smaller, compared to no prediction. However, for higher sea states, the performance gain seems to decrease, likely due to inaccurate predictions. The brute force optimization of the kinematic prediction method presented in Figure 7.11, showed that shorter prediction times are preferred for sea state 8 than for sea state 4, which is supported by these results.

Furthermore the performance for the pitch error seems to be significantly improved, but no improvement is observed for the confidence intervals for the surge error. These results support the RSME results for the kinetic prediction method on the tuning evaluation scenario, presented in Table 7.9, as the RSME improvement of the kinematic prediction method for the surge error is minor compared to the brute force pose controller without prediction.

7.4.4. Polynomial prediction

Figure 7.19 presents the 99.7 % confidence intervals of the polynomial prediction method using the brute force controller. The best two parameter settings from Table 7.8 are compared to the brute force

pose controller with no prediction. In addition, Table 7.14 presents the maximum operational sea states based on the capture limits of the DS described in Section 6.3.4.

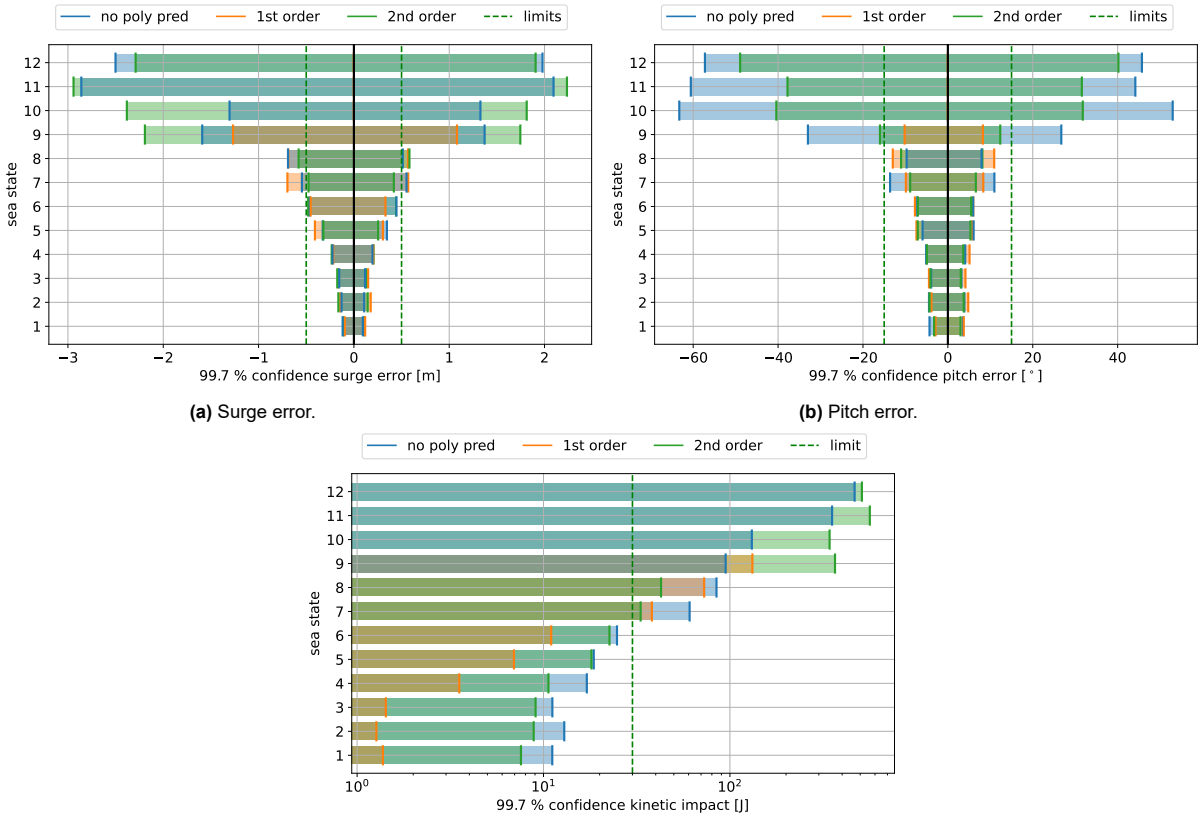

(a) Surge error.

(b) Pitch error.

(c) Kinetic impact energy.

Figure 7.20: The 99.7 % confidence interval over sea state for the polynomial prediction method. Best first order and second order polynomial are plotted. Predicting for both the AUV and the USV.

Table 7.14: Maximum operational sea state for the polynomial methods.

Method	Surge	Pitch	Kinetic energy	Total	Uptime [%]
Brute force pose	6	8	6	6	82.7
First order	6	9	6	6	82.7
Second order	7	8	6	6	82.7

The results suggest that the polynomial prediction method leads to smaller confidence intervals up to sea state 9 but larger confidence intervals for even higher sea states. However, it did not improve the maximum operational sea state. Overall, the first-order polynomial performed slightly better than the second-order polynomial at lower sea states, which is in agreement with the results obtained in the tuning evaluation scenario.

7.4.5. Wave cancellation waiting strategy

Figure 7.21 presents the 99.7 % confidence intervals of the brute force controller using the wave cancellation waiting strategy. The maximum simulation time frame was increased to 300 seconds, as it was expected that this strategy generally requires more time to dock. Various relative velocity thresholds were simulated, ranging from slightly below to slightly above the maximum impact velocity of 0.7 $\frac{\text{m}}{\text{s}}$. Furthermore, Table 7.15 presents the maximum operational sea states based on the capture limits of the DS described in Section 6.3.4 for these velocity thresholds.

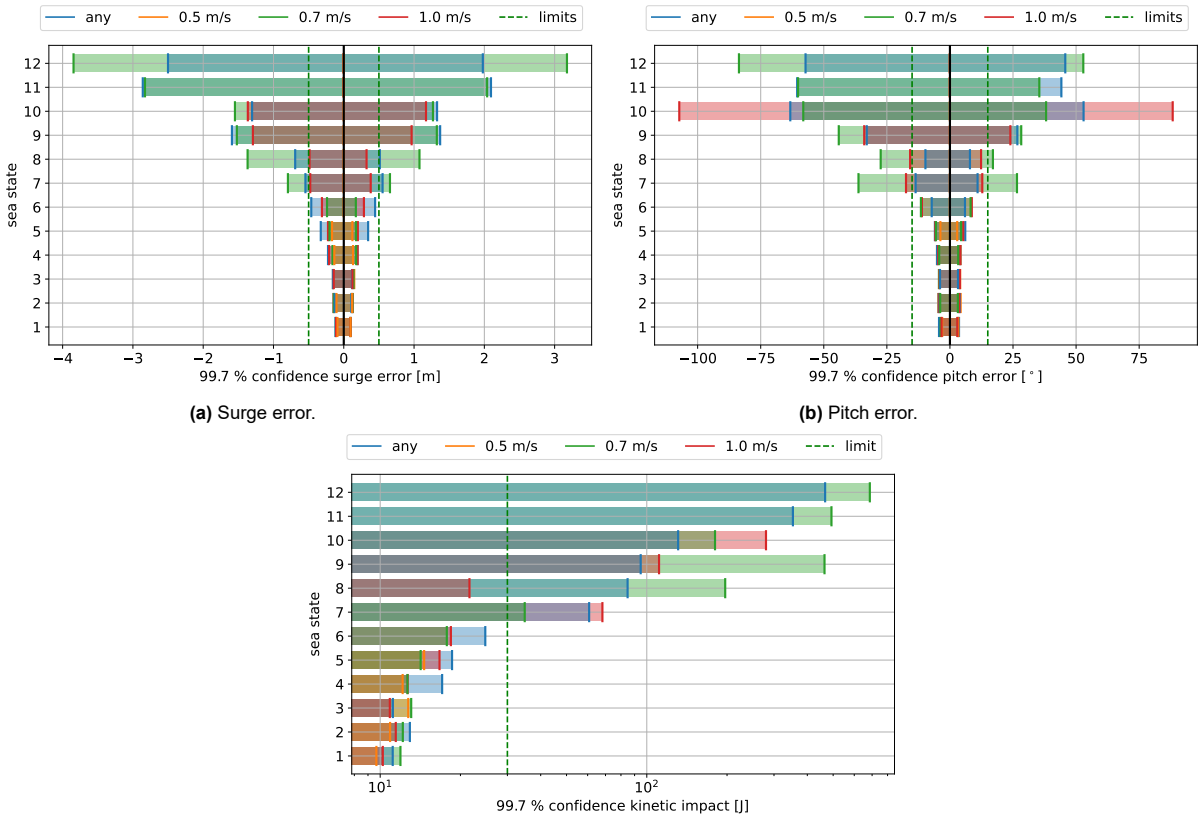

(a) Surge error.

(b) Pitch error.

(c) Kinetic impact energy.

Figure 7.21: The 99.7 % confidence interval over sea state for the brute force pose controller using the wave cancellation waiting strategy for various relative velocity thresholds.

Table 7.15: Maximum operational sea state for the brute force pose controller using the wave cancellation waiting strategy for a simulation time of 300 s

Threshold $[\frac{\text{m}}{\text{s}}]$	Surge	Pitch	Kinetic energy	Total	Uptime [%]
any	6	8	6	5	82.7
0.5	5	5	5	5	59.4
0.7	6	6	6	6	82.7
1.0	8	6	6	6	82.7

As anticipated, the relative velocity threshold increases the time required to dock. For example, using a 0.5 $\frac{\text{m}}{\text{s}}$ threshold, the simulation time of 300 seconds was only able to reach sea state 5, but did perform very well up to that sea state. Therefore, increasing the simulation time beyond 300 seconds may improve performance for this threshold. Up to sea state 6, all methods decreased the kinetic impact energy confidence interval significantly. Surprisingly, the 0.7 $\frac{\text{m}}{\text{s}}$ threshold resulted in a significant decrease in performance from sea state 7 compared to not waiting. The animation suggests that this results from the proximity of the last waypoint to the goal state, combined with more severe wave motion, which cannot be adequately controlled for, resulting in the Scout docking unwillingly. Moreover, since the control is aimed at reaching the waypoint before the goal waypoint, this can lead to an increased spread in the docking distributions The 1.0 $\frac{\text{m}}{\text{s}}$ threshold is likely to result in similar behavior, but only for higher sea states, which is observed at sea state 10. The 1.0 $\frac{\text{m}}{\text{s}}$ threshold performed well in terms of surge distributions, reaching the effectiveness benchmark of sea state 8. Furthermore, if it wasn't for the outlier at sea state 7 for the kinematic impact energy, it would have more or less made it to the effectiveness benchmark.

The wave cancellation waiting strategy has also been combined with the CPV and the CPVA controller.

The results are presented in Figure 7.22 and Figure 7.23 and the maximum operational sea state in Table 7.16 and Table 7.17 respectively.

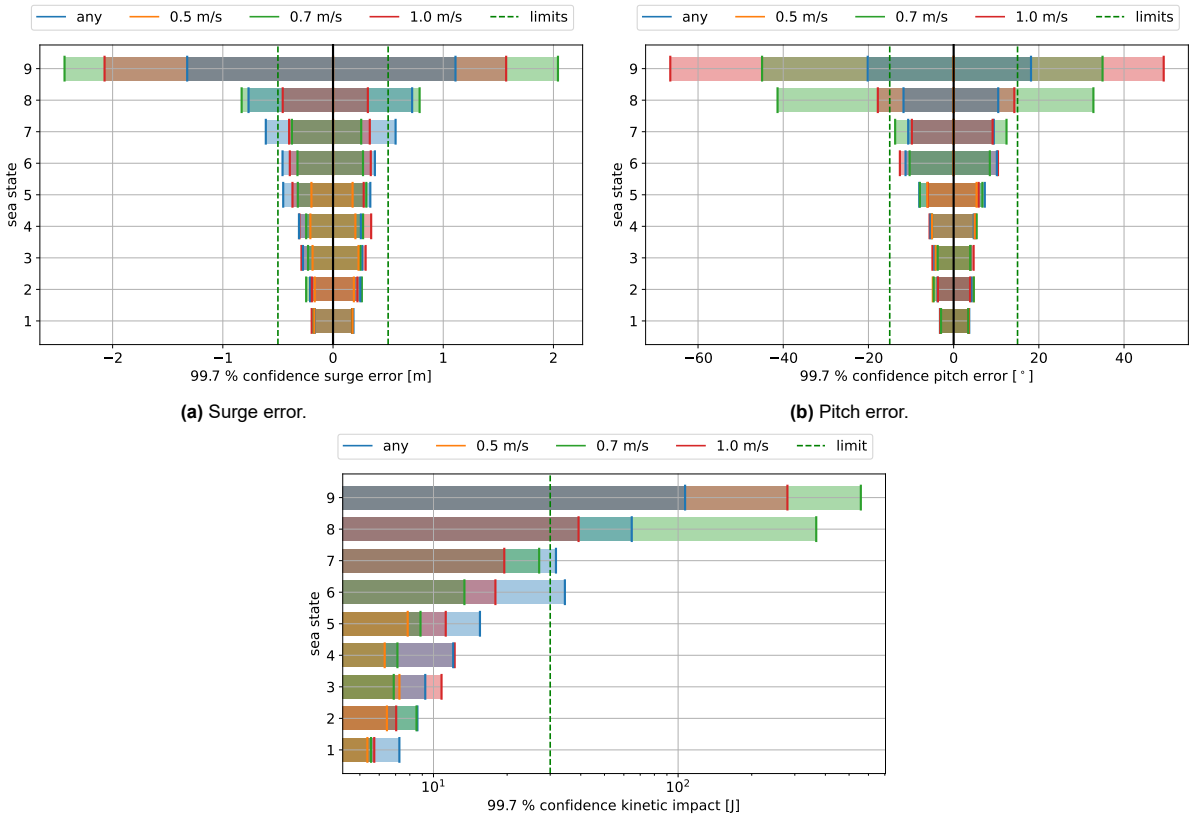

(a) Surge error.

(b) Pitch error.

(c) Kinetic impact energy.

Figure 7.22: The 99.7 % confidence interval over sea state for the CPV controller using the calm water assumption for various relative velocity thresholds.

Table 7.16: Maximum operational sea state for the CPV controller using the wave cancellation waiting strategy for a simulation time of 300 s

Threshold $\left[\frac{\text{m}}{\text{s}}\right]$	Surge	Pitch	Kinetic energy	Total	Uptime [%]
any	6	8	5	5	59.4
0.5	5	5	5	5	59.4
0.7	7	7	7	7	93.6
1.0	8	7	7	7	93.6

Both the 0.7 $\frac{\text{m}}{\text{s}}$ and the 1.0 $\frac{\text{m}}{\text{s}}$ threshold performed well for the CPV controller, achieving a maximum operational sea state that was two levels higher compared to not using the wave cancellation waiting strategy. The performance for the 0.7 $\frac{\text{m}}{\text{s}}$ relative velocity threshold showed a severe decrease at sea state 8. The same is observed from the 1.0 $\frac{\text{m}}{\text{s}}$ threshold at sea state 9, which agrees with the observations from the brute force pose controller using the waiting strategy.

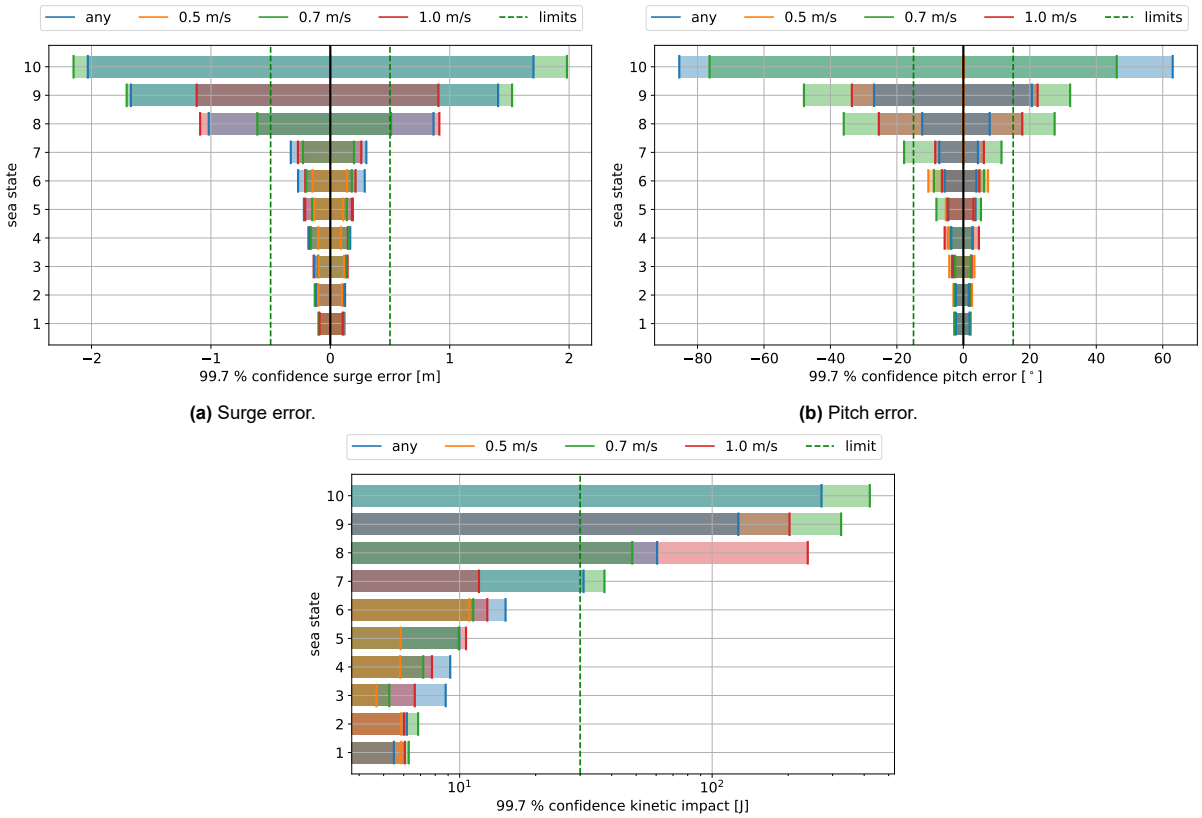

(a) Surge error.

(b) Pitch error.

(c) Kinetic impact energy.

Figure 7.23: The 99.7 % confidence interval over sea state for the CPVA controller using the calm water assumption for various relative velocity thresholds.

Table 7.17: Maximum operational sea state for the CPVA controller using the wave cancellation waiting strategy for a simulation time of 300 s

Threshold $\left[\frac{\text{m}}{\text{s}}\right]$	Surge	Pitch	Kinetic energy	Total	Uptime [%]
any	7	8	6	6	82.7
0.5	6	6	6	6	82.7
0.7	7	6	6	6	82.7
1.0	7	7	7	7	93.6

The CPVA with the waiting strategy performed better for the 1.0 $\frac{\text{m}}{\text{s}}$ threshold than the 0.7 $\frac{\text{m}}{\text{s}}$ threshold, with a maximum operational sea state of 7 compared to 6. The 0.5 $\frac{\text{m}}{\text{s}}$ threshold reached sea state 6, which is higher than for the CPV controller and the brute force pose controller for this threshold. Finally, the same severe decrease in performance is observed at higher sea states.

7.5. Discussion

The RSME scores presented in Table 7.9 obtained from the tuning evaluation scenario, provide a useful measure of the performance of the controllers evaluated in this study. The results indicate that the CPVA controller is the most effective, achieving a maximum operational sea state very close to sea state 7 (93.6 % operational uptime). The strong correlation between the RSME score and the maximum operational sea state achieved by the different guidance methods each controller presented in Table 7.12 highlights the value of this metric and the tuning evaluation scenario for tuning the controllers. With additional tuning efforts, the CPVA could potentially reach the effectiveness benchmark. This is for example indicated by the difference in maximum operation sea state of the manual pose target controller (sea state 2) and the brute force target controller (sea state 6), where only the tuning is different.

However, it should be noted that the lowest summed RSME is not a perfect predictor of performance for predictive guidance methods. For instance, even though the kinematic prediction method had the lowest summed RSME, it didn't result in a higher operational sea state than other methods. This is because achieving a high maximum operational sea state requires the confidence intervals for the surge error, the pitch error and the kinetic impact energy to fall the capture limits. If any of these intervals is larger than the capture limits, such as the surge error distribution in the case of the kinematic prediction method, the maximum operational sea state is limited to that distribution.

Combining the controllers with the wave cancellation waiting strategy is effective. For instance, the CPV method combined with the wave cancellation waiting strategy achieving a maximum operational sea state of 7, as opposed to 5 without the waiting strategy, increasing the operational uptime to 93.6 % from 59.4 %. Similarly, the waiting strategy was effective for the brute force pose controller and the CPVA controller in achieving a higher sea state. This simple strategy could possibly increase the maximum operational sea state even more, when lower relative velocity threshold are combined with longer simulating times. However, this would likely require to increase the distance between the last waypoint and the goal waypoint as well, to account for the more severe wave motion.

The brute force PID controller combined with the polynomial prediction method or the kinematic prediction method both decrease the confidence intervals. However, their performance increase tends to diminish at higher sea states. Nonetheless, combining these methods with the CPV and CPVA controllers in the future is promising for achieving a higher maximum operational sea state.

Finally, it should be noted that more simulations have been done for the polynomial and kinematic prediction methods. Although only the results of predicting for both the AUV and the USV are presented, separate simulations were conducted to evaluate the effectiveness of predicting for only the AUV or only the USV. The results from these additional simulations have not been included in the report in favor of increased readability, but support that predicting for both vehicles results in the best performance. This was also observed during the tuning of the prediction methods.

7.5.1. Contributions

This chapter makes several contributions to the field of underwater docking. Besides the vertical docking approach itself, which differs from the traditional horizontal approach used in previous studies, the study introduces several new guidance and prediction methods that are novel in the context of docking. These include the target state guidance combined with the CPV or the CPVA controllers, the polynomial prediction method, and the kinematic prediction method. These methods have the potential to improve the efficiency and accuracy of all underwater docking approaches.

Secondly, unlike previous studies that only evaluated the approach under a limited number of wave scenarios using a regular wave model, this study evaluated the approach across a range of sea states using an irregular wave model, providing a more comprehensive understanding of its effectiveness.

Finally, the study introduces the wave cancellation waiting strategy to the field of docking. While this is used in time-critical operations of construction vessels [6], the author has not yet seen this strategy used in the context of docking. Note that this strategy is only possible using a hovering AUV and not a cruising AUV, which is likely one of the reasons this strategy is not yet used.

7.5.2. Limitations

This chapter has several limitations. First, since the thruster dynamics were not modelled, unrealistic high-frequency oscillations were observed in the control forces using the kinematic and polynomial prediction methods, which are not realistic to be produced by the actual thrusters of the Lobster Scout. However, given that these dynamics are significantly faster than the Scouts dynamics, the control signal is essentially low pass filtered, thereby maintaining some degree of accuracy. Second, the chosen sample size is on the small side, making it difficult to distinguish between a change in the confidence interval caused by randomness or by a genuine change in the population. Third, the simulation time window was limited, which limited the insights gained at higher sea states for some methods as they

were not able to dock consistently within this time window. Finally, the waypoints were not varied, even though doing so could have increased docking performance.

7.5.3. Recommendations

The effectiveness benchmark for sea state 8 was not achieved by any of the guidance and control methods. A number of recommendations to increase the maximum operational sea state of the guidance methods in future research are listed below:

- One can simply accept a higher probability of failure for higher sea states, resulting in decreased confidence intervals.
- The DS capture limits can be increased with a different design.
- The guidance methods can be tuned, adapted, and combined to improve their performance.
- An increase in the maximum control force of the Lobster Scout or a control force that is symmetric in the surge direction will likely result in better performance.
- Since a slight shift in the mean of the surge and pitch distribution was observed with an increase in sea state. One could slightly bias the last goal waypoint to counter this effect, thereby centering the confidence intervals within the capture limits.
- Future research should explore MPC and ANFIS, for potentially improved performance.

7.6. Conclusion

This chapter aimed to answer the question *What are effective vertical guidance and control methods for the Lobster Scout?* The effectiveness benchmark for sea state 8 ($H_{\frac{1}{3}} = 4.85$ m, $\bar{T} = 7.9$ s and 98.3 % uptime) was not achieved by any of the guidance and control methods. However, the CPVA method and the CPV method combined with the wave cancellation waiting strategy are promising by achieving a maximum operational sea state of 7 ($H_{\frac{1}{3}} = 3.6$ m, $\bar{T} = 6.7$ s and 93.6 % uptime) which is certainly workable. With additional tuning efforts, these methods could potentially also meet the effectiveness benchmark.

The brute force PID controller combined with the polynomial prediction method and the kinematic prediction method led to smaller confidence intervals, indicating that these prediction methods are promising for increasing the maximum operational sea state. Future research exploring the combination of these methods with the CPV or CPVA controllers could yield better performance.

All in all, excluding the manually tuned target pose guidance method, the vertical guidance methods are promising for achieving an AUV-USV combination that is operational under medium (sea state 5) to rough seas (sea state 7). However, deteriorated navigation performance could severely limit the maximum operational sea state, and this is investigated in the next chapter.

8

Docking navigation model

An AUV that has onboard sensors to determine its location with respect to the earth navigation frame and given it has some idea of where the DS is as well, can cruise towards the neighborhood of the DS. However, even with a fixed DS, this information is likely not sufficient, and accurate relative pose information is required to dock [15]. In the case of vertical docking of the Lobster Scout to a USV this need for accurate pose information is even more severe due to the constant movement of the USV and the DS in response to the waves. Therefore, in order to evaluate to what extent vertical docking to a USV is viable with the Lobster Scout it is important to take into account docking navigation. The main research question to be answered in this chapter is:

What is the influence of navigation on vertical docking performance?

The objective of the navigation model is to estimate the true state of the AUV, the USV, and the DS. While the true states are available in the simulation, it cannot be assumed that they are available in the real world. The inputs of the navigation model are the true state of the AUV and the USV. A measurement model generates noisy measurements of the true states which are then processed by an EKF to produce state estimates. An overview of the navigation model is presented in Figure 8.1.

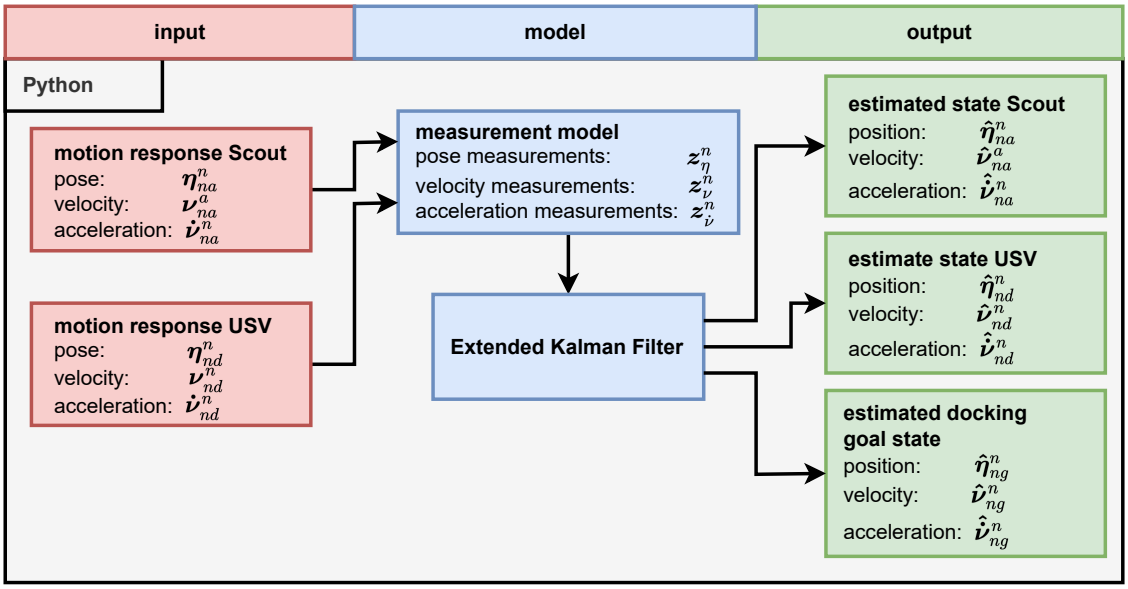

Figure 8.1: an input-output diagram of the navigation model

This chapter first discusses the general navigation strategy envisioned for vertical docking in Section 8.1. Then, the measurement model is discussed in Section 8.2. The discrete EKF is discussed in Section 8.3. Realistic parameter ranges for the measurements as well as the parameters for the EKF are determined in Section 8.4. The navigation model is verified in Section 8.5 and the results are presented in Section 8.6. The results are discussed in Section 8.7 and finally a conclusion is provided in Section 8.8.

8.1. Vertical docking navigation strategy

In this section, a navigation strategy is developed to answer the research question. First, the desired states to estimate are determined, which resulted in requiring the states of the AUV, the USV and the DS to be estimated. Then, various options for obtaining these state estimates are discussed, including the use of onboard sensors of the Scout, the USV and the use of docking sensors. Finally, the navigation strategy used to evaluate the influence of navigation is explained. This strategy was based the use of a USBL and a vision system as well as the onboard sensors of the Scout to obtain system measurements. These measurements were then filtered using two kinematic EKFs to obtain the desired state estimates.

8.1.1. Desired state estimates

For the AUV to successfully dock, it must accurately determine its own state as well as the state of the DS. However, since the relative pose between the $\{d\}$ and $\{g\}$ frames is fixed, the estimated state of the DS in $\{g\}$ is obtained from the estimated state of the USV in $\{d\}$ using the same transformation functions outlined in Section 5.4.

To conclude, the desired state estimates include those from AUV, the USV and the DS, each consisting of their estimated pose $\hat{\boldsymbol{\eta}}$, velocity $\hat{\boldsymbol{\nu}}$ and accelerations $\hat{\dot{\boldsymbol{\nu}}}$ respectively. In 3D, this results in 54 states, while 27 states are required in 2D for all three systems combined.

8.1.2. State information sources

This section discusses various options for obtaining estimates of desired states. State measurements can be obtained from a number of sources:

- **Scout navigation** The Scout can use its onboard sensors to produce measurements of its own state underwater. The onboard sensors of the Scout currently used for underwater navigation consist of a DVL, an accelerometer, a gyroscope, and a pressure sensor.
- **Docking navigation** Generally, three options for docking sensors are available, which include, acoustic, visual, and electromagnetic, as discussed in Section 2.2.4. These can be used to produce measurements of the DS or the USV relative to the AUV.
- **USV navigation** The goal of an USV is generally to do hydrographic surveys of the sea floor. For these surveys, the USV also has onboard sensors to measure its own state. Generally, the USV can measure its state using an onboard gyroscope, accelerometer, and GNSS as it is above the sea surface. Acoustic communication can be used to communicate the state of the USV to the Scout. Acoustic modems can communicate over $62.5\ \frac{\text{kbit}}{\text{s}}$ [17]. Furthermore, combined communication and localization systems exist such as the S2C R 42/65 USBL Underwater Acoustic Modem by Evologics [18].

Measurement filtering While the measurements of the various systems could be trusted directly, this likely leads to poor docking results as the direct measurements from most sensors are not sufficient [40]. A filter can be used to improve state estimates. A common filter to obtain state estimates for AUVs is the EKF, which is also used in the Lobster Scout [6, 70]. An EKF sequentially estimates the true state vector and uses Taylor series approximations to account for nonlinearities in the system dynamics and the measurements.

An EKF consists of a time update step and a measurement update step. In the time update step, a process model is used to compute the current (priori) state estimate using the previous state estimate and a correspondent priori covariance matrix that expresses the uncertainty of the state estimate. This time update step can be repeated many times as long as no measurement is received, however, the

uncertainty of the estimate will grow. In the measurement update step, the current (postiori) state estimate is computed using a received measurement and the latest priori state estimate. The uncertainty captured in the posterior covariance matrix is likely also reduced as a result of the measurement.

8.1.3. Strategy

Although various combinations between the options presented in Section 8.1.2 are possible, each with its own advantages and disadvantages, it is clear that it is at least possible for the Scout to obtain measurements of the USV, the DS and the Scout. For this study, it is less important to find the best navigation implementation, but rather, to gain a general understanding of the influence of the measurement performance on docking distributions and the maximum operational sea state. Therefore, the navigation strategy used in this thesis is based on the current kinematic EKF implementation of the Lobster Scout, combined with a common docking navigation strategy. The main rationale for using this strategy is that a lot of information is available about it, unlike other strategies. However, it is worth noting that other strategies may result in better performance.

The navigation strategy used in this thesis combines a USBL system and a vision system, both installed on the AUV, to measure the relative position and velocity of the USV and the DS. This approach has been successfully used in prior docking studies, such as [75, 14, 66, 22, 83, 82]. Additionally, it is assumed that the Scout's onboard sensors are used to determine its own state. In addition, an EKF is used to filter the states, which utilizes a kinematic process model as opposed to a kinetic process model. This is a common approach to model the state evolution of a system and is also used in the Lobster Scout [32, 6]. Finally, it is assumed that the same EKF is used to estimate the states of the Scout and the USV, and that all measurements are processed on the Scout.

The use of a kinematic model has the advantage of being less sensitive to model inaccuracies or parameter uncertainties, as highlighted in [32]. In contrast to a kinetic process model, a kinematic process model uses accelerations as inputs instead of forces. This approach enables the state estimates of the USV and the AUV to be updated at a high frequency between the relatively low-frequency velocity and pose measurements by the docking sensors, which is particularly relevant for dynamic docking under the presence of wave disturbances. Given that the GNC loop frequency is set at 100 Hz, as discussed in Section 7.3, these accelerations should be available at 100 Hz from both the Scout and the USV. It is feasible for the Scout to provide these accelerations at this rate, as its accelerometer updates at 300 Hz, which is higher than the GNC loop frequency. Additionally, it is assumed that the accelerations of the USV are measurable and transmitted to the Scout. A single precision float is around 4 bytes, and the acceleration vector in 3D for the USV consists of 6 states. Thus, it takes approximately 24 bytes to send an acceleration measurement of the USV to the Scout. The combined S2C R 42/65 USBL Underwater Acoustic Modem by Evologics, which can communicate up to 31.2 $\frac{\text{kbit}}{\text{s}}$ [18], should be capable of communicating these accelerations over 160 Hz. Therefore, this assumption is reasonable, and the kinematic EKF is used.

8.2. Measurements

This section discusses the model for sensor measurements. First, various docking sensor performance characteristics are presented. Then it is discussed which performance metrics to evaluate. Finally, the measurement model is developed.

8.2.1. Docking navigation sensors performance

A definition of the ideal homing (docking) sensor is given by [15] as: 'The ideal homing sensor would allow the AUV to reliably sense the relative location of the dock at any distance with high accuracy, and would update that information many times a second with no latency'. Unfortunately such a sensor does not exist and each sensor has a trade-off between the key performance characteristics presented in Table 8.1.

Table 8.1: Key sensor characteristics based on [15].

Characteristic	Description
Acquisition distance	The maximum range where measurements can be taken.
Accuracy	The bias of the measurements
Precision	The spread of the measurements
Update rate	The frequency at which measurement are taken.
Latency	The time delay between the request of a measurement and obtaining the measurement.
Environmental sensitivity	The degree to which measurements are disturbed by the environment.

8.2.2. Measurement simplifications

A number of simplifications are made for the measurement model. It was determined to simplify sensor measurements as direct noisy measurements of the true state of the AUV and the USV as well as to only consider the performance characteristics update rate and precision.

Sensor measurements To simplify the navigation model, it has been decided generate direct noisy measurements of the true states of the Scout and the USV, rather than simulating each sensor independently with its own performance characteristics. For the accelerations, these noisy measurements are taken at 100 Hz, but for the pose and velocity measurements, the influence of the update rate is investigated.

The performance metrics presented in Table 8.1 offer a comprehensive view of navigation performance. However, evaluating the influence of all of them would be both time-consuming and complex. Since this study limits itself to the final meters to the DS as this is the most critical and unique part of vertical docking, the analysis can be somewhat simplified. The paragraphs below discuss why acquisition distance, latency, environmental sensitivity and accuracy are neglected for an initial analysis.

Neglecting acquisition distance The range of the vision system is most limiting in poor water quality, but light markers can be added to the USV, which can extend the range of the vision system to at least a couple meters [75, 15], Therefore, it is assumed that measurements can be taken in the final docking stage and thus the acquisition distance of sensors, although important to consider when the AUV is further away from the DS, is ignored.

Neglecting latency Latency is neglected in this study because it is negligible compared to the slow dynamics of the robot. Physical and process latency are the two types of latency. Physical latency is negligible for light signals because of its high propagation speed. Acoustic signals propagate through salt water at a speed of approximately 1500 $\frac{\text{m}}{\text{s}}$. Assuming the final docking approach starts 10 m from g, the round-trip time for a signal to travel to the DS and back is approximately 6 ms. The maximum speed of the Scout is 2 $\frac{\text{m}}{\text{s}}$, which results in a negligible displacement of about 1 cm during this time. In addition, process latency varies based on factors within the Scout and differs for different sensors, but it is also assumed to be small compared to the robot's dynamics.

Neglecting environmental sensitivity Environmental sensitivity can result in two types of measurement faults. The first type occurs when the measurement is missed entirely due to the signal being indistinguishable from background noise. The second type is a false positive, which can lead to a poor measurement of the true system state. The occurrence of these poor measurements depends heavily on the operating environment and the type of sensors used. Fortunately, there are various algorithms available to detect and reject false positives, essentially resulting again in the first measurement fault where a measurement is missed altogether. Therefore, investigating the influence of missed measurements can also be achieved by observing the effect of a reduced update rate, which is already considered.

Neglecting accuracy Chapter 6 explains that the probability of a successful dock can be calculated by comparing the area under the docking distribution curve that falls within the cradle capture limits to the total area of the distribution. Any bias that cannot be compensated for by the navigation system or that does not trend to zero with decreasing distance between the AUV and the DS will shift the docking distribution curves. The influence of this absolute bias can thus be assessed by calculating the probability of success for the shifted distributions after the fact. Even then, if the absolute bias can be compensated for by shifting the last waypoint slightly, this impact is minimized. Therefore, to investigate the impact of navigation performance, the study focuses on the update rate and precision since their effects on the docking distributions are not straightforward and not easily compensated for.

Conclusion In summary, it was decided to model measurements as direct noisy measurements of the true state of the AUV and the USV, rather than separately modelling each sensor to simplify the navigation model. Additionally, measurement quality is investigated in terms of update rate and precision. By examining the impact of these two factors on docking performance, this study aims to provide a practical understanding of the importance of navigation performance on vertical docking.

8.2.3. Measurement model

The measurement model should capture the performance metrics: measurement precision and update rate. How these performance metrics are included in the measurement model is addressed below.

Update rate The acceleration measurements are taken at every time step, while the pose and velocity measurements made by the docking sensors are taken at a set update rate, with update period t_z.

Precision The precision of the acceleration, velocity and pose measurements are each captured by a diagonal measurement noise covariance matrix, denoted with Σ^2. This matrix modelled as a constant precision that is independent of the distance or angle between the AUV and the USV.

Acceleration measurements The acceleration measurements $\boldsymbol{z}_{\dot{\nu},k}$ for the AUV and the USV for at times step k are modelled as:

$$\begin{aligned} \boldsymbol{z}^a_{\dot{\nu}_{na},k} &= \dot{\boldsymbol{\nu}}^a_{na,k} + \boldsymbol{e}^a_{\dot{\nu}_{na},k}, \\ \boldsymbol{z}^n_{\dot{\nu}_{nd},k} &= \dot{\boldsymbol{\nu}}^n_{nd,k} + \boldsymbol{e}^n_{\dot{\nu}_{nd},k}, \\ \boldsymbol{e}^a_{\dot{\nu}_{na},k} &\sim \mathcal{N}(\mathbf{0}, \Sigma^2_{\dot{\nu}_{na}}), \\ \boldsymbol{e}^n_{\dot{\nu}_{nd}} &\sim \mathcal{N}(\mathbf{0}, \Sigma^2_{\dot{\nu}_{nd}}). \end{aligned} \tag{8.1}$$

Here, the measurement noise $\boldsymbol{e}^n_{\dot{\nu}_i,k}$ for $i \in \{na, nd\}$ is modelled as a zero mean multivariate normal distribution where $\Sigma^2_{\dot{\nu}_i}$ is the diagonal covariance matrix that captures the acceleration measurement noise, given by:

$$\Sigma^2_{\dot{\nu}_i} = \begin{bmatrix} \Sigma^2_{\dot{v}_i} & 0 \\ 0 & \Sigma^2_{\dot{q}_i} \end{bmatrix}. \tag{8.2}$$

Furthermore, the acceleration measurements are used directly as estimate for the acceleration of the AUV or USV, that is:

$$\begin{aligned} \hat{\dot{\boldsymbol{\nu}}}^a_{na,k} &= \boldsymbol{z}^a_{\dot{\nu}_{na},k}, \\ \hat{\dot{\boldsymbol{\nu}}}^n_{nd,k} &= \boldsymbol{z}^n_{\dot{\nu}_{nd},k}. \end{aligned} \tag{8.3}$$

Pose and velocity measurements The pose and velocity measurements made by the docking sensors, taken after the time period t_z has passed, are modelled identically for the AUV and the USV. The velocity measurements for $i \in \{na, nd\}$ at time step k is given by:

$$\begin{aligned} \boldsymbol{z}_{\nu_i,k} &= \boldsymbol{\nu}_{i,k} + \boldsymbol{e}_{\nu_i,k}, \\ \boldsymbol{e}_{\nu_i,k} &\sim \mathcal{N}(\mathbf{0}, \Sigma^2_{\nu_i}), \\ \Sigma^2_{\nu_i} &= \begin{bmatrix} \Sigma^2_{v_i} & 0 \\ 0 & \Sigma^2_{q_i} \end{bmatrix}, \end{aligned} \tag{8.4}$$

where $\Sigma^2_{\nu_i}$ is the diagonal covariance matrix that captures the velocity measurement noise. The pose measurements for $i \in \{na, nd\}$ are given by:

$$\begin{aligned} \boldsymbol{z}_{\eta_i,k} &= \boldsymbol{\eta}_{i,k} + \boldsymbol{e}_{\eta_i,k}, \\ \boldsymbol{e}_{\eta_i,k} &\sim \mathcal{N}(\mathbf{0}, \Sigma^2_{\eta_i}), \\ \Sigma^2_{\eta_i} &= \begin{bmatrix} \Sigma^2_{p_i} & 0 \\ 0 & \Sigma^2_{\Theta_i} \end{bmatrix}, \end{aligned} \tag{8.5}$$

where $\Sigma^2_{\eta_i}$ is the diagonal covariance matrix that captures the pose measurement noise.

8.3. Discrete EKF

This sub-section describes the two discrete EKF which estimate the pose and velocity of the AUV and the USV. The state estimate of the DS is derived from the state estimate of the USV, which is discussed separately in Section 8.3.4. The EKF described here is developed using [51, 40, 34, 65]. In general, the EKF model is written as follows:

$$\begin{aligned} \boldsymbol{x}_{k+1} &= f(\boldsymbol{x}_k, \boldsymbol{u}_k, \boldsymbol{w}_k), \\ \boldsymbol{z}_k &= h(\boldsymbol{x}_k, \boldsymbol{e}_k), \end{aligned} \tag{8.6}$$

where:

- $\boldsymbol{x}_k$ is the true state vector consisting of the pose and velocity vector at time step k.
- $f(.)$ is the process model function.
- $\boldsymbol{u}_k$ is the input vector.
- $\boldsymbol{w}_k \sim \mathcal{N}(\mathbf{0}, Q_k)$ is the Gaussian process noise.
- $\boldsymbol{z}_k$ is the measurement vector.
- $h(.)$ is the measurement model function.
- $\boldsymbol{e}_k \sim \mathcal{N}(\mathbf{0}, R_k)$ is the Gaussian measurement noise.

Both f and h can be dependent on the step number k as well.

A fundamental assumption of the EKF is that the state vector is Gaussian distributed, that is for $i \in \{na,\ nd\}$:

$$p(\boldsymbol{x}_{i,k}) \sim \mathcal{N}(\boldsymbol{x}_{i,k}, P_{i,k}) \tag{8.7}$$

8.3.1. Process model

This section discusses the discrete kinematic process model $f(\boldsymbol{x}_k, \boldsymbol{u}_k, \boldsymbol{w}_k)$ for both the AUV and the USV.

True states
The true state contains the pose and velocities of the AUV and the USV, and is defined as:

$$\boldsymbol{x}_{na,k} = \begin{bmatrix} \boldsymbol{\eta}^n_{na,k} \\ \boldsymbol{\nu}^a_{na,k} \end{bmatrix}, \ \boldsymbol{x}_{nd,k} = \begin{bmatrix} \boldsymbol{\eta}^n_{nd,k} \\ \boldsymbol{\nu}^n_{nd,k} \end{bmatrix}. \tag{8.8}$$

Input
The acceleration is used as input and is given by rewriting the above equations as:

$$\begin{aligned} \dot{\boldsymbol{\nu}}^a_{na,k} &= \boldsymbol{z}^a_{\dot{\nu}_{na},k} - \boldsymbol{e}^a_{\dot{\nu}_{na},k} = \boldsymbol{z}^a_{\dot{\nu}_{na},k} + \boldsymbol{e}^a_{\dot{\nu}_{na},k}, \\ \dot{\boldsymbol{\nu}}^n_{nd,k} &= \boldsymbol{z}^n_{\dot{\nu}_{nd},k} - \boldsymbol{e}^n_{\dot{\nu}_{nd},k} = \boldsymbol{z}^n_{\dot{\nu}_{nd},k} + \boldsymbol{e}^n_{\dot{\nu}_{nd},k}. \end{aligned} \tag{8.9}$$

Note that the acceleration noise is assumed to be Gaussian and zero mean, thus the sign of the noise term can be changed.

Process model AUV
The discrete EKF assumes that the true state of the AUV evolves with the following kinematic equation:

$$\begin{aligned} \begin{bmatrix} \boldsymbol{p}^n_{na,k+1} \\ \Theta_{na,k+1} \\ \boldsymbol{v}^a_{na,k+1} \\ \omega_{na,k+1} \end{bmatrix} &= \begin{bmatrix} \boldsymbol{p}^n_{na,k} + TR^n_a(\Theta_{na,k})\boldsymbol{v}^a_{na,k} + \boldsymbol{w}^n_{p,k} \\ \Theta_{na,k} + T\omega_{na,k} + w_{\Theta,k} \\ \boldsymbol{v}^a_{na,k} + T(\boldsymbol{z}^a_{\dot{v}_{na},k} + \boldsymbol{e}^a_{\dot{v}_{na},k}) + \boldsymbol{w}^a_{v,k} \\ \omega_{na,k} + T(z_{\dot{\omega}_{na},k} + \boldsymbol{e}^a_{\dot{\omega}_{na},k}) + w_{\omega,k} \end{bmatrix} \\ &= f_{na}(\boldsymbol{x}_{na,k},\ \boldsymbol{u}_{na,k},\ \boldsymbol{w}_{na,k}) \\ \boldsymbol{x}_{na,k} &= [(\boldsymbol{p}^n_{na,k})^T,\ \Theta_{na,k},\ (\boldsymbol{v}^a_{na,k})^T,\ \omega_{na,k}]^T, \\ \boldsymbol{u}_{na,k} &= [(\boldsymbol{z}^a_{\dot{v}_{na},k})^T,\ z_{\dot{\omega}_{na},k}]^T, \\ \boldsymbol{w}_{na,k} &= [(\boldsymbol{w}^n_{p,k})^T,\ w_{\Theta,k},\ (\boldsymbol{w}^a_{v,k})^T,\ w_{\omega,k},\ (\boldsymbol{e}^a_{\dot{v}_{na},k})^T,\ e^a_{\dot{\omega}_{na},k}]^T, \\ T &= t_{k+1} - t_k. \end{aligned} \tag{8.10}$$

These equations are rewritten as:

$$\begin{bmatrix} \boldsymbol{\eta}^n_{na,k+1} \\ \boldsymbol{\nu}^a_{na,k+1} \end{bmatrix} = \begin{bmatrix} I_{3x3} & T\tilde{R}^n_a(\Theta_{na,k}) \\ 0_{3x3} & I_{3x3} \end{bmatrix} \begin{bmatrix} \boldsymbol{\eta}^n_{na,k} \\ \boldsymbol{\nu}^a_{na,k} \end{bmatrix} + \begin{bmatrix} 0_{3x3} \\ TI_{3x3} \end{bmatrix} (\boldsymbol{z}^a_{\dot{\nu}_{na},k} + \boldsymbol{e}^a_{\dot{\nu}_{na},k}) + \begin{bmatrix} \boldsymbol{w}^n_{\eta_{na},k} \\ \boldsymbol{w}^a_{\nu_{na},k} \end{bmatrix} \tag{8.11}$$

The notation of the rotation matrix $\tilde{R}^n_a(\Theta_{na,k|k})$ is not entirely correct, but is convenient to write this way. $\tilde{R}^n_a(\Theta_{na,k|k})$ is of the form:

$$\tilde{R}^n_a(\Theta_{na,k}) = \begin{bmatrix} cos(\theta_{na,k}) & sin(\theta_{na,k}) & 0 \\ -sin(\theta_{na,k}) & cos(\theta_{na,k}) & 0 \\ 0 & 0 & 1 \end{bmatrix} \tag{8.12}$$

Process model USV
The process model $f(.)$ for the USV differs slightly from the one used for the AUV. Since it has been assumed in Section 5.5.3 that the USV only rotates with small angles, the kinematic motion model is simplified by assuming that $\tilde{R}a^n(\Theta na, k) \approx I_{3x3}$. Consequently, the kinematic process model is given by:

$$\begin{aligned} \begin{bmatrix} \boldsymbol{\eta}^n_{nd,k+1} \\ \boldsymbol{\nu}^n_{nd,k+1} \end{bmatrix} &= \begin{bmatrix} I_{3x3} & TI_{3x3} \\ 0_{3x3} & I_{3x3} \end{bmatrix} \begin{bmatrix} \boldsymbol{\eta}^n_{nd,k} \\ \boldsymbol{\nu}^n_{nd,k} \end{bmatrix} + \begin{bmatrix} 0_{3x3} \\ TI_{3x3} \end{bmatrix} (\boldsymbol{z}^n_{\dot{\nu}_{nd},k} + \boldsymbol{e}^n_{\dot{\nu}_{nd},k}) + \begin{bmatrix} \boldsymbol{w}^n_{\eta_{nd},k} \\ \boldsymbol{w}^n_{\nu_{nd},k} \end{bmatrix} \\ &= f_{nd}(\boldsymbol{x}_{nd,k},\ \boldsymbol{u}_{nd,k},\ \boldsymbol{w}_{nd,k}). \end{aligned} \tag{8.13}$$

8.3.2. EKF measurement model

In Section 8.2.3 the model used to simulate pose and velocity measurements was presented. The measurement model function $h(\boldsymbol{x}_k, \boldsymbol{e}_k)$ is equivalent to the combined velocity and pose measurement model and relates the measurements $\boldsymbol{z}_{i,k}$ to the true states $\boldsymbol{x}_{i,k}$. The measurement model function for $i \in \{na,\ nd\}$ is given by:

$$\begin{aligned} \boldsymbol{z}_{i,k} = h(\boldsymbol{x}_k, \boldsymbol{e}_k) &= \boldsymbol{x}_{i,k} + \boldsymbol{e}_{i,k}, \\ \boldsymbol{e}_{i,k} &\sim \mathcal{N}(\boldsymbol{0}, R_{i,k}), \\ R_{i,k} &= \Sigma_i^2, \\ \Sigma_i^2 &= \begin{bmatrix} \Sigma_{\eta_i}^2 & 0 \\ 0 & \Sigma_{\nu_i}^2 \end{bmatrix}. \end{aligned} \tag{8.14}$$

The EKF measurement noise covariance matrix R_i is set to be identical to the measurement noise covariance matrix $\Sigma_{i,}^2$. Since R_i is designed to approximate the measurement noise and $\Sigma_{i,}^2$ is known, it makes sense to choose them to be equal. Although R_i may differ from $\Sigma_{i,}^2$ under certain conditions (e.g. when considering delays), it is reasonable to choose them to be identical for an initial evaluation.

8.3.3. EKF algorithm

This section describes the EKF algorithm. The derivation of the EKF can be found in [65]

Time update

If no measurement is received, for $i \in \{na,\ nd\}$, the priori state $\hat{\boldsymbol{x}}_{i,k+1|k}$ and priori covariance matrix $P_{i,k+1|k}$ is obtained with the following equations:

$$\begin{aligned} \hat{\boldsymbol{x}}_{i,k+1|k} &= f_i(\hat{\boldsymbol{x}}_{i,k|k}, \boldsymbol{u}_{i,k}, \boldsymbol{0}), \\ P_{i,k+1|k} &= F_{i,k+1|k} P_{i,k|k} F_{i,k+1|k}^T + G_{i,k+1|k} Q_i G_{i,k+1|k}^T, \end{aligned} \tag{8.15}$$

where the F matrix is calculated by partially differentiating the function f_i to $\boldsymbol{x}$ and evaluating it at the priori state estimate:

$$\begin{aligned} F_{i,k+1|k} &= \left. \frac{\partial f(\boldsymbol{x}, \boldsymbol{u}, \boldsymbol{w})}{\partial \boldsymbol{x}} \right|_{\boldsymbol{x}=\hat{\boldsymbol{x}}_{i,k+1|k}, \boldsymbol{u}=\boldsymbol{u}_{i,k}, \boldsymbol{w}=\boldsymbol{0}}, \\ F_{na,k+1|k} &= \begin{bmatrix} I_{3x3} & T\tilde{R}_a^n(\hat{\Theta}_{na,k}) \\ 0_{3x3} & I_{3x3} \end{bmatrix}, \\ F_{nd,k+1|k} &= \begin{bmatrix} I_{3x3} & TI_{3x3} \\ 0_{3x3} & I_{3x3} \end{bmatrix}. \end{aligned} \tag{8.16}$$

Note that only the AUV $F_{na,k+1|k}$ is non-linear due to the rotation matrix, while the $F_{nd,k+1|k}$ is linear. Furthermore, the G matrix is calculated with:

$$G_{i,k+1|k} = \left. \frac{\partial f(\boldsymbol{x}, \boldsymbol{u}, \boldsymbol{w})}{\partial \boldsymbol{w}} \right|_{\boldsymbol{x}=\hat{\boldsymbol{x}}_{i,k+1|k}, \boldsymbol{u}=\boldsymbol{u}_{i,k}, \boldsymbol{w}=\boldsymbol{0}} = \begin{bmatrix} I_{3x3} & 0_{3x3} & 0_{3x3} \\ 0_{3x3} & I_{3x3} & TI_{3x3} \end{bmatrix} \tag{8.17}$$

Finally, the noise independence between the states is assumed as such, Q_i is diagonal and given by:

$$Q_i = diag([q_{x,i}^2,\ q_{y,i}^2,\ q_{\theta,i}^2,\ q_{u,i}^2,\ q_{w,i}^2,\ q_{q,i}^2,\ \Sigma_{\dot{\nu}_i}^2]). \tag{8.18}$$

Measurement update
At step $k = k_z$ a measurement is received that is used to obtain the posterior state estimate and the estimated covariance matrix. The measurement update is then given by:

$$\begin{aligned} \hat{\boldsymbol{x}}_{i,k+1|k+1} &= \hat{\boldsymbol{x}}_{i,k+1|k} + K_k(\boldsymbol{z}_{i,k} - H\hat{\boldsymbol{x}}_{i,k+1|k}), \\ P_{i,k+1|k+1} &= P_{i,k+1|k} - K_k H P_{i,k+1|k}, \\ K_{i,k} &= P_{i,k+1|k} H^T (H P_{i,k+1|k} H^T + R_i)^{-1}, \\ H &= I_{6x6}, \end{aligned} \tag{8.19}$$

(8.20)

where the H matrix is obtained by taking the partial derivative of $h(.)$ to $\boldsymbol{x}$ and $K_{i,k}$ is the Kalman gain.

EKF algorithm overview
Now that both the time update and the measurement update are described, an overview of the complete EKF algorithm is given in Algorithm 1.

Algorithm 1 EKF algorithm

initialize $\hat{\boldsymbol{x}}_{\mathbf{0}}, P_0$
while not docked **do**
time update

$$\begin{aligned} \hat{\boldsymbol{x}}_{k+1|k} &= f(\hat{\boldsymbol{x}}_{k|k}, \boldsymbol{u}_k, \mathbf{0}) \\ F_{k+1|k} &= \left.\frac{\partial f(\boldsymbol{x}, \boldsymbol{u}, \boldsymbol{w})}{\partial \boldsymbol{x}}\right|_{\boldsymbol{x}=\hat{\boldsymbol{x}}_{k+1|k}, \boldsymbol{u}=\boldsymbol{u}_k, \boldsymbol{w}=\mathbf{0}} \\ G_{k+1|k} &= \left.\frac{\partial f(\boldsymbol{x}, \boldsymbol{u}, \boldsymbol{w})}{\partial \boldsymbol{w}}\right|_{\boldsymbol{x}=\hat{\boldsymbol{x}}_{k+1|k}, \boldsymbol{u}=\boldsymbol{u}_k, \boldsymbol{w}=\mathbf{0}} \\ P_{k+1|k} &= F P_{k|k} F^T + G Q G^T \end{aligned}$$

if measurement received **then**
measurement update

$$\begin{aligned} K_k &= P_{k+1|k} H^T (H P_{k+1|k} H^T + R)^{-1} \\ \hat{\boldsymbol{x}}_{k+1|k+1} &= \hat{\boldsymbol{x}}_{k+1|k} + K_k(\boldsymbol{z}_k - H\hat{\boldsymbol{x}}_{k+1|k}) \\ P_{k+1|k+1} &= P_{k+1|k} - K_k H P_{k+1|k} \end{aligned}$$

end if
$k = k + 1$
end while

8.3.4. Estimating the docking goal state

Section 5.4 explains how the true goal-state is obtained from the true state of the $\{d\}$ frame. Similarly, the estimated goal state is obtained from the estimated USV state. For illustration purposes, Equation 8.21 shows how to estimate the pose of $\{g\}$ given an estimate of the pose of $\{d\}$ using the transformation equations:

$$\hat{\boldsymbol{\eta}}^n_{ng} = \begin{bmatrix} \hat{\boldsymbol{p}}^n_{ng} \\ \hat{\Theta}_{ng} \end{bmatrix} = \begin{bmatrix} \hat{\boldsymbol{p}}^n_{nd} + R^n_d(\hat{\Theta}_{nd}) \boldsymbol{r}^d_{gd} \\ \hat{\Theta}_{nd} + \Theta_{dg} \end{bmatrix}. \tag{8.21}$$

The goal state velocity is obtained in a similar manner using Equation 5.23 and the goal state acceleration is obtained using Equation 5.24.

8.4. Navigation scenarios

To evaluate the influence of navigation, a realistic range of measurement performances for the pose, velocity, and acceleration measurements is determined in Section 8.4.1. The different measurement scenarios are then defined in Section 8.4.2. Finally, the parameters for the EKF are determined.

8.4.1. Measurement performance range

To establish a realistic range of sensor measurement performance, relevant literature is reviewed in this section.

Update rate To establish a baseline for onboard sensor performance, the Lobster Scout's sensor specifications are consulted. Table 8.2 summarizes the update rates of various sensors used in the Lobster Scout [6].

Acoustic docking sensors typically update at rates between 0.2 and 1 Hz, with a maximum update rate of 1 Hz [37, 52, 69, 87, 19]. According to [19], the update rate of acoustic docking sensors is usually lower than 0.5 Hz.

Vision systems for docking update at rates between 1 and 30 Hz. For instance, the vision system in [43] updated at 1 Hz, while the system used in [7] updated at over 10 Hz. In [45], a vision system achieved an update rate of 14 Hz, while in [57], a system achieved a rate of 15 Hz. Finally, in [37], the vision system had an update rate of over 30Hz.

Precision To obtain an initial estimate of the measurement noise matrix $\Sigma^2_{i,k}$, the measurement covariance matrix R used in the EKF of the Lobster Scout [6] provides a good estimate. The standard deviations assumed for various measurements in the Lobster Scout are presented in Table 8.2.

Table 8.2: The assumed measurement standard deviation for the Lobster Scout from [6] only considering the surge, heave and pitch DOF.

Description	Measures	Standard deviation	Update rate [Hz]
Accelerometer	$\dot{\boldsymbol{v}}^a_{na}$	$\sqrt{0.02} I_{2x2}$ $\frac{\text{m}}{\text{s}^2}$	300
Angular accelerometer	$\dot{q}^a_{na}$	$\sqrt{0.05}$ $\frac{\text{rad}}{\text{s}^2}$	300
Gyroscope	θ^a_{na}	0.004 $\frac{\text{rad}}{\text{s}}$	300
DVL	$\boldsymbol{v}^a_{na}$	$0.005 I_{2x2}$ $\frac{\text{m}}{\text{s}}$	4-15
Pressure sensor	z^a_{na}	$0.05 I_{2x2}$ m	16

Furthermore in [75], a vision system was developed for autonomous docking of an ROV. To determine the standard deviation of their vision system, a test was conducted where their ROV was positioned approximately 7.1 m from the light markers on the DS. The DS was fixed on the sea floor with a known pose and the estimated ROV position by the vision system with respect to the DS was measured. The test results showed a position standard deviation of $\sigma^g_{x_{ag}} = 0.32$ m in surge, $\sigma^g_{y_{ag}} = 0.33$ m in sway and $\sigma^g_{z_{ag}} = 0.13$ m for heave. However, a correction was applied using the more accurate angle estimates of the INS, which significantly reduced the position standard deviation to $\sigma^g_{x_{ag}} = 0.03$ m in surge, $\sigma^g_{y_{ag}} = 0.08$ m in sway and $\sigma^g_{z_{ag}} = 0.12$ m for heave.

Moreover, in [47] and [42], precision parameters for state estimation were obtained through experiments and were used for docking to a sea floor-based DS. Table 8.3 presents these parameters. Note that the pose standard deviations are given in spherical coordinates, whereas Cartesian coordinates are required for the simulation, so these parameters should only be used as a rough indication.

Table 8.3: Experimentally obtained standard deviations for a DS navigation system from [47, 42]. r and α are the distance and the angle between the AUV and the Light Emitting Diode (LED) array respectively.

Description	Standard deviation
DVL velocity	$0.00084 + 0.038\sqrt{\lvert \boldsymbol{v}_{na} \rvert}$ $\frac{\text{m}}{\text{s}}$
Fiber-Optic Gyroscope angular velocity	0.0 $\frac{^\circ}{\text{s}}$
Acoustic system radial distance	$\sqrt{0.66^2 + (0.01(\boldsymbol{p}^n_{na} - \boldsymbol{p}^n_{nd})^2}$ m
Acoustic system polar angle	0.174 rad
Acoustic system azimuthal angle	0.087 rad
Vision system radial distance	$0.2 + 0.0046r + 0.0122r^2$ m
Vision system polar angle	0.087 rad
Vision system azimuthal angle	$0.087 + 0.463(\pi - \lvert \alpha)$ rad

Performance range Overall, determining a realistic measurement performance range remains a challenge due to the large variety of sensors and the vast number of parameters involved. However, a broad range is established by utilizing values obtained from literature to obtain an impression of the influence of different performance parameters. In order to reduce the number of parameters for evaluation, some simplifying assumptions are made:

- The measurement parameters for the USV and AUV navigation are identical.
- The measurement update period for position and velocity measurements are identical
- The measurement position variance for x and z are identical.
- The measurement velocity variance for u and w are identical.
- The measurement acceleration variance for $\dot{u}$ and $\dot{w}$ are identical.

Using these assumptions, Table 8.4 provides the measurement performance range for the update rate and the measurement precision used in this Thesis.

Table 8.4: Measurement range for $i \in \{na,\ nd\}$

Description	Variable	Minimum	Maximum
Measurement update period	t_z	0.04 s	2 s
Linear acceleration noise	$\Sigma^2_{\dot{v}_i}$	$0.001 I_{2x2}$ $(\frac{\text{m}}{\text{s}^2})^2$	$0.1 I_{2x2}$ $(\frac{\text{m}}{\text{s}^2})^2$
Angular acceleration noise	$\Sigma^2_{\dot{q}_i}$	0.005 $(\frac{\text{rad}}{\text{s}^2})^2$	0.5 $(\frac{\text{rad}}{\text{s}^2})^2$
Linear velocity noise	$\Sigma^2_{v_i}$	$0.005^2 I_{2x2}$ $(\frac{\text{m}}{\text{s}})^2$	$0.2^2 I_{2x2}$ $(\frac{\text{m}}{\text{s}})^2$
Angular velocity noise	$\Sigma^2_{q_i}$	0.0001^2 $(\frac{\text{rad}}{\text{s}})^2$	0.01^2 $(\frac{\text{rad}}{\text{s}})^2$
Position noise	$\Sigma^2_{p_i}$	$0.05^2 I_{2x2}$ m^2	$1.0^2 I_{2x2}$ m^2
Attitude noise	$\Sigma^2_{\Theta_i}$	0.01^2 rad^2	0.5^2 rad^2

8.4.2. Measurement scenarios

Due to the large number of measurement parameters, it is infeasible to test all possible combinations of navigation performance parameters. Therefore, the navigation parameter space can only be roughly scanned using a set of scenarios. These scenarios range roughly from only using USBL to using both USBL and a high-performance vision system. In reality, the high-performance vision system should be available in the Terminal Homing step, while the USBL is available from the Approach Setup step as explained in Section 2.2.2. The scanning approach is further explained below.

Approach The approach used to scan the navigation parameter space is presented in Figure 8.2. A base scenario is defined with average navigation performance, located approximately in the middle of the navigation parameter space. Orthogonal scans are then performed along the update rate range, acceleration measurement precision range, and pose and velocity measurement precision range. This approach enables the investigation of the influence of the critical navigation performance factors, while

keeping the number of simulations limited. The resulting data from these scenarios is used to draw conclusions about the impact of navigation performance on the docking process. The base configuration is presented in Table 8.5. Furthermore, the different orthogonal scenarios are presented in 8.6.

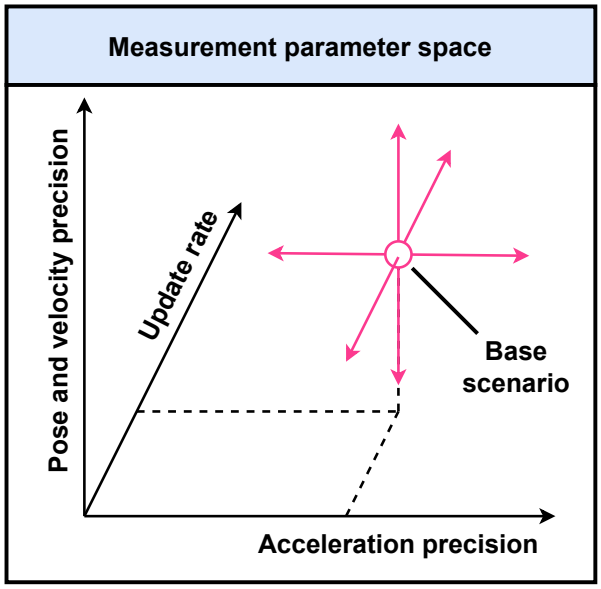

Figure 8.2: Approach for scanning the navigation parameter space.

Table 8.5: Measurement base scenario for $i \in \{na, nd\}$.

Description	Variable	Noise covariance
Measurement update period	t_z	0.2 s
Linear acceleration noise	$\Sigma^2_{\dot{v}_i}$	$0.01 I_{2x2}\ (\frac{\text{m}}{\text{s}^2})^2$
Angular acceleration noise	$\Sigma^2_{\dot{q}_i}$	$0.05\ (\frac{\text{rad}}{\text{s}^2})^2$
Linear velocity noise	$\Sigma^2_{v_i}$	$0.05^2\ \frac{\text{m}}{\text{s}})^2$
Angular velocity noise	$\Sigma^2_{q_i}$	$0.001^2\ (\frac{\text{rad}}{\text{s}})^2$
Position noise	$\Sigma^2_{p_i}$	$0.5^2 I_{2x2}$ m^2
Attitude noise	$\Sigma^2_{\Theta_i}$	0.1^2 rad^2

Table 8.6: Measurement parameter scenarios for $i \in \{na, nd\}$.

Scenario	Parameter	Value
1	$\Sigma^2_{\dot{\nu}_i}$	$diag([0.001,\ 0.001,\ 0.005])$
2		$diag([0.1,\ 0.1,\ 0.5])$
3	t_z	0.04 s
4		0.1 s
5		0.5 s
6		1 s
7		2 s
8	Σ^2_i	$diag([0.05^2,\ 0.05^2,\ 0.01^2,\ 0.005^2,\ 0.005^2,\ 0.0001^2])$
9		$diag([1^2,\ 1^2, 0.5^2,\ 0.2^2,\ 0.2^2,\ 0.01^2])$

8.4.3. EKF configurations

The EKF of the AUV and the USV is configured using the parameters presented in Table 8.7. Here the following considerations are made:

1. The initial state estimate is set to be equal to the first measurement, as this provides a reasonable starting point for the filter.
2. The initial covariance matrix is set to be large to account for the large uncertainty of the initial state estimate. Since the initial state estimate is set to be equal to the first measurement, $P_{i,0}$ is set proportional to the measurement noise variance. This ensures that the filter will quickly converge in the initial seconds as more measurements are incorporated.
3. The process noise covariance matrix Q_i is manually tuned to minimize the RSME between the true states and the estimated states.. In tuning, a balance must be struck between smoothing the estimate and allowing it to respond to rapid dynamic changes.

Table 8.7: EKF parameters for $i \in \{na, nd\}$.

Parameter	Value
$\hat{\boldsymbol{x}}_{\boldsymbol{i,0}}$	$\boldsymbol{z}_{i,0}$
$P_{i,0}$	$9\Sigma_i^2$
Q_i	$diag([0.003^2, 0.003^2, 0.001^2, 0.001^2, 0.001^2, 0.01^2, \Sigma_{\dot{\nu},i}^2])$
R_i	Σ_i^2

8.5. Verification

The EKF of the AUV and the USV are verified by checking the covariance of each of the state estimates and comparing the state estimates to the true states and the measurements. Finally, a visual analysis is done by observing the position state estimates in the animation.

8.5.1. Covariance convergence

A number of observations for a correctly implemented EKF are expected:

- The initial values of the diagonal state covariance matrix are large due to Consideration 2.
- As time progresses, the values of the diagonal state covariance matrix should gradually decrease and settle to a stable range.
- This range is established by the ratio of time updates to measurement updates. The covariance matrix should decrease at every measurement update while it should increase at every time update. As the ratio between time updates and measurement updates is greater than 1, a 'shark teeth' pattern is expected.

The convergence of covariance is verified using the base scenario, but with an update period of 0.1 seconds instead of 0.2 seconds The control loop operates at a frequency of 100 Hz, which means that time updates are performed every 0.01 seconds. For a measurement update period of 0.1 seconds, a 10-to-1 ratio between time updates and measurement updates is expected. Figure 8.3a displays the covariance for each state estimate for the AUV, while Figure 8.3b shows the covariance of the USV state estimates. To illustrate the 'shark teeth' pattern, Figure 8.4 is a zoomed-in version of Figure 8.3a.

All of the expected observations are observed in the various sub-figures. However, in the standard deviation plot of the angular velocity, the measurement covariance is very small and the measurements are trusted heavily, therefore the transient behavior is almost zero and the covariance reaches its stable range after the first measurement. In conclusion, the covariance plot supports that the EKF is working as expected.

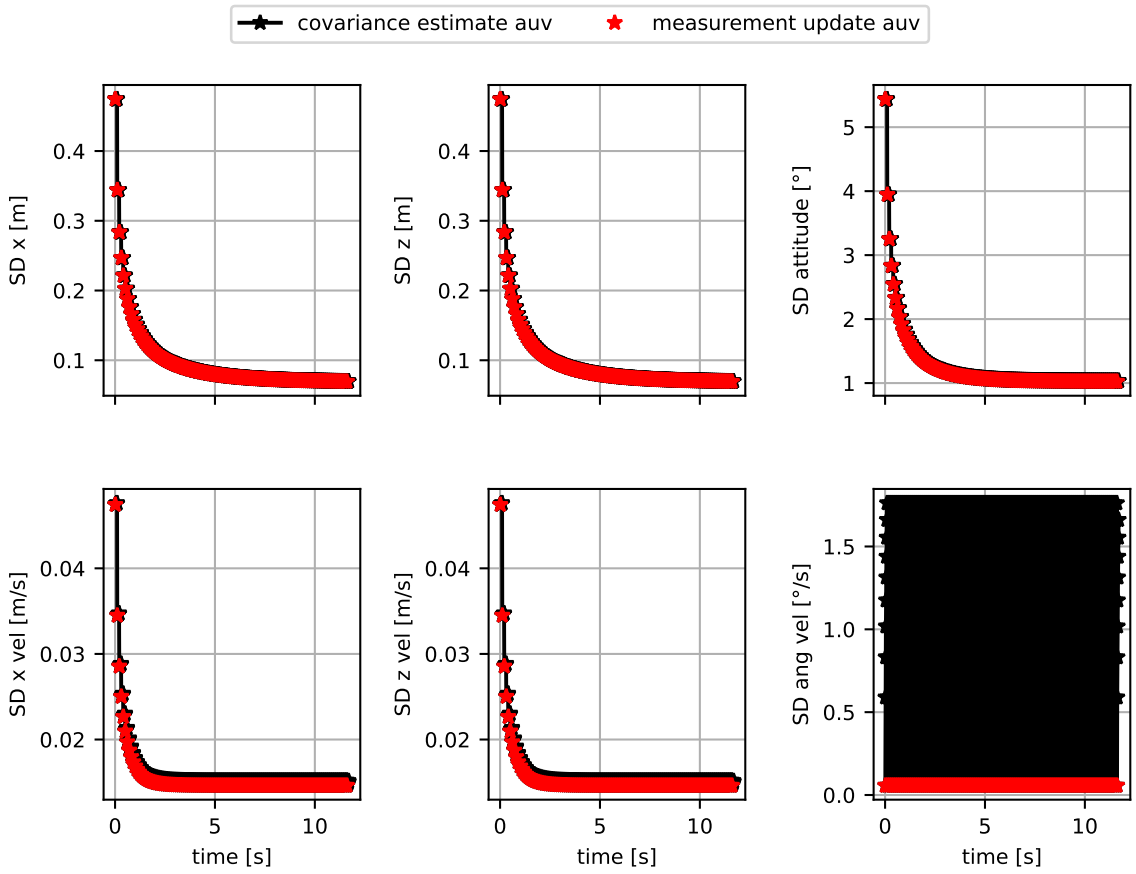

(a) The covariance plot of the Scout state estimate.

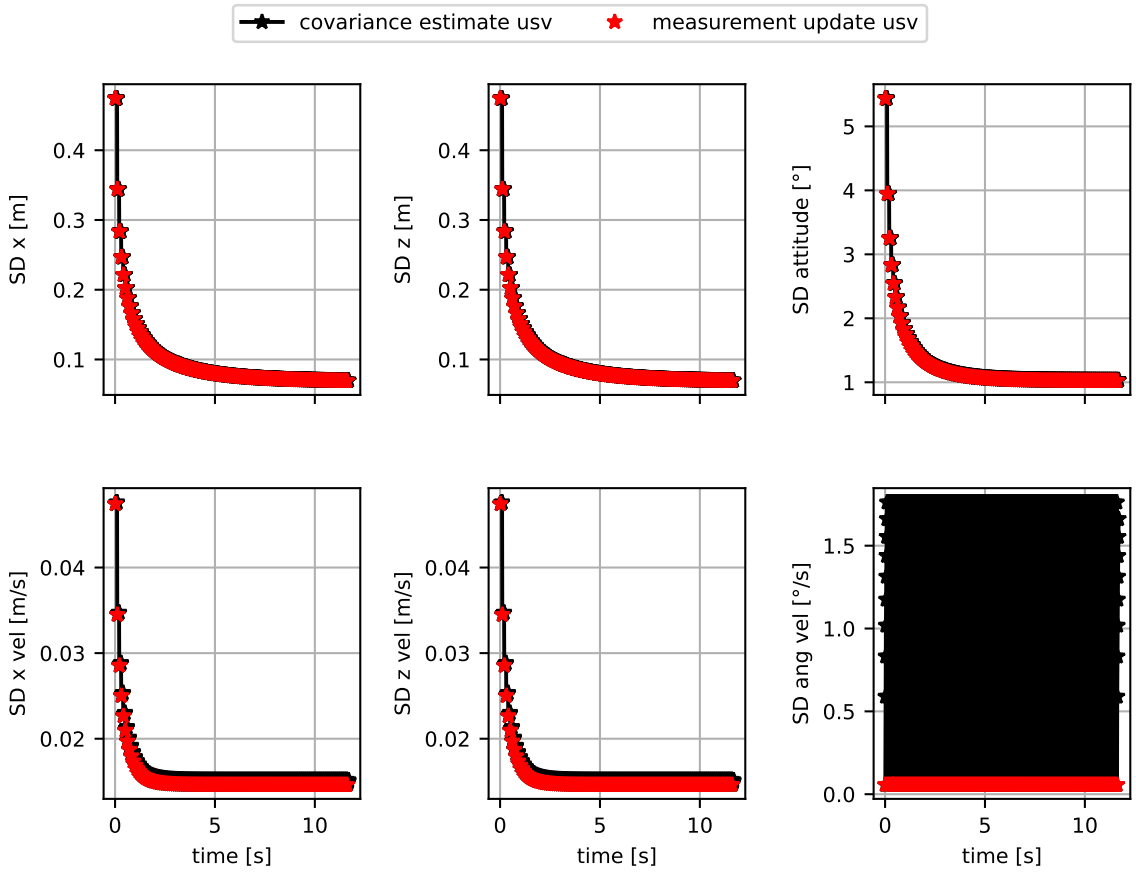

(b) The covariance plot of the USV state estimate covariance.

Figure 8.3: The covariance plots of the Lobster Scout and the USV.

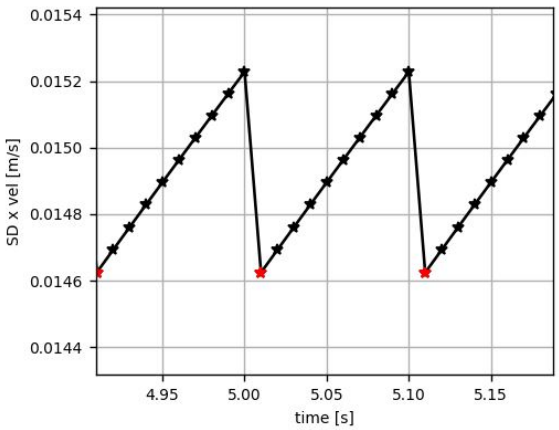

Figure 8.4: The covariance plot of the AUV EKF zoomed in. Each star is a time update while the red stars indicate that a measurement update is performed in addition.

8.5.2. State estimation

To assess the performance of state estimation, the true states, the measurements, and the estimated states are visually compared in Figure 8.5 for the Lobster Scout and in Figure 8.6 for the USV.

Additionally, comparing the RSME between the measurements and the true state, as well as the RSME between the state estimates and the true can provide a quantitative performance indication. These results are presented in Table 8.8. The filtering indeed results in significant improvement over the raw measurements as the RSME is significantly smaller. Furthermore, the long-term measurement RSME should converge to the measurement noise standard deviation, which the results support.

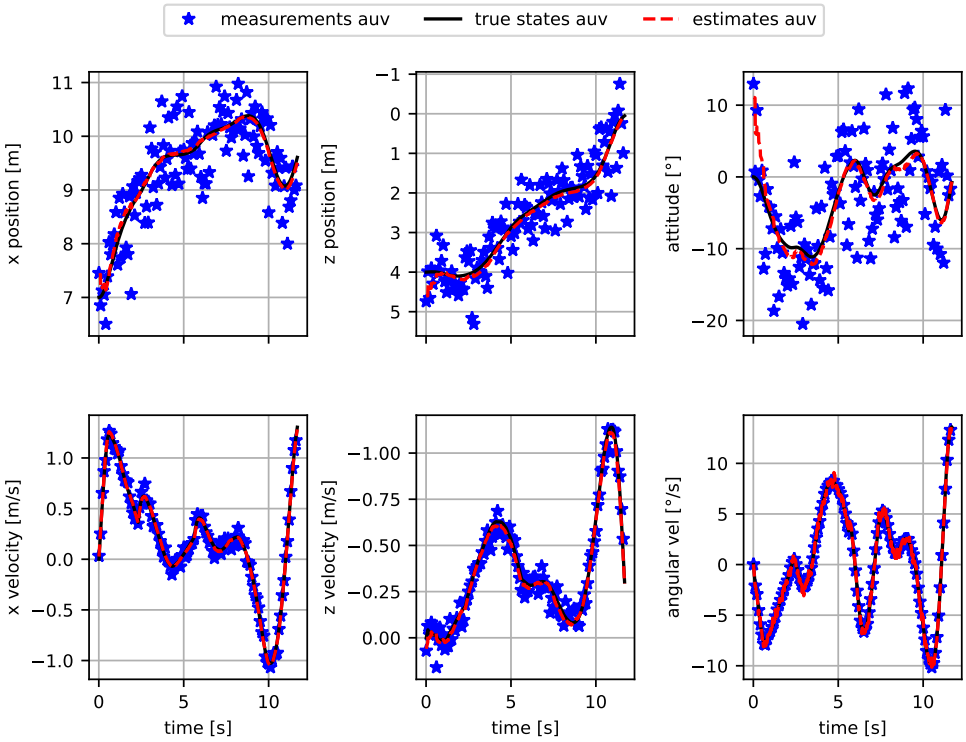

Figure 8.5: Comparison of the true states, state estimates and measurements for the USV.

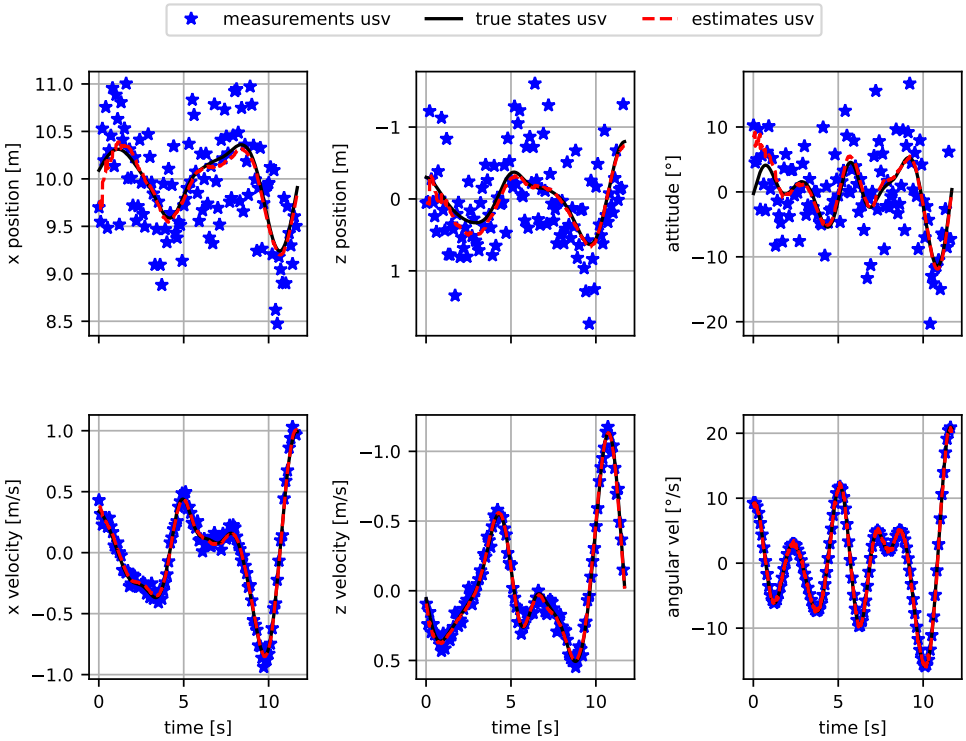

Figure 8.6: Comparison of the true states, state estimates and measurements for the Lobster Scout.

Table 8.8: RSME of the measurements and the state estimates.

Description	$rmse_x$	$rmse_z$	$rmse_\theta$	$rmse_u$	$rmse_w$	$rmse_q$	Sum
AUV measurements	0.51	0.51	0.097	0.055	0.053	0.006	1.23
USV measurements	0.43	0.52	0.092	0.05	0.052	0.008	1.16
AUV state estimates	0.068	0.11	0.03	0.012	0.017	0.005	0.24
USV state estimates	0.075	0.09	0.025	0.012	0.017	0.005	0.22

8.5.3. Visual analysis

Figure 8.7 displays the navigation tracking of the Scout and the USV position, and the associated QR code allows viewing of the animation, which confirms that the Scout and USV are correctly tracked.

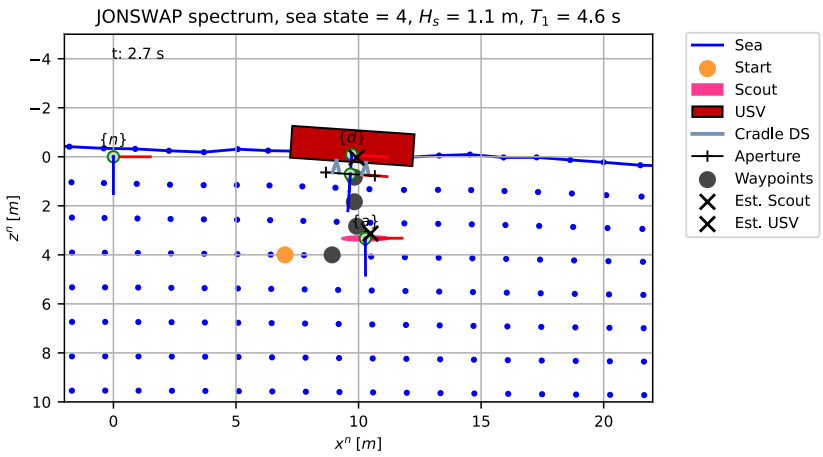

Animation

Figure 8.7: Position estimates of the AUV and the USV represented by black crosses.

8.6. Results

This section investigates the influence of various navigation factors on docking performance. These factors include update rate, pose and velocity measurement precision, and acceleration measurement precision. Due to time constraints, only two guidance methods from Chapter 7 were considered. The first method is the brute force pose controller for target state guidance, which is the simplest method. If effective, it could potentially lower the navigation system requirements as it only relies on pose state estimates. The second method is the CPV controller combined with the wave cancellation waiting strategy, which uses a relative velocity threshold of 1.0 $\frac{\text{m}}{\text{s}}$. This method was selected as it achieved the best performance overall using perfect state estimates.

The maximum simulation time was set to 120 seconds for the brute force pose controller and to 300 seconds for the CPV controller with the waiting strategy in order to account for the waiting time. Only sea state 0 to 8 were simulated, since these methods using perfect navigation did not exceed sea state 8 for any of the three docking distributions. Therefore, it was not expected to achieve a higher sea state.

Investigation of the influence of navigation on the polynomial prediction method and the kinematic prediction method was not possible due to time constraints. However, it is expected that their performance is highly dependent on navigational performance, as they amplify state estimate errors. This is left for future research to explore.

8.6.1. Update rate

In this section, the influence of update rate, with update period t_z is investigated.

Brute force pose control

Figure 8.8 presents the 99.7 % confidence intervals of the brute force pose controller for various update periods. The results for the brute force pose controller obtained in Chapter 7 using perfect navigation are also shown as a baseline. Furthermore, Table 8.9 presents the maximum operational sea states for each of the update periods based on the capture limits defined in Section 6.3.4.

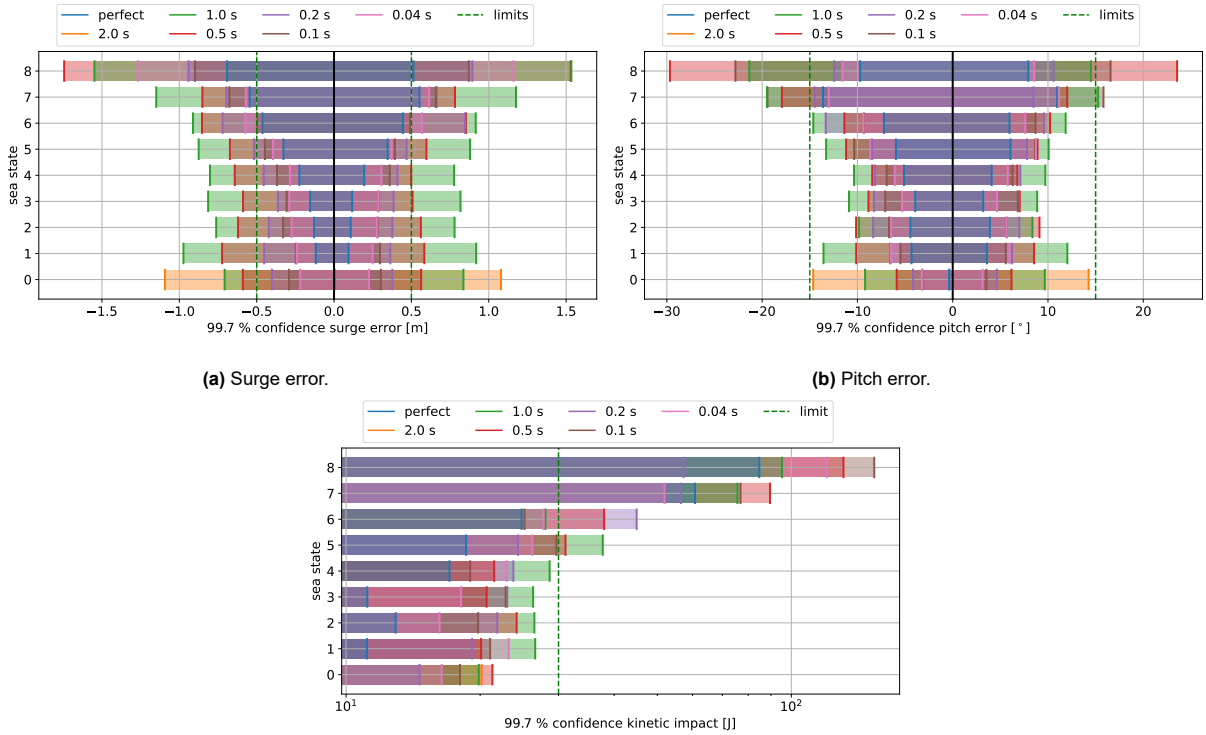

(a) Surge error.

(b) Pitch error.

(c) Kinetic impact energy.

Figure 8.8: The 99.7 % confidence intervals over sea states for the brute force pose controller for various measurement update periods.

Table 8.9: Maximum operational sea state for the brute force pose controller for various update periods.

Update period [s]	Surge	Pitch	Kinetic energy	Total	Up-time [%]
Perfect	6	8	6	6	82.7
2.0	-	0	0	-	0.0
1.0	-	6	6	-	0.0
0.5	-	6	4	-	0.0
0.2	4	8	6	4	36.7
0.1	6	6	6	6	82.7
0.04	5	8	6	5	59.4

The results show that decreasing the update period between measurements has a significant positive impact on the attained maximum operational sea state for the brute force pose controller, which is expected. Out of the evaluated update periods, a minimum update period of 0.2 seconds is required to achieve a sea state above zero. Interestingly, the update period of 0.04 seconds obtained a lower maximum operational sea state than with an update rate of 0.1 seconds. This may be due to randomness or inappropriate tuning of the Q matrix, which is only tuned for the base scenario and kept constant for all update period variations.

CPV control with waiting strategy

Figure 8.9 presents the 99.7 % confidence intervals of the for the CPV controller combined with the wave cancellation waiting strategy with a relative velocity threshold of 1.0 $\frac{\text{m}}{\text{s}}$ for various update periods. Additionally, Table 8.10 presents the maximum operational sea states for each of the update periods, based on the capture limits defined in Section 6.3.4. In order to reduce simulation time, the update period of 2.0 seconds is not evaluated since it did not perform well for the brute force pose controller.

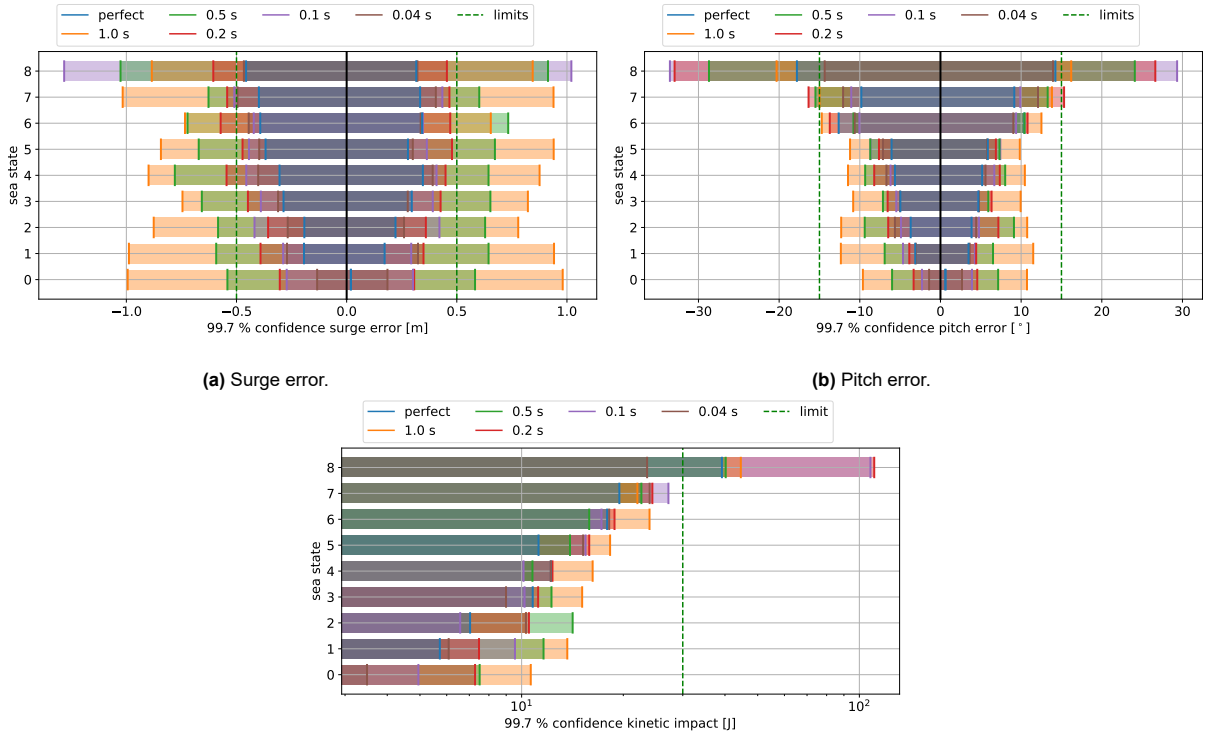

(a) Surge error.

(b) Pitch error.

(c) Kinetic impact energy.

Figure 8.9: The 99.7 % confidence intervals over sea states for the CPV controller combined with the wave cancellation waiting strategy with a relative velocity threshold of 1.0 $\frac{\text{m}}{\text{s}}$ for various measurement update periods.

Table 8.10: Maximum operational sea state for the CPV controller combined with the wave cancellation waiting strategy with a relative velocity threshold of 1.0 $\frac{\text{m}}{\text{s}}$ for various update periods.

Update period [s]	Surge	Pitch	Kinetic energy	Total	Up-time [%]
Perfect	8	7	7	7	93.6
1.0	-	7	7	-	0.0
0.5	-	6	7	-	0.0
0.2	5	6	7	5	59.4
0.1	6	7	7	6	82.7
0.04	8	8	8	8	98.3

The performance of the CPV controller combined with the wave cancellation waiting strategy remains impressive with an update period of 0.2 seconds or smaller. With an update time of 0.1 seconds, a maximum operational sea state of 7 was almost reached, if the surge confidence interval did not fall slightly fall outside the surge capture limits. No significant difference in performance is observed between the 0.04-second update period and perfect navigation across the range of sea states. However, using an update period of 0.04 seconds did result in a higher maximum operational sea state than using perfect navigation explored in Section 7.4.5. This unexpected outcome is likely due to randomness acting favorably for this update period.

8.6.2. Pose and velocity measurement precision

The influence of the pose and velocity measurement precision is investigated using the three scenarios given in Table 8.11.

Table 8.11: Pose and velocity measurement precision scenarios for $i \in \{na, nd\}$.

Scenario	Parameter	Value
Best	Σ_i^2	$diag([0.05^2,\ 0.05^2,\ 0.01^2,\ 0.005^2,\ 0.005^2,\ 0.0001^2])$
Base		$diag([0.5^2,\ 0.5^2,\ 0.1^2,\ 0.05^2,\ 0.05^2,\ 0.001^2])$
Worst		$diag([1^2,\ 1^2, 0.5^2,\ 0.2^2,\ 0.2^2,\ 0.01^2])$

Brute force pose control

Figure 8.10 presents the 99.7 % confidence intervals of the brute force controller for the different pose and velocity measurement precision scenarios presented in Table 8.11. Furthermore, Table 8.12 presents the maximum operational sea states based on the capture limits defined in Section 6.3.4.

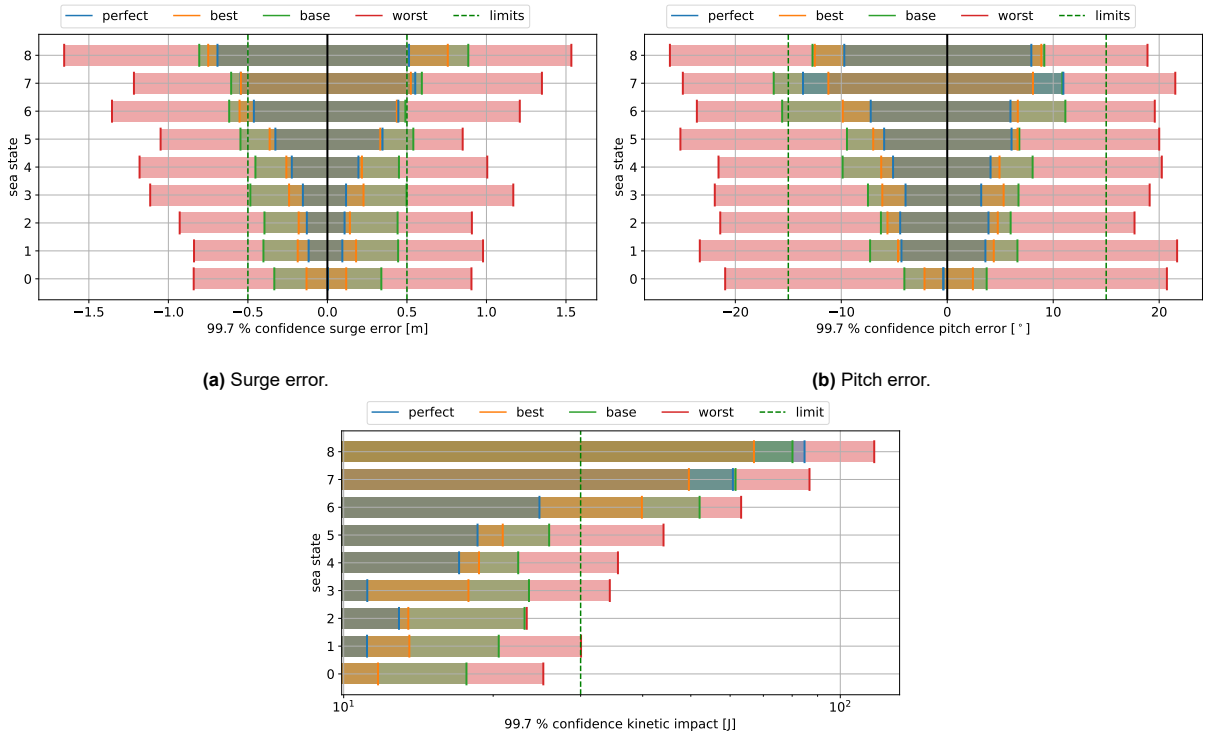

(a) Surge error.

(b) Pitch error.

(c) Kinetic impact energy.

Figure 8.10: The 99.7 % confidence intervals over sea states for the CPV controller for various pose and velocity measurement covariances.

Table 8.12: Maximum operational sea state for the brute force pose controller for various pose and velocity measurement covariances.

Scenario	Surge	Pitch	Kinetic energy	Total	Up-time [%]
Perfect	6	8	6	6	82.7
Best	5	8	5	5	59.4
Base	4	5	5	4	36.7
Worst	-	-	2	-	0.0

The overall results align with expectations, although some inconsistencies are observed which likely result from randomness. For instance, in the base scenario, the pitch error confidence interval is within the capture limits for sea state 8, but not for sea states 6 and 7. Another observation is that the worst-case scenario had a measurement covariance that was just too large for successful docking at any sea state. Looking at this scenario, the confidence intervals for surge error and pitch error were mostly dominated by the navigation performance. On the other hand, the kinetic energy distribution was significantly dependent on the sea state, as indicated by the significant increase in confidence interval with increasing sea state.

CPV control with waiting strategy

Figure 8.11 presents the 99.7 % confidence intervals of the CPV control with the waiting strategy for the different pose and velocity measurement precision scenarios presented in Table 8.11. Furthermore, Table 8.13 presents the maximum operational sea states for each scenario.

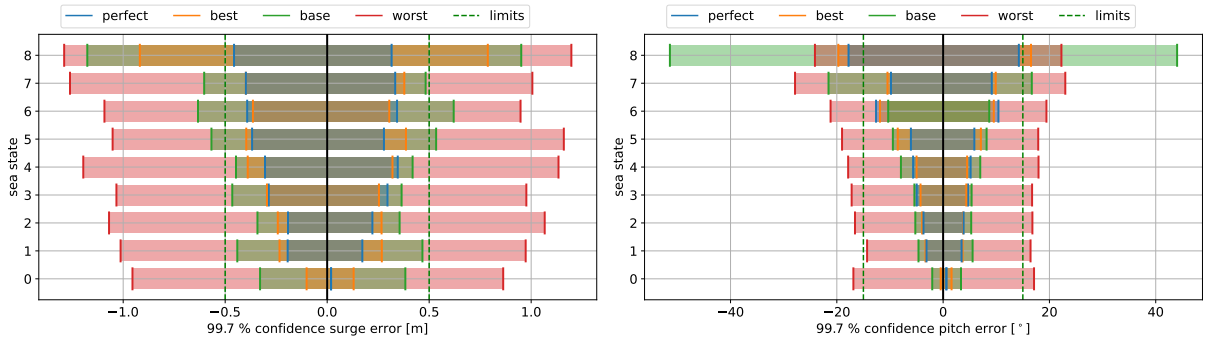

(a) Surge error.

(b) Pitch error.

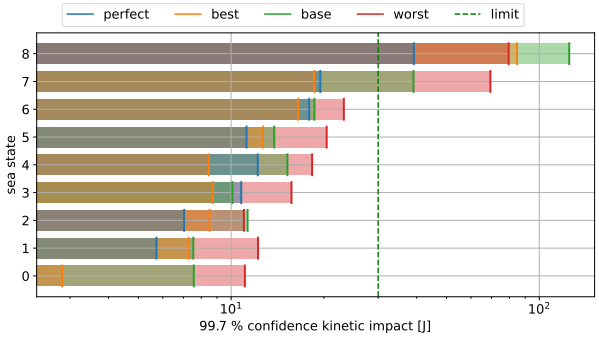

(c) Kinetic impact energy.

Figure 8.11: The 99.7 % confidence intervals over sea states for the CPV controller combined with the wave cancellation waiting strategy with a relative velocity threshold of 1.0 $\frac{\text{m}}{\text{s}}$ for various pose and velocity measurement covariances.

Table 8.13: Maximum operational sea state for the CPV controller combined with the wave cancellation waiting strategy with a relative velocity threshold of 1.0 $\frac{\text{m}}{\text{s}}$ for various pose and velocity measurement covariances.

Scenario	Surge	Pitch	Kinetic energy	Total	Up-time [%]
Perfect	8	7	7	7	93.6
Best	7	7	7	7	93.6
Base	4	6	6	4	36.7
Worst	-	-	6	-	0.0

The results indicate that the best-case scenario performs similarly to the perfect navigation case, achieving a maximum operational sea state of 7. This suggests that with sufficient pose and velocity measurement precision and an average update period of 0.2 seconds, significant up-time is expected for the AUV-USV combination. The base-case scenario also performed well, although increasing the capture limit for the surge error could improve its performance further.

8.6.3. Acceleration measurement precision

The influence of the acceleration measurement precision is investigated using the three scenarios given in Table 8.14.

Table 8.14: Acceleration measurement precision scenarios for $i \in \{na, nd\}$.

Scenario	Parameter	Value
Best	$\Sigma^2_{\dot{\nu}_i}$	$diag([0.001,\ 0.001,\ 0.005])$
Base		$diag([0.01,\ 0.01,\ 0.05])$
Worst		$diag([0.1,\ 0.1,\ 0.5])$

Brute force pose control

Figure 8.12 presents the 99.7 % confidence intervals of the brute force controller for the different acceleration measurement precision scenarios presented in Table 8.11. Furthermore, Table 8.15 presents the maximum operational sea states based on the capture limits defined in Section 6.3.4.

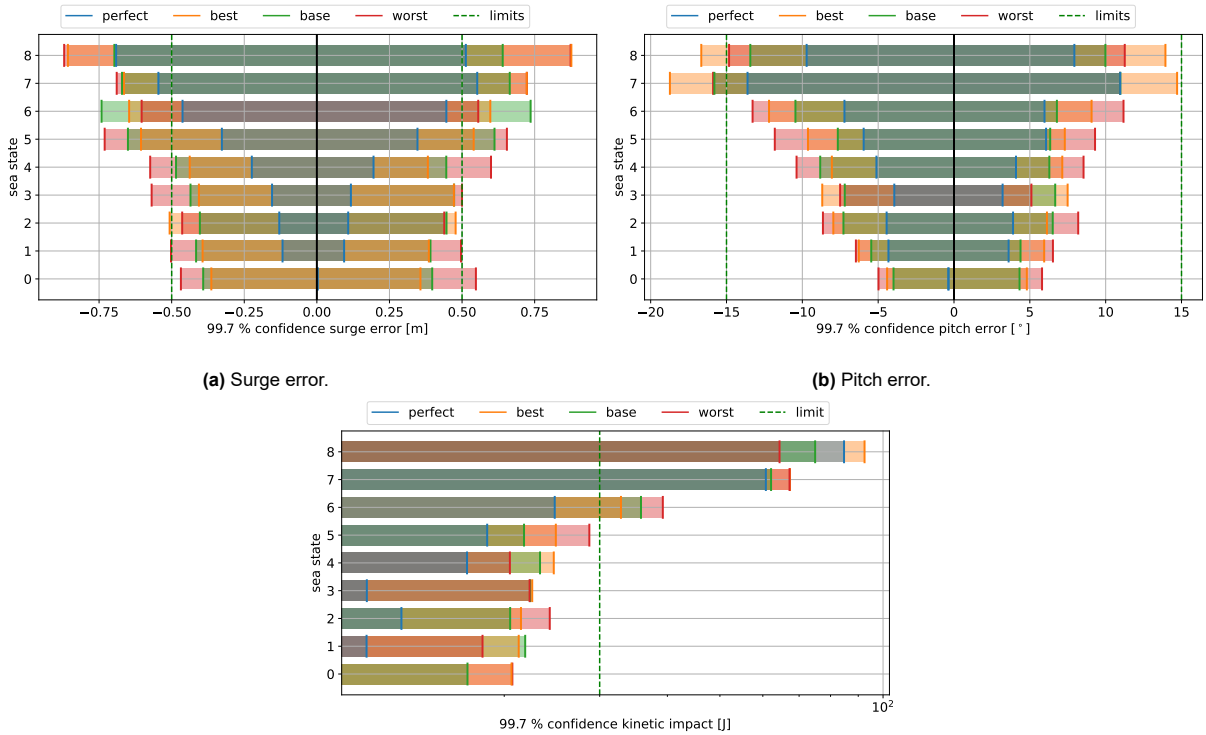

(a) Surge error.

(b) Pitch error.

(c) Kinetic impact energy.

Figure 8.12: The 99.7 % confidence intervals over sea states for the brute force pose controller for various for various acceleration measurement covariances.

Table 8.15: Maximum operational sea state for the brute force pose controller for various acceleration measurement covariances.

Scenario	Surge	Pitch	Kinetic energy	Total	Up-time [%]
Perfect	6	8	6	5	59.4
Best	4	6	5	4	36.7
Base	4	8	5	4	36.7
Worst	2	8	5	2	14.8

The results demonstrate that there is minimal sensitivity to variations in acceleration measurement precision. Despite the two orders of magnitude difference in acceleration measurement covariance across the three scenarios, there was no clear correlation with increased confidence intervals. This implies that achieving the highest maximum operational sea state with the brute force pose controller depends more on maximizing the pose and velocity measurement precision and update rate, rather than focusing on maximizing acceleration measurement precision.

CPV control with waiting strategy

Figure 8.13 presents the 99.7 % confidence intervals of the CPV control with the waiting strategy for the different acceleration measurement precision scenarios presented in Table 8.11. Furthermore, Table 8.16 presents the maximum operational sea states for each scenario.

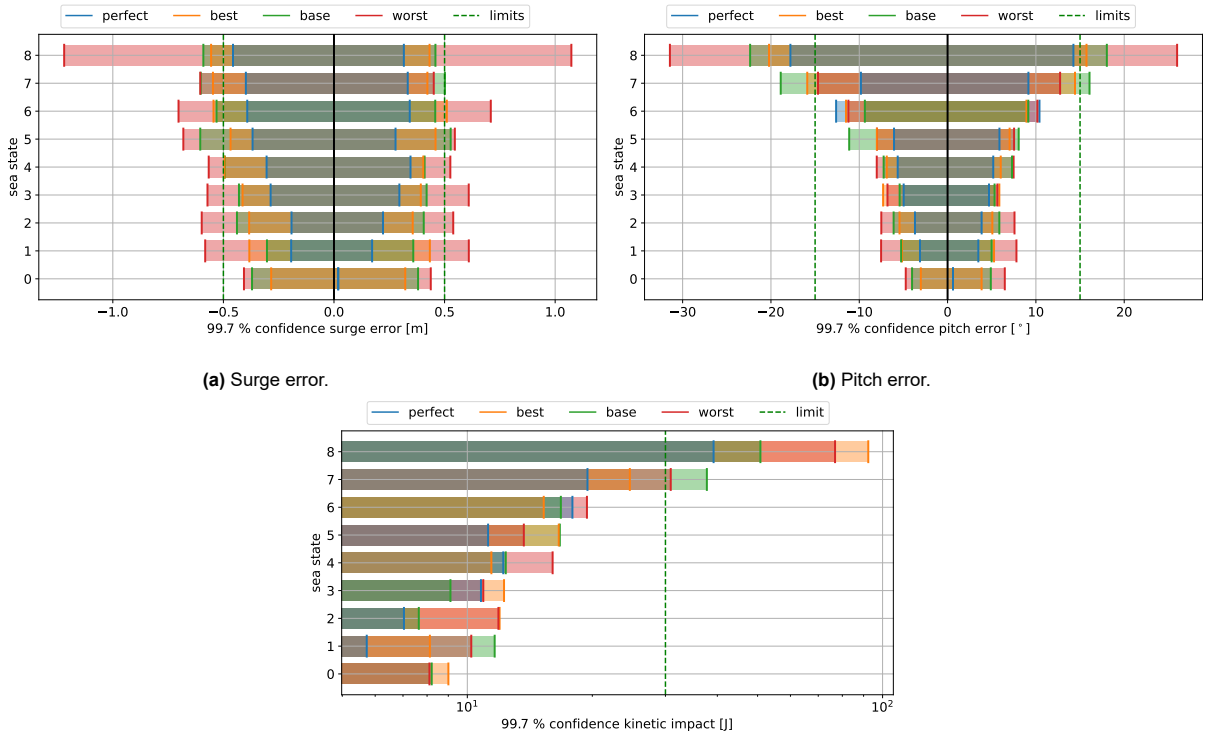

(a) Surge error.

(b) Pitch error.

(c) Kinetic impact energy.

Figure 8.13: The 99.7 % confidence intervals over sea states for the CPV controller combined with the wave cancellation waiting strategy with a relative velocity threshold of 1.0 $\frac{\text{m}}{\text{s}}$ for various acceleration measurement covariances.

Table 8.16: Maximum operational sea state for the CPV controller combined with the wave cancellation waiting strategy with a relative velocity threshold of 1.0 $\frac{\text{m}}{\text{s}}$ for various acceleration measurement covariances.

Scenario	Surge	Pitch	Kinetic energy	Total	Up-time [%]
Perfect	8	7	7	7	93.6
Best	5	6	7	5	59.4
Base	4	6	6	4	36.7
Worst	0	7	6	0	0.0

The results suggest that the surge error confidence intervals for the CPV controller, which controls for pose and velocity, are more dependent on the level of acceleration measurement precision compared to the brute force pose controller, which only controls for pose. This is expected as acceleration noise will have a greater impact on velocity estimates than on pose estimates. In contrast, no significant correlation is observed between acceleration noise and confidence intervals for the docking pitch error and kinetic impact energy. This observation could result from the slower dynamics of the Scout in pitch and heave motion, which essentially acts as a low pass filter that attenuates the high-frequency impact of the control force. As a result, the influence of the acceleration noise on the pitch error distribution and the kinetic impact energy is decreased.

8.7. Discussion

The results showed that decreasing the update period positively affects the maximum operational sea state up to around an update rate of 10 Hz after which the size of the docking confidence intervals is mainly dominated by the wave disturbance. The confidence intervals for the surge error were most limiting and an update rate equal to 2 Hz or lower resulted in a surge error confidence interval that was too large to even dock with no waves. However, an update rate of 5 Hz was enough to dock up to sea state 4 for the brute force pose controller and up to sea state 5 for the CPV controller combined with the

wave cancellation waiting strategy. From 10 Hz and above, the maximum operational sea state seems to be similar to the perfect navigation case, with small differences mainly resulting from randomness.

The pose and velocity measurement precision, under the best-case scenario also demonstrated good performance, as the maximum operational sea state was only decreased by one for the brute force controller and by zero for the CPV controller using the waiting strategy compared to their attained maximum operational sea state using perfect navigation. This result was obtained with an update rate of only 5 Hz, which suggests that a lower update rate can be compensated by a higher pose and measurement precision, which provides some freedom in the design space of the navigation system.

The results suggested that the docking performance was less dependent on the acceleration measurement precision. However, the CPV controller was more sensitive than the brute force controller, as it also controls for velocity. This suggests that the CPVA controller, which directly controls for acceleration, is even more sensitive to the precision of acceleration measurements. If this is the case, filtering of the acceleration measurements could be beneficial.

A vision system should be capable of obtaining both a high update rate of nearly 30 Hz [37] and the required position precision [75] of around 5 cm, while the Scout onboard sensors can further aid the required angular and velocity precision. This indicates that navigation for vertical docking, although significant performance is required, does not need to limit the success of the vertical docking approach.

8.7.1. Contributions

In this chapter, several contributions were made. Firstly, a navigation strategy for docking to an USV using the vertical docking approach was developed. This approach incorporated the use of an acoustic modem into the navigation system to communicate the state of the USV to the Scout. To the best of the author's knowledge, utilizing the onboard sensors of the USV and communicating their measurements using an acoustic modem to an AUV for docking purposes is not yet been studied. Secondly, the general requirements for the navigation system to function effectively when vertically docking in the wave-affected zone were identified. The insights presented in this chapter could prove helpful to future docking studies that investigate docking navigation in a dynamic environment. Finally, an initial evaluation of the performance of the vertical docking approach in rough seas was carried out, taking into consideration all the key elements outlined in Chapter 2. This contributes to determining the viability of the vertical docking approach and advancing the knowledge on autonomous underwater docking.

8.7.2. Limitations and recommendations

This chapter was indented as a high-level investigation of the influence of navigation on the vertical docking performance. However, many aspects were only discussed briefly and require more thorough research in the future:

- The navigation model in this thesis assumed that position, velocity, and acceleration measurements could be obtained from both the AUV and the USV, and that this information could be communicated between the vehicles. Furthermore, the current navigation strategy was chosen based on information availability rather than an optimized strategy for vertical docking. However, the required navigation systems and sensors should be thoroughly considered based on system integration, pricing, and performance. Future research can also investigate the feasibility of utilizing the existing onboard navigation systems on the USV for docking navigation.
- While generating noisy measurements directly from the true states of the Scout and the USV was convenient for the initial evaluation, obtaining realistic measurement performance ranges for these direct noisy measurements required transforming the performance of various underwater navigation and docking sensors. This transformation required some level of free interpretation and several simplifications. Future modelling efforts should incorporate various sensor models to obtain a more accurate measurement model which provides more insight into the required navigation performance of individual sensors for vertical docking.
- This initial evaluation did not explore the influence of acquisition range, environmental sensitivity, accuracy, and latency on navigation performance. Therefore, further exploration of these factors is necessary for a more thorough evaluation of navigation.

- The scanning approach through the measurement parameter space presented in Figure 8.2 was very brief and limited in scope. Different combinations of update rate and precision could be explored to gain more insight.
- Given the chosen sample size it was challenging to determine to what extent changes in the confidence interval are due to natural randomness or result from actual changes in the population distribution. This limitation impacts the overall accuracy and reliability of the presented findings. Future studies should consider increasing the sample size to better mitigate the effect of randomness and improve the validity of the results.
- Further exploration is required to determine the influence of navigation performance on the other guidance and prediction methods.

8.8. Conclusion

This chapter aimed to answer the question: *What is the influence of navigation on vertical docking performance?* To investigate this, a navigation strategy was developed based on the current kinematic EKF implementation and onboard sensors of the Lobster Scout and a common docking navigation strategy based on a USBL system and a vision system installed on the Scout to measure the relative position and velocity of the USV and the DS. Furthermore, the accelerations of the USV were communicated to the Lobster Scout at a high update rate using an acoustic modem.

The most critical measurement performance characteristics were determined for an initial evaluation, which included the precision of the acceleration, velocity, and pose measurements, as well as the update rate of the pose and velocity measurements. Using the literature a range of measurement performances was determined roughly ranging from using only USBL to using a high-performing vision system for the final vertical docking approach. The influence of these factors was investigated on the target state guidance method using the brute force pose controller and the target state guidance method using the CPV method combined with the wave cancellation waiting strategy.

It was found that the navigation performance is highly influential to the docking performance of these methods. More specifically, both a high update rate and a high pose and velocity measurement precision are beneficial for the docking performance, while the influence of acceleration measurement precision is smaller for the chosen methods.

The results showed that both guidance methods, when using a high update rate of 10 Hz to 25 Hz and average acceleration, pose, and velocity measurement precision can achieve similar performance to using perfect navigation. Moreover, an update rate of only 5 Hz was sufficient to achieve comparable results to perfect navigation, as long as a high measurement precision for pose and velocity was obtained. This indicates that the docking distributions for these scenarios are mostly dominated by wave disturbances rather than navigation performance. Both of these scenarios can be realized using a vision system, which supports the viability of the vertical docking approach.

9

Conclusion

AUVs are still laborious and expensive to operate due to their limited range and autonomy. Human labor can be severely decreased by combining an AUV with an USV, however, current docking solutions have limited the operational employability of this combination in rough seas. In this study, a new vertical docking approach from below the USV was proposed, which could possibly dock in higher sea states due to wave phase synchronization, ultimately enabling more cost-effective underwater operations. To investigate this, the Lobster Scout was used as a case study, leading to the main research question of this thesis:

To what extent is a vertical docking approach of the Lobster Scout to an USV viable in rough seas?

In conclusion, the vertical docking approach shows promise for enabling a reliable AUV-USV combination for the Lobster Scout in sea state 5 ($H_{\frac{1}{3}} = 1.65$ m, $\bar{T} = 5.1$ s) to sea state 7 ($H_{\frac{1}{3}} = 3.6$ m, $\bar{T} = 6.7$ s), resulting in an estimated annual operational up-time of 59.4 % to 93.6 % in the North Sea. Furthermore, there is potential to achieve even higher sea states with improved GNC methods. The vertical docking approach is a viable solution to achieve a workable AUV-USV combination and the obtained results are an improvement over current studies using horizontal docking approaches. However, the author is of the opinion that both horizontal and vertical docking approaches require further investigation.

9.1. Answers to research sub-questions

Five research sub-questions were defined to answer this question. These questions led to the identification of the key elements to consider for an initial performance evaluation (Chapter 2), a model of the vertical docking system (Chapter 3-5), a method for evaluating docking performance (Chapter 6), identification and evaluation of effective vertical guidance and control methods (Chapter 7) and an assessment of the influence of noisy measurements on the docking performance (Chapter 8). Below are the conclusions for each of the research sub-questions:

What are the key elements to consider for an initial performance evaluation of the vertical docking approach to an USV?

It was found that for an initial evaluation, the surge, heave, and pitch DOF should be considered as they are most impacted by waves given that the AUV and USV will align with the main wave direction. Furthermore, the key elements include environmental conditions, the USV, the Lobster Scout, the DS, and vertical docking guidance navigation and control. Environmental conditions were limited to waves due to their differential impact on the USV and the Lobster Scout, while current and wind are neglected and the study was evaluated for the North Sea. The USV was limited to a free-floating box and its specifications are roughly based on the DUS V5750 USV by Demcon [72]. The DS mounted on the USV was analyzed and an upside-down cradle DS design was found to best suit the Lobster Scout.

The focus of the GNC methods was limited to the final meters to the dock, as this is the most critical and unique part of the vertical docking procedure. Overall, this concludes the key elements for obtaining an initial performance evaluation of a vertical docking approach.

How can the vertical docking system be modelled?

The vertical docking system requires modelling of waves, the Lobster Scout, and the USV with the attached DS. Linear velocity potential theory was used to approximate the irregular waves of the North Sea. Kinematic and dynamics matrix equations were used to obtain a general AUV model, which relates the control forces and the wave disturbance forces to its motion. The model parameters for the Lobster Scout were then estimated through field experiments for control and drag forces, while Ansys Aqua was used to estimate the added mass parameters. The CAD design was used to estimate its inertial, gravitational, and buoyancy forces. Finally, assuming a linear mass-spring-damper model, Ansys Aqua was used to obtain the motion RAOs of the box-shaped USV, which were then used to simulate its motion response. The motion of the DS was obtained by transforming these motions. All in all, the resulting model can simulate the primary motions of the system in irregular North Sea waves.

How to evaluate vertical docking performance?

As docking success is described probabilistically, a probability distribution method was developed to estimate the success probability of a vertical docking approach. This method defines a docking attempt as the moment when the AUV enters the capture mechanism of the DS. For a particular GNC method, the docking probability distributions of the key docking entry metrics are obtained. In a 2D setting, these metrics include the docking surge error, docking pitch error, and the kinetic impact energy. Viability was determined using the maximum operational sea state and estimated operational up-time. The 99.7 % confidence intervals of these distributions were used to obtain the maximum operational sea state of the USV-AUV combination, by evaluating whether they fall within reasonable capture limits of a certain cradle-type DS design. The operational up-time in the North Sea was then determined using statistical sea state data. Sea state 8 with a significant wave height of 4.85 m, which just exceeds the operating limit of the Demcon's DUS V5750 USV [72] was identified as a good performance benchmark for determining the effectiveness of the vertical docking approach using different GNC methods.

What are effective vertical guidance and control methods for the Lobster Scout?

A target state guidance method using way-points was designed for guiding the Lobster Scout to the DS. The target state guidance method was implemented using various controllers which included a pose PID controller, a CPV controller, and a CPVA controller, which progressively control for more AUV states. It was furthermore evaluated whether kinematic prediction, polynomial prediction, and a wave cancellation waiting strategy could increase the maximum operational sea state. It is important to note that in this chapter, the guidance methods were evaluated using perfect navigation, which results in optimistic results.

None of the guidance and control methods were able to achieve the effectiveness benchmark for sea state 8. However, the CPVA method and the CPV method combined with the wave cancellation waiting strategy achieved a maximum operational sea state of 7, resulting in an impressive annual operational up-time of 93.6 % for the AUV-USV combination in the North Sea. Moreover, combining the pose controller with the polynomial and kinematic prediction methods led to smaller confidence intervals, which is promising. By combining these predictive methods with the CPV or CPVA controllers in the future, or with additional tuning, they could potentially meet the effectiveness benchmark.

What is the influence of navigation on vertical docking performance?

The navigation system was modelled using a measurement model that generated direct noisy measurements of the true state of the Lobster Scout and the USV, and an EKF was implemented to improve the state estimates. The investigation focused on the influence of the most critical factors in the final docking stage, namely, the influence of pose, velocity, and acceleration measurement precision,

as well as the influence of the update rate of the pose and velocity measurements. Only target state guidance using the brute force pose controller and using the CPV controller combined with the wave cancellation waiting strategy were evaluated.

It was found that the two guidance methods could achieve comparable docking performance to their performance with perfect navigation at an update rate above 10 Hz with average pose and velocity measurement precision, or an update rate of 5 Hz with excellent pose and velocity measurement precision. The docking distributions were found to be mostly dominated by the wave disturbance at this level of navigation performance. Hence, the study suggests that navigation is not an immediate barrier to the viability of the vertical docking approach, as this level of navigation performance is achievable with a docking vision system. Additionally, the influence of acceleration measurement precision was found to be small compared to other factors.

The answers to these sub-research questions result in the final outcomes of this project:

- A system model of the vertical docking system.
- A high-level concept design and the main design requirements of a vertical DS for the Scout.
- Identification of effective vertical docking guidance and control methods.
- Identification of critical factors affecting vertical docking performance.
- An initial performance indication for the vertical docking approach.

9.2. Comparison with existing literature

Now that an initial performance indication of the vertical docking approach to an USV is available, it is compared to existing studies that utilized horizontal docking concepts to a floating element.

A direct comparison of the results is done with studies where a horizontal DS was directly attached to the floating object. For example, in [64] a modified cruising Hydroid REMUS 100 AUV was docked to a station-keeping USV using a short taut vertical cable under the USV that served as the docking line. Trials were performed in lakes with very limited waves and currents, and docking attempts at higher sea states than sea states 0 or 1 were unlikely to be successful. Furthermore, a cage type DS mounted on a wave energy converter for a BLUE ROV 2 Heavy was proposed in [79] and evaluated in simulation. The DS motion was limited to heave sinusoidal motion with an amplitude of 1m and a period of around 20 seconds. While the amplitude is significant, the period is very long, so the wave disturbance remains small. In comparison, the vertical docking approach proposed in this study was evaluated under more realistic waves with larger disturbances over a broader range of sea states, resulting in successful docking with rougher seas. These findings support the competitiveness of the vertical docking concept presented in this thesis.

Furthermore, several studies investigated the concept of horizontal autonomous docking to a funnel-shaped DS suspended with a cable from a vessel. By lowering the DS below the wave-affected zone, the wave disturbance only acts indirectly through the cable, and all motions of the vessel are coupled to the heave motion of the DS. Additionally, a heave compensation system can be added to the cable to almost fully decouple the motion between the vessel and the DS. These suspended DS can possibly also be lowered to close to the sea floor for extended periods of time to service the AUV from there, which is especially relevant for deep waters, where diving and surfacing of the AUV can take significant time and energy. In [30], the simulated scenario involved the DS performing a sinusoidal motion with an amplitude of 0.15 m at 6500 m depth, while the mother ship moved with 2.2 meters of amplitude. In another study [37], the suspended funnel-shaped DS was tested only in calm waters. However, since the AUV was only controlled relatively to the DS in the horizontal plane, this solution only worked with small to no waves. Finally, the autonomous docking capability of an ROV to a suspended cage-type DS hanging from a vessel was tested in [75], where they were able to sustain 2 meters of heave motion during sea trials. However, deploying these suspended DS systems requires the development of a reliable cable system, and it also increases navigational complexity since the DS requires its own navigation system. Both of these additional systems aren't necessary for directly vertically docking to the USV. Additionally, the benefits of deploying close to the sea floor to save on dive time are less

relevant in the North Sea since it's relatively shallow. An interesting avenue for future research is to combine the vertical docking approach with a suspended vertical cradle-type DS in order partially or fully decouple the motion of the USV and the DS and reduce the effect of the wave disturbance.

Another approach presented in [46] involved a system that could retrieve a non-functioning AUV floating on the sea surface. To achieve this, all docking GNC methods were placed on the USV. One significant benefit of a sea surface-based docking is the availability of GNSS and high-bandwidth communication between an AUV and the USV, which simplifies navigation requirements and essentially limits the docking problem to the horizontal plane. In contrast, vertical docking navigation has substantial underwater navigation requirements, which are more difficult to achieve. Therefore, autonomous sea surface docking may be an attractive alternative to vertical docking and should be further explored. However, a disadvantage of sea surface-based docking is that most AUVs lose a substantial part of their control authority, and the wave disturbance is severe.

All in all, it can not definitively be said that the concept presented in this thesis, vertical docking directly to the USV, works better or worse than these horizontal docking concepts, especially since both can be optimized further in future research. Therefore, all of the concepts mentioned here require further investigation to determine their relative effectiveness in different applications.

9.3. Contributions

This thesis has made significant contributions to the development of efficient and effective docking solutions for AUVs to USVs, ultimately enabling greater operational flexibility and cost savings in underwater surveys. The contributions include:

- **Novel vertical docking approach** This study has introduced a novel approach for vertical docking to an USV, utilizing phase synchronization of wave disturbances. This method is specifically designed for hovering AUVs and broadens the range of possible docking solutions.
- **New docking guidance and prediction methods** This study has explored novel guidance methods for underwater docking that have not been previously investigated, including target state guidance using the CPV controller and the CPVA controller. Additionally, kinematic and polynomial prediction methods, which have not yet been utilized for docking purposes, have been evaluated in this research. These methods have shown to be effective for docking and therefore provide value for underwater docking in general.
- **Underwater docking in the presence of large waves** Current studies on underwater docking have primarily focused on regular waves at small sea states. However, this study has extended the research by examining docking in the presence of more realistic irregular waves at large sea states, which is relevant in providing a better understanding of docking in actual ocean environments.
- **Probability distribution based docking evaluation** This study proposes a novel approach for evaluating docking performance using probability distributions to obtain a probabilistic docking success rate, which is an improvement over the mostly binary (failed/successful dock) evaluation based on certain docking conditions used in current studies. The proposed method allows for a direct coupling of some of the design requirements of the docking system to its success probability, providing valuable insights to the DS designer.

9.4. Recommendations

This thesis served as an exploratory investigation of the viability and effectiveness of a vertical docking approach to an USV. This thesis has the following recommendations for future research:

- **3D setting** The study was performed in a 2D setting, which limited the investigation to only three out of six degrees of freedom between the AUV and the USV. This could overestimate the performance of the vertical docking approach. Additionally, certain wave properties such as directional spreading were not investigated, as they are only present in a 3D setting. Future research should expand the simulation to a 3D setting, taking into account all DOF and 3D wave properties.

- **Increase model accuracy** At higher sea states, the wave steepness assumption doesn't hold and higher-order wave models should be explored. To increase the realism of USV motions, the current approximation of the USV as a simple box shape is not sufficient and a more realistic boat shape should be used. Finally, the real Lobster Scout's asymmetries cause coupling between motions, which is not currently taken into account and should be addressed in future research. Finally, accurate modelling of the control forces can lead to more realistic responses and more precise drag coefficients.
- **Docking navigation** The navigation model in this thesis assumed that position, velocity, and acceleration measurements could be obtained from both the AUV and the USV, and that this information could be communicated between the vehicles. However, in order to implement this type of vertical docking, the required navigation systems and sensors should be thoroughly considered based on system integration, pricing, and performance. Future research can also focus on investigating the feasibility of utilizing the existing onboard navigation systems on the USV for docking navigation.
- **DS design** It was assumed that the capture mechanism could align the AUV with the latch, provided that certain entry conditions to the capture mechanism were met. However, this assumption was not verified due to the complex modelling of impact dynamics. Further exploration of the vertical cradle type DS design should be a priority when continuing this research.
- **Investigation of other concepts** While the results suggest that vertical docking can achieve a viable AUV-USV combination, the author believes that alternative docking concepts that aim to decouple the motion of the DS and the USV may yield similar or superior performance while providing additional benefits should also require more attention in future research.
- **Guidance and prediction methods** The exploratory investigation of predictive guidance methods for vertical docking in this thesis have shown promising results. Further research should focus on a more extensive investigation of these methods for vertical docking using a larger sample size, resulting in more certainty in their docking distributions and as well as a possible increase in performance.

All in all, this research indicates that the vertical docking approach to an USV using a hovering AUV such as the Lobster Scout can operate in medium to rough seas and achieve significant operational up-time. Furthermore, there is potential to increase performance further using more sophisticated guidance, prediction and control methods indicating that the vertical docking approach is relevant and worthy of further investigation.

Bibliography

[1] Allseas. *Allseas pilot nodule collection tests, Pacific, Oct 2022*. 2022. URL: https://allseas.com/videos/allseas-pilot-nodule-collection-tests-pacific-oct-2022/.

[2] Inc. Ansys. *Aqua Reference Manual*. English. Version 2021 R2. Ansys, Inc. 2023. 320 pp.

[3] Inc. Ansys. *Aqua Theory Manual*. English. Version 2021 R2. Ansys, Inc. 2023. 208 pp.

[4] Inc. Ansys. *Aqua User's Manual*. English. Version 2021 R2. Ansys, Inc. 2023. 292 pp.

[5] K. J. Åström and R. M. Murray. *Feedback systems: an introduction for scientists and engineers*. Princeton university press, 2021.

[6] Lobster Innovations B.V. *Lobster Scout*. 2022. URL: https://lobster-robotics.com/.

[7] A. Bianchi Figueiredo and A. Coimbra Matos. "Mvido: a high performance monocular vision-based system for docking a hovering auv". In: *Applied Sciences* 10.9 (2020), p. 2991.

[8] BSH. *Sea state statistics - Fino 1*. 2022. URL: https://www.bsh.de/EN/DATA/Climate-and-Sea/Sea_state/Sea_state_statistics/sea_state_statistics_node.html.

[9] M. Caccia, G. Bruzzone, and G. Veruggio. "Guidance of unmanned underwater vehicles: Experimental results". In: *Proceedings 2000 ICRA. Millennium Conference. IEEE International Conference on Robotics and Automation. Symposia Proceedings (Cat. No. 00CH37065)*. Vol. 2. IEEE. 2000, pp. 1799–1804.

[10] M. Caccia and G. Veruggio. "Guidance and control of a reconfigurable unmanned underwater vehicle". In: *Control engineering practice* 8.1 (2000), pp. 21–37.

[11] K. P. Carroll et al. "AUV path planning: an A* approach to path planning with consideration of variable vehicle speeds and multiple, overlapping, time-dependent exclusion zones". In: *Proceedings of the 1992 symposium on autonomous underwater vehicle technology*. IEEE. 1992, pp. 79–84.

[12] R. D. Christ and R. L. Wernli Sr. *The ROV manual: a user guide for remotely operated vehicles*. Butterworth-Heinemann, 2013.

[13] J. Cohen. "Statistical power analysis". In: *Current directions in psychological science* 1.3 (1992), pp. 98–101.

[14] N. A. Cruz et al. "A lightweight docking station for a hovering AUV". In: *2017 IEEE Underwater Technology (UT)*. IEEE. 2017, pp. 1–7.

[15] M. R. Dhanak and N. I. Xiros. *Springer handbook of ocean engineering*. Springer, 2016.

[16] J. Esteba et al. "Docking of Non-Holonomic AUVs in Presence of Ocean Currents: A Comparative Survey". In: *IEEE Access* 9 (2021), pp. 86607–86631.

[17] Evologics. *Acoustic modems*. 2022. URL: https://evologics.de/acoustic-modems.

[18] Evologics. *Acoustic modems*. 2022. URL: https://evologics.de/product/s2c-r-42-65-usbl-26.

[19] S. Fan et al. "AUV docking based on USBL navigation and vision guidance". In: *Journal of Marine Science and Technology* 24.3 (2019), pp. 673–685.

[20] S. Fan et al. "Impact of current disturbances on AUV docking: Model-based motion prediction and countering approaches". In: *IEEE Journal of Oceanic Engineering* 43.4 (2017), pp. 888–904.

[21] M. D. Feezor et al. "Autonomous underwater vehicle homing/docking via electromagnetic guidance". In: *IEEE Journal of Oceanic Engineering* 26.4 (2001), pp. 515–521.

[22] B. Fletcher et al. "From the lab to the ocean: Characterizing the critical docking parameters for a free floating dock with a REMUS 600". In: *OCEANS 2017-Anchorage*. IEEE. 2017, pp. 1–7.

[23] M. Forgione. *pyMPC*. 2023. URL: https://github.com/forgi86/pyMPC.

[24] T. I. Fossen. *Handbook of marine craft hydrodynamics and motion control*. John Wiley & Sons, 2011.

[25] T. I. Fossen. “Marine control systems–guidance. navigation, and control of ships, rigs and underwater vehicles”. In: *Marine Cybernetics, Trondheim, Norway, Org. Number NO 985 195 005 MVA, www. marinecybernetics. com, ISBN: 82 92356 00 2* (2002).

[26] Fugro. *Blue Essencet*. 2022. URL: https://www.fugro.com/about-fugro/our-expertise/remote-and-autonomous-solutions/remote-and-autonomous-vessels.

[27] J. Gerritsma. *Hydromechanica 4 - Golven*. May 2022.

[28] K. Hasselmann et al. “Measurements of wind-wave growth and swell decay during the Joint North Sea Wave Project (JONSWAP).” In: *Ergaenzungsheft zur Deutschen Hydrographischen Zeitschrift, Reihe A* (1973).

[29] M. Hildebrandt and L. Christensen. “Visual Station Keeping and Target Tracking with a Hovering Underwater Vehicle”. In: ().

[30] Y. Hong et al. “Development of the homing and docking algorithm for AUV”. In: *The Thirteenth International Offshore and Polar Engineering Conference*. OnePetro. 2003.

[31] Ocean Observatories Initiative. *AUVs*. 2022. URL: https://oceanobservatories.org/marine-technologies/robotic-auvs/.

[32] S. Jeon and M. Tomizuka. “Benefits of acceleration measurement in velocity estimation and motion control”. In: *Control Engineering Practice* 15.3 (2007), pp. 325–332.

[33] J. M. J. Journée and W. W. Massie. “Offshore hydromechanics”. In: (2008).

[34] M. Kok, J. D. Hol, and T. B. Schön. “Using inertial sensors for position and orientation estimation”. In: *arXiv preprint arXiv:1704.06053* (2017).

[35] A. A. Kushnerik, A. V. Vorontsov, and A. P. Scherbatyuk. “Small AUV docking algorithms near dock unit based on visual data”. In: *OCEANS 2009*. IEEE. 2009, pp. 1–6.

[36] H. Lamb. *Hydrodynamics*. 6th ed. Cambridge: Cambridge University Press, 1932.

[37] M. Lin et al. “Docking to an underwater suspended charging station: Systematic design and experimental tests”. In: *Ocean Engineering* 249 (2022), p. 110766.

[38] R. Lin et al. “A non-contact docking system for charging and recovering autonomous underwater vehicle”. In: *Journal of Marine Science and Technology* 24.3 (2019), pp. 902–916.

[39] T. Liu. “Evolutionary understanding of airfoil lift”. In: *Advances in Aerodynamics* 3.1 (2021), p. 37.

[40] D. Looman. “Survey of position aiding techniques for low-cost AUVs”. MA thesis. Delft, 2022.

[41] S. Lucia and F. Fiedler. *do-mpc*. 2023. URL: https://www.do-mpc.com/en/latest/.

[42] T. Maki. “Research on autonomous observation of seafloor environment”. PhD thesis. Thesis, 2008.

[43] T. Maki et al. “Docking method for hovering type AUVs by acoustic and visual positioning”. In: *2013 IEEE international underwater technology symposium (UT)*. IEEE. 2013, pp. 1–6.

[44] T. Maki et al. “Docking method for hovering-type AUVs based on acoustic and optical landmarks”. In: *Journal of Robotics and Mechatronics* 30.1 (2018), pp. 55–64.

[45] S. Martin et al. “Characterizing the critical parameters for docking unmanned underwater vehicles”. In: *OCEANS 2016 MTS/IEEE Monterey*. IEEE. 2016, pp. 1–7.

[46] A. Martins et al. “Autonomous surface vehicle docking manoeuvre with visual information”. In: *Proceedings 2007 IEEE International Conference on Robotics and Automation*. IEEE. 2007, pp. 4994–4999.

[47] T. Matsuda et al. “Resident autonomous underwater vehicle: Underwater system for prolonged and continuous monitoring based at a seafloor station”. In: *Robotics and Autonomous Systems* 120 (2019), p. 103231.

[48] MBARI. *Autonomous Underwater Vehicle Docking*. 2022. URL: https://www.mbari.org/autonomous-underwater-vehicle-docking/.

[49] R. S. McEwen et al. “Docking control system for a 54-cm-diameter (21-in) AUV”. In: *IEEE Journal of Oceanic Engineering* 33.4 (2008), pp. 550–562.

[50] MetMatters. *The Beaufort Wind Scale*. 2022. URL: https://www.rmets.org/metmatters/beaufort-wind-scale.

[51] P. A. Miller et al. “Autonomous underwater vehicle navigation”. In: *IEEE Journal of Oceanic Engineering* 35.3 (2010), pp. 663–678.

[52] M. Miranda II. *Mobile docking of REMUS-100 equipped with USBL-APS to an unmanned surface vehicle: A performance feasibility study*. Florida Atlantic University, 2014.

[53] W. Naeem et al. “A review of guidance laws applicable to unmanned underwater vehicles”. In: *the Journal of Navigation* 56.1 (2003), pp. 15–29.

[54] M. C. Nielsen et al. “Constrained multi-body dynamics for modular underwater robots—Theory and experiments”. In: *Ocean Engineering* 149 (2018), pp. 358–372.

[55] B. R. Page and N. Mahmoudian. “AUV docking and recovery with USV: An experimental study”. In: *OCEANS 2019-Marseille*. IEEE. 2019, pp. 1–5.

[56] B. R. Page et al. “Underwater docking approach and homing to enable persistent operation”. In: *Frontiers in Robotics and AI* 8 (2021), p. 621755.

[57] N. Palomeras et al. “AUV homing and docking for remote operations”. In: *Ocean Engineering* 154 (2018), pp. 106–120.

[58] J. Park et al. “Docking problem and guidance laws considering drift for an underactuated AUV”. In: *OCEANS 2011 IEEE-Spain*. IEEE. 2011, pp. 1–7.

[59] J. Park et al. “Improvement of vision guided underwater docking for small AUV ISiMI”. In: *OCEANS 2009*. IEEE. 2009, pp. 1–5.

[60] J. Park et al. “Underwater docking approach of an under-actuated AUV in the presence of constant ocean current”. In: *IFAC proceedings volumes* 43.20 (2010), pp. 5–10.

[61] Rijkswaterstaat. *Noordzee*. 2023. URL: https://www.rijkswaterstaat.nl/water/vaarwegenoverzicht/noordzee.

[62] A. Sans-Muntadas et al. “A hybrid approach to underwater docking of AUVs with cross-current”. In: *OCEANS 2016 MTS/IEEE Monterey*. IEEE. 2016, pp. 1–7.

[63] S. Saravanakumar and T. Asokan. “Multipoint potential field method for path planning of autonomous underwater vehicles in 3D space”. In: *Intelligent Service Robotics* 6.4 (2013), pp. 211–224.

[64] E. I. Sarda and M. R. Dhanak. “Launch and recovery of an autonomous underwater vehicle from a station-keeping unmanned surface vehicle”. In: *IEEE Journal of Oceanic Engineering* 44.2 (2018), pp. 290–299.

[65] S. Särkkä. *Bayesian filtering and smoothing*. 3. Cambridge university press, 2013.

[66] Y. Sato et al. “Autonomous docking of hovering type AUV to seafloor charging station based on acoustic and visual sensing”. In: *2017 IEEE Underwater Technology (UT)*. IEEE. 2017, pp. 1–6.

[67] K. Shi, X. Wang, and H. Xu. “On the Offset-free Nonlinear Model Predictive Control for AUV Docking”. In: *2021 WRC Symposium on Advanced Robotics and Automation (WRC SARA)*. IEEE. 2021, pp. 117–122.

[68] K. Shi et al. “Efficient 3D Homing Path Planning for AUV Docking”. In: *2020 35th Youth Academic Annual Conference of Chinese Association of Automation (YAC)*. IEEE. 2020, pp. 353–358.

[69] Solardyne. *Ranger 2*. 2022. URL: https://www.sonardyne.com/products/ranger-2-subsea-positioning-usbl/.

[70] L. Stutters et al. “Navigation technologies for autonomous underwater vehicles”. In: *IEEE Transactions on Systems, Man, and Cybernetics, Part C (Applications and Reviews)* 38.4 (2008), pp. 581–589.

[71] Subsea7. *Remotely Operated Vehicles (ROVs)*. 2022. URL: https://irm.subsea7.com/capabilities/assets/rovs.

[72] Demcon Unmanned Systems. *DUS V5750*. 2023. URL: https://demcon-unmanned.nl/products/dus-v5750/.

[73] K. Teo, E. An, and P. J. Beaujean. “A robust fuzzy autonomous underwater vehicle (AUV) docking approach for unknown current disturbances”. In: *IEEE Journal of Oceanic Engineering* 37.2 (2012), pp. 143–155.

[74] C. Thomas, E. Simetti, and G. Casalino. “A unifying task priority approach for autonomous underwater vehicles integrating homing and docking maneuvers”. In: *Journal of Marine Science and Engineering* 9.2 (2021), p. 162.

[75] P. Trslić. “Autonomous docking for work class ROVs”. In: (2020).

[76] A. Tsourdos, B. White, and M. Shanmugavel. *Cooperative path planning of unmanned aerial vehicles*. John Wiley & Sons, 2010.

[77] R. Vivekanandan, D. Chang, and G. A. Hollinger. “Model Predictive Control for Underwater Vehicle Rendezvous and Docking with a Wave Energy Converter”. In: *Proc. IEEE International Conf. on Robotics and Automation Workshop on Reliable AI for Marine Robotics: Challenges and Opportunities*. 2021.

[78] J. Wallen and Z. Song. “Development of an adaptive docking station for resident underwater vehicles”. In: *OCEANS 2019-Marseille*. IEEE. 2019, pp. 1–7.

[79] J. Wallen, N. Ulm, and Z. Song. “Underwater docking system for a wave energy converter based mobile station”. In: *OCEANS 2019 MTS/IEEE SEATTLE*. IEEE. 2019, pp. 1–8.

[80] Wikipedia. *Alpha Ventus Offshore Wind Farm*. 2023. URL: https://en.wikipedia.org/wiki/Alpha_Ventus_Offshore_Wind_Farm.

[81] Wikipedia. *Noordzee*. 2023. URL: https://nl.wikipedia.org/wiki/Noordzee.

[82] M. Wirtz, M. Hildebrandt, and C. Gaudig. “Design and test of a robust docking system for hovering AUVs”. In: *Proc. IEEE/MTS OCEANS*. 2012, pp. 1–6.

[83] Z. Yan et al. “Modeling, strategy and control of UUV for autonomous underwater docking recovery to moving platform”. In: *2017 36th Chinese Control Conference (CCC)*. IEEE. 2017, pp. 4807–4812.

[84] C. Yang et al. “Study on docking guidance algorithm for hybrid underwater glider in currents”. In: *Ocean Engineering* 125 (2016), pp. 170–181.

[85] A. M. Yazdani et al. “A survey of underwater docking guidance systems”. In: *Robotics and Autonomous Systems* 124 (2020), p. 103382.

[86] T. Zhang, D. Li, and C. Yang. “Study on impact process of AUV underwater docking with a cone-shaped dock”. In: *Ocean Engineering* 130 (2017), pp. 176–187.

[87] Y. Zhang et al. “Acoustics-Based Autonomous Docking for A Deep-Sea Resident ROV”. In: *China Ocean Engineering* 36.1 (2022), pp. 100–111.

[88] M. Zuo et al. “A Unified Approach for Underwater Homing and Docking of over-Actuated AUV”. In: *Journal of Marine Science and Engineering* 9.8 (2021), p. 884.

[89] W. E. Zwart. “Analysis of Ship Motions in Shallow Water”. In: (2017).

A

Modelling preliminaries

This section discusses some of the relevant concepts, notations and definitions used for modelling purposes of marine vehicles. In Section A.1 the scalar and vector notations for motions and forces are explained. In Section A.2, important reference points are defined. Finally, in Section A.3, commonly used transforms are presented.

A.1. Notation for motion and forces

The notation used in this thesis to describe motion is based on [24] but is slightly altered since multiple frames are considered. The notation can take some time to get used to, therefore this section explicitly describes the motion en force scalar and vector notation.

Scalar notation for motions and forces

The complete notation used to describe the motion of and forces on a body is shown in Table A.1. In explaining the complete notation, the $\{a\}$ and $\{n\}$ frames are used as an example, however, this notation is generally applicable to all frames. The $\{a\}$ and $\{n\}$ frames can thus be substituted with the $\{d\}$, $\{g\}$ or $\{s\}$ frame. Scalar notation for motions and forces should be read as follows:

- The position scalar x^n_{na} - the x position of o_n to o_a expressed in the $\{n\}$ frame.
- The orientation scalar θ^n_{na} - the rotation of the $\{a\}$ frame with respect to the $\{n\}$ frame expressed in the $\{n\}$ frame.
- The force scalar Y^n_a - the force along the y-axis acting on the $\{a\}$ frame expressed in the $\{n\}$ frame.

Table A.1: Notation of the forces on and motions of a marine vehicle.

DOF	Description	Forces	Positions	Linear velocities
1	Motion along x-axis (surge)	X^n_a	x^n_{na}	u^n_{na}
2	Motion along y-axis (sway)	Y^n_a	y^n_{na}	v^n_{na}
3	Motion along z-axis (heave)	Z^n_a	z^n_{na}	w^n_{na}
		Moments	**Euler angles**	**Angular velocities**
4	Rotation around x-axis (roll)	K^n_a	ϕ^n_{na}	p^n_{na}
5	Rotation around y-axis (pitch)	M^n_a	θ^n_{na}	q^n_{na}
6	Rotation around z-axis (yaw)	N^n_a	ψ^n_{na}	r^n_{na}

Vector notation for motions and forces

Vectors are defined by a bold letter but other than that the notations are similar to motion scalars. For example, the vector $\boldsymbol{p}^n_{na}$ is the vector from o_n to o_a expressed in the $\{n\}$ frame. Commonly used vectors are defined in Table A.2.

Table A.2: A definition on vectors based as described in [24]

Description	Vectors	Definition
NED position	$\boldsymbol{p}_{na}^{n}$	$[x_{na}^{n}\ y_{na}^{n}\ z_{na}^{n}]^T \in \mathbb{R}^3$
Attitude	$\boldsymbol{\Theta}_{na}^{n}$	$[\phi_{na}\ \theta_{na}\ \psi_{na}]^T \in \mathbb{S}^3$
Body-fixed linear velocity	$\boldsymbol{v}_{na}^{a}$	$[u_{na}^{a}\ v_{na}^{a}\ w_{na}^{a}]^T \in \mathbb{R}^3$
Body-fixed angular velocity	$\boldsymbol{\omega}_{na}^{a}$	$[p_{na}\ q_{na}\ r_{na}]^T \in \mathbb{R}^3$
Body-fixed force	$\boldsymbol{f}_{a}^{a}$	$[X_a^a\ Y_a^a\ Z_a^a]^T \in \mathbb{R}^3$
Body-fixed moment	$\boldsymbol{m}_{a}^{a}$	$[K_a\ M_a\ N_a]^T \in \mathbb{R}^3$

Note that the integration of an angular velocity in its own frame doesn't have a physical interpretation [24]. For example, integrating the vector $\boldsymbol{\omega}_{na}^{a}$ would not be defined.

Finally the three vectors that define the motion of a marine vehicle are given by:

- $\boldsymbol{\eta}_{na}^{n}$ - The generalized position and orientation (i.e. pose) vector defined in the $\{n\}$ frame.
- $\boldsymbol{\nu}_{na}^{n}$ - The generalized linear and angular velocity vector defined in the $\{a\}$ frame.
- $\boldsymbol{\tau}_{a}^{a}$ - The generalized force and moment vector defined in the $\{a\}$ frame.

Where:

$$\boldsymbol{\eta}_{na}^{n} = \begin{bmatrix} \boldsymbol{p}_{na}^{n} \\ \boldsymbol{\Theta}_{na} \end{bmatrix},\ \boldsymbol{\nu}_{na}^{a} = \begin{bmatrix} \boldsymbol{v}_{na}^{a} \\ \boldsymbol{\omega}_{na}^{a} \end{bmatrix},\ \boldsymbol{\tau}_{a}^{a} = \begin{bmatrix} \boldsymbol{f}_{a}^{a} \\ \boldsymbol{m}_{a}^{a} \end{bmatrix}. \tag{A.1}$$

A.2. Reference points

Reference points are needed to express an equation of motion. Three important reference points are defined here:

- **CO** - The origin o_a of the $\{a\}$ frame
- **CG** - The center of gravity located relatively to o_a with the distance vector $\boldsymbol{r}_{ag}^{a} = [x_{ag}^{a},\ y_{ag}^{a},\ z_{ag}^{a}]^T$
- **CB** - The center of buoyancy located relatively to o_a with the distance vector $\boldsymbol{r}_{ab}^{a} = [x_{ab}^{a},\ y_{ab}^{a},\ z_{ab}^{a}]^T$

A.3. Transformations

This section provides a short overview of the kind of transformations used between reference frames.

Rotation matrices

Coordinates or vectors in a reference frame $from$ can be rotated to another frame to by using a rotation matrix denoted as R_{from}^{to}. A rotation matrix is orthogonal and has a determinant of 1, hence $R^{-1} = R^T$ and thus $RR^{-1} = RR^T = R^TR = I$. In this thesis, a rotation matrix is used as follows:

$$\boldsymbol{v}^{to} = R_{from}^{to}\boldsymbol{v}^{from}. \tag{A.2}$$

Euler angle rotations

Let the NED frame $\{n\}$ and the AUV body frame $\{a\}$ be related by the Euler angles ψ_{na}^{n}, θ_{na}^{n} and ϕna^{n}, then the rotation matrices around each of these axes individually are given by:

$$R_{x,\phi_{na}^{n}} = \begin{bmatrix} 1 & 0 & 0 \\ 0 & c\phi & -s\phi \\ 0 & s\phi & c\phi \end{bmatrix},\ R_{y,\theta_{na}^{n}} = \begin{bmatrix} c\theta & 0 & s\theta \\ 0 & 1 & 0 \\ -s\theta & 0 & c\theta \end{bmatrix},\ R_{z,\psi_{na}^{n}} = \begin{bmatrix} c\psi & -s\psi & 0 \\ s\psi & c\phi & 0 \\ 0 & 0 & 1 \end{bmatrix}, \tag{A.3}$$

where, s and a c are used for sine and cosine respectively.

These matrices can be used to construct a single rotation matrix from $\{a\}$ to $\{n\}$. The order of multiplication here matters. Following the zyx-convention, the combined rotation matrix from these principal rotations is given by:

$$R_a^n(\mathbf{\Theta}_{na}^n) = R_{z,\psi_{na}^n} R_{y,\theta na^n} R_{x,\phi_{na}^n}. \tag{A.4}$$

Expanding this equation results in Equation A.5:

$$R_a^n = \begin{bmatrix} c\psi c\theta & -s\psi c\phi + c\psi s\theta s\phi & s\psi s\theta + c\psi c\phi s\theta \\ s\psi c\theta & c\psi c\phi + s\phi s\theta s\psi & -c\psi s\phi + s\theta s\psi c\phi \\ -s\theta & c\theta s\phi & c\theta c\phi \end{bmatrix}. \tag{A.5}$$

In a 2D setting in the North-Down plane only pitch rotation is of interest. In this case the rotation matrix is given by:

$$R_a^n = \begin{bmatrix} c\theta & s\theta \\ -s\theta & c\theta \end{bmatrix}. \tag{A.6}$$

.

Cross-product operator

The cross-product operator $\times$ between two vectors $\boldsymbol{\lambda}$ and $\boldsymbol{\alpha}$ is defined as:

$$\begin{aligned} \boldsymbol{\lambda} \times \boldsymbol{a} &:= S(\boldsymbol{\lambda})\boldsymbol{a}, \\ S(\boldsymbol{\lambda}) = -S^T(\boldsymbol{\lambda}) &= \begin{bmatrix} 0 & -\lambda_3 & \lambda_2 \\ \lambda_3 & 0 & -\lambda_1 \\ -\lambda_2 & \lambda_1 & 0 \end{bmatrix}, \\ \boldsymbol{\lambda} &= \begin{bmatrix} \lambda_1 \\ \lambda_2 \\ \lambda_3 \end{bmatrix}. \end{aligned} \tag{A.7}$$

In a 2D setting in the North-Down plane, the 'cross-product operator' is given by:

$$\begin{aligned} \boldsymbol{\lambda} \times \boldsymbol{a} &:= \lambda_1 a_2 - \lambda_2 a_1, \\ \boldsymbol{a} &= \begin{bmatrix} a_1 \\ a_2 \end{bmatrix}. \\ \boldsymbol{\lambda} &= \begin{bmatrix} \lambda_1 \\ \lambda_2 \end{bmatrix}. \end{aligned} \tag{A.8}$$

However, note that this results in a scalar and not a vector, as this vector is perpendicular to the 2D plane spanned by the two input vectors.

B

A review on docking studies

In this appendix, a number of docking studies are reviewed, which resulted in the identification of the two knowledge gaps addressed in this thesis:

- The vertical docking approach to a floating DS has not yet been attempted.
- Docking near the sea surface docking has predominantly been limited to mild ocean conditions.

These gaps have been identified by reviewing docking systems for hovering AUVs and by reviewing studies on dynamic docking of cruising AUVs near the sea surface, summarized in Section B.1 and Section B.2 respectively.

B.1. Overview of docking systems for hovering AUVs

Most early AUVs were of the cruising type and attention for hovering type AUVs has so far been smaller [14]. Therefore, the literature on docking for hovering AUV has so far been limited [29]. This section summarizes the review on docking systems for hovering AUVs which the objective of identifying knowledge gaps.

A docking system based on the hovering Dagon AUV was presented by [82]. In this work, a fixed pole-type DS combined with a cradle-type DS was developed and tested in a water tank. The docking methodology included a USBL system for the homing stage and a vision system based on passive markers for yaw alignment with the cradle. Finally, a chessboard marker on the DS allowed for final adjustment until the vehicle was docked. During the publication of the paper, their guidance algorithm was not yet ready and thus the vehicle was manually steered to the dock. A Sure Simultaneous Localisation and Mapping (SLAM) algorithm was used to detect and track the markers' position relative to the vehicle.

The MARES AUV is another hovering-type AUV that can dock to a cradle-type DS. The algorithm used here was interesting since its computational complexity was low enough that it could be run on a Raspberry Pi 2 while being able to track a colored with temporary occlusion [14, 7]. The results showed it could be run at approximately 12 Hz, which is high enough for the authors to get smooth control.

Another paper discussed the autonomous docking capability of an ROV to a submerged cage-type DS hanging from a vessel [75]. In contrast to the aforementioned papers, this is a dynamic docking situation where both significant heave and yaw motion of the DS was present due to wave disturbances. The navigation system consisted of USBL based homing with an active marker-based vision system. An ANFIS algorithm was developed that could predict the location of the DS in advance in order to guide the ROV to the future DS position. The docking algorithms used here were run on a PC and could afford high computational complexity, which may not be available on an AUV.

A DS mounted on a wave energy converter for a BLUE ROV 2 Heavy was proposed in [79]. The

DS motion was limited to heave sinusoidal motion and MPC was used to generate the docking trajectory with a prediction horizon of 10 control steps or 1 second into the future. In this paper, the position and dynamical model of the DS are assumed to be known, thus greatly simplifying the motion prediction step. The link between getting positional information of the DS and using that to create a model of the motion of the DS was not shown.

In [22] it was attempted to dock a 5 DOF hovering AUV to a floating funnel-shaped DS. The vehicle used acoustic positioning and vision-based positioning to determine its relative position to the DS. It was shown that when the DS marker was moved, the AUV could follow the marker in hovering mode from 0.5 meters in front of the DS using a quadrant detector and a USBL system. The simplicity of the single Light Emitting Diode (LED) quadrant detector solution is attractive, however, the solution was reliable on the USBL, and pose estimates of the AUV can only be made using acoustic navigation and the INS. This approach only works when the hovering AUV can match the dynamics of the moving DS directly, and is therefore fundamentally limited by the control authority of the AUV. Furthermore, optical pose estimation was not utilized, but could increase the update rate and accuracy of the pose estimate, therefore possibly increasing performance. Furthermore, it was only tested in very mild conditions where wave motion was very limited.

A number of other studies on hovering type Unmanned Underwater Vehicle (UUV) docking systems were found in the literature, which were evaluated and summarized in Table B.1.

Table B.1: A summary of docking systems for hovering UUV. The Navigation (N), Guidance (G) and Control (C) of each solution are shown in the docking methodology column.

Year	UUV type	DS type	Environment	GNC	Limitations
2009	TSL UUV [35]	Fixed cradle-type DS	Sea	(N) Rectangular marker vision system based docking (G) Cross-track guidance (C) N/A.	Homing stage not considered; Fixed DS; Unknown docking performance.
2012	DAGON AUV [82, 29]	Fixed pole + cradle type DS	Water tank	(N) USBL based Homing, two phase vision system. Marker set for yaw alignment. Chessboard marker for final position adjustments using SURE SLAM (G) N/A (C) N/A.	Not validated in real-world environments; Currents not considered; Fixed DS; Manual guiding since guidance algorithm was not ready.
2013-2018	AUV Tri-TON 2 [66, 43, 44]	Fixed cage-type DS	Sea	(N) 3 mode system: Mode 1: Acoustic navigation. Mode 2: Camera vision system on AUV + LED on DS, relative altitude control. Mode 3: Camera vision system on AUV + LED on DS, force control. Pinhole model used for LED tracking (G) Waypoint guidance (C) N/A.	Effect of current not discussed; Fixed DS; Validation in bad visibility not discussed.

Table B.1: A summary of docking systems for hovering UUV. The Navigation (N), Guidance (G) and Control (C) of each solution are shown in the docking methodology column.

Year	UUV type	DS type	Environment	GNC	Limitations
2017	Remus 600 AUV [22]	Floating funnel-type DS	Sea	(N) Acoustic homing aid and optical quadrant detector for docking stage (G) LoS waypoint guidance (C) REMUS controller.	Sea conditions were mild; No optical pose estimation; algorithm was tested but actual soft docking not performed.
2017	5 DOF AUV [83]	Moving platform-type DS	Simulation	(N) USBL based homing, vision based docking (G) two-stage approach based on error-based guidance and dual reference point tracking (C) grey-prediction based PID control.	Not tested in real-world environment; Constant linear motion of DS; Currents not considered.
2017-2020	Mares AUV [14, 7]	Fixed cradle-type DS	Water tank	(N) USBL based homing and vision system + hybrid markers for close range pose and position estimates (G) Guidance keeps marker in frame (C) N/A.	Not validated in real-world environments; Effect of current not discussed; Fixed DS.
2019	BLUEROV2 Heavy [79]	Horizontal floating cage-type DS	Simulation	(N) - (G) MPC (C) N/A.	2D model; limited to heave prediction; Known simplified DS dynamic model; no real-world environment; Currents not considered.
2020	Work-class ROV [75]	Horizontal submerged cage-type DS	Sea	(N) USBL based homing, active LED vision based docking (G) ANFIS (C) Modified PID control.	Poor performance during visual occlusion; Vision system wasn't added to Kalman Filter (KF); Applicability in low visibility water not discussed; Vision pose estimation and image processing done on dedicated PC.
2021	Over-actuated AUV [88]	Fixed platform-type DS	Simulation	(N) USBL based homing, vision with LED markers + USBL based docking (G) Target state guidance or LoS guidance (C) Sliding mode controller.	Fixed DS; Not tested in real-world environment; Currents not considered.

Table B.1: A summary of docking systems for hovering UUV. The Navigation (N), Guidance (G) and Control (C) of each solution are shown in the docking methodology column.

Year	UUV type	DS type	Environment	GNC	Limitations
2021	X300 AUV [74]	Moving platform-type DS	Simulation	(N) USBL based homing, vision-based docking (G) Unified task priority approach including various local guidance algorithms (C) PI velocity control	Linear motion of moving DS with constant heading; Velocity of DS assumed to be known; Not tested in real-world environment; Navigation not considered in simulation; Current not considered; Straight line DS motion.
2021	6 DOF AUV [67]	Fixed funnel-type DS	Simulation	(N) N/A (G) Non-linear MPC with current estimator and Field of View (FoV) constraints (C) Non-linear MPC + Single Input Single Output (SISO) controller.	Not tested in real-world environment; Navigation not considered; Fixed DS.
2022	ROVER ROV [87]	Fixed cage-type DS	Deep sea	(N) USBL based homing and docking. (G) 2D LoS based homing and docking trajectory (C) N/A.	Fixed DS; Effect of currents not discussed.

Conclusion To the best of the author's knowledge, this literature review considers at least most studies on the topic of docking for hovering AUVs. This review reveals some limitations in the current literature for docking systems for hovering AUVs. Firstly, the number of studies considering docking for hovering AUVs is small compared to the number of studies on docking for cruising AUVs. This conclusion is also drawn in other studies such as [82]. Secondly, the studies that have focused on the dynamic docking case have been either significantly simplified, that is, tested in mild sea conditions, or performed in simplified simulations. Only [75] is considered to address the dynamic docking case in real-world offshore conditions under the influence of waves. Thirdly, in the proposed solutions, the UUV always approaches the DS from a horizontal orientation, thus the ability of some hovering-type UUV to pitch to a vertical orientation is not utilized in the docking procedure. New solutions may be available by orienting the vehicle vertically before the docking procedure. Fourthly, the case where a floating DS is approached vertically from below is never addressed. In [83] the AUV did dock to a moving DS vertically from above, however, the DS moved with a constant linear horizontal velocity close to the seafloor and was representing a towed DS, which has significantly different dynamics than a floating DS that is influenced by waves and currents. Furthermore, the effect of currents for hovering type UUV and docking attempts is barely discussed or tested, even though the characteristics of a hovering AUV make it better suited to dock in less ideal environmental conditions compared to cruising AUVs. Finally, the discussion on the applicability of vision-based systems in poor visibility water is limited. In summary, the following limitations are identified in the literature:

- Literature on hovering-type UUV and docking systems is still limited, even though hovering capability may allow for docking in rougher environmental conditions.

- Most reviewed studies that focus on the dynamic docking case assume simple motion.
- The ability of hovering-type UUV to pitch to a vertical orientation is not utilized in the docking procedure.
- Vertically docking to a floating DS is not considered.
- Most reviewed studies have not discussed the presence of currents.
- Limited discussion on the applicability of vision-based systems in poor visibility water.

B.2. A review on dynamic sea surface docking for cruising AUVs

In Section B.1, it was found that dynamic docking to a floating DS from below is a gap in the literature. The objective of this section is to review and obtain more knowledge about docking methodologies used in the dynamic docking case where the DS is suspended from a vessel or floating on the surface. This section focuses only on cruising type AUVs, as all hovering-type studies are already reviewed in Section B.1. A summary of the reviewed studies is provided in Table B.2.

In [30], it was assumed that the DS performed a sine motion and a linear backward motion with a constant yaw angle for a funnel-shaped DS. The homing procedure consisted of LBL aided guidance using an Sequential Quadratic Programming (SQP) optimization strategy to generate the shortest path up to 10 meters in front of the DS given a minimum curvature constraint. The docking procedure was divided into two stages. In the first stage, a path was computed that anticipated the future position of the DS. In the second stage, the vertical sine dynamics of the DS were matched directly using a vision-based navigation system without generating a path, and a prediction algorithm was used to compensate for the linear motion of the DS. It was shown in an experiment that the relative position and orientation of a LED marker could be obtained using a camera. Furthermore, it was shown in simulation that when the DS position and how it evolved over time was known and modelled with perfectly linear and sinusoidal motion the AUV could dock with the DS. However, it was assumed that the motion of the DS with constant velocity can be known, which is a significant assumption to make. In other words, the link between how from camera frames, a model of the motion of the DS and how it evolved over time could be obtained was not shown.

A different approach was taken in [46], where it was envisioned that an AUV should still be recoverable even if it is out of power and without communication. To that end, the docking strategy was performed by the USV while the AUV was floating uncontrollably on the sea surface. The navigation system of the USV to find the AUV used only a vision system based on a camera pinhole model to find the AUV, since if the AUV was actually completely out of power, it could not send its location to the USV. In experiments only the docking procedure was performed where the USV was in proximity of the AUV. A LoS guidance system was used to get into the neighborhood of the AUV, then an alignment function positioned the USV in alignment with the AUV. This alignment function generated a waypoint in front of the AUV, aligned with the x-axis (surge-direction) of the AUV. Then a final docking approach moved the USV from this point to above the AUV, where it could be mechanically locked. The USV was controlled using PD control for the surge and yaw control.

In [64] a modified cruising Hydroid REMUS 100 AUV was docked to a station-keeping USV using USBL communication. In this case, it was assumed that the USV did not move in between position measurements, and the trials were performed without waves and limited currents. A taut vertical line served as a docking line to which the AUV docked 3 out of 8 attempts. The simple LoS guidance strategy used here, pointing the AUV directly towards the source of the acoustic signal, seems unlikely to work in rougher waters under the influence of waves and currents.

Another funnel-shaped DS suspended from a surface vessel with a taut cable was shown [37]. They implemented USBL based homing and a combination of acoustic, vision, and pressure (i.e. depth measurements) based docking and a LoS guidance method. 24 out of 39 attempts were successfully docked to the terminal guidance structure. The update rate of the USBL modem was 0.5 Hz while the vision-based system could reach 30 Hz. In this work, the AUV always starts in front of the DS, and the orientation of the DS was known. Furthermore, currents and waves were small during the test so the

docking methodology was approaching the problem similar to a fixed docking case.

In [55], a novel planar funnel-shaped DS was presented that could engage with a T-shaped structure on the DS. This DS was envisioned to be deployed from an USV which could be approached by the AUV while in motion. Their tests were limited to the docking stage, but have shown that their docking system worked in calm waters. A simple vision system combined with cross-track guidance and PID control was used to guide the vehicle to the dock. However, they state that their strategy is limited to small waves.

Table B.2: A summary of dynamic docking systems for cruising UUV. The Navigation (N), Guidance (G) and Control (C) of each solution are shown in the docking methodology column.

Year	UUV type	DS type	Environment	GNC	Limitations
2003	Cruising AUV [30]	Funnel-type DS	Simulation	(N) LBL based homing, SBL + vision based docking (G) SQP homing guidance, predictive (C) Sliding mode controller.	No obstacles; Known velocities of DS; Fixed orientation of the DS.
2007	ISURUS AUV [46]	N/A	River	(N) Vision-based docking with pinhole camera model to estimate states (G) LoS guidance with USV-AUV alignment algorithm (C) PI control.	Only tested in calm waters; Homing not considered; AUV marked with attached navigation buoy; Mechanical locking not shown.
2018	Hydroid REMUS 100 [64]	Cable-shaped DS	Lake	(N) USBL based homing and docking (G) LoS Guidance (C) N/A.	Still lake, barely waves or currents.
2019	Bluefin Sand-Shark [55]	Planar cone-shaped DS	Lake	(N) Vision based docking with LED marker (G) Cross-track guidance (C) PID control.	Limited applicability in large waves; Homing not considered; Latching not considered.
2022	Cruising AUV [37]	Suspended funnel-type DS	River	(N) USBL based homing. USBL + vision based docking. (G) LoS guidance (C) double-layer PID control.	Currents and DS motion were small to none; DS position prediction was not utilized.

Conclusion The purpose of this section was to obtain knowledge on the docking methodologies presented used in the dynamic docking case. It can be concluded that non of the studies have successfully tested their docking strategies under rough ocean conditions except [30] in simulation. However, only a single wave scenario was tested in [30] where the DS was subject to simplified sinusoidal heave motion. Moreover, the waves themselves did not directly disturb the AUV, as the DS was hanging from a cable well below the sea surface, outside the wave-affected zone. Therefore, it is concluded that the dynamic sea surface docking strategies for cruising AUVs are not thoroughly tested under various ocean conditions. Consequently, it can be concluded that the dynamic sea surface docking strategies for cruising AUVs have not been thoroughly tested under diverse ocean conditions. This emphasizes the need for a hydrodynamic performance analysis of a docking system near the sea surface, considering various wave and/or current conditions.

C

Modelling in Ansys Aqua

This appendix explains how to build a ship model in Ansys Aqua and consequently obtain its motions and RAOs. The box-shaped USV is taken as an example. It would be tedious to describe all the simple steps of the model, which should be known by an experienced Ansys Aqua user. Therefore, emphasis is put on the interesting steps. For more details about Ansys Aqua, the reader is referred to [4, 3, 2].

C.1. Model setup and overview

To start a new model, add a hydrodynamic diffraction system to Ansys Workbench. By clicking on the system, this hydrodynamic diffraction system is opened in a new window. The overview tree shows the steps to be completed, which is shown in Figure C.1. These steps include creating a geometry and a mesh, setting up the hydrodynamic diffraction analysis, and finally computing the solution and the results.

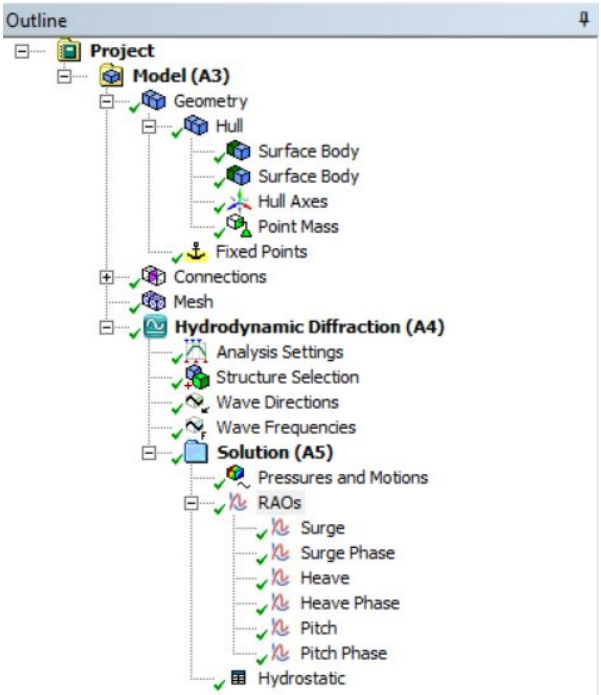

Figure C.1: The outline of the Ansys Aqua hydrodynamic diffraction system.

C.2. Geometry

The box-shaped USV geometry is created with the following steps:

- Create a rectangular sketch and extrude it to obtain the right general geometry.
- Ansys Aqua requires a surface body. Thin the extrusion such that a zero-thickness surface body remains.
- Move the surface body downwards by creating a plane and moving the geometry to this new plane. This defines the draft of the USV as the origin x-y plane defines the still water surface.
- Slice the surface body into two bodies on the waterline x-y plane. Ansys Aqua only uses the body below the waterline for diffraction calculation. Note that for simulating the AUV, the geometry is completely submerged such that only one diffraction surface body is required.
- Combine the two bodies into one part. This step finishes setting up the geometry. This results in the geometry shown in Figure C.2.

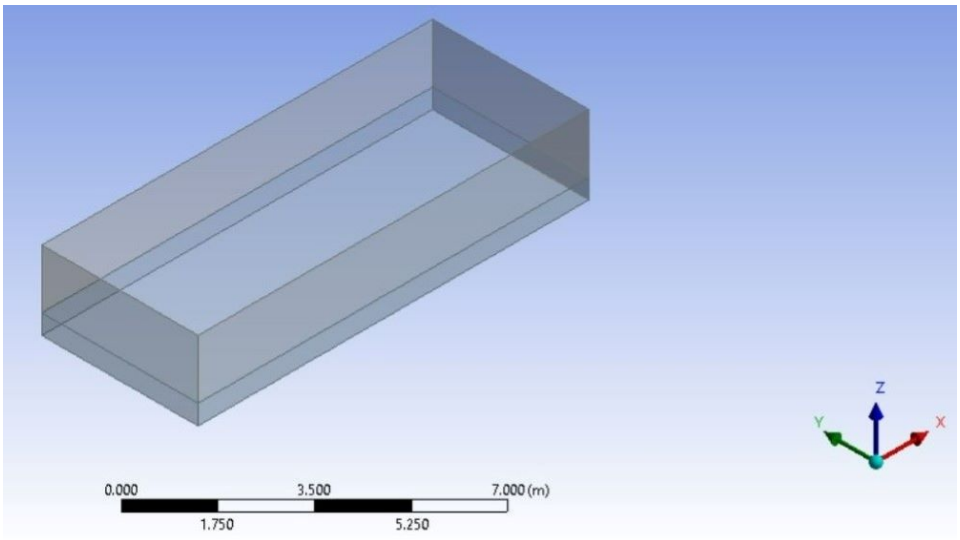

Figure C.2: The USV geometry

C.3. Model

The model is created using the following steps:

- The previously defined geometry is automatically loaded into the model. It is important to add a point mass that serves as the mass of the ship. Ansys Aqua can calculate the mass of the point mass and other hydrostatic properties automatically, based on its water plane level and water properties. The inertia of the ship has to be added manually which can be obtained from for example CAD.
- For the fully submerged AUV, the submerged structure detection option should be set to fully submerged. The submerged structure detection option can be found under Geometry-[part name]-advanced options.
- Now a mesh can be created and the mesh size should be specified as shown in Figure C.3.

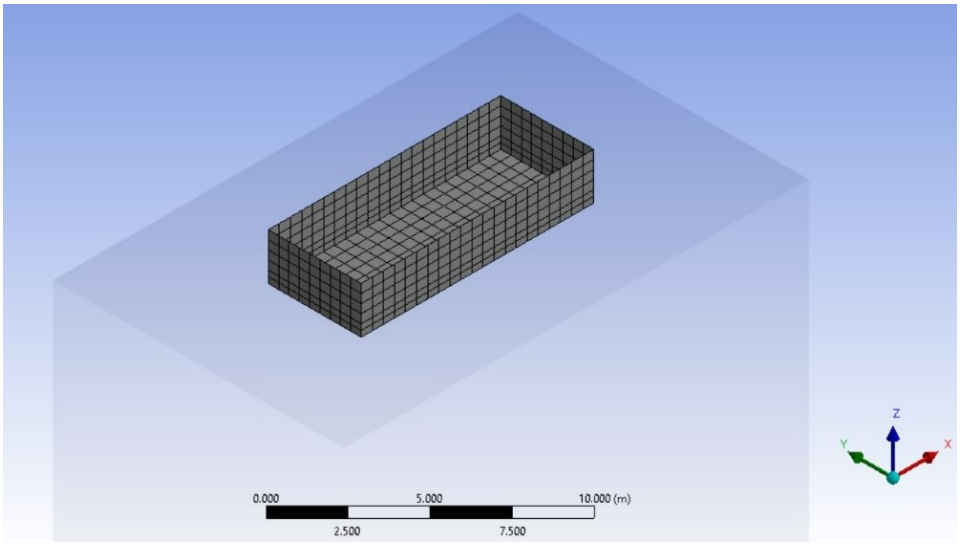

Figure C.3: The USV mesh

C.4. Setup

The model is setup consists of the Analysis Settings, the Structure Selection, the Wave Direction and the Wave Frequencies selections:

- **Analysis Settings:** Nothing major is changed here.
- **Structure Selection:** Select the USV geometry.
- **Wave Directions:** In this section, the wave directions can be specified. Only the vertical plane for a 2D simulation is of interest, however, a minimum of 4 wave directions is required by Aqua. Therefore the wave range is selected from $-180°$ to $180°$ and 3 intermediate directions are chosen such that the wave direction interval is $90°$. This is shown in Figure C.4
- **Wave Frequencies:** The wave frequencies are selected manually using period-based intervals. The evaluation periods are chosen in the range of $1\ s$ to $30\ s$ as this range contains most of the wave spectrum energy.

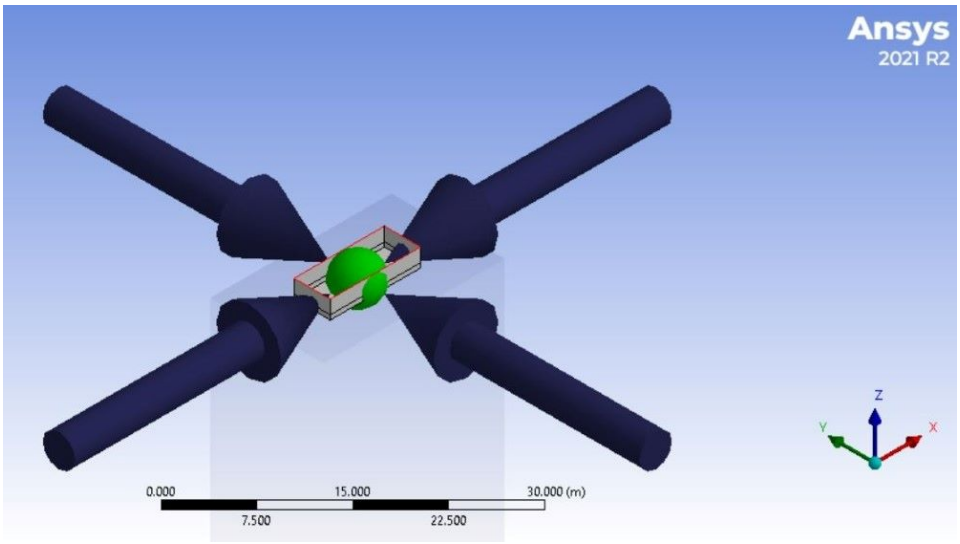

Figure C.4: The four wave directions

C.5. Solution and results

In the solution section, it can be selected which results are computed. The results relevant to this thesis include:

- **Pressures and Motions:** gives a visual representation of the pressures and motions of the structure as shown in Figure C.5a.
- **Added mass:** provides the added mass coefficients for the selected wave frequency range and was used to obtain the added mass coefficients for the Lobster Scout.
- **RAOs:** provide the distance and rotation gain of the USV with respect to the wave amplitude and the phase of these motions with respect to the wave phase over the selected wave frequency range, as shown in Figure C.5b. The wave phase is zero when the wave is at its highest positive amplitude. The RAOs are exported to a CSV file which is then imported into the Python simulation model.

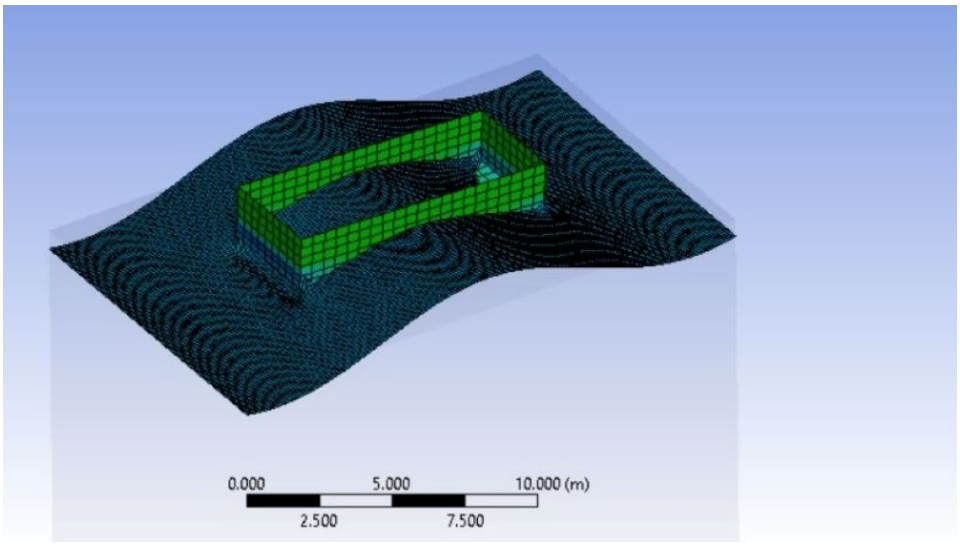

(a) The pressures and motions result.

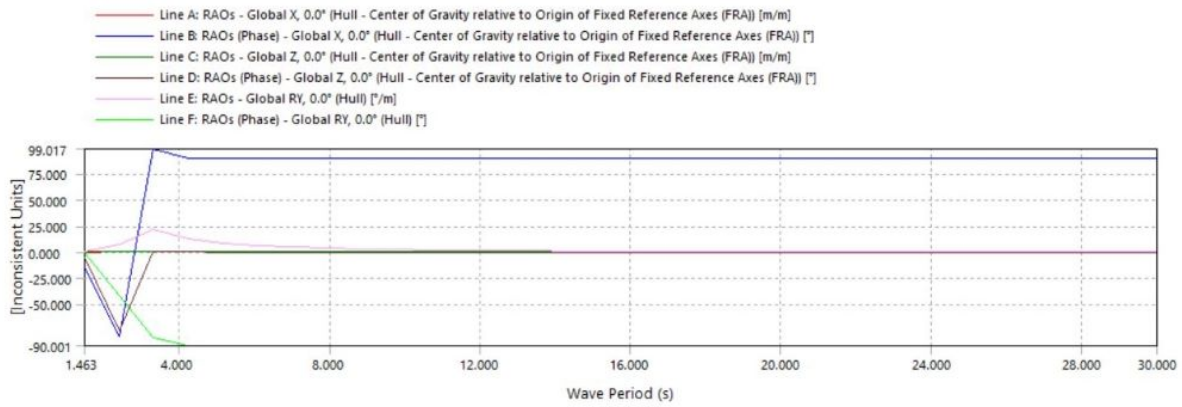

(b) The motion RAOs and phases.

Figure C.5: Results

D

Docking guidance methods

Docking guidance methods use the map created by the navigation system to plan a path from the AUV to the DS. The complexity of this map has a large influence on the suitability of various guidance methods. For example, if a lot of obstacles are present in the map, a collision-free path is less trivial than in an obstacle-free map and thus more capable guidance method is required.

Ideally, a single guidance method can directly guide the AUV from any initial position to any DS position, in any scenario, with a path that is optimal in some sense. Optimization criteria may involve finding the shortest path, the most energy-efficient path, or the most controllable path. However, implementing such a comprehensive guidance method can quickly become overly complex and may not be practical.

In the docking problem, it is often assumed that there are no obstacles or that the obstacles are always fixed with respect to the DS position. Since a large part of the oceans is open water, this assumption is often justified. As a result, if the relative position of the AUV is known with respect to the DS, even simple guidance methods can work well.

Docking guidance methods are categorized into three types, local, global, and predictive guidance methods. Local guidance methods, discussed in Section D.1, are relatively simple and typically involve pointing the AUV to the DS or some variation thereof. Global guidance methods can create more complex paths and can deal with for example obstacles, which are discussed in Section D.2. Predictive guidance, detailed in Section D.3, can anticipate and plan for future states of the system, which is relevant for dynamic docking. Finally, guidance methods can be combined with trajectory interpolation techniques to create longer and smoother paths, which are discussed in Section D.4.

D.1. Local guidance methods

Local guidance methods are often suitable for both cruising and hovering AUVs as they don't require full position control. They are typically used for docking of to an unidirectional DS and this scenario is used below to illustrate the various methods. Most of these local methods are reviewed in two literature surveys on docking guidance for AUVs, namely [85] and [16].

LoS guidance

This method is very simple, as the vehicle is just pointed straight to the DS and keeps a constant surge velocity (see Figure D.1). This method does not take into account any currents and thus when the vehicle drifts, it starts changing the angle of approach, resulting in a curved path towards the DS. Similarly, when the DS moves, it will result in a curved path as the line of sight changes. This curved path also means the AUV will arrive at the DS at an angle, which is especially critical in unidirectional DS where only a limited set of entry angles allow for docking. This methods is commonly used for AUV docking guidance, such as in [37, 22, 87, 46, 64, 57].

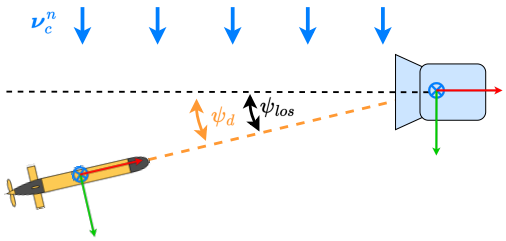

Figure D.1: The LoS method visualized. The AUV moves with a constant surge velocity and aims to follow the desired heading angle ψ_d.

PNG guidance

This method changes the heading angle of the vehicle in proportion to the rate of change in direction of the LoS vector (see Figure D.2). In effect, this method steers the vehicle more aggressively towards the DS and can therefore reduce the drift due to currents. There are variants proposed that are more suited to dealing with moving targets like augmented PNG, velocity compensated PNG, pursuit plus PNG, and dynamic lead guidance. The method is further explained in [53] and evaluated in [37] and [84] in simulation.

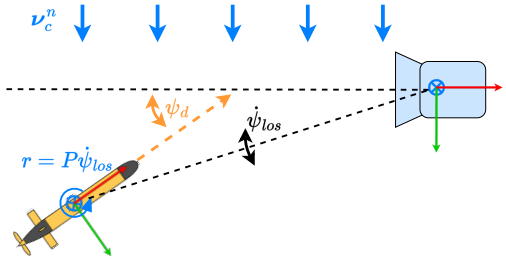

Figure D.2: The PNG method visualized. The angular rate r is proportional to the rate of change of the LoS angle.

Pure pursuit guidance

This method generates a linear path centered on the DS. The AUV computes a heading angle from its current position towards a look-ahead point somewhere on this line (see Figure D.3). The AUV moves with constant surge velocity towards this look-ahead point and adjusts its heading accordingly. The pure pursuit guidance algorithm has been used in [84] to dock an underwater vehicle to a rotating DS, and has been evaluated in [16] and [58] in simulation. Other experimental studies include [20].

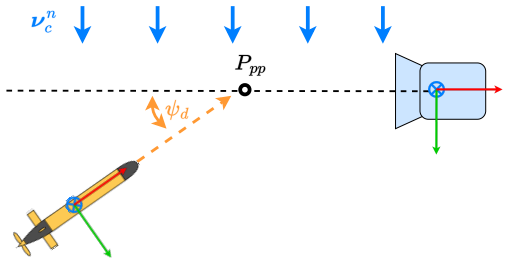

Figure D.3: The pure pursuit method visualized. The AUV steers towards the look-ahead point P_{pp}.

Crab angle guidance: current compensation

This method can be used in combination with other local guidance methods to allow for uniform constant current compensation of a cruising AUV. A corrective crab angle is calculated, which steers the nose of the AUV in the direction of the current such that the vehicle does not drift off track (see Figure D.4). A disadvantage of this method is that the AUV arrives at the DS entrance under an angle. This method requires knowledge of the current velocity and thus requires current measurements or estimates, which

can be done with for example an Acoustic Doppler Current Profiler (ADCP). Pure pursuit variants with current compensation using a crab angle are presented in [84, 58, 16, 20].

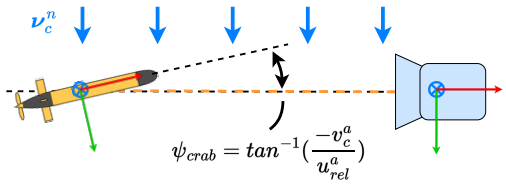

Figure D.4: The crab method visualized.

Cross-track guidance

In this method, the error between the position of the AUV and the shortest (perpendicular) distance to the linear path centered on the DS is used to calculate a heading of the vehicle that steers it towards this line (see Figure D.5). A PID controller is used to convert the error to a heading. An advantage of this method is that it is more resistant to currents as the yaw angle increases if the error is not reduced fast enough. The vehicle again moves with a constant surge velocity to reach the DS. This method is commonly used, such as in [49, 35, 55, 38].

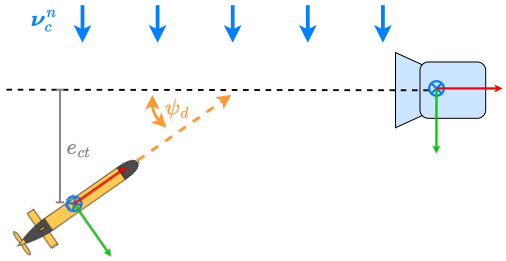

Figure D.5: The cross-track method visualized. The desired heading direction is calculated using the cross-track error e_{ct} using PID control.

Touchdown alignment guidance

The above-mentioned guidance laws all have the disadvantage of arriving at the DS under an angle, which decreases the chance of a successful dock. This method uses a cross-track controller to guide the vehicle to the DS, but gradually aligns the attitude of the vehicle with the center line of the DS at the final meters before arriving at the DS entrance (see Figure D.6). The vehicle may drift away from the center line in exchange of a more desired entrance angle. This method is proposed in [60] using a cosine curve to gradually adjust the reference attitude and was tested in simulation. Furthermore, it was evaluated in [16] in simulation.

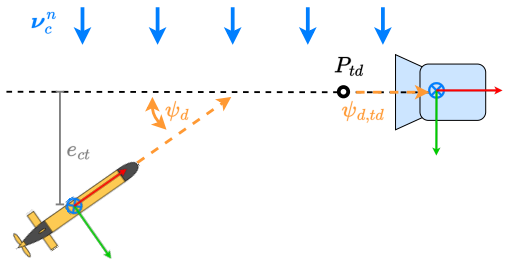

Figure D.6: The touchdown alignment method visualized. At a certain distance before the DS, the desired heading is aligned with the DS entrance center-line.

Side-slip guidance

This method is similar to touchdown alignment guidance, however, the vehicle first overcompensates for the current, by guiding the vehicle to a line parallel to the center-line of the DS but upstream the cross-velocity component of the current to the center-line path of the DS (see Figure D.7). This way, when the vehicle's attitude is gradually aligned with the DS entrance direction, the vehicle has some margin to drift downstream. This method was first proposed and evaluated in simulated in [59] and later evaluated in simulation in [16].

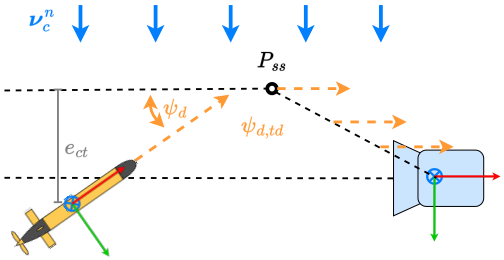

Figure D.7: The side-slip method visualized.

Sliding path guidance

Similar to side-slip guidance, this method first over-compensates for the current by steering the vehicle to a line parallel to the center line of the DS but upstream the cross-velocity component of the current. Subsequently, crab angle guidance is used to navigate the vehicle towards point P_{sp}. This method then uses an integral LoS controller to decrease the cross-track component to zero, while a Speed Regulated Guidance (SRG) controller aligns the heading of the AUV to the DS entrance direction. These two controllers take over control based on a maximum allowable cross-track error (see Figure D.8). The method was simulated in prior works [62, 16].

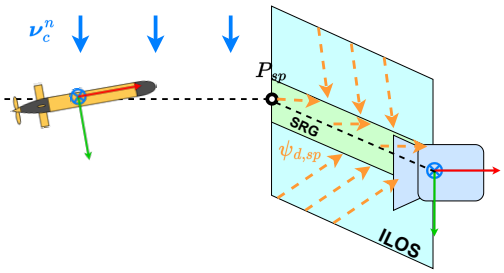

Figure D.8: The sliding path method visualized.

Target state guidance

Target state guidance simply decreases the error between each vehicle state to the respective DS state (see Figure D.9). This method is only applicable to hovering vehicles as it requires control over all DOF independently. This method is for example used in the Lobster Scout [6] and in [83, 88].

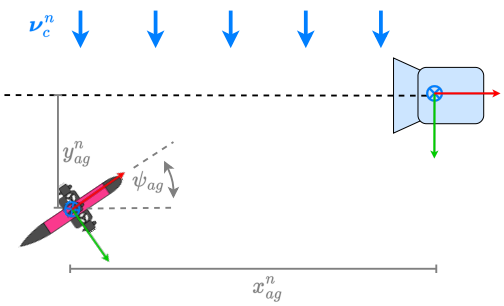

Figure D.9: Target state guidance visualized.

Fuzzy controller based guidance
This method uses fuzzy logic to compute a reference angle and surge velocity. Fuzzy control consists of 3 stages, an input stage, a processing stage, and an output stage. The input stage maps the cross-track error and the approach range to the membership function. The processing stage takes computes the weighted average of all the fuzzy rules. Finally, the output stage uses this result to generate a specific surge velocity and reference angle. This method is for example used in [73].

Artificial potential fields
Artificial potential fields are methods that compute a potential that guides the vehicle toward the goal state. The vehicle follows the minimum potential towards the DS. This method is able to deal with obstacles as a higher potential is computed around the obstacle, resulting in the vehicle moving around the obstacle. Two methods exist, global and local artificial potential fields. Local methods have a tendency to get trapped in local minima but are able to be run online, as they are less computationally demanding, while global methods require a lot of compute and are less suited for docking. An example of this method is implemented in [63].

Lyapunov-based guidance
This method steers the vehicle towards the minimum generalized energy point of a Lyapunov function. This method was used in [9] and was identified as a medium-range manoeuvring guidance method. The implementation in this study was similar to target state guidance.

D.2. Global guidance methods
Global guidance methods are directly able to plan a path from the initial location of the AUV to the DS location. These types of algorithms can consider various constraints and avoid obstacles. A number of methods are briefly discussed below.

Graph search methods
Graph search methods compute a graph by regularly dividing the map into a grid of connected nodes and edges. This in a sense discretizes the space. Nodes that interfere with obstacles are removed hence these algorithms can make an obstacle-free graph. The initial position of the AUV and the position of the DS are then connected to the graph and a path can be searched by a graph search algorithm. An example of a graph search method used for AUV guidance is [11].

Probabilistic sampling-based methods
Sampling-based methods compute a path by directly sampling the configuration space and producing a graph that can be used to find a path from the initial position of the AUV to the DS. Sampling-based methods are able to deal with obstacles and create an obstacle-free path by removing nodes that sample in the obstacle space. Sampling-based methods are faster and more memory efficient than search-based methods as they do not need to keep a discretized map of the configuration space. Various sampling-based algorithms exist such as Probabilistic Roadmap Method (PRM) and Random Rapid Tree (RRT). RRT* does a rerouting step in addition to the steps in RRT, which enables it to asymptotically find the optimum, with the downside that it is slower than RRT. RRT* has been used in path planning for autonomous underwater vehicles in [68].

D.3. Predictive guidance methods
Predictive guidance methods have the ability to anticipate future states of the system. This is especially relevant in dynamic docking situations where the DS location can move during the docking operation. Predictive algorithms can then help guide the vehicle to a future position of the DS and thereby increase the docking success rate in rough ocean conditions.

ANFIS
An ANFIS algorithm was used to predict the heave motion of a DS in a dynamic docking scenario in [75]. The ANFIS algorithm was trained and tested using a pre-recorded dataset from ocean trials to autonomously dock an under-powered ROV to a moving DS. The ANFIS algorithm could predict the

heave motion $2.5s$ into the future while keeping the prediction error smaller than $0.55m$ for 95% of the time. While the ANFIS network was able to predict the future motion of the DS, the ANFIS network performance degraded with changing heave motion frequency and amplitude. Therefore, it might be needed to have a database of various trained ANFIS networks for different sea conditions, or the ANFIS network has to be retrained every time a docking attempt is done.

Grey model prediction

In [83], a gray model prediction method was used to estimate the future relative position and angle errors between the AUV and the linear constant velocity moving DS. This resulted in smaller overshoots between the PID controller and prevented collisions.

MPC

MPC is a control strategy that can take in a number of constraints and find an optimal control input to reach a certain state. MPC uses a dynamic model of the process to predict the future states of the process, given certain inputs. A cost function can then be defined that is used to find the inputs that minimize this cost. The first input is then executed and the optimization problem is then optimized again and so forth. In other words, an optimization problem is being solved at each time step. The prediction horizon determines how far MPC predicts in the future. An advantage of increasing the prediction horizon is that future events can be anticipated. Examples of this method used in simulation are shown in [79, 67].

D.4. Trajectory interpolation

Typically, a path towards a DS can be constructed with a set of waypoints that are connected with a certain construction technique that varies in continuity and smoothness. Such a set of waypoints is either generated by a global guidance method, or a predetermined set of waypoints determined by the developer. Smooth paths can be better followed by non-holonomic vehicles such as cruising AUVs and are therefore desirable. This section discusses a number of methods of connecting waypoints.

Waypoint guidance

In this method, the waypoints are not interpolated, but out of the set of waypoints only the target waypoint is chosen for the AUV and a local guidance method like LoS or PNG is used to get there (see Figure D.10). A region of acceptance conditions is often used to determine if the vehicle is in the vicinity of the target waypoint. When this condition is satisfied, the target waypoint is switched to the succeeding one. Examples of this method in use are given by [66, 43, 44].

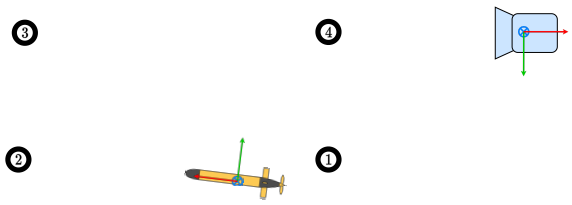

Figure D.10: Waypoint method visualized

Straight-line interpolation

In this method, all the waypoints are directly connected using affine lines segments, and a local guidance method like the cross-track guidance or the pure pursuit guidance method, steers the vehicle towards a line segment (see Figure D.11). These paths are non-smooth and will result in path deviations for non-holonomic vehicles like cruising AUVs. These paths are able to be perfectly followed by a holonomic AUV like a hovering AUV. Similarly to a waypoint guidance method, a region of acceptance conditions can be used to determine if the vehicle has traversed over a line segment, then a succeeding line segment is chosen.

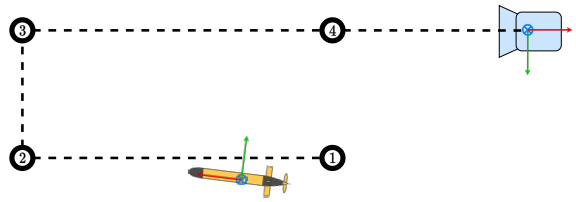

Figure D.11: Straight-line method visualized

Dubins-based interpolation

A Dubins curve is a path interpolator method between an initial state and a final state, subject to constant speed and a minimum turning radius constraint. Given these constraints, a Dubins curve can provide the shortest smooth path between the 2 states (see Figure D.12). A 2D Dubins curve consists of 3 connected segments of curves, straight lines. 3D Dubins curves can be constructed using two orthogonal Dubins curves. An example of this method used in a AUVs docking simulation is shown in [68] and experimentally in [56]. A drawback of this method is that it has a high computational cost, which makes the method less suitable for real-time use where frequent re-planning of the path is required [76].

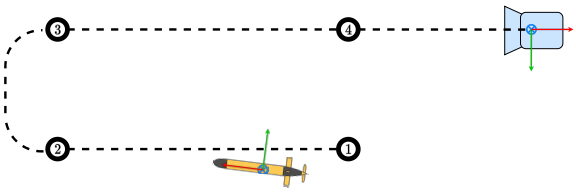

Figure D.12: dubins path method visualized

Spline and piece-wise polynomial interpolation

Various interpolator methods use smooth splines and polynomials to construct a smooth path through a number of waypoints (see Figure D.13). An example of a cubic spline function used to construct a 3D smooth path for an AUV was presented in [30].

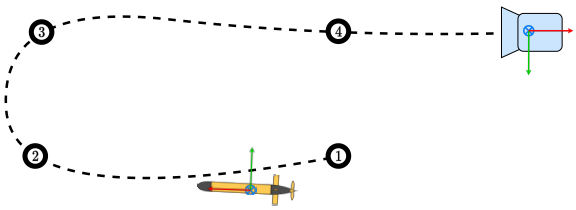

Figure D.13: Spline and piece-wise polynomial interpolation visualized